In depth study of charge compensation mechanism in novel 2D layered anode materials for Lithium and Sodium Ion Batteries

Cindy Nunes Soares

This dissertation is submitted for the degree of Doctor of Philosophy

November 2021

Department of Chemistry

"Our lives are composed of a finite set of moments that we choose how to spend."

- *John Green*

Declaration

This thesis has not been submitted in support of an application for another degree at this or any other university. It is the result of my own work and includes nothing that is the outcome of work done in collaboration except where specifically indicated. Many of the ideas in this thesis were the product of discussion with my supervisor Dr Nuria Tapia Ruiz.

The research presented within this thesis was in part financially supported by the Engineering and Physical Sciences Research Council (EPSRC), however the author declares no conflicts of interest.

Cindy Nunes Soares, MSc

Lancaster University, UK

Abstract

The development of high-performance electrode materials has become a critical area of research in the lithium and sodium-ion battery (LIBs and SIBs) community to meet the high energy and power density demands of the current and future electrical energy storage applications. So far, the progress in the development of suitable anode materials has been mostly limited to carbon-based materials, metal sulphides and oxides to a minor extent. Overall, these electrodes show room for improvement given their low voltage, low gravimetric density and poor long-term cyclability. Thus, at this juncture, alternative anodes to these with an excellent rate performance and a high capacity with long cyclability must be sought. The discovery of graphene initiated a surge of interest in other two-dimensional (2D) atomically thin materials, such as transition metal dichalcogenides (TMDs). These types of materials have been studied as promising materials for a broad range of applications for decades. The rising interest in these materials is due to their earth-abundant presence in nature, excellent mechanical properties, ability to tune interlayer spacing, good performance when large current densities are applied, long life capability and wide operation range temperatures. Although the excellent theoretical properties of these materials have not yet been reached, TMDs are a group of very promising materials to be used in energy storage.

This thesis is a proof of concept to study the viability of two different TMD materials (WTe_2 and $TaTe_2$) as anode materials for both LIBs and SIBs. With this study, we will shed a light on the charge compensation mechanisms for these materials during lithium and sodium ion intercalation. The structure of the materials studied in this work was characterised using XRD, SEM and TEM. Their electrochemical response was tested using electrochemical techniques such as galvanostatic cycling, CV and EIS to probe ion (de)intercalation into the electrode crystal structure. Moreover, electrochemical tests were coupled with operando synchrotron XRD and XANES spectroscopy to understand the structural evolution upon ion insertion and extraction.

Acknowledgements

First and foremost, I would like to thank my supervisor Dr Nuria Tapia Ruiz for taking me as a research student and for her guidance and help throughout my PhD years. I would like to thank Dr Zdenek Sofer for generously providing the samples that were characterized in this thesis. I would also like to thank my colleagues at the Tapia-Ruiz group for their assistance and wonderful teamwork in and outside the lab. A special thank you to Sara Costa and Mangayarkarasi Nagarathinam for your friendship and patience with me during these past years.

The experimental work in this thesis was undertaken at the Chemistry Department at Lancaster University and I would like to express my sincere gratitude to the department for allowing me to do my research by use of their facilities as well as all the departmental staff. A big thank you to Dr Nathan Halcovitch for sharing his XRD experience, helping me every time that the equipment decided to stop working and for the walks and talks that helped me to stay sane during these years. I would also like to thank Dr Sara Baldock, Dr David Rochester and John Baum for the huge help throughout my PhD. I can't forget to thank all my fellow PhD student colleagues Marine Aublette, Dhruv Trivedi, Dr Shahin Nikman, Dr Craig Armstrong and Sapphire McNeil for your support, help and guidance. I am very happy to have been able to share my PhD with you and will always be very grateful for your endless support both in and outside the lab, the laughs shared when the research was not working and the friendship that you guys always showed me.

Finally, I would like to thank my family and friends for all their support, even far away you guys were always there to hear my complaints and give me good advice which helped me not giving up on everything and cry my heart out. Mike Toal thank you for always being there for me, for hearing all grumbles, supporting me no matter what and for making me realise that a PhD is just a PhD and more important things are important in life. I will always be massively thankful to be surrounded by amazing people. I wouldn't have been able to finish this PhD without your help, moral support, and patience to hear all my moaning. Thank you from the bottom of my heart!

Cindy

Contents

List of Tables

List of Figures

List of Abbreviations and Acronyms

Abbreviation/ Acronym	Meaning
2D	Two Dimensional
a.u.	Arbitrary Unit
cm	Centimetre
CPE	Constant Phase Element
CV	Cyclic Voltammetry
DEC	Diethyl Carbonate
DFT	Density Functional Theory
DMC	Dimethyl Carbonate
EC	Ethylene Carbonate
EDX	Energy Dispersive X-ray Spectroscopy
EIS	Electrochemical Impedance Spectroscopy
eV	Electronvolt
FESEM	Field Emission Scanning Electron Microscopy
HRTEM	High-Resolution Transmission Electron Microscopy
LIB	Lithium-ion Battery
mA	Milliamp
mm	Millimetre
nm	Nanometre
NMP	1-Methyl-2-Pyrrolidinone
OCV	Open Circuit Voltage
PVDF	Polyvinylidene Fluoride
PXRD	Powder X-ray Diffraction
R	Resistance

SAED	Selected Area Electron Diffraction
SEI	Solid Electrolyte Interphase
SEM	Scanning Electron Microscopy
SIB	Sodium-ion Battery
SXRD	Synchrotron X-ray Diffraction
TEM	Transmission Electron Microscopy
TM	Transition Metal
TMD	Transition Metal Dichalcogenide
V	Volts
XAS	X-ray Absorption Spectroscopy
XRD	X-ray Diffraction
µm	Micrometre

1 Literature Review

1.1 Energy context

Energy consumption patterns have changed throughout history as new energy sources are developed and the energy demand has risen. From the mid to late 1800s, wood served as the main form of energy, changing to coal in the late 19^{th} century and being replaced by petroleum products in the middle of the last century. Until now, oil, petroleum and natural gas remain the main energy sources used by humanity to sustain their way of life (Figure 1.1) [1]. All societies require energy to meet simple human needs which can be categorized into five energy-use sectors: industrial, transportation, residential, commercial and electric power sectors [1]. Access to energy has allowed the development of human beings and is nowadays a key pillar for human wellbeing, economic development, and poverty alleviation. However, energy systems have important environmental impacts [2]. The production of carbon dioxide (CO_2) and other greenhouse gases is intrinsically related to the intensive use of fossil fuels (such as coal, oil and gas) [2]. The release of these gases is among the key drivers of global climate changes, contributing mainly to the global warming effect, which has led to a general increase in average global temperature as well as to an increase in the number of extreme weather conditions affecting the globe [2]. The steady growth of the population is leading to a global increase in energy demand which therefore is related to an increase in emissions of CO_2 into the atmosphere and the associated global warming effects [3].

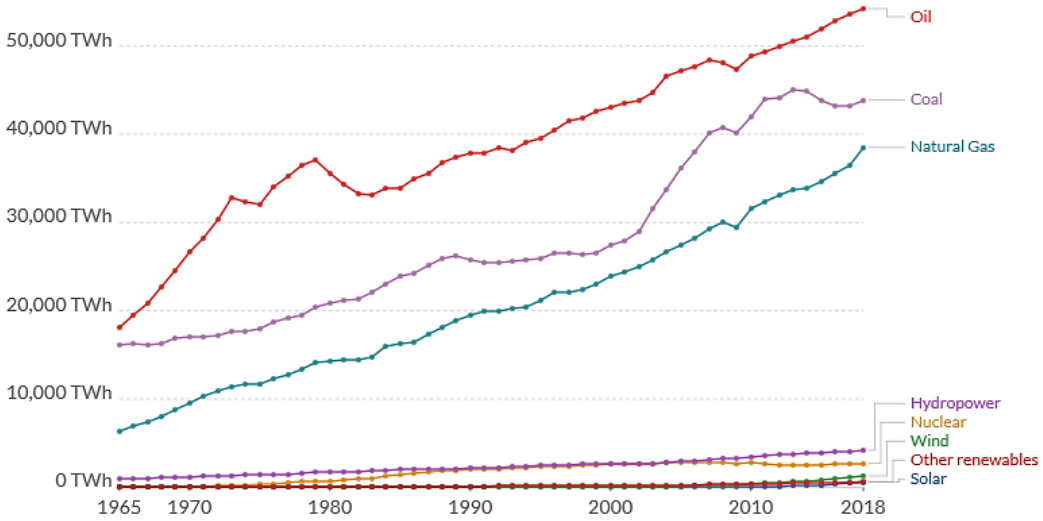

Figure 1.1 - Worldwide primary energy consumption by source, from 1965 to 2018, Source: BP Statistical Review of Global Energy (2019) [3]

The International Energy Outlook 2019 (IEO2019) provided by the US Energy Information Administration (EIA) predicts that the energy consumption in non-OECD (Organisation for Economic Co-operation and Development) countries (regions such as India, China and Africa) will increase by nearly 70 % between 2018 and 2050 in contrast to a 15 % increase in OECD countries (main Europe and the USA) [4]. China and India are among the world's fastest-growing economies worldwide for the past decade and remain the primary contributors to future growth in world energy demand [4]. The world's fossil fuel reserves are finite by nature and ever more declining due to this high energy demand. This results in higher prices and raises in extraction technologies associated with severe environmental issues. The high energy demand and shortage of petroleum sources are now one of the main issues that governments are facing [2]. Therefore, a balance between development and the environment must be achieved to ensure that the population has access to enough energy to maintain a high standard of living. New strategies must be taken to sustain the worldwide economic growth at a relatively low cost without damaging the environment.

Renewable energy systems are the main candidates to replace fossil fuels due to their low environmental impact, therefore, mitigating climate change [5]. These include wind, wave hydroelectric, biomass, geothermal, tidal and photovoltaic energy systems.

The EIA predicts that by 2050, renewable energies will displace petroleum as the most used energy source, as electricity use grows faster than any other end-use fuel [4]. The world invested 286 billion USD in renewable technologies by 2015, which represents an increase of more than 600 % compared with 2004 (47 billion USD) [3]. The trends in the investments in renewable energies suggest that investors see solar and wind energy as the dominant renewable technologies of the future accounting for 94 % of global financial investment in 2016 [3].

Despite their advantages, renewable energies possess some drawbacks due to their sporadic nature and strong dependence on unforeseeable variations, which leads to high fluctuations in energy production [5]. Demand, on the other hand, is relatively constant and does not follow these variations which result in off-peak availability of energy [5]. Therefore, it is important to develop electrical energy storage systems (EESs) which can integrate renewable energy into the grid smoothly and effectively, to store it so that it can be available when required [5]. Among the various EESs, electrochemical storage devices have gained a lot of attention in recent years, especially rechargeable batteries (or secondary batteries) [6]. Now, these represent the most promising means for storing electricity on a large scale, due to their flexibility and high-energy conversion efficiency [6]. Rechargeable batteries can be used in either large devices, such as grid storage, intermediary devices, such as electric vehicles (EVs) and portable devices, such as mobile phones and laptops [5], [6].

1.2 Electrochemical Principles of Rechargeable batteries

An electrochemical cell is a device used to convert electrical energy into chemical energy or vice versa. A battery is a closed system that converts the chemical energy contained in its active materials directly into electric energy by electrochemical oxidation-reduction reactions. This kind of reaction involves the transfer of electrons between the materials that compose the battery [7]. The basic electrochemical unit of a battery is known as a cell. One or more cells can be connected in series or parallel depending on the desired output voltage and capacity required [8]. A cell consists of three major components: anode, cathode and electrolyte. The two electrodes (cathode

and anode) will be oxidized and reduced during the electrochemical process and are connected through an external circuit that allows the transport of electrons from one electrode to the other. The electrolyte acts as the ionic conductor providing the medium for the transfer of ions between the anode and cathode [7]. In practical systems, all components of the cell must present specific properties: the anode and cathode materials should be efficient reducing and oxidizing agents, stable, and the electrolyte must be stable and have good ionic conductivity but be electronically insulator [8]. Physically the anode and cathode are electronically insulated in the cell to prevent internal short-circuiting [8]. In a practical cell design using a liquid electrolyte, a separator material is used to mechanically separate both electrodes, however, this should be permeable to the electrolyte to allow the desired ionic conductivity [8]. Depending on if the redox reaction happening inside the cell is reversible or not, batteries can be classified as secondary or primary batteries, respectively. Although secondary batteries typically present lower energy densities when compared with primary batteries, the capacity lost on standing can be restored by recharging [8].

Two main processes occur in a battery as a result of the redox processes happening known as charge and discharge and are represented in Figure 1.2. In both cases, the cell needs to be connected to an external load, or current flow, to allow spontaneous electron transfer from the more negative to the more positive potential [8], [9]. During the discharge process, the electrons flow from the anode, oxidizing it, through the external load to be accepted by the cathode leading to its reduction [8]. The ions move through the electrolyte in the same direction to compensate for the charge imbalance [8]. The battery releases the energy stored during the process. During the charging process, the current flow is reversed, and oxidation takes place at the positive electrode while reduction occurs on the negative side. The ions move from the cathode to the anode allowing the storage of energy by the battery [8].

Equations 1.1 and 1.2 show the typical overall discharge and charge reactions respectively, that occur in a battery during a cycle, where M represents a metal or counter electrode and A the cathode material.

Discharge reaction:

$$M + A^+ + e^- \rightarrow M^+ + A + e^- \quad (1.1)$$

Charge reaction:

$$M^+ + A + e^- \rightarrow M + A^+ + e^- \quad (1.2)$$

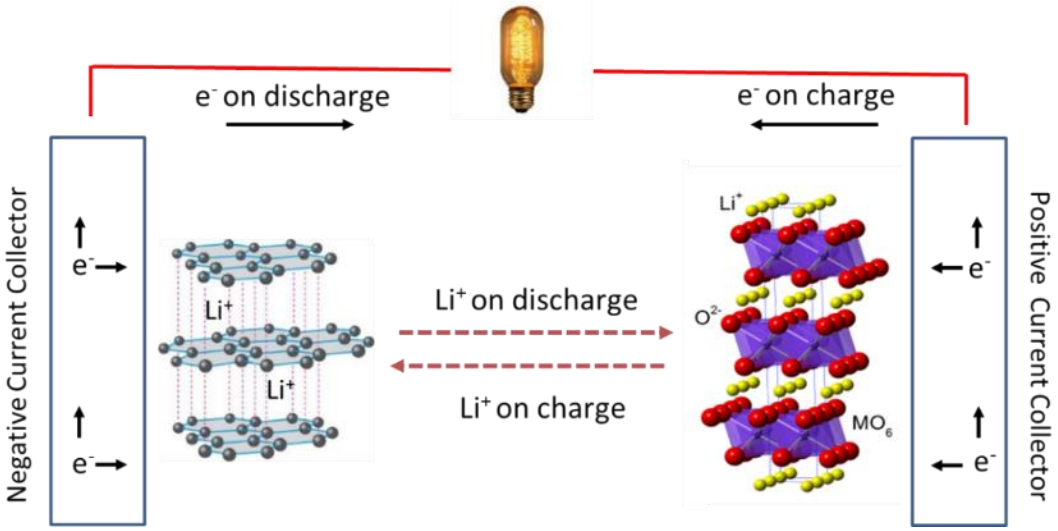

Figure 1.2 - Schematic representation of the charge and discharge mechanisms in LIBs. Adapted from [10]

Four main criteria are used to evaluate the performance of a battery:

- the output voltage (in V): voltage released by a device.
- the energy density (also known as specific energy, in Wh kg^{-1} or Wh L^{-1}): nominal battery energy per unit mass or volume characteristic of the battery chemistry and packaging.
- the specific capacity (in mAh g^{-1} or Ah L^{-1}): represents the specific energy in ampere-hours (Ah) per total mass or volume of active material.
- the electrical power density (also known as specific power in W kg^{-1} or W L^{-1}): the amount of energy that can be stored in a given mass (or volume) of a substance or system. The higher the energy density of a system or material, the greater the amount of energy stored in its mass [7].

One important parameter of a battery system is the voltage at which it operates during cycling. Associated with the movement of ions during the charge/discharge process, electrons will flow through the external circuit [7]. Assuming that the two electrodes on each side of the electrolyte are good electronic conductors, an external voltage (E) between the points where the external circuit contacts both electrodes can be measured. Depending on the chemical reaction occurring within the circuit, an open-circuit voltage (OCV) or equilibrium cell voltage can be measured, which is determined primarily by the thermodynamics of the chemical reactions between the components of the electrodes [7]. During use, the operating voltage will vary from the theoretical OCV value, depending on various kinetic factors (for example, impedance and no external voltage applied) [7].

The theoretical specific capacity of a cell is determined by the amount of active materials in the cell and is expressed as the total quantity of electricity necessary for the electrochemical reaction to happen. This value is defined in terms of coulombs or ampere-hours and is theoretically equivalent to the specific energy per 1 gram-equivalent weight of active material. The theoretical capacity of an electrochemical cell, based only on the active materials participating in the electrochemical reaction, is calculated from the equivalent weight of the reactants (Equation 1.3):

$$Theoretical\ Capacity = \frac{nF}{3600\ x\ MW} \tag{1.3}$$

Where *n* represents the number of electrons exchanged during the electrochemical process, *F* is the Faraday constant (96487 C mol^{-1}) and *MW* is the molecular weight of the active material species. The value obtained is based only on the active anode and cathode materials, other materials that may be involved in the cell reaction, such as water or electrolyte, are not included in the calculation. The specific capacity or amount of electrical energy per mass or volume that a battery can deliver is related to the amount of charge carriers that can be reversibly moved from one electrode to the other and is directly dependent on the chemistry of the system [9].

During cycling, a current is applied to the cell to allow the redox reaction in the electrodes to occur, this current is defined as the galvanostatic rate and can be normalised with the active mass of the electrode (A g^{-1}) or presented in C-rate [11]. A

C-rate of 1C means that the electrode is fully charged or discharged within an hour, regardless of its capacity. The rate capability can then be described as the maximum charge/discharge rate of a battery or cell expressed in multiple of the C-rate [9], [11]. The theoretical capacity is usually the target capacity to be achieved, however, in most electrode materials, the reversible capacity achieved is far less than the theoretical capacity. This subtly differentiates the rate capability from the capacity.

The energy stored in a specific system can be described using the terms gravimetric and volumetric energy density to interpret the power of a cell. Along with the energy consumption of a system, it determines the battery weight or volume required to achieve a given electric range [8]. This value is directly related to the electrochemical capacity and operation potential of the battery being used as a characteristic of the battery chemistry and packaging [8]. The value of the specific energy (E_g) of a half-cell is calculated from the chemical cell information and the weights of the reactants using the following equation:

$$Eg = \frac{v \text{ x } m_a \text{ x } C}{\sum w_i} \tag{1.4}$$

Where v represents the average cell operating voltage (V), m_a the area of active material (in g cm^{-2}), C (mAh g^{-1}) represents the capacity and w_i area of individual cell components (in g cm^{-2}). Power depends partly on the battery's engineering and crucially on the chemicals that compose the battery and is another important parameter to consider [9]. The energy stored in a battery can be maximized by (i) increasing the chemical potential difference between the two electrodes and (ii) ensuring no consumption of electrolytes during battery cycling [9]. Other characteristics such as cycle life, cost, safety, volume, shape, and sustainability are also important factors to consider depending on the various aimed applications.

1.3 Metal-ion Batteries

1.3.1 Lithium-Ion Batteries

Batteries are currently present in our everyday life and have countless applications from smartphones to medical and military uses. Lithium-ion batteries

(LIBs) started to attract a lot of attention in the past few years due to good performance, high energy and power density and low-memory effect (gradual loss of the battery's maximum capacity due to repeat incomplete discharge) and are nowadays one of the most advanced rechargeable batteries used [12]. Compared with earlier systems like Pb-acid or nickel-metal hydride batteries, LIBs possess higher energy density, longer cycle life, superior Coulombic efficiency and are more environmentally friendly [13]. Economic reports show overall annual growth in batteries of 7-8% during the period between 2010 and 2015 [14]. In 2019, rechargeable batteries accounted for 54 % of the total demand for lithium chemicals and as the market for rechargeable batteries grows it is expected an even bigger demand for this element [14]. According to the International Energy Agency (IEA), future growth is forecast to be led by the use of LIBs in electrified vehicles (EVs) expecting an overall growth of 30% between today and 2040 [14]. The LIB annual production is forecasted to ramp to 30 % by 2035 to meet demand. According to Navigant Research, the global market for automotive LIBs is expected to grow from $7.8 billion in 2015 to $30.6 billion in 2024 [15].

LIBs have many advantages over other conventional batteries as a high working voltage (can go up to 4.0 V depending on the cathode used compared with 2.1 V for Pb-acid batteries) and high specific energy (over 200 Wh kg^{-1} and 400 Wh L^{-1}). Moreover, LIBs can operate over a wide temperature range (from -40 to 70 °C), show a flat discharge curve (constant voltage and resistance through most of the discharge process) and present a superior shelf-life (can be stored up to 10 years at room temperature) [16]. These advantages result in part from the low weight of Li (MW = 6.94 g mol^{-1}) and its low standard potential (-3.04 V *vs* H^+/H_2) [17], [18].

Although Li metal batteries possess higher theoretical energy density than LIBs, problems associated with dendrite formation which can result in thermal runaway and consequent combustion due to the presence of flammable liquid electrolyte is one of their main known disadvantages [12]. To avoid this problem, alternatives to a liquid electrolyte such as solid electrolytes, for example, polymers, gels, and ceramics, or ionic liquids are being explored [19]. The ever-increasing demand for LIBs can limit the available Li resources of Earth and influence the cost of battery making in the long term [20]. The need to develop cheaper and more environmentally friendly batteries has led researchers to look for other alternatives to replace LIBs. Among the more suitable

candidates are lithium-air, lithium-sulphur, and sodium-ion batteries [9]. The first two systems have however similar disadvantages reported for LIBs, and problems associated with the size of reserves and higher consumption of Li which makes Na-ion batteries the next best candidate.

1.3.2 Sodium-Ion Batteries

Sodium-ion batteries (SIBs) have been recently intensively studied due to the sodium wide occurrence and relatively low price of the raw material when compared with other kinds of metals [21]. Sodium is the fourth most abundant element on Earth, and it is widely distributed while Li resources are localized mainly in South America [22]. Compared with the amounts available in the Earth's crust, Na represents more than 2 % while Li is only about 7 x 10^{-4} % [23]. Sodium also has the advantage that its resources in the ocean are immense as it is possible to use salt (NaCl) as a source of Na [23]. However, one of the main concerns of developing SIBs is the difficulty to achieve high efficiency when compared with LIBs, mainly due to the differences between both ions [24]. Although they share similar chemical properties in many aspects, these two elements possess several critical physical differences since Na^+ ions are larger and heavier when compared with Li^+ ions (1.06 Å and 23 g mol^{-1} and 0.76 Å and 6.9 g mol^{-1}, respectively) [24]. This is known to influence the interphase formation, transport properties and phase stability of the active material structure, making materials that allow lithium reversible incorporation to be unsuitable for reversible incorporation of a large quantity of sodium [25]. This change in size also leads to larger volume changes in the host material during cycling being responsible for the lower stability of interphases formed and faster degradation [26]. The higher redox potential of sodium (-2.71 V *vs* H^+/ H_2) when compared with lithium also contributes to lower power and energy densities of SIBs [22]. For that reason, Na-batteries cannot be used for applications that require high energy densities such as electric vehicles, however, many applications may benefit from sodium technology such as grid storage, where the weight/volume of the battery is of no concern [21]. The softness of sodium metal towards lithium makes it easier to handle and process, also helping to minimise the formation of dendrites through mechanical pressure [26]. Researchers have been

focused on finding suitable electrode materials and electrolytes to achieve the high efficiency of SIBs.

Several cathode and anodes are successfully used for both LIBs and SIBs and will be explored in the following sections.

1.4 Cathode materials in LIBs and SIBs

Two main types of cathode materials for metal-ion batteries exist, those where insertion/extraction reactions occur, also called intercalation materials, and those dealing with conversion reactions [27]. Conversion cathodes can transfer more than one electron per reaction resulting in a higher capacity [27]. Intercalation cathode materials are the most studied and rely on the relationship between a solid host network and a guest, in this case, Li^+ or Na^+ ions [20]. In this kind of system, the guest is reversibly inserted into or removed from the host network, without affecting its original structure [27]. The next section provides an overview of several cathode materials used in LIBs and SIBs with their advantages and disadvantages.

1.4.1 Layered metal oxides

Layered metal oxides have been widely studied as cathodes for LIBs. These materials can be represented using the nomenclature $LiMO_2$, where M represents one or more transition metals. Usually possessing a trigonal structure with a space group of $R\bar{3}m$, these materials have a very organized crystalline structure where the oxygen atoms are arranged in a face-centred cubic close-packed arrangement, being the transition metal located within the oxygen octahedral [28]. The Li^+ ions are located in empty layers formed between the oxygen layers, being inserted and removed from the structure during charge and discharge cycles [12]. Figure 1.3 depicts the average discharge potential and specific capacity of the most common cathode materials for LIBs.

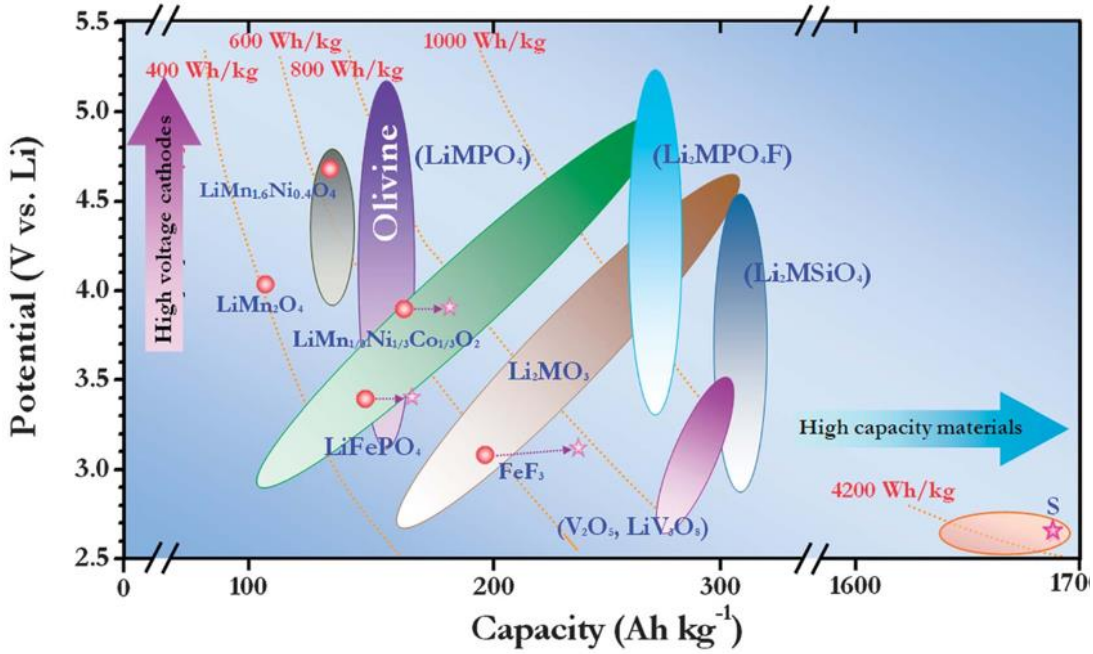

Figure 1.3 - Approximate range of average discharge potentials and specific capacity of some of the most common cathodes for LIBs. Adapted from [20]

The first layered compound to be commercialized was the cathode $LiCoO_2$ (LCO). This material was firstly reported by Goodenough *et al.* in 1980 [29] and was originally commercialized by SONY in 1991 and it is still used in most commercial LIBs [29]. LCO is a very attractive cathode material due to its relatively high theoretical specific capacity of 274 mAh g^{-1}, high discharge voltage and good cyclability performance [30]. Although LCO is one of the main cathodes used in the rechargeable lithium battery market nowadays, the limited reserves of Co, its high toxicity, the fact that it is unethically sourced and thermal instability led to the demand for the development of alternative cathode materials [31].

Following the commercialization of LCO, research on alternative layered oxide $LiMO_2$ was pursued, suggesting the replacement of Co for Ni in the compound, obtaining $LiNiO_2$ (LNO) at a relatively lower cost, environmental friendliness, and high energy density [32]. However, despite the similarities between $LiCoO_2$ and $LiNiO_2$ reports suggest that the LNO cathode is more unstable mainly due to the presence of the Ni^{3+}/Ni^{2+} redox pair [33]. Reports confirm that during the synthesis of the electrode, the spontaneous reduction of Ni^{3+} to Ni^{2+} leads to the formation of $Li_{1-x}Ni_{1+x}O_2$ compounds,

which results in excess of Ni^{2+} ions [33]. These Ni^{2+} ions can diffuse into the lithium pathways resulting in loss of capacity and lower power capability of the electrode [34]. Problems related to the release of oxygen into the electrolyte at elevated temperatures due to the metastable nature of LNO when heated in a non-oxidant atmosphere affects the thermal stability in long cycling [34].

The use of Mn, a cheap and less toxic element compared to Co and Ni, led to the development of $LiMnO_2$ (LMO) as a new promising cathode material. However, stability problems related to a transformation from a layered to a spinel structure during Li^+ extraction and Mn^{2+} ions dissolution into the electrolyte which leads to destabilization of the SEI (Solid Electrolyte Interphase) on the anode, are some problems related to this material [35], [36]. These processes are observed in most cathode material containing Mn and tend to intensify with cell ageing [35].

Other approaches have been tested, such as TM mixing. In 1992, Dahn *et al.* reported a solid solution for $LiNi_{1-y}Mn_yO_2$ $y \leq 0.5$ [37]. $LiNi_{1/2}Mn_{1/2}O_2$ shows a high reversible specific capacity of 200 mAh g^{-1} when cycled in a voltage range between 2.5 – 4.5 V [38] Although it is cheaper and less toxic than LCO, reported issues concerning the low Li diffusion related to cation mixing results in low rate capability. To note that as it happens in LNO, about 10 % of Ni is found to be in the Li layers after successive charge-discharge cycles [39]. The addition of Co to the NMO structure was developed as an effective way to enhance structural stability in a two-dimensional way, blocking the Ni^{2+} ions to enter the lithium layer [40].

$LiNi_{1-y-z}Mn_yCo_zO_2$, also called NMC, has a similar or higher theoretical capacity than LCO and operates at similar voltage ranges with the advantage that it is cheap since the content of Co is reduced [41]. Mixing proper levels of each three transition metals to get the advantage of each one led to the discovery of $LiNi_{1/3}Mn_{1/3}Co_{1/3}O_2$ [42]. $LiNi_{1/3}Mn_{1/3}Co_{1/3}O_2$ (NMC333 or NMC111) was first reported by Ohzuku *et al.* in 2001 and has been extensively studied since then [43]. The layered structure is composed of crystals assuming a trigonal system with a space group of $R\bar{3}m$ [44]. The average oxidation state of the transition metals is +3 assuming that the valence states of Ni, Mn, and Co are +2, +4 and +3, respectively [45]. As happens with NMO, the redox pair

Ni^{2+}/Ni^{4+} is responsible for the electrochemical behaviour of the cathode material and major contribution to the electrode storage capacity [40]. However, here the Co^{3+}/Co^{4+} pair also contributes to these features as well as structural stability [46]. Mn^{4+} cations are responsible for crystal field stabilization energy at octahedral sites facilitating the overall stability of the compound remaining electrochemically inactive. This material shows a high theoretical specific capacity of 278 mAh g^{-1} with a reversible discharge capacity of 200 mAh g^{-1} when cycled in a voltage range between 2.5 – 4.6 V [43]. Studies indicated that this material is structurally unstable at voltages above 4.6 V showing capacity retention of 80 % after 50 cycles [43]. Researchers have been investigating different metal ratios to reach an equilibrium in terms of good performance and electrochemical properties concluding that too much Co leads to a decrease in capacity, too much Ni results in cation mixing and too much Mn leads to a transformation into a spinel structure [47]. Nowadays, the great interest lies in NMC materials with even higher Ni content (such as NMC811) as they can provide higher specific capacity within the same voltage and further decrease the Co content [48].

Similarly, to lithium-based layered oxides in LIBs, sodium-based layered Na_xMO_2 oxides have been widely studied for SIBs, with the main advantage that Na-based oxides can be synthesized from a wide variety of transition metal elements (M = Ti, V, Cr, Mn, Fe, Co or Ni) while Li layered oxides are typically limited mainly to Co, Ni and Mn. These materials can crystallize in several polymorphs dependent on their sodium content and synthesis conditions (temperature and partial pressure of oxygen) [49]. Sodium-based layered materials can be categorized into two main groups: P2 type or O3 type materials according to the surrounding Na^+ environment, sodium content and the number of unique oxide layer stacking [50]. P2-type materials consist of two different kinds of TMO_2 layers (AB and BA layers) with all Na^+ ions located at trigonal "prismatic" (P) sites with a typical space group of $P6_3/mmc$ [51]. In O3- type phases, the Na^+ ions are located in octahedral (O) sites and can be classified as one of the cation-ordered rock-salt superstructure oxides, where the NaO_6 and TMO_6 are ordered into alternate layers forming Na and TMO_2 slabs, respectively [51]. Figure 1.4 depicts the average discharge potential and specific capacity of the most common cathode materials for SIBs.

Although layered transition metals oxides are promising candidates for SIBs as high-capacity cathode materials, three major disadvantages are associated with this kind of electrode materials. Irreversible phase transitions occurring in the P2 and O3 phases are one of the main disadvantages. Transitions from P2 to O3 occur due to loss of stability of the prismatic sites due to Na^+ extraction as a consequence of gliding of TMO_2 sheets during desodiation [51], [52]. Na^+ ions extraction from P2 and O3-type phases generally induces more complex phase transition compared with what happens in LIBs mainly due to larger Na^+ ions couples with charge ordering and the arrangement between ions and vacancies at different Na contents [51]. Another major challenge associated with this kind of cathode material is their hygroscopic character after exposure to air [51]. Intercalation of water in between TMO_2 slabs results in volume expansion and oxidation of TM in the lattice to higher valence leading to problems of storage stability for these materials [49], [53]. The formation of electrochemically inactive species on the surface of active materials, as NaOH or Na_2CO_3, is also related to the faster deterioration of the battery performance [51]. Nonetheless, the use of layered cathode materials prevents cation mixing, a process usually observed in lithium metal oxides, due to the ionic radius difference between Na^+ and the transition metal ions. These materials also allow the activation of some redox couples that are inactive *vs* Li^+/Li representing the more suitable candidate to compete against LIBs [49].

The two most studied single-metal-based oxides for SIBs are Na_xCoO_2 and Na_xMnO_2 [51]. Delmas *et al.* investigated for the first time the electrochemical properties of both P2 and O3 phases of Na_xCoO_2 [54]. It was reported that the extraction of Na^+ ions ($0.5 \leq x \leq 1.48$) is responsible for the phase transformation of the O3 phase into monoclinic O'3 and then P3, while the P2 phase was observed to preserve its structure throughout all the electrochemical processes ($0.46 \leq x \leq 0.83$) [54]. Ordering transitions of the Na^+ ions between the layers of the cathode material upon cycling causes phase changes leading to diverse Na^+/ vacancy ordered distributions which results in several reversible biphasic and single-phase domains during cycling [55]. The study shows that a reversible amount between 0.45 and 0.9 moles of sodium can be exchanged during cycling, which corresponds to a specific capacity of 140 mAh g^{-1}, however, cyclability limitations associated with the cathodic material were also observed [55]. Analogues of P2-Na_xCoO_2 have suggested including Mn substituted P2-Na_xMnO_2 due to the cost-

effectiveness of the Na and Mn elements [36]. Na_xMnO_2 presents two different structures depending on the content of Na^+ in the structure: a 3D tunnel structure for low amount of Na ($0 < x < 0.44$) and a 2D layered structures for higher amount of Na ($0.5 < x < 1$) [51]. The reversibility of Na^+ extraction/ insertion from O'3-type α - $NaMnO_2$ was reported by Mendiboure *et al.*, showing a discharge capacity of 197 mAh g^{-1} correspondent to a reversible insertion of 0.15 Na^+ ions into the structures with, like observed with $NaCoO_2$, a multistep discharge process [56]. A significant reduction of the Jahn-Teller distortion was noticed upon electrochemical Na^+ extraction from $NaMnO_2$, associated with the redox couple Mn^{3+}/Mn^{4+} [57]. Several studies demonstrated that the Jahn-Teller effect is responsible for the rapid capacity decay of Na_xMnO_2 as a result of the presence of Mn^{3+} and instability of the structure in the presence of moisture [51]. To overcome this problem, the substitution of Mn^{3+} by lithium and magnesium ion in the structure might stabilize the structure of P2-type Na_xMnO_2 as well as enhance its cycle life [58].

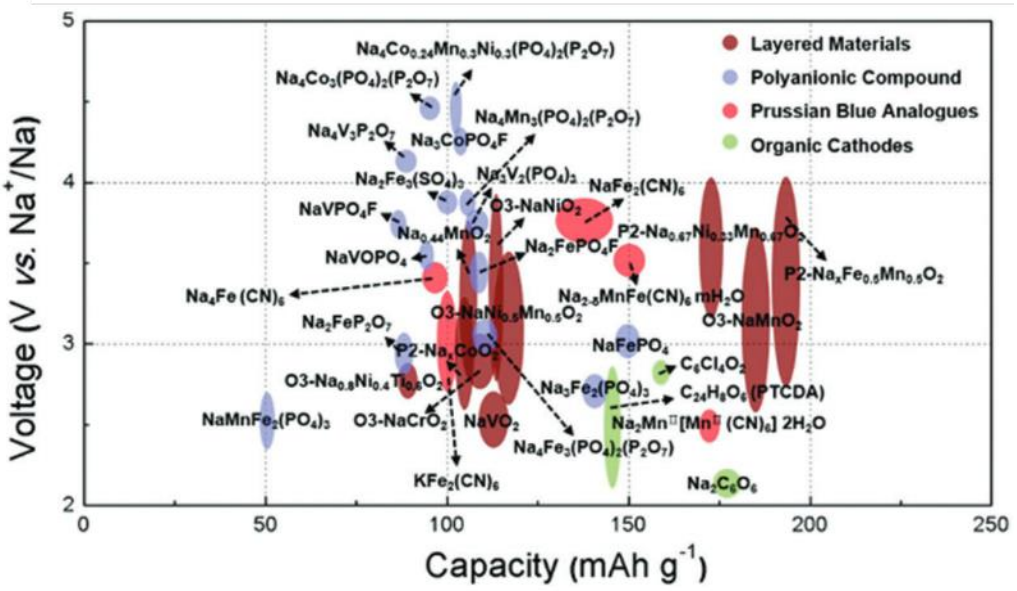

Figure 1.4 - Approximate range of average discharge potentials and specific capacity of some of the most common cathodes for SIBs. Adapted from [59]

1.4.2 Polyanions

Polyanionic compounds are a class of materials formed by a polyanion ion $(XO_4)^{n-}$ and their derivates $(X_mO_{3m+1})^{n-}$ (X = P, S, As, Mo or W). The tetrahedral polyanion structure is covalently bonded to a MO_x (M = transition metal) polyhedra [60]. Compared to layered transition metal oxides, polyanions possess higher thermal and structural stability due to their strong covalently bonded oxygen atoms turning them more suitable for largescale LIB applications [60].

$LiFePO_4$-based cathodes for LIBs have attracted a lot of attention in the past decade due to their low cost and low environmental impact. $LiFePO_4$ (LFP) is the representative material for the olivine structure and is known for its thermal stability and high-power capability. The presence of the polyanion PO_4^{3-} generates a strong inductive effect that moderates the energetics of the transition metal redox couple generating high operating potentials [12]. Problems related to low electronic and ionic conductivities are however responsible for the low capacity of this cathode family.

In SIBs, $NaFePO_4$ can be used as cathode materials in two different structure modifications, olivine and maricite [61]. Both polymorphs are electrochemically active showing a specific capacity of 147 mAh g^{-1} [61], [62], however, have the disadvantages of poor reversibility and electrode degradation during cycling [62].

NASICON-related compounds have shown to be promising cathode materials for LIBs, exhibiting high Li^+ ion mobility and reasonable discharges capacities. NASICON states for Na^+ superionic conductor and these materials are usually characterized by their high ionic mobilities [24]. This type of compound has the general formula $A_nM_2(XO_4)_3$ (A = Na, Ba, K) and can insert both Li^+ and Na^+ ions due to their 3D framework [63]. The compatibility of these types of compounds with aqueous electrolytes is one of the main advantages of making these materials very interesting from an economical point of view.

1.5 Anode materials

The anode is the negative electrode in a battery, the species that is oxidized during the battery discharge reaction storing the lithium/sodium ions in the process [64].

To be considered as a good anode electrode, the material should have to be electrochemically active, have a low ion diffusion barrier, high electronic conductivity, and good structure stability to prevent significant structural changes during the charge/discharge process [13]. Figure 1.5 depicts the average discharge potential and specific capacity of the most common anode materials for LIBs and SIBs.

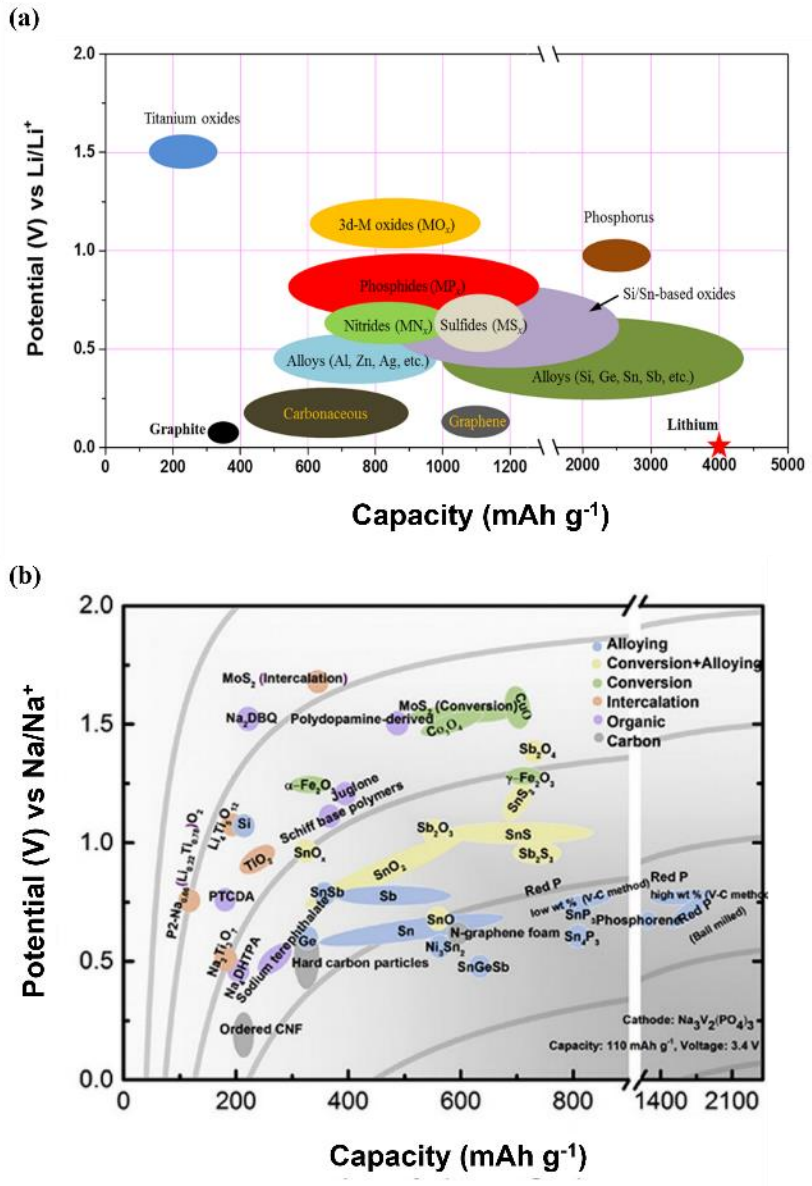

Figure 1.5 - Schematic illustration of active anode materials for next-generation lithium and SIBs. Adapted from [64], [65]

1.5.1 Carbon-based materials

Carbon anodes have been used in commercial batteries for more than 20 years, being the most employed anode material for LIBs nowadays [66]. Intercalation of Li^+ ions between the graphene planes offers graphite a good 2D mechanical stability, electrical conductivity, and easy Li^+ transport [20]. Graphite possesses several advantages such as low cost, abundance, moderate energy density, low delithiation potential *vs* Li^+/Li and relatively low volume change during lithiation/ delithiation [20]. Graphite possesses a crystalline and flexible structure with a small volume change of less than 9 % upon lithiation since the layered structure is held together by van-der-Waals forces [67]. The low voltage potential (around 100 mV) at which Li^+ ions intercalate prevents the plating of the Li^+ and consequent formation of Li dendrites [68], [69]. Despite all the advantages of graphite carbons, researchers figured that this material is not compatible with the use of propylene carbonate (PC) electrolytes as it induces degradation of the graphite structure [70]. This can be overcome using other kinds of electrolytes like alkyl carbonates or ethylene carbonate-based solvents; however, stability issues are not totally avoided. Another problem is related to the formation of a passivation layer between the anode and the electrolyte also called the SEI layer, which usually affects the kinetic stability of the redox reaction [71]. In the case of graphite-based electrodes, an excess capacity for lithium is observed in the first insertion cycle exceeding its theoretical capacity [72]. However, this capacity is not entirely recovered in the subsequent cycles as only 80 to 90 % of the lithium is recovered, being the rest consumed in the first cycle referred to as an irreversible reaction and creation of this layer [71]. The SEI formed in graphite anodes in LIBs is very stable, and avoids further degradation, resulting only in an initial capacity loss and stable cycling afterwards [71].

Considering the good performance in LIBs, carbon-based materials are also the first choice as anodes for SIBs as they possess low voltage against sodium and are chemically and thermally stable [65]. Graphite, however, cannot effectively intercalate Na^+ ions as the weak interactions present between Na^+ ions and graphite lead to deposition of the ion onto the graphite. Several intercalation methods were studied to insert sodium into the graphite layers, however, a lower amount of Na^+ compared to Li^+ was inserted [73]. Other kinds of carbonaceous materials have been studied to be used

as anodes for SIBs such as expanded graphite, carbon nanomaterials (as carbon nanotubes - CNTs), disordered carbons (soft and hard carbons) and metal-organic frameworks (MOFs) [65], [74]. Hard carbons are now one of the most studied anode materials for SIBs as they can be synthesized in several different ways and can achieve a capacity as high as 300 mAh g^{-1} [65]. However, their low density and the fact that most of their usable capacity is located near the sodium plating voltage makes its use challenging. More recently, expanded graphite was reported and the larger interlayer spacing present in this structure is shown to allow easier and more reversible intercalation of Na^+ ions [65]. The doping and engineering of the structure of carbon nanomaterials can also improve the performance of rechargeable batteries as the doping with heteroatoms (N, B, S and P) leads to the creation of defect sites, which enhances ion storage and improves the electrode/electrolyte interaction [65].

1.5.2 Metal oxides materials

Among the transition metal oxides, lithium titanium oxide ($Li_4Ti_5O_{12}$, LTO) has been successfully commercialized and researchers believe it to be a promising alternative to the use of graphite [75]. LTO is a zero-strain material that possesses superior thermal stability, high rate performance, high volumetric capacity and high cycle life when compared with graphite which makes this material interesting for applications whenever the price is not a concern [20]. Due to its stable structure, LTO can accept up to 3 Li^+ ions, resulting in the final structure of $Li_7Ti_5O_{12}$ [75]. One of the biggest disadvantages related to the use of LTO anodes is related to its intrinsically low electrical conductivity (10^{-13} S cm^{-1}) and Li^+ ion diffusion coefficient (10^{-13} S cm^{-1}), which results in poor rate performance [76]. These problems can be circumvented however by the use of surface engineering strategies such as carbon coating.

In SIBs, anatase TiO_2 has been reported as one of the most promising anode materials for SIBs due to its high theoretical capacity of 355 mAh g^{-1} [24]. The 3D network of TiO_2 possesses an interstitial site for Na^+ accommodation and suitable sized pathways for ion diffusion [21]. This leads to an activation barrier close to that of lithium facilitating the insertion of large Na^+ ions into the structure [21]. Sodium titanates of the form $Na_2Ti_nO_{2n+1}$ have also been studied as promising anode materials for SIBs.

The two most studied titanates for SIBs are $Na_2Ti_3O_7$ and $Na_2Ti_6O_{13}$ [77]. These compounds are characterized by zig-zagged edge- and corner-sharing TiO_6 octahedra. These structures form layers that possess sites for Na^+ ions intercalation between them [78]. The large interlayer spacing of these materials (as large as 8 Å) makes them a suitable electrode for easy intercalation of Na^+ ions [79]. This inherent characteristic is ideal to tolerate large volume changes occurring during cycling resulting in more stable cycling performance [79]. $Na_2Ti_3O_7$ is one of the most promising anodes of this class since it shows the lowest insertion voltage for Na^+ (0.3 V *vs* Na^+/Na) with a theoretical capacity of 177 mAh g^{-1} [78].

1.5.3 Alloying materials

"Alloying materials" refer to elements that can electrochemically alloy and form compound phases with Li or Na [20]. Several elements such as Sn, Pb, Al, Sb, Zn and Si can reversibly form alloys when in contact with these ions at low potential [80]. Alloying materials are very appealing due to their high theoretical specific capacities, which can exceed that of graphite up to tenfold, and high energy densities. One of the major issues regarding these materials is related to the large volume expansion experienced upon ion insertion (from 100 to 420 % depending on the material) [81]. This causes fracturing of active material particles and the consequent loss of electrical contact leading to pulverization of the electrode [82], [83]. The most successful strategy found by researchers to avoid this problem has been to produce carbon composites to act as a carbon matrix in which the active material particles are embedded. Another strategy consists of the preparation of hollow carbon nanospheres and core-shell nanostructures, that creates secondary particle structures which can buffer this volume expansion [84]–[86]. This leads to superior mechanical stability, electron and ion transport while maintaining paths within the electrode big enough for a facile ionic diffusion [80], [87].

1.5.4 Conversion Materials

Conversion electrodes undergo a solid-state redox reaction during intercalation/ de-intercalation of ions, leading to changes in the crystalline structure of the cathodes as a result of breaking and recombining of chemical bonds [27]. Initially,

this type of reactions was considered to be irreversible at room-temperature as the energy necessary for bond breakage, formation of new bonds and atomic reorganization was considered to be too high [88]. The first reversible lithium storage in a conversion material was reported by Poizet *et al.* in 2000, where the use of transition metal oxides as active materials resulted in specific capacity higher than 700 mAh g^{-1} [89]. Equation 1.5 represents a typical conversion reaction for electrode materials, where M represents a transition metal:

$$M_xA_y + 2ye^- + 2yLi^+ \rightarrow xM^0 + yLi_2A \quad (1.5)$$

Upon lithiation, the transition metal is reduced to its metallic state and inserted in the simultaneously formed lithium-comprising compound Li_2A (where A stands for O, N, P, F and others) [89]. Compared with intercalation cathodes, conversion cathodes can transfer more than one electron per reaction resulting in a higher capacity [27]. However, the high structural reorganization which happens during the conversion reaction is considered one of the main drawbacks of this type of materials as it may lead to a loss of electrical contact and electrode pulverization [90]. Moreover, conversion materials suffer from a high reactivity towards commonly used electrolytes and voltage hysteresis, which considerably affects the energy storage efficiency of such electrodes [9], [90].

1.6 Transition Metal Dichalcogenides

TMDs were first discovered in the early 1970s, being considered as single-layer crystals with very weak interlayer bonds [91]. Transition metal dichalcogenides (TMDs) have been studied as promising materials for a broad range of applications for decades. Transition metal dichalcogenides have attracted a lot of attention to be used as anode materials in the energy storage field due to their structural similarity to graphite, versatile chemistry and high capacity and energy density.

1.6.1 Structure of TMDs

These compounds form a class of materials that includes 60 compounds and are usually represented with the chemical formula MX_2, where M stands for a transition metal from group 4 to 7 and X represents a chalcogen atom (such as S, Se and Te) [92]–[95]. The presence of a chalcogenide atom creates a very stable binary compound with conjugates with transition elements, forming a layered or also called "graphite-like" crystalline structure (Figure 1.6 a) [94], [96]. These 2D layered materials usually possess a layer with a thickness of around 6 to 7 Å and consist of a hexagonally packed layer of metal atoms sandwiched between two layers of chalcogen atoms with an X-M-X composition. These layers are weakly bound by weak van-der-Waals forces whereas the in-plane M-X is covalent [97]. This arrangement allows the unique ability to intercalate guest species into the van-der-Waals gap. Importantly, the hexagonal structure of TMDs is not atomically thin as in the case of graphene (Figure 1.6 b) [94], [96]. The use of heavier elements leads to the tendency to form a 2D structure pillared by Van-der-Walls forces. These materials tend to form crystal structures with a 3D symmetry when in the presence of first-row transition metal dichalcogenides [97], [98]. Versions of these materials were initially studied including first-row transition metals as the main centre of focus, however heavier transition metals have shown impressive properties in the structure of chalcogenides. Heavier chalcogens provide better electrical conductivity, an important characteristic for energy storage, optoelectronic and magnetic applications [99]–[101].

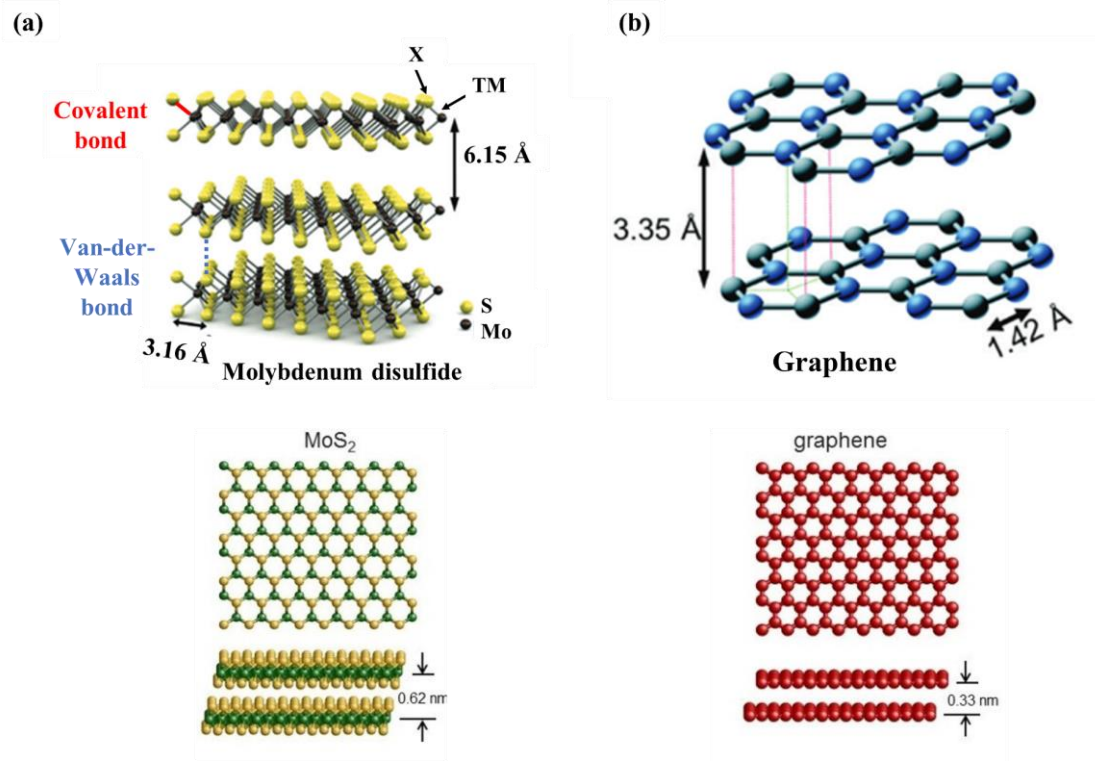

Figure 1.6 - (a) Schematic representation of the crystal structure of bilayer graphene and (b) 3-layers MoS_2 TMDs [92], [95], [97], [102]

The covalent bond between the metal and chalcogen atoms is formed by the filling of the bonding states of TMDs by four electrons of the metal atom [103]. This gives the metal (M) and chalcogen (X) atoms an oxidation number of +4 and -2, respectively [103]. The extra lone pair electron of the chalcogen atoms ends up in the layers' surface and the fact that these layers do not have dangling bonds turns them chemically stable [103]. Depending on the size of the metals and chalcogens in the structure, the bond length between two metal atoms ranges between 3.15 Å and 4.00 Å (Figure 1.6).

In terms of crystal structure, TMD materials exhibit two different polymorph structures depending on the metal coordination by the six chalcogen atoms. Materials either crystallize in a trigonal prismatic (2H) or octahedral coordinated (1T) arrangement [104]. Both 1T and 2H phases can coexist for the same material like for example in chemically exfoliated nanosheets WS_2 and MoS_2 [105], although generally one of the phases will tend to be more stable than the other for a certain composition. The preferred phase adopted by a TMD is entirely dependent on the d-electron count of the transition

metal. Transition metals featuring d0 centres (such as group 4 TMDs) are all in the octahedral structure while both octahedral and trigonal prismatic phases are observed in group 5 TMDs (d1 centres) [103]. Group 6 TMDs (d2 centres) are mainly found in trigonal prismatic geometry while groups 7 and 10 (d3 and d6 centres) are typically in an octahedral structure, distorted and normal respectively [103]. Due to differences in electronic structure, in terms of physical properties, T phases are usually associated with metallic properties while H phases have a more semiconducting character, being this phenomenon stronger for lightweight TMDs. Phase transition for a certain compound can be induced by exfoliation, changes in pressure, temperature and ion insertion being the semi-metallic phase (1T phase) more stable in most of these materials. In terms of ion insertion, studies show that intercalation of Li^+ ions into MoS_2 is responsible for the change in the metal coordination from trigonal prismatic 2H phase into the octahedral 1T phase [105]. Indeed, the electron transfer from the lithium during the intercalation process causes a transition from the d2 to the d3 inducing destabilization of the original bulk structure and consequent phase transition.

1.6.2 Synthesis and Applications of TMDs

Two main approaches are employed for the synthesis of layered transition metal dichalcogenides: bottom-up and top-down methods [106]. The bottom-up method consists of synthesizing the layers from either gas or liquid phase molecular precursors. Chemical vapour deposition (CVD) is the main bottom-up method employed to synthesize TMDs. In CVD the precursors react on transition metal substrates at high temperatures to form single or few-layered 2D nanosheets [107]. The need for harsh growth conditions such as high temperature and high vacuum and the fact that is size-limited is one of the main disadvantages of this technique [107]. The reverse happens in the top-down approach where 3D bulk powders of layered materials are exfoliated into their elementary building blocks or single layers of the material [106]. Solution-based exfoliation of TMD, as a top-down method, has been regarded as the most suitable route to bulk production of 2D sheets [108]. The top-down approach, as opposed to the bottom-up one, results in larger quantities of layered material but with lower purity. It can be done by micromechanical cleavage, chemical exfoliation, and

solution-based ultrasonic exfoliation [107]. The discovery that layered crystals can be exfoliated in liquids has led researchers to explore different synthesis processes involving several solvents and ions intercalation [108]. The possibility to produce large quantities of material is the main advantage of liquid exfoliation. This technique possesses other advantages as the ability to store compounds in a phase that can enable easy deposition onto any substrate and the possibility to easily blend with other materials for further functionalization or post-treatment [109].

Three steps need to be followed for the preparation of layered TMDs via solution-based exfoliation: (1) break the van-der-Waals forces that connect the layers to separate them, (2) further increase the separation distance among the layers by exfoliation into the solvent and (3) stabilise the liquid suspension to avoid re-aggregation of flakes and removal of any possible by-products [110]. The three most common methods employed as liquid exfoliation process are sonication in solvents, ion exchange, and ions intercalations.

The unique properties of TMDs turn them attractive materials for diverse applications including electronics, photonics, sensing and energy devices. Their unique thin atomic profile represents the ideal conditions for maximum electrostatic efficiency, mechanical strength, tunable electronic structure and sensor sensitivity [97]. In the area of electronics and optoelectronics, conventional silicon-based technology has revealed several scaling limitations over the past decade and for that reason, atomically thin conductors such as TMDs have recently got attention as future generation large-scale electronics. The huge demand for developing highly sensitive, selective, reliable, and portable sensors has stimulated extensive research on new sensing materials based on TMDs after the success of graphene for sensing applications [111]. In terms of energy storage devices, TMDs are gaining a lot of attention to be used in supercapacitors and LIBs due to their atomically layered structure, high surface area and excellent electrochemical properties [112]. Their layered structure provides more sites for ion storage while maintaining structural stability during cycling. When coming to their high surface area with surface functionality and electrical conductivity, 2D TMD materials are ideal to be used as an electrode for energy storage [112]. This application will be further discussed for LIBs and SIBs in the following sections.

1.6.3 Energy storage properties of TMDs

1.6.3.1 Anodes in LIBs technology

TMDs have been researched as promising electrode materials in rechargeable batteries and capacitors. The rising interest in these materials is due to their earth-abundant presence in nature, excellent mechanical properties, ability to tune interlayer spacing, good performance when large current densities are applied, long life capability and wide operation range temperatures [113]. Their graphite-like layered structure allows them to host ions between the layers due to their large interlayer distance and high theoretical capacity. Compared with the commonly used graphite, TMDs possess higher theoretical capacity (670 mAh g^{-1} *vs.* 342 mAh g^{-1} for MoS_2 and graphite, respectively), show less volume change and better rate capability and cycle life due to the independent nature of their layered structure [113].

The Li^+ storage mechanism in MX_2 compounds has been widely studied by both experimental methods and theoretical calculations. Studies show that alkali metals show a similar charge storage behaviour compared to carbon-based materials due to their analogous physical properties [114], [115]. Depending on the cut-off voltage used and the specific properties of each MX_2, different storage mechanisms can be described for TMDs. When the lower cycling cut-off voltage is limited to above 1.0 V, MX_2 materials present reversible intercalation and extraction reactions, forming A_nMX_2 ($0 < n < 4$) where A represent the intercalating species (Li^+/Na^+) [116]. When the material is cycled at voltages below 1.0 V, a two-phase mechanism (intercalation and conversion) occurs usually during the first cycle. During the first discharge, an intercalation mechanism is observed at high potential (MX_2 turns into A_nMX_2), while the low potential (around 0.1 V) leads to the conversion of A_nMX_2 into metallic M and A_2X. Some exceptions are TiX_2 and NbX_2 due to their strong metal-chalcogenide bonding interactions [117]. Poor dynamic properties can lead to the irreversible formation of metallic M and alloy form X after the initial charge process (Figure 1.7).

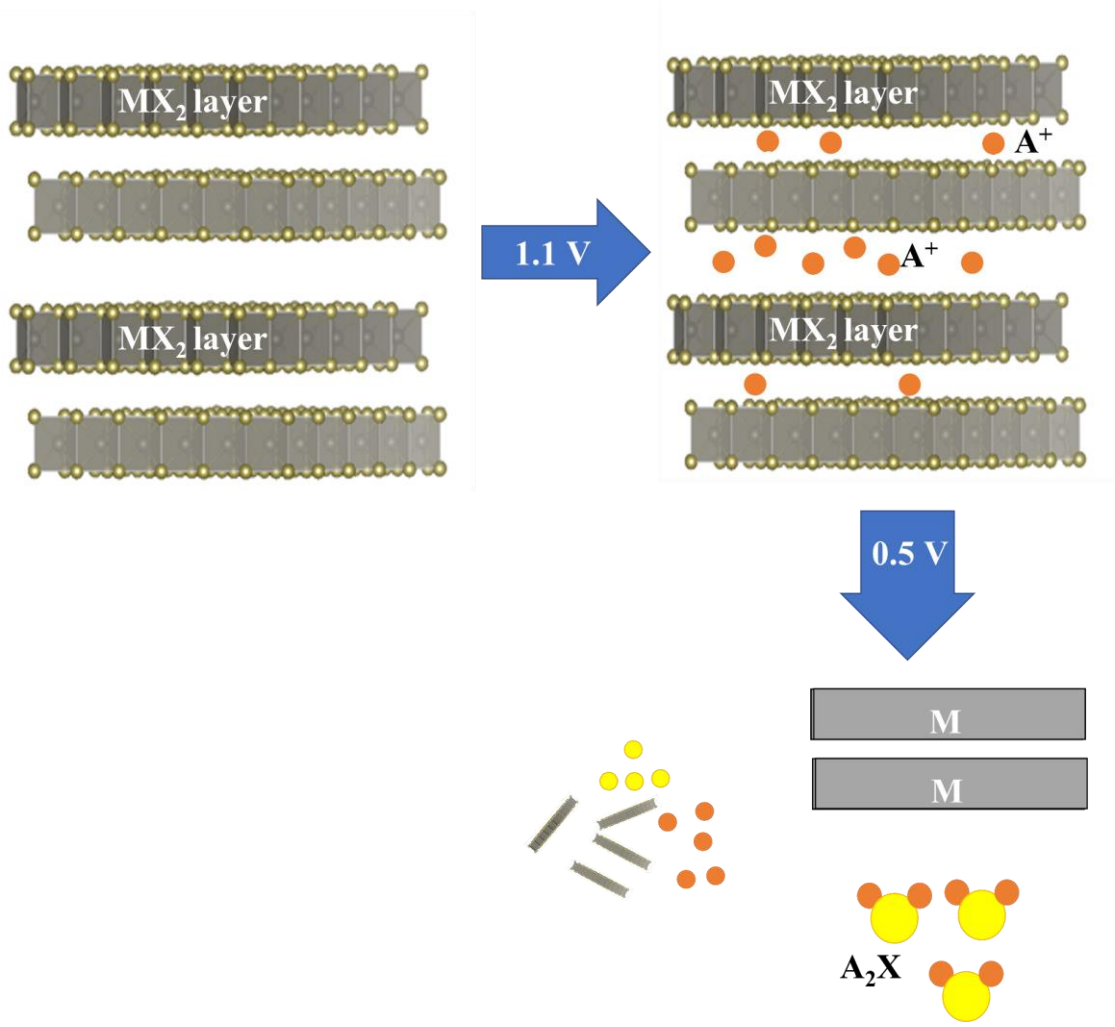

Figure 1.7 - Schematic representation of the intercalation and conversion reactions happening in MX_2 materials.

Metallic MX_2 materials including V-based dichalcogenides (such as VS_2 and VSe_2) exhibit a partially reversible conversion mechanism in alkaline metal-ion batteries [118]. The fact that VS_2 is cheap and abundant makes this a promising electrode material for use in high-performance batteries. VS_2 was studied as anode material for LIBs due to its excellent electrical conductivity and metallic nature that facilitate charge transfer [119]. The faster Li^+ ion diffusion rate in VS_2 compared with other layered materials predicted by theoretical calculations is another advantage of this material for its application in energy storage [119]. As an anode material, monolayered VS_2 can intercalate a maximum of 2 moles of lithium per formula unit (Li_2VS_2) with a maximum theoretical capacity of 466 mAh g^{-1} [120]. *Ex situ* and *in situ* XAS experiments show

that this is one of the many materials that undergo both intercalation and conversion reactions during the discharge process, forming V metal and Li_2S. However, during the charging process, these reactions are partially reversible, detecting the existence of three compounds after the first cycle: VS_2, V and S [118].

In terms of semi-metallic reversible TMDs, MoS_2 is one of the most studied transition metal dichalcogenides for Li^+ ions. These TMDs has drawn a lot of attention due to their high theoretical capacity of around 670 mAh g^{-1}, which corresponds to the intercalation of 4 moles of lithium per formula unit [121]. Studies report that the nanostructured MoS_2 – graphene composite electrode can deliver a capacity as high as 1290 mAh g^{-1} (Figure 1.8) [122]. Compared to other conversion materials such as silicon or germanium, MoS_2 possess less volumetric expansion upon lithiation [122]. Despite these advantages, MoS_2 presents poor electrical/ionic conductivity which prevents it to achieve its full capacity [123]. Moreover, their intermediate lithiation voltage (1.1 – 2.0 V *vs* Li^+/Li), reduces the energy density of the material when used in a full-cell [121]. *In situ* X-ray diffraction and HRTEM studies were used to study structural changes in commercial MoS_2. At higher voltages, i.e. 1.1. V, the material presents a 2H phase (Figure 1.8 a, Equation 1.6) with a reversible insertion and deinsertion of Li^+ ions is observed up to 0.8 V [124].

$$\text{Intercalation phase: } MoS_2 + xLi^+ + xe^- \leftrightarrow Li_xMoS_2 \ (\sim 1.1 \text{ V } vs. \text{ Li}^+/\text{Li}) \ (167 \text{ mAh g}^{-1}) \quad (1.6)$$

Upon further Li^+ intercalation, a phase transition from 2H to 1T phase happens the first discharge/charge which leads to a decrease in the electrical conductivity of the material affecting its cycling ability [125]. Raman spectroscopy measurements demonstrated that Li^+ ions intercalate into MoS_2 nanosheets from the edges and gradually diffuse towards the centre of the material. To increase the capacity obtained by using MoS_2, studies using a lower cut-off window were undertaken. Studies show that the layered structure of MoS_2 starts to degrade when the electrode is discharged down to 0.5 V [123]. TEM analysis revealed that the interlayer spacing in MoS_2 expands when decreasing the cut-off from 1.0 to 0.5 V, as a result of the conversion reaction starting between 0.6 and 0.5 V [123]. CV results show the existence of a reduction peak at 0.5

V that can be assigned to the conversion reaction from 1T – Li_xMoS_2 to Mo and Li_2S (Figure 1.8 b, Equation 1.7) [123].

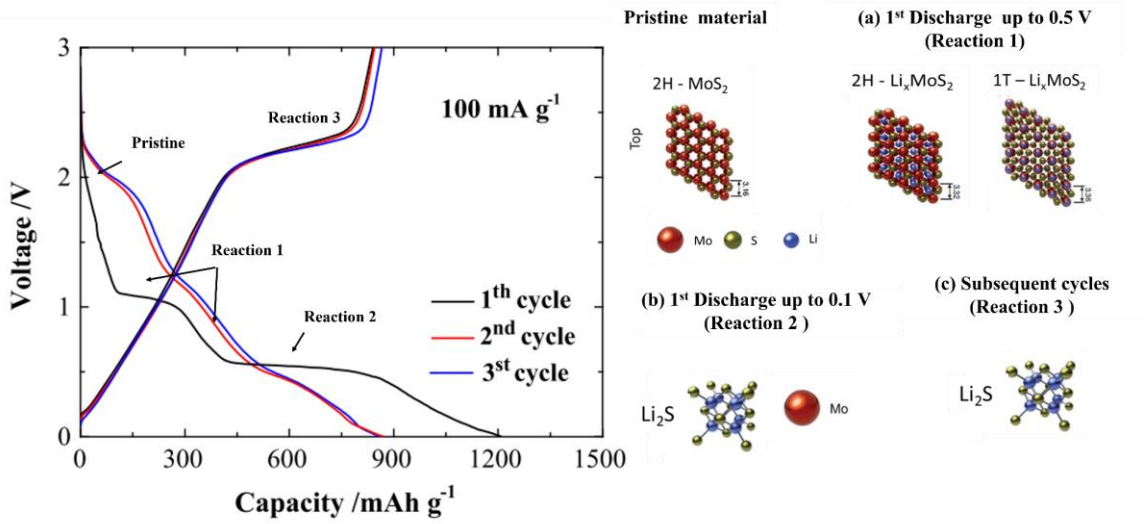

Figure 1.8 - Charge–discharge profiles of the hierarchical MoS_2 microsphere anode at 100 mA g^{-1}. Electrochemical lithiation process of MoS_2. (a) Start from the original 2H MoS_2 structure, the lithiation proceeds through a phase transition from 2H to 1T structure, (b) the Mo layers start to collapse when more Li^+ ions are inserted. (c) Li^+ ion intercalation stops after that and the lithiation reaction switches to the conversion style with the final phase featured with Li_2S and isolated Mo atoms [121], [123].

$$\text{Conversion phase: } Li_xMoS_2 + (4-x)Li^+ + (4-x)e^- \rightarrow Mo + 2Li_2S \ (\sim 0.5 \text{ V } vs. \text{ Li}^+/\text{Li}) \ (669 \text{ mAh g}^{-1}) \quad (1.7)$$

During the charging process, an oxidation reaction from Li_2S to S occurs, which tell us that below 0.5 V, the original MoS_2 is irreversibly converted into Mo and S [113], [123]. The subsequent cycles result from the cycling between Li_2S and elemental S after irreversible decomposition of the initial material (Figure 1.8 c, Equation 1.8). The reaction leads to rapid decay due to the poor structural stability and the shuttle effect of polysulfides. This reaction mechanism can be extrapolated to other MX_2 type materials including W and S-based dichalcogenides. The formation of Li_2S, a non-conductive material, increases this effect [126].

$$\text{Subsequent cycles: } S + 2Li^+ + 2e^- \leftrightarrow Li_2S \ (\sim 2.2\ \text{V}\ vs.\ \text{Li}^+/\text{Li}) \quad (1.8)$$

(1675 mAh g^{-1})

To improve the electrochemical performance of semiconducting MX_2 anode materials new strategies need to be adopted to suppress the irreversible conversion reaction that occurs at low potentials. An efficient method is the incorporation of highly conductive carbon (reduced graphene oxide (rGO), carbon nanotubes (CNTs), amorphous carbon, etc.) into the semiconducting TMDs, as studies revealed that the graphene coating layer is an effective way to suppress the dissociation of MoS_2 during the discharge process [127]. Within this scope, a new class of materials have been studied: Van-der-Waals heterostructures made by stacking of different atomic layers. Sandwich-like heterostructures composed of 2H-MoS_2 and modified graphene layers have been studied and revealed to be a promising anode material for LIBs. In these compounds, as opposed to MoS_2 alone, it has been shown that after being discharged to low potentials, the back-formation of MoS_2 is partially reversible as revealed by the presence of MoS_2 upon the charge [127]. The reversibility of this process results in better cycling stability and higher electrical conductivity. As a result, the MoS_2 anode material exhibits a high initial coulombic efficiency (CE) and excellent cycling performance delivering a specific capacity of 820 mAh g^{-1} after 100 cycles at a current density of 1 A g^{-1} [127]. Uniform graphene-like few-layered WS_2 supported on rGO were produced and tested in LIBs showing to deliver a specific capacity of 400 – 450 mAh g^{-1} at a current density of 100 mA g^{-1} at 50 cycles [128]. A recent study observed that free-standing sandwich-type WS_2-nanotubes/GNs hybrids can maintain a stable capacity of 318.6 mAh g^{-1} over 500 cycles when cycled at 1 A g^{-1} [129]. Sulphur-doped WS_2 delivered a reversible capacity of 566.8 mAh g^{-1} after 50 cycles and proved that the sulphuration process can be extended to other TMDs and provide versatile electrode materials for LIBs [130].

Expansion of the interlayer spacing in several TMDs has been demonstrated to show enhanced performance for applications as electrodes in LIBs [131]. Significant volume variation during charge/discharge cycles can be prevented by an increased spacing in between layers enabling effective accommodation of Li^+ in the interlayer gaps. This feature benefits the structure during cycling leading to higher discharge capacity, better

rate retention capability and cycling stability [131]. Ultrathin interlayer expanded WS_2 nanosheets on a three-dimensional graphene framework (3DG), WS_2/3DG composite, with an interlayer spacing of 0.623 nm shows better cycling stability and rate performance for LIBs when compared to its annealed counterpart and bulk WS_2 [132]. A specific capacity of 766 mAh g^{-1} is delivered by the WS_2/3DG composite against 416 mAh g^{-1} for its annealed composite [132]. Expanded MoS_2, with an interlayer distance from 0.69 nm (*vs* 0.62 nm in the raw material), demonstrated to deliver a much higher specific capacity (700 mAh g^{-1}) [133] compared to raw MoS_2 [134]. To perform ultrafast lithium-ion storage, Qiao *et al.* synthesized mesoporous MoS_2 nanostructures (interlayer spacing of 0.66 nm). These nanostructures exhibit high discharge capacity and excellent rate capacity in LIBs even after 100 cycles [135]. Synthesis of MoS_2 hollow nanospheres possessing an interlayer spacing of 0.66 nm was reported by Lou *et al.* delivering a high capacity of 1100 mAh g^{-1} at 0.5 A g^{-1} retaining this capacity for 100 cycles, showing good rate retention and long cycle life [136]. New approaches to produce larger interspacing between layers of TMDs have been recently studied. The PVP-assistant hydrothermal method was used for the synthesis of 3D radially oriented MoS_2 nanospheres with less than five layers and an interlayer spacing of 0.707 nm. This structure can be described as a highly oriented structure due to the presence of PVP attached to the (002) plane of MoS_2 [137]. This location prevents the structure from restacking during the hydrothermal process and is beneficial for ion and mass transport. MoS_2 nanosphere electrode in LIBs shows an initial discharge and charge specific capacity of 1498 and 1170 mAh g^{-1}, respectively [137]. The radially oriented structure is kept after 100 cycles, supporting the excellent cycling stability for lithium-ion storage [137]. These studies (Table 1.1) show that the electrochemical lithium storage capacity and cycling stability of MoS_2 can be improved by tuning the electrode's interlayer spacing.

Doped TMDs nanosheets were also studied with the intent to improve the stability and cyclability of the electrode for lithium intercalation. Fu *et al.* reported Mo-doped SnS_2-based electrodes grown on carbon cloth (CC@$Sn_{0.9}Mo_{0.1}S_2$) via facile hydrothermal synthesis [138]. With an expanded interlayer spacing of 0.618 nm, the CC@$Sn_{0.9}Mo_{0.1}S_2$ sample exhibits a high-rate performance with a reversible capacity of 914.5 mAh g^{-1} even at a high current density of 5 A g^{-1}. A reversible discharge

capacity of 1950.8 mAh g^{-1} after 200 cycles at 1 A g^{-1} was observed which shows the improved cycling performance of this electrode compared with the undoped sample SnS_2 (645 mAh g^{-1}) [138].

Table 1.1 – Comparison of MoS_2 dichalcogenide anode material in LIBs

Sample	Voltage Range (V)	Interlayer Spacing (nm)	Initial Specific Capacity (mAh g^{-1})	50th cycle Specific Capacity (mAh g^{-1})	Current Density (mA g^{-1})	Cycle Number	Capacity Retention (%)	Ref
MoS_2	0.01 - 3	0.620	800	226	50	50	28	[134]
MoS_2 Expanded	0.01 - 3	0.635	800	750	50	50	94	[134]
MoS_2 Nanoplates	0 - 3	0.69	917	907	1062	50	98	[133]
Mesoporous	0.01 - 3	0.66	1055	~895	100	50	84	[135]
MoS_2 Hollow nanospheres	0.01 - 3	0.66	1100	~1100	50	50	~100	[136]
3D radially oriented nanospheres	0 - 3	0.707	1037	~ 430	50	50	41	[137]

1.6.3.2 Anodes in SIBs technology

As mentioned in Section 1.2, Na possesses similar characteristics to Li which led researchers to investigate the feasibility to use the same electrode materials for both Li and Na^+ ion systems. However, Na^+ ions are much larger than Li^+ ions and electrode designs must be altered to accommodate: (i) the slower diffusion kinetics in the bulk materials and (ii) structural changes in the host material associated with large volume changes upon Na^+ ions insertion/extraction [84], [139]. The intercalation/extraction mechanism of Na^+ ions into TMD materials has been recently studied and revealed to be similar to the one happening in LIBs, with an intercalation and conversion reaction during the first discharge. The sodium storage performance associated with both intercalation and conversion reactions has been extensively studied [117]. MX_2 typically show enhanced capacity when both intercalation and conversion reaction occur however reduced cycling life is observed.

TiS_2 nanoplates have been reported as capable of fast and reversible Na^+ intercalation and deintercalation, delivering a capacity of 186 mAh g^{-1}, which is close to one sodium per formula unit [140].

MoS_2-based compounds were previously proved to be good anode materials for LIBs and recent studies have shown a similar reaction mechanism for Na^+ insertion and extraction. In the average potential 0.75 – 1.25 V, the insertion of Na^+ ions into 2H-MoS_2 monolayer structure can be described as intercalation (Equation 1.9) followed by a conversion reaction (Equation 1.10), delivering a reversible capacity of 146 mAh g^{-1} [141].

$$\text{Intercalation phase: } MoS_2 + xNa^+ + xe^- \leftrightarrow Na_xMoS_2 \text{ (above 0.4V } vs.\ \text{Na}^+/\text{Na}) \quad (1.9)$$

$$\text{Conversion phase: } Na_xMoS_2 + (4-x)Na^+ + (4-x)e^- \leftrightarrow Mo + 2Na_2S\ (\sim 0.4\ \text{V}\ vs.\ \text{Na}^+/\text{Na}) \quad (1.10)$$

The intercalation and extraction of Na^+ ions are electrochemically controlled in the interlayers of raw MoS_2. 2H-MoS_2 goes through a series of two-phase transitions upon Na^+ intercalation involving phases such as:

$$2H\text{-}MoS_2 \rightarrow 2H\text{-}\ Na_{0.5}MoS_2 \rightarrow 1T\text{-}NaMoS_2 \rightarrow\ Mo + Na_xS$$

Studies show that the 2H-MoS_2 structure is irreversibly decomposed to metallic Mo and Na_xS when more than 1.5 moles of Na^+ ions are inserted into MoS_2 [142]. Preventing layer structure destruction between MoS_2 and Na_xMoS_2 can be done by controlling the voltage above 0.4 V [142].

Similarly, to LIBs, research have been made to improve the cyclability and stability of raw MoS_2 focusing on using MoS_2 and carbon-based composites for SIBs applications. One of the best working methods was stabilized to be the enlargement of the Na diffusion channels. Polymer-decorated compounds such as poly (ethylene oxide)-intercalated MoS_2 composites were tested in SIBs, as PEO is ionically conducting and electrochemically inert, not affecting the intercalating path of Na^+ ions [143]. The enhanced ion diffusivity in bilayer composites (PEO2L-MoS_2) as a result of larger structural channels, improves the discharge capacity, as well as rate performance and cycling stability [143]. A value of 225 mAh g^{-1} as discharge capacity can be obtained when cycling PEO2L-MoS_2, which is twice as high as that of commercial MoS_2. David *et al.* produced a flexible paper anode composed of a few-layered MoS_2 combined with rGO showing a specific capacity of 218 mAh g^{-1} [144]. However, the absence of a 3D structure in the MoS_2 nanosheet and difficulty to form robust chemical bonds between the nanosheet and the carbon matrix results in low reversible capacity [144]. Hydrothermal route synthesis prevents some of these issues allowing to achieve larger current densities during charge-discharge cycling. MoS_2 nanoflowers synthesised by hydrothermal methods cycled against Na showed a higher specific capacity of 495 mAh g^{-1} [145]. Chen and co-workers synthesized graphene-like MoS_2 nanoflowers (FG-MoS_2) with expanded interlayer spacings of 0.66-0.69 nm (compared to 0.62 nm of raw MoS_2), showing that FG-MoS_2 (larger interlayer spacing) delivers a higher discharge capacity (200 mAh g^{-1}) when compared to bulk MoS_2 (120 mAh g^{-1}) [141]. The rate performance of both compounds is coincident with the interlayer distance from large to small, indicating that faster reaction kinetics are improved by larger interlayer distance [141]. Oriented compounds have also been studied and CMC-coated MoS_2 nanosheets on carbon (MoS_2@C-CMC) electrodes have been reported to be used in SIBs. MoS_2@C-CMC electrodes were stable while cycled against Na, offering a charge capacity of 286 mAh g^{-1} after 100 cycles [146]. Other synthesis routes were successfully

employed to produce MoS_2 carbon composites for anode materials of SIBs such as electrospinning, spray pyrolysis, microwave-assisted synthesis and electrospinning combined with atomic layer deposition (ALD) [99]. The electrochemical performance of all these materials is summarised in Table 1.2.

WS_2 nanowires with an expanded interlayer spacing of 0.83 nm were synthesized through a solvothermal method followed by a heat treatment for SIBs applications. The nanowires cycled over the potential window 0.01 – 2.5 V deliver a high specific capacity of 605.3 mAh g^{-1} maintaining 79 % of the initial capacity after 50 cycles (483.2 mAh g^{-1}) [147]. The modified WS_2 nanowires show better performance compared with bulk WS_2 (interlayer spacing 0.62 nm). When cycled between 0.5 – 3 V, the WS_2 nanowires show a reversible intercalation mechanism exhibiting a longer cycles life (up to 1400 cycles) delivering 330 mAh g^{-1} at 1000 mA g^{-1} [147]. Carbon-doped ternary $Mo(Se_{0.85}S_{0.15})_2$:C nanotubes were demonstrated to have superior sodium storage performance when compared with undoped $MoSe_2$ exhibiting an interlayer spacing of 0.99 -1.09 nm. A specific capacity of 440 mAh g^{-1} was obtained showing high capacity retention of 82 % [148].

Table 1.2 - Comparison of MoS_2 dichalcogenide anode material in SIBs

Sample	Voltage Range (V)	Initial Specific Capacity (mAh g^{-1})	50th cycle Specific Capacity (mAh g^{-1})	Current Density (mA g^{-1})	Cycle Number	Capacity Retention (%)	Ref
MoS_2	0.1 – 2.25	223	100	25	20*	45	[144]
MoS_2 - PEO	0.1 - 3	225	~152	50	50	67	[143]
MoS_2 – rGO	0.1 – 2.25	338	218	25	20*	65	[144]
MoS_2 - nanoflowers	1 - 3	1065	495	67	50	47	[145]
MoS_2@C-CMC	0.1 - 3	556	~300	80	50	54	[146]

*samples cycled only up to 20 cycles

1.7 Scope of this thesis

In the light of the context presented so far, this thesis aims to entail a prospective study of several layered dichalcogenide materials as possible negative electrode materials for LIBs and SIBs. These novel anode materials must fulfil several criteria in terms of energy density, performance, and long-term stability as well as structural stability during ion insertion/extraction. Therefore, the objective of this project is to examine all aspects of the new materials and test them to assess their viability. The target compounds studied in this thesis contain row 5 and row 6 transition metals, namely W and Ta. Chapters 3 and 4 are devoted to studying the structural and electrochemical properties of WTe_2 in both SIBs and LIBs. In chapter 5, the study of the viability of $TaTe_2$ as anode material for LIBs was accessed.

1.8 References

[1] Energy Information Administration, “History of energy consumption in the United States, 1775–2009 - Today in Energy - US Energy Information Administration,” *www.eia.gov*, 2011. https://www.eia.gov/todayinenergy/detail.php?id=10 (accessed Sep. 30, 2020).

[2] “European Environment Agency’s home page — European Environment Agency.” https://www.eea.europa.eu/ (accessed Sep. 30, 2020).

[3] “Energy - Our World in Data.” https://ourworldindata.org/energy (accessed Sep. 30, 2020).

[4] U. S. E. I. Administration, “International Energy Outlook 2019 with projections to 2050,” *Choice Rev. Online*, p. 85, 2019, doi: 10.5860/CHOICE.44-3624.

[5] D. Gielen, F. Boshell, D. Saygin, M. D. Bazilian, N. Wagner, and R. Gorini, “The role of renewable energy in the global energy transformation,” *Energy Strateg. Rev.*, vol. 24, no. January, pp. 38–50, 2019, doi: 10.1016/j.esr.2019.01.006.

[6] B. Dunn, H. Kamath, and J. Tarascon, “Eletrical Energy Storage for the Grid : A

Battery of Choices," *Science (80-.).*, vol. 334, no. 6058, p. 928, 2011, doi: 10.1126/science.1212741.

[7] R. A. Huggins, *Advanced batteries: Materials science aspects*. 2009.

[8] D. Linden, "Basic Concepts," in *Handbook of Batteries*, 4 edition., M.-H. Education, Ed. New York: McGraw-Hill Education, 2004, pp. 1.1-1.18.

[9] M. Armand and J. M. Tarascon, "Building better batteries," *Nature*, vol. 451, no. 7179, pp. 652–657, 2008, doi: 10.1038/451652a.

[10] M. D. Bhatt and C. O'Dwyer, "Recent progress in theoretical and computational investigations of Li-ion battery materials and electrolytes," *Phys. Chem. Chem. Phys.*, vol. 17, no. 7, pp. 4799–4844, 2015, doi: 10.1039/C4CP05552G.

[11] A. Eftekhari, "Lithium-Ion Batteries with High Rate Capabilities," *ACS Sustain. Chem. Eng.*, vol. 5, no. 4, pp. 2799–2816, 2017, doi: 10.1021/acssuschemeng.7b00046.

[12] D. Deng, "Li-ion batteries: Basics, progress, and challenges," *Energy Sci. Eng.*, vol. 3, no. 5, pp. 385–418, 2015, doi: 10.1002/ese3.95.

[13] N. Loeffler, D. Bresser, and S. Passerini, "Secondary Lithium-Ion Battery Anodes: From First Commercial Batteries to Recent Research Activities," *Johnson Matthey Technol. Rev.*, vol. 59, no. 1, pp. 34–44, 2015, doi: 10.1595/205651314X685824.

[14] S. Bhatia, "Lithium: An Economic Overview," 2012.

[15] Y. Ding, Z. P. Cano, A. Yu, J. Lu, and Z. Chen, "Automotive Li-Ion Batteries: Current Status and Future Perspectives," *Electrochem. Energy Rev.*, vol. 2, no. 1, pp. 1–28, 2019, doi: 10.1007/s41918-018-0022-z.

[16] D. Linden and T. B. Reddy, "Lithium Batteries," in *Handbook of Batteries*, 4 Edition., M.-H. Education, Ed. New York: McGraw-Hill Education, 2004, pp. 14.1-14.106.

[17] J. M. Tarascon and M. Armandi, "Issues and challenges facing rechargeable

lithium batteries," *Nature*, vol. 414, pp. 359–367, 2001.

[18] Thomas B. Reddy and S. Hossain, "Rechargeable lithium batteries (ambient temperature)," in *Handbook of batteries*, 4 Edition., McGraw-Hill Education, Ed. McGraw-Hill Education, 2002, pp. 34.1-34.25.

[19] K. Liu, Y. Liu, D. Lin, A. Pei, and Y. Cui, "Materials for lithium-ion battery safety," *Sci. Adv.*, vol. 4, no. 6, 2018, doi: 10.1126/sciadv.aas9820.

[20] N. Nitta, F. Wu, J. T. Lee, and G. Yushin, "Li-ion battery materials: Present and future," *Mater. Today*, vol. 18, no. 5, pp. 252–264, 2015, doi: 10.1016/j.mattod.2014.10.040.

[21] A. M. Skundin, T. L. Kulova, and A. B. Yaroslavtsev, "Sodium-Ion Batteries (a Review)," *Russ. J. Electrochem.*, vol. 54, no. 2, pp. 113–152, 2018, doi: 10.1134/S1023193518020076.

[22] M. I. Jamesh and A. S. Prakash, "Advancement of technology towards developing Na-ion batteries," *J. Power Sources*, vol. 378, no. October 2017, pp. 268–300, 2018, doi: 10.1016/j.jpowsour.2017.12.053.

[23] R. S. Carmichael, *Practical handbook of physical properties of rocks and minerals*, 2 Edition. Florida: CRC Press, 1989.

[24] V. Palomares, P. Serras, I. Villaluenga, K. B. Hueso, J. Carretero-González, and T. Rojo, "Na-ion batteries, recent advances and present challenges to become low cost energy storage systems," *Energy Environ. Sci.*, vol. 5, no. 3, pp. 5884–5901, 2012, doi: 10.1039/c2ee02781j.

[25] S. W. Kim, D. H. Seo, X. Ma, G. Ceder, and K. Kang, "Electrode materials for rechargeable sodium-ion batteries: Potential alternatives to current lithium-ion batteries," *Adv. Energy Mater.*, vol. 2, no. 7, pp. 710–721, 2012, doi: 10.1002/aenm.201200026.

[26] P. Adelhelm, P. Hartmann, C. L. Bender, M. Busche, C. Eufinger, and J. Janek, "From lithium to sodium: Cell chemistry of room temperature sodium-air and sodium-sulfur batteries," *Beilstein J. Nanotechnol.*, vol. 6, no. 1, pp. 1016–1055,

2015, doi: 10.3762/bjnano.6.105.

[27] M. Yoshio, R. J. Brood, and A. Kozawa, *Lithium-Ion Batteries*. New York: Springer Science and Bussiness, 2009.

[28] H. Du, Y. Zheng, Z. Dou, and H. Zhan, "Material for Lithium Ion Battery : Preparation , Characterization , and Electrochemical Properties," *Jounal Nanomater.*, vol. 2015, no. Cv, pp. 1–6, 2015.

[29] K. Mizushima, P. C. Jones, P. J. Wiseman, and J. B. Goodenough, "LixCoO2 (0<x≤1): A new cathode material for batteries of high energy density," *Solid State Ionics*, vol. 3–4, no. C, pp. 171–174, 1981, doi: 10.1016/0167-2738(81)90077-1.

[30] A. Du Pasquier, I. Plitz, S. Menocal, and G. Amatucci, "A comparative study of Li-ion battery, supercapacitor and nonaqueous asymmetric hybrid devices for automotive applications," *J. Power Sources*, vol. 115, no. 1, pp. 171–178, 2003, doi: 10.1016/S0378-7753(02)00718-8.

[31] *Advances in Lithium-Ion Batteries*. 2002.

[32] H. Arai, "Thermal behavior of Li1−yNiO2 and the decomposition mechanism," *Solid State Ionics*, vol. 109, no. 3–4, pp. 295–302, 1998, doi: 10.1016/S0167-2738(98)00075-7.

[33] A. Rougier, P. Gravereau, and C. Delmas, "Optimization of the composition of the Li1-zNi1+zO2 Electrode Materials: Structural, Magnetic and Electrochemical Studies," *J. Electrochem. Soc.*, vol. 143, no. 4, pp. 1168–1175, 1996.

[34] S. Yamada, M. Fujiwara, and M. Kanda, "Synthesis and properties of LiNiO2 as cathode material for secondary batteries," *J. Power Sources*, vol. 54, pp. 209–2013, 1995, doi: 10.1016/B978-0-444-41345-1.50007-1.

[35] J. Tu, X. B. Zhao, G. S. Cao, D. G. Zhuang, T. J. Zhu, and J. P. Tu, "Enhanced cycling stability of LiMn2O4 by surface modification with melting impregnation method," *Electrochim. Acta*, vol. 51, no. 28, pp. 6456–6462, 2006, doi:

10.1016/j.electacta.2006.04.031.

[36] A. R. Armstrong and P. G. Bruce, “Synthesis of layered LiMnO2 as an electrode for rechargeable lithium batteries,” *Nature*, vol. 381, no. 6582. pp. 499–500, 1996, doi: 10.1038/381499a0.

[37] L. A. Godinez, J. Lin, and M. Marc, “Electrochemical and *In situ* X-Ray Diffraction Studies of Lithium Intercalation in LixCo02,” *J. Electrochem. Soc.*, vol. 139, no. 8, pp. 2–8, 1996, doi: 10.3791/50770.Semiconductor-Metal.

[38] T. Ohzuku and Y. Makimura, “Layered Lithium Insertion Material of LiNi1/2Mn1/2O2: A Possible Alternative to LiCoO2 for Advanced Lithium-Ion Batteries.,” *Chem. Lett.*, vol. 2, pp. 744–745, 2001, doi: 10.1246/cl.2001.744.

[39] H. H. Li *et al.*., “Changes in the Cation Ordering of Layered O3 Li x Ni 0.5 Mn 0.5 O 2 during Electrochemical Cycling to High Voltages: An Electron Diffraction Study,” *Chem. Mater.*, vol. 19, no. 10, pp. 2551–2565, 2007, doi: 10.1021/cm070139+.

[40] F. Breu, S. Guggenbichler, and J. Wollmann, “SYNTHESIS AND CHARACTERIZATION OF LITHIUM-ION CATHODE MATERIALS IN THE SYSTEM (1-x-y)LiNi1/3Mn1/3Co1/3O2 · xLi2MnO3 · yLiCoO2,” *Vasa*, 2012, [Online]. Available: http://medcontent.metapress.com/index/A65RM03P4874243N.pdf.

[41] J. Li, H. Li, W. Stone, R. Weber, S. Hy, and J. R. Dahn, “Synthesis of Single Crystal LiNi $_{0.5}$ Mn $_{0.3}$ Co $_{0.2}$ O $_{2}$ for Lithium Ion Batteries,” *J. Electrochem. Soc.*, vol. 164, no. 14, pp. A3529–A3537, 2017, doi: 10.1149/2.0401714jes.

[42] P. Zhang, L. Zhang, X. Ren, Q. Yuan, J. Liu, and Q. Zhang, “Preparation and electrochemical properties of LiNi1/3Co1/3Mn1/3O2-PPy composites cathode materials for lithium-ion battery,” *Synth. Met.*, vol. 161, no. 11–12, pp. 1092–1097, 2011, doi: 10.1016/j.synthmet.2011.03.021.

[43] T. Ohzuku and Y. Makimura, “Layered Lithium Insertion Material of LiCo 1/3 Ni 1/3 Mn 1/3 O 2 for Lithium-Ion Batteries,” *Chem. Lett.*, vol. 30, no. 7, pp.

642–643, 2001, doi: 10.1246/cl.2001.642.

[44] A. Deb, U. Bergmann, S. P. Cramer, and E. J. Cairns, “Local structure of LiNi0.5Mn0.5O2 cathode material probed by *in situ* x-ray absorption spectroscopy,” *J. Appl. Phys.*, vol. 99, no. 6, p. 063701, 2006, doi: 10.1063/1.2179198.

[45] Y. Bai, Q. Chang, Q. Yu, S. Zhao, and K. Jiang, “A novel approach to improve the electrochemical performances of layered LiNi1/3Co1/3Mn1/3O2cathode by YPO4surface coating,” *Electrochim. Acta*, vol. 112, pp. 414–421, 2013, doi: 10.1016/j.electacta.2013.09.002.

[46] J. P. Baboo *et al.*., “Facile Redox Synthesis of Layered LiNi1/3Co1/3Mn1/3O2 for Rechargeable Li-ion Batteries,” *Electrochim. Acta*, vol. 224, pp. 243–250, 2017, doi: 10.1016/j.electacta.2016.12.050.

[47] J. Reed and G. Ceder, “Charge, Potential, and Phase Stability of Layered Li(Ni[sub 0.5]Mn[sub 0.5])O[sub 2],” *Electrochem. Solid-State Lett.*, vol. 5, no. 7, p. A145, 2002, doi: 10.1149/1.1480135.

[48] K. Märker, P. J. Reeves, C. Xu, K. J. Griffith, and C. P. Grey, “Evolution of Structure and Lithium Dynamics in LiNi0.8Mn0.1Co0.1O2 (NMC811) Cathodes during Electrochemical Cycling,” *Chem. Mater.*, vol. 31, no. 7, pp. 2545–2554, 2019, doi: 10.1021/acs.chemmater.9b00140.

[49] E. Talaie, V. Duffort, H. L. Smith, B. Fultz, and L. F. Nazar, “Structure of the high voltage phase of layered P2-Na $_{2/3-z}$ [Mn $_{1/2}$ Fe $_{1/2}$]O $_{2}$ and the positive effect of Ni substitution on its stability,” *Energy Environ. Sci.*, vol. 8, no. 8, pp. 2512–2523, 2015, doi: 10.1039/C5EE01365H.

[50] C. Delmas, C. Fouassier, and P. Hagenmuller, “Structural classification and properties of the layered oxides,” *Phys. B+C*, vol. 99, no. 1–4, pp. 81–85, 1980, doi: 10.1016/0378-4363(80)90214-4.

[51] P. F. Wang, Y. You, Y. X. Yin, and Y. G. Guo, “Layered Oxide Cathodes for Sodium-Ion Batteries: Phase Transition, Air Stability, and Performance,” *Adv.*

Energy Mater., vol. 8, no. 8, pp. 1–23, 2018, doi: 10.1002/aenm.201701912.

[52] J. J. Braconnier, C. Delmas, and P. Hagenmuller, "Etude par desintercalation electrochimique des systemes NaxCrO2 et NaxNiO2," *Mater. Res. Bull.*, vol. 17, no. 8, pp. 993–1000, 1982, doi: 10.1016/0025-5408(82)90124-6.

[53] J. Cabana *et al.*., "Study of the transition metal ordering in layered NaxNix/2Mn1-x/2O2($2/3 \leq x \leq 1$) and consequences of Na/Li exchange," *Inorg. Chem.*, vol. 52, no. 15, pp. 8540–8550, 2013, doi: 10.1021/ic400579w.

[54] P. Ge, M. Fouletier, and D. Claude, "ELECTROCHEMICAL INTERCALATION OF SODIUM IN NaxCoO2 BRONZES," *Solid State Ionics*, vol. 28–30, pp. 165–169, 1981, doi: 10.1016/0167-2738(88)90351-7.

[55] R. Berthelot, D. Carlier, and C. Delmas, "Electrochemical investigation of the P2–NaxCoO2 phase diagram," *Nat. Mater.*, vol. 10, no. 1, pp. 74–80, 2011, doi: 10.1038/nmat2920.

[56] A. Mendiboure, C. Delmas, and P. Hagenmuller, "Electrochemical intercalation and deintercalation of NaxMnO2 bronzes," *J. Solid State Chem.*, vol. 57, no. 3, pp. 323–331, 1985, doi: 10.1016/0022-4596(85)90194-X.

[57] J. Billaud *et al.*., "β-NaMnO2: A high-performance cathode for sodium-ion batteries," *J. Am. Chem. Soc.*, vol. 136, no. 49, pp. 17243–17248, 2014, doi: 10.1021/ja509704t.

[58] E. de la Llave *et al.*., "Electrochemical performance of $Na_{0.6}[Li_{0.2}Ni_{0.2}Mn_{0.6}]O_2$ cathodes with high-working average voltage for Na-ion batteries," *J. Mater. Chem. A*, vol. 5, no. 12, pp. 5858–5864, 2017, doi: 10.1039/C6TA10577G.

[59] H. Kim *et al.*., "Recent Progress in Electrode Materials for Sodium-Ion Batteries," *Adv. Energy Mater.*, vol. 6, no. 19, pp. 1–19, 2016, doi: 10.1002/aenm.201600943.

[60] Z. Gong and Y. Yang, "Recent advances in the research of polyanion-type cathode materials for Li-ion batteries," *Energy Environ. Sci.*, vol. 4, no. 9, pp. 3223–3242, 2011, doi: 10.1039/c0ee00713g.

[61] J. Kim *et al.*., "Unexpected discovery of low-cost maricite NaFePO4 as a high-performance electrode for Na-ion batteries," *Energy Environ. Sci.*, vol. 8, no. 2, pp. 540–545, 2015, doi: 10.1039/c4ee03215b.

[62] P. Moreau, D. Guyomard, J. Gaubicher, and F. Boucher, "Structure and stability of sodium intercalated phases in olivine FePO 4," *Chem. Mater.*, vol. 22, no. 14, pp. 4126–4128, 2010, doi: 10.1021/cm101377h.

[63] N. Yabuuchi and S. Komaba, "Recent research progress on iron- and manganese-based positive electrode materials for rechargeable sodium batteries," *Sci. Technol. Adv. Mater.*, vol. 15, no. 4, 2014, doi: 10.1088/1468-6996/15/4/043501.

[64] J. Lu, Z. Chen, F. Pan, Y. Cui, and K. Amine, "High-Performance Anode Materials for Rechargeable Lithium-Ion Batteries," *Electrochem. Energy Rev.*, vol. 1, no. 1, pp. 35–53, 2018, doi: 10.1007/s41918-018-0001-4.

[65] T. Perveen, M. Siddiq, N. Shahzad, R. Ihsan, A. Ahmad, and M. I. Shahzad, "Prospects in anode materials for sodium ion batteries - A review," *Renew. Sustain. Energy Rev.*, vol. 119, no. October 2019, p. 109549, 2020, doi: 10.1016/j.rser.2019.109549.

[66] K. Zaghib, A. Mauger, H. Groult, J. B. Goodenough, and C. M. Julien, "Advanced electrodes for high power Li-ion batteries," *Materials (Basel).*, vol. 6, no. 3, pp. 1028–1049, 2013, doi: 10.3390/ma6031028.

[67] C. M. Hayner, X. Zhao, and H. H. Kung, "Materials for Rechargeable Lithium-Ion Batteries," *Annu. Rev. Chem. Biomol. Eng.*, vol. 3, no. 1, pp. 445–471, 2012, doi: 10.1146/annurev-chembioeng-062011-081024.

[68] J. R. D. Rosamaría Fong, Ulrich von Sacken, "Studies of Lithium Intercalation into Carbons Using Nonaqueous Electrochemical Cells," *J. Electrochem. Soc.*, vol. 137, no. 7, pp. 2009–2013, 1990, doi: 10.1149/1.2086855.

[69] H. F. ANDERSEN, "New Materials for Lithium-Ion Batteries," 2013.

[70] A. N. Dey and B. P. Sullivan, "The Electrochemical Decomposition of Propylene Carbonate on Graphite," *J. Electrochem. Soc.*, vol. 117, no. 2, p. 222, 1970, doi:

10.1149/1.2407470.

[71] N. A. Kaskhedikar and J. Maier, “Lithium storage in carbon nanostructures,” *Adv. Mater.*, vol. 21, no. 25–26, pp. 2664–2680, 2009, doi: 10.1002/adma.200901079.

[72] Q. Cheng, Y. Okamoto, N. Tamura, M. Tsuji, S. Maruyama, and Y. Matsuo, “Graphene-Like-Graphite as Fast-Chargeable and High-Capacity Anode Materials for Lithium Ion Batteries,” *Sci. Rep.*, vol. 7, no. 1, pp. 1–14, 2017, doi: 10.1038/s41598-017-14504-8.

[73] J. Sangster, “C-Na (carbon-sodium) system,” *J. Phase Equilibria Diffus.*, vol. 28, no. 6, pp. 571–579, 2007, doi: 10.1007/s11669-007-9194-7.

[74] D. Saurel, B. Orayech, B. Xiao, D. Carriazo, X. Li, and T. Rojo, “From Charge Storage Mechanism to Performance: A Roadmap toward High Specific Energy Sodium-Ion Batteries through Carbon Anode Optimization,” *Adv. Energy Mater.*, vol. 8, no. 17, pp. 1–33, 2018, doi: 10.1002/aenm.201703268.

[75] Z. Chen, I. Belharouak, Y. K. Sun, and K. Amine, “Titanium-based anode materials for safe lithium-ion batteries,” *Adv. Funct. Mater.*, vol. 23, no. 8, pp. 959–969, 2013, doi: 10.1002/adfm.201200698.

[76] L. Zhou *et al.*, “Recent Developments on and Prospects for Electrode Materials with Hierarchical Structures for Lithium-Ion Batteries,” *Adv. Energy Mater.*, vol. 8, no. 6, pp. 1–23, 2018, doi: 10.1002/aenm.201701415.

[77] C. Wu *et al.*, “Design and Synthesis of Layered Na2Ti3O7 and Tunnel Na2Ti6O13 Hybrid Structures with Enhanced Electrochemical Behavior for Sodium-Ion Batteries,” *Adv. Sci.*, vol. 5, no. 9, 2018, doi: 10.1002/advs.201800519.

[78] L. Zennaro *et al.*, “Stable aqueous solutions of naked titanate nanotubes,” *ChemPhysChem*, vol. 14, no. 12, pp. 2786–2792, 2013, doi: 10.1002/cphc.201300292.

[79] Y. Xu, D. Bauer, M. Lübke, T. E. Ashton, Y. Zong, and J. A. Darr, “High-power

sodium titanate anodes; a comparison of lithium vs sodium-ion batteries," *J. Power Sources*, vol. 408, no. September, pp. 28–37, 2018, doi: 10.1016/j.jpowsour.2018.10.038.

[80] A. Anani and R. A. Huggins, "Multinary alloy electrodes for solid state batteries II. A new LiSiMg alloy negative electrode material for use in high energy density rechargeable lithium cells," *J. Power Sources*, vol. 38, no. 3, pp. 363–372, 1992, doi: 10.1016/0378-7753(92)80126-V.

[81] D. Larcher, S. Beattie, M. Morcrette, K. Edsröm, J.-C. Jumas, and J.-M. Tarascon, "Recent findings and prospects in the field of pure metals as negative electrodes for Li-ion batteries," *J. Mater. Chem.*, vol. 17, no. 36, p. 3759, 2007, doi: 10.1039/b705421c.

[82] C.-M. Park, J.-H. Kim, H. Kim, and H.-J. Sohn, "Li-alloy based anode materials for Li secondary batteries," *Chem. Soc. Rev.*, vol. 39, no. 8, p. 3115, 2010, doi: 10.1039/b919877f.

[83] H. Kim, G. Jeong, Y.-U. Kim, J.-H. Kim, C.-M. Park, and H.-J. Sohn, "Metallic anodes for next generation secondary batteries," *Chem. Soc. Rev.*, vol. 42, no. 23, p. 9011, 2013, doi: 10.1039/c3cs60177c.

[84] Y.-G. Guo, J.-S. Hu, and L.-J. Wan, "Nanostructured Materials for Electrochemical Energy Conversion and Storage Devices," *Adv. Mater.*, vol. 20, no. 15, pp. 2878–2887, 2008, doi: 10.1002/adma.200800627.

[85] Y. Qiu, K. Yan, and S. Yang, "Ultrafine tin nanocrystallites encapsulated in mesoporous carbon nanowires: scalable synthesis and excellent electrochemical properties for rechargeable lithium ion batteries," *Chem. Commun.*, vol. 46, no. 44, p. 8359, 2010, doi: 10.1039/c0cc03385e.

[86] Y. Yu, L. Gu, C. Wang, A. Dhanabalan, P. A. Van Aken, and J. Maier, "Encapsulation of Sn@carbon nanoparticles in bamboo-like hollow carbon nanofibers as an anode material in lithium-based batteries," *Angew. Chemie - Int. Ed.*, vol. 48, no. 35, pp. 6485–6489, 2009, doi: 10.1002/anie.200901723.

[87] A. N. Dey, “Electrochemical Alloying of Lithium in Organic Electrolytes,” *J. Electrochem. Soc.*, vol. 118, no. 10, p. 1547, 1971, doi: 10.1149/1.2407783.

[88] D. W. Murphy and P. A. Christian, “Solid State Electrodes for High Energy Batteries,” *Science (80-.).*, vol. 205, no. 4407, pp. 651–656, 1979.

[89] P. Poizot, S. Laruelle, S. Grugeon, L. Dupont, and J. Tarascon, “Nano-sized transition-metal oxides as negative-electrode materials for lithium-ion batteries,” *Lett. Nat.*, vol. 407, no. September, 2000.

[90] J. Cabana, L. Monconduit, D. Larcher, and M. R. Palacín, “Beyond intercalation-based Li-ion batteries: The state of the art and challenges of electrode materials reacting through conversion reactions,” *Adv. Mater.*, vol. 22, no. 35, pp. 170–192, 2010, doi: 10.1002/adma.201000717.

[91] Y. Gong *et al.*., “Vertical and in-plane heterostructures from WS 2 /MoS 2 monolayers,” *Nat. Mater.*, vol. 13, no. 12, pp. 1135–1142, 2014, doi: 10.1038/nmat4091.

[92] B. E. Brown, “The crystal structures of NbT_2 and $TaTe_2$,” *Acta Crystallogr.*, vol. 20, no. 2, pp. 264–267, 1966, doi: 10.1107/S0365110X66000501.

[93] A. Eftekhari, “Tungsten Dichalcogenides (WS2, WSe2, and WTe2): Materials Chemistry and Applications,” *J. Mater. Chem. A*, pp. 18299–18325, 2017, doi: 10.1039/C7TA04268J.

[94] G. Bin Liu, D. Xiao, Y. Yao, X. Xu, and W. Yao, “Electronic structures and theoretical modelling of two-dimensional group-VIB transition metal dichalcogenides,” *Chem. Soc. Rev.*, vol. 44, no. 9, pp. 2643–2663, 2015, doi: 10.1039/c4cs00301b.

[95] T. Sörgel, J. Nuss, U. Wedig, R. K. Kremer, and M. Jansen, “A new low temperature modification of TaTe2-Comparison to the room temperature and the hypothetical 1T-TaTe2modification,” *Mater. Res. Bull.*, vol. 41, no. 5, pp. 987–1000, 2006, doi: 10.1016/j.materresbull.2006.02.020.

[96] G. Zhang, H. Liu, J. Qu, and J. Li, “Two-dimensional layered MoS2: Rational

design, properties and electrochemical applications," *Energy Environ. Sci.*, vol. 9, no. 4, pp. 1190–1209, 2016, doi: 10.1039/c5ee03761a.

[97] R. Lv *et al.*., "Transition metal dichalcogenides and beyond: Synthesis, properties, and applications of single- and few-layer nanosheets," *Acc. Chem. Res.*, vol. 48, no. 1, pp. 56–64, 2015, doi: 10.1021/ar5002846.

[98] S. Zhang *et al.*., "Porous Organic Frameworks: Advanced Materials in Analytical Chemistry," *Adv. Sci.*, vol. 5, no. 12, 2018, doi: 10.1002/advs.201801116.

[99] S. Wu, Y. Du, and S. Sun, "Transition metal dichalcogenide based nanomaterials for rechargeable batteries," *Chem. Eng. J.*, vol. 307, pp. 189–207, 2017, doi: 10.1016/j.cej.2016.08.044.

[100] N. Choudhary *et al.*., "Centimeter Scale Patterned Growth of Vertically Stacked Few Layer Only 2D MoS2/WS2 van der Waals Heterostructure," *Sci. Rep.*, vol. 6, no. April, pp. 4–10, 2016, doi: 10.1038/srep25456.

[101] J. A. Cody and J. A. Ibers, "Uranium Tellurides: New One- and Two-Dimensional Compounds CsUTe6, CsTiUTes, Cs8Hf5UTe3o.6, and CsCuUTe3," *Inorg. Chem.*, vol. 34, no. 12, pp. 3165–3172, 1995, doi: 10.1021/ic00116a006.

[102] C. Li *et al.*., "Engineering graphene and TMDs based van der Waals heterostructures for photovoltaic and photoelectrochemical solar energy conversion," *Chem. Soc. Rev.*, vol. 47, no. 13, pp. 4981–5037, 2018, doi: 10.1039/c8cs00067k.

[103] L.-J. Li, G. Eda, H. Zhang, K. P. Loh, H. S. Shin, and M. Chhowalla, "The chemistry of two-dimensional layered transition metal dichalcogenide nanosheets," *Nat. Chem.*, vol. 5, no. 4, pp. 263–275, 2013, doi: 10.1038/nchem.1589.

[104] E. Torun, H. Sahin, S. Cahangirov, A. Rubio, and F. M. Peeters, "Anisotropic electronic, mechanical, and optical properties of monolayer WTe2," *J. Appl. Phys.*, vol. 119, no. 7, 2016, doi: 10.1063/1.4942162.

[105] M. A. Py and R. R. Haering, " Structural destabilization induced by lithium intercalation in MoS 2 and related compounds ," *Can. J. Phys.*, vol. 61, no. 1, pp. 76–84, 2011, doi: 10.1139/p83-013.

[106] R. J. Smith *et al.*., "Large-scale exfoliation of inorganic layered compounds in aqueous surfactant solutions," *Adv. Mater.*, vol. 23, no. 34, pp. 3944–3948, 2011, doi: 10.1002/adma.201102584.

[107] L. Niu, J. N. Coleman, H. Zhang, H. Shin, M. Chhowalla, and Z. Zheng, "Production of Two-Dimensional Nanomaterials via Liquid-Based Direct Exfoliation," *Small*, vol. 12, no. 3, pp. 272–293, 2016, doi: 10.1002/smll.201502207.

[108] C. Backes *et al.*., "Guidelines for exfoliation, characterization and processing of layered materials produced by liquid exfoliation," *Chem. Mater.*, vol. 29, no. 1, pp. 243–255, 2017, doi: 10.1021/acs.chemmater.6b03335.

[109] J. Kang, V. K. Sangwan, J. D. Wood, and M. C. Hersam, "Solution-Based Processing of Monodisperse Two-Dimensional Nanomaterials," *Acc. Chem. Res.*, vol. 50, no. 4, pp. 943–951, 2017, doi: 10.1021/acs.accounts.6b00643.

[110] V. Nicolosi, M. Chhowalla, M. G. Kanatzidis, M. S. Strano, and J. N. Coleman, "Liquid exfoliation of layered materials," *Science (80-.).*, vol. 340, no. 6139, pp. 72–75, 2013, doi: 10.1126/science.1226419.

[111] F. Schedin *et al.*., "Detection of individual gas molecules adsorbed on graphene," *Nat. Mater.*, vol. 6, no. 9, pp. 652–655, 2007, doi: 10.1038/nmat1967.

[112] W. Choi, N. Choudhary, G. H. Han, J. Park, D. Akinwande, and Y. H. Lee, "Recent development of two-dimensional transition metal dichalcogenides and their applications," *Mater. Today*, vol. 20, no. 3, pp. 116–130, 2017, doi: 10.1016/j.mattod.2016.10.002.

[113] B. Chen, D. Chao, E. Liu, M. Jaroniec, N. Zhao, and S.-Z. Qiao, "Transition metal dichalcogenides for alkali metal ion batteries: engineering strategies at the atomic level," *Energy Environ. Sci.*, vol. 13, no. 4, pp. 1096–1131, 2020, doi:

10.1039/c9ee03549d.

[114] A. Senyshyn, M. J. Mühlbauer, O. Dolotko, and H. Ehrenberg, “Low-temperature performance of Li-ion batteries: The behavior of lithiated graphite,” *J. Power Sources*, vol. 282, pp. 235–240, 2015, doi: 10.1016/j.jpowsour.2015.02.008.

[115] L. F. Cui, Y. Yang, C. M. Hsu, and C. Yi, “Carbon-silicon Core-shell nanowires as high capacity electrode for lithium lon batteries,” *Nano Lett.*, vol. 9, no. 9, pp. 3370–3374, 2009, doi: 10.1021/nl901670t.

[116] J. Kibsgaard, Z. Chen, B. N. Reinecke, and T. F. Jaramillo, “Engineering the surface structure of MoS 2 toÂ preferentially expose active edge sites forÂ electrocatalysis,” *Nat. Mater.*, vol. 11, no. 11, pp. 963–969, 2012, doi: 10.1038/nmat3439.

[117] U. K. Sen and S. Mitra, “High-rate and high-energy-density lithium-ion battery anode containing 2D MoS2 nanowall and cellulose binder,” *ACS Appl. Mater. Interfaces*, vol. 5, no. 4, pp. 1240–1247, 2013, doi: 10.1021/am3022015.

[118] F. Xia, X. Hu, Y. Sun, W. Luo, and Y. Huang, “Layer-by-layer assembled MoO2-graphene thin film as a high-capacity and binder-free anode for lithium-ion batteries,” *Nanoscale*, vol. 4, no. 15, pp. 4707–4711, 2012, doi: 10.1039/c2nr30742a.

[119] Q. Ji *et al.*, “Metallic vanadium disulfide nanosheets as a platform material for multifunctional electrode applications,” *Nano Lett.*, vol. 17, no. 8, pp. 4908–4916, 2017, doi: 10.1021/acs.nanolett.7b01914.

[120] N. S. Mikhaleva, M. A. Visotin, A. A. Kuzubov, and Z. I. Popov, “VS2/Graphene Heterostructures as Promising Anode Material for Li-Ion Batteries,” *J. Phys. Chem. C*, vol. 121, no. 43, pp. 24179–24184, 2017, doi: 10.1021/acs.jpcc.7b07630.

[121] T. Stephenson, Z. Li, B. Olsen, and D. Mitlin, “Lithium ion battery applications of molybdenum disulfide (MoS_2) nanocomposites,” *Energy Environ. Sci.*, vol.

7, no. 1, pp. 209–231, 2014, doi: 10.1039/C3EE42591F.

[122] K. Chang and W. Chen, "*In situ* synthesis of MoS2/graphene nanosheet composites with extraordinarily high electrochemical performance for lithium ion batteries," *Chem. Commun.*, vol. 47, no. 14, pp. 4252–4254, 2011, doi: 10.1039/c1cc10631g.

[123] Y. Zhang, Y. Li, H. Li, F. Yin, Y. Zhao, and Z. Bakenov, "Synthesis of hierarchical MoS2 microspheres composed of nanosheets assembled via facile hydrothermal method as anode material for lithium-ion batteries," *J. Nanoparticle Res.*, vol. 18, no. 3, pp. 1–9, 2016, doi: 10.1007/s11051-016-3366-5.

[124] P. Sun, W. Zhang, X. Hu, L. Yuan, and Y. Huang, "Synthesis of hierarchical MoS2 and its electrochemical performance as an anode material for lithium-ion batteries," *J. Mater. Chem. A*, vol. 2, no. 10, pp. 3498–3504, 2014, doi: 10.1039/c3ta13994h.

[125] D. Lin *et al.*., "Fast preparation of MoS2 nanoflowers decorated with platinum nanoparticles for electrochemical detection of hydrogen peroxide," *RSC Adv.*, vol. 6, no. 58, pp. 52739–52745, 2016, doi: 10.1039/c6ra07591f.

[126] X. Fang *et al.*., "Mechanism of lithium storage in MoS 2 and the feasibility of using Li 2S/Mo nanocomposites as cathode materials for lithium-sulfur batteries," *Chem. - An Asian J.*, vol. 7, no. 5, pp. 1013–1017, 2012, doi: 10.1002/asia.201100796.

[127] C. Zhao *et al.*., "Self-Assembly-Induced Alternately Stacked Single-Layer MoS2 and N-doped Graphene: A Novel van der Waals Heterostructure for Lithium-Ion Batteries," *ACS Appl. Mater. Interfaces*, vol. 8, no. 3, pp. 2372–2379, 2016, doi: 10.1021/acsami.5b11492.

[128] K. Shiva, H. S. S. Ramakrishna Matte, H. B. Rajendra, A. J. Bhattacharyya, and C. N. R. Rao, "Employing synergistic interactions between few-layer WS2 and reduced graphene oxide to improve lithium storage, cyclability and rate capability of Li-ion batteries," *Nano Energy*, vol. 2, no. 5, pp. 787–793, 2013,

doi: 10.1016/j.nanoen.2013.02.001.

[129] R. Chen *et al.*., "Free-Standing Hierarchically Sandwich-Type Tungsten Disulfide Nanotubes/Graphene Anode for Lithium-Ion Batteries," *Nano Lett.*, pp. 1–6, 2014.

[130] L. Zhou, S. Yan, L. Pan, X. Wang, Y. Wang, and Y. Shi, "A scalable sulfuration of WS2to improve cyclability and capability of lithium-ion batteries," *Nano Res.*, vol. 9, no. 3, pp. 857–865, 2016, doi: 10.1007/s12274-015-0966-9.

[131] J. Xu, J. Zhang, W. Zhang, and C. S. Lee, "Interlayer nanoarchitectonics of two-dimensional transition-metal dichalcogenides nanosheets for energy storage and conversion applications," *Advanced Energy Materials*, vol. 7, no. 23. pp. 1–30, 2017, doi: 10.1002/aenm.201700571.

[132] G. Huang *et al.*., "Hierarchical architecture of WS2 nanosheets on graphene frameworks with enhanced electrochemical properties for lithium storage and hydrogen evolution," *J. Mater. Chem. A*, vol. 3, no. 47, pp. 24128–24138, 2015, doi: 10.1039/c5ta06840a.

[133] H. Hwang, H. Kim, and J. Cho, "MoS2 nanoplates consisting of disordered graphene-like layers for high rate lithium battery anode materials," *Nano Lett.*, vol. 11, no. 11, pp. 4826–4830, 2011, doi: 10.1021/nl202675f.

[134] G. Du, Z. Guo, S. Wang, R. Zeng, Z. Chen, and H. Liu, "Superior stability and high capacity of restacked molybdenum disulfide as anode material for lithium ion batteries," *Chem. Commun.*, vol. 46, no. 7, pp. 1106–1108, 2010, doi: 10.1039/b920277c.

[135] H. Liu, D. Su, R. Zhou, B. Sun, G. Wang, and S. Z. Qiao, "Highly ordered mesoporous MOS2 with expanded spacing of the (002) crystal plane for ultrafast lithium ion storage," *Adv. Energy Mater.*, vol. 2, no. 8, pp. 970–975, 2012, doi: 10.1002/aenm.201200087.

[136] Y. Wang, L. Yu, and X. W. (David) Lou, "Synthesis of Highly Uniform Molybdenum–Glycerate Spheres and Their Conversion into Hierarchical

MoS2Hollow Nanospheres for Lithium-Ion Batteries," *Angew. Chemie - Int. Ed.*, vol. 55, no. 26, pp. 7423–7426, 2016, doi: 10.1002/anie.201601673.

[137] H. Luo, L. Zhang, and L. Yue, "Synthesis of MoS 2/C submicrosphere by PVP-assisted hydrothermal method for lithium ion battery," *Adv. Mater. Res.*, vol. 531, pp. 471–477, 2012, doi: 10.4028/www.scientific.net/AMR.531.471.

[138] Q. Chen, F. Lu, Y. Xia, H. Wang, and X. Kuang, "Interlayer expansion of few-layered Mo-doped SnS2 nanosheets grown on carbon cloth with excellent lithium storage performance for lithium ion batteries," *J. Mater. Chem. A*, vol. 5, no. 8, pp. 4075–4083, 2017, doi: 10.1039/c7ta00236j.

[139] N. Yabuuchi, K. Kubota, M. Dahbi, and S. Komaba, "Research development on sodium-ion batteries," *Chem. Rev.*, vol. 114, no. 23, pp. 11636–11682, 2014, doi: 10.1021/cr500192f.

[140] Y. Liu *et al.*., "TiS2 nanoplates: A high-rate and stable electrode material for sodium ion batteries," *Nano Energy*, vol. 20, pp. 168–175, 2016, doi: 10.1016/j.nanoen.2015.12.028.

[141] Z. Hu *et al.*., "MoS2Nanoflowers with Expanded Interlayers as High-Performance Anodes for Sodium-Ion Batteries," *Angew. Chemie - Int. Ed.*, vol. 53, no. 47, pp. 12794–12798, 2014, doi: 10.1002/anie.201407898.

[142] X. Wang, X. Shen, Z. Wang, R. Yu, and L. Chen, "Atomic-scale clarification of structural transition of MoS2upon sodium intercalation," *ACS Nano*, vol. 8, no. 11, pp. 11394–11400, 2014, doi: 10.1021/nn505501v.

[143] Y. Li, Y. Liang, F. C. Robles Hernandez, H. Deog Yoo, Q. An, and Y. Yao, "Enhancing sodium-ion battery performance with interlayer-expanded MoS2-PEO nanocomposites," *Nano Energy*, vol. 15, pp. 453–461, 2015, doi: 10.1016/j.nanoen.2015.05.012.

[144] L. David, R. Bhandavat, G. Singh, and D. E. T. Al, "MoS 2 / graphene Composite Paper For Sodium-Ion Battery Electrodes - Supporting Information," no. Xx, pp. 1–17, 2014.

[145] P. R. Kumar, Y. H. Jung, and D. K. Kim, “High performance of MoS2 microflowers with a water-based binder as an anode for Na-ion batteries,” *RSC Adv.*, vol. 5, no. 97, pp. 79845–79851, 2015, doi: 10.1039/c5ra16297a.

[146] X. Xie, T. Makaryan, M. Zhao, K. L. Van Aken, Y. Gogotsi, and G. Wang, “MoS2 Nanosheets Vertically Aligned on Carbon Paper: A Freestanding Electrode for Highly Reversible Sodium-Ion Batteries,” *Adv. Energy Mater.*, vol. 6, no. 5, pp. 1–7, 2016, doi: 10.1002/aenm.201502161.

[147] Y. Liu, N. Zhang, H. Kang, M. Shang, L. Jiao, and J. Chen, “WS2 Nanowires as a High-Performance Anode for Sodium-Ion Batteries,” *Chem. - A Eur. J.*, vol. 21, no. 33, pp. 11878–11884, 2015, doi: 10.1002/chem.201501759.

[148] Z. T. Shi *et al.*, “*In situ* Carbon-Doped Mo(Se0.85S0.15)2 Hierarchical Nanotubes as Stable Anodes for High-Performance Sodium-Ion Batteries,” *Small*, vol. 11, no. 42, pp. 5667–5674, 2015, doi: 10.1002/smll.201501360.

2 Experimental Part

In this chapter, the fundamentals of the techniques used to characterize the materials in Chapters 3, 4 and 5 are discussed.

Powder X-ray diffraction was the principal method used for structural characterization, allowing the detection of impurities and secondary phases in the as-synthesized materials. Several spectroscopic techniques including Raman spectroscopy were used to provide extra information on the structure and properties of the materials analysed. Combined microscopic techniques such as scanning electron microscopy and energy-dispersive X-ray spectroscopy (SEM/EDX) and transmission electron microscopy (TEM) were used to gain an insight into the particle size, morphology, structure determination and elemental composition of these materials. Electrochemical studies such as galvanostatic cycling, impedance spectroscopy and cyclic voltammetry have been employed to study the materials' ion storage properties including specific capacity, cyclability, redox pairs and resistivity. Finally, synchrotron techniques (XANES and operando X-ray diffraction) were used to explore phase transition and oxidation state changes during ion intercalation and deintercalation.

2.1 Structural determination and characterisation techniques

2.1.1 Powder X-ray diffraction technique

Powder X-ray diffraction (PXRD) is a versatile and non-destructive characterisation technique used primarily for phase identification of crystalline materials (molecular and crystal structures), crystallinity and phase purity of a compound [1]. This technique also allows obtaining relevant crystallographic information on the lattice parameters, planar spacing and crystallite size of the crystals present in a sample. In this method, monochromatic X-rays irradiate the sample interacting with the electrons of the atoms of a crystal resulting in the formation of a diffraction pattern [2]. X-rays are produced in a device called an X-ray tube which consists of an evacuated chamber with a tungsten filament at one end (cathode) and a

metal target at the other end (anode). The most common anode used in in-house diffractometers is copper (Cu, K_α radiation ~ 1.542 Å). When electrical current is passed through the filament, excited electrons from the tungsten filament are emitted moving towards the anode target under an electric field. The electron produced (primary electrons) strike the target atoms in the material, dislodging the inner shell electrons (secondary electron). As a result, electrons from the outer shell (higher energy) move to fill the void in the inner shell (lower energy). This energy difference between electrons results in the emission of radiation in the form of high energy X-rays. The cathode-ray tube present in the equipment under a vacuum atmosphere then produces monochromatic radiation from the mix of X-rays generated, which is concentrated and directed toward the sample [3] (Figure 2.1).

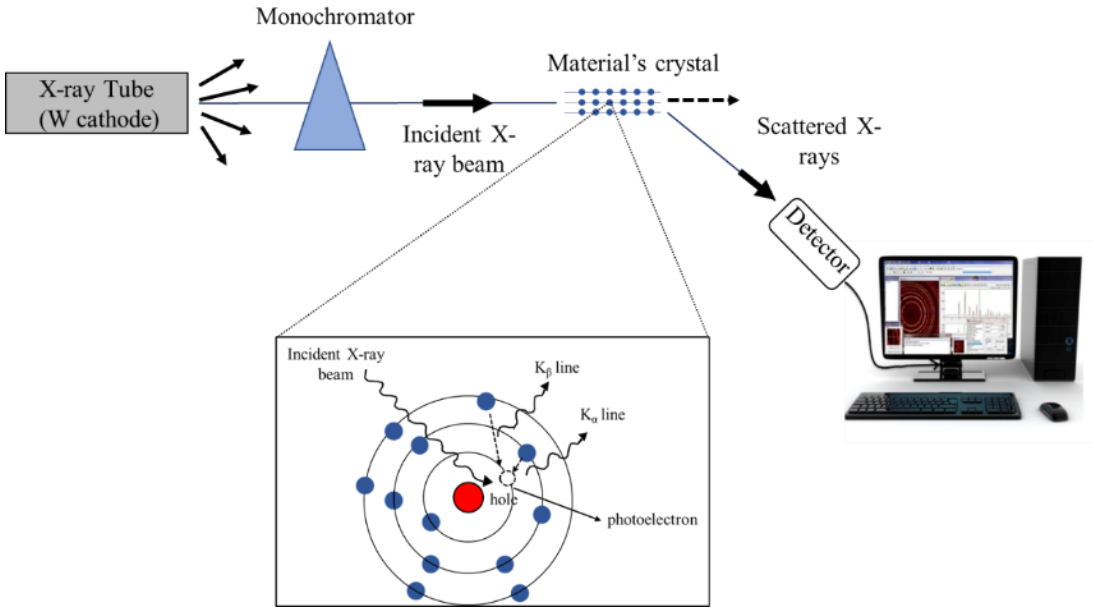

Figure 2.1 The mechanism of characteristic X-ray generation. Adapted from [1]

This technique is based on the interaction of monochromatic X-rays and a crystalline sample if the emitted X-rays are of the same order of magnitude as the spacing of the atomic planes (~ 0.1 – 10 Å). This interaction can be constructive or non-constructive depending on the nature of the material. In case that a non-constructive (destructive) interaction occurs, no structural information is obtained. Constructive interference occurs if Bragg's Law (Equation 2.1) is satisfied and a diffraction pattern of the crystal can be obtained reflecting the distances between planes of atoms measured by the intensity of the beam after colliding with the sample [1], [4]. This law relates the

wavelength of the incident X-ray beam (λ) with the distance between successive atomic planes in the crystal (d) and the angle of incidence of the beam (θ) in presence of a specific order of diffracted beams (n) [3], [4]. Constructive interference occurs if the difference in the path length ($2d$) between two waves interacting with successive planes of atoms is equal to an integer multiple n (λ) of the wavelength. A detector placed on the opposite side of the equipment records and detects the diffracted X-rays allowing its processing and the generation of a diffraction pattern [2] (Figure 2.2).

$$\lambda n = 2d_{hkl} sin\theta \quad (2.1)$$

Miller indices are the most extensive notation used to characterize crystal lattices [1]. These indices are written as h, k and l and allow to define the d-spacing or interplanar distance from the corresponding diffracting plane [5]. These are a symbolic vector representation for the orientation of an atomic plane within a crystal lattice and are the reciprocal of the fractional intercepts which the plane makes with the crystallographic axes [1].

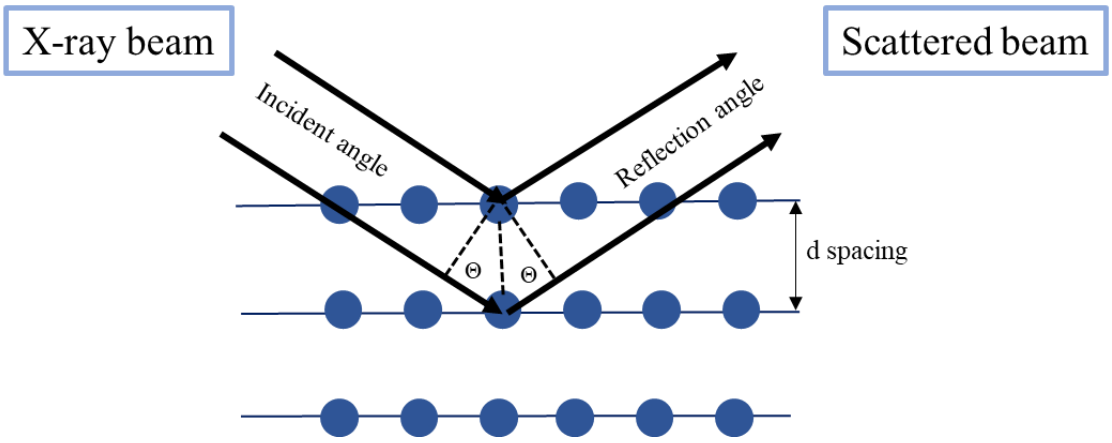

Figure 2.2 - A schematic depicting the constructive interference according to Bragg's Law. Adapted from [1].

A crystal is a highly ordered microscopic structure formed of atoms, molecules or ions. Each crystal structure is characterized by its unit cell, the smallest group of atoms within a crystal which the entire lattice is built by the repetition of the unit in three dimensions in a specific spatial arrangement [1]. The unit cell is defined by six parameters (cell constants): three dimensions (a, b, c) and three angles (α, β, γ), which are related to the geometry of the unit cell [1], [5]. The presence or absence of symmetry elements used

to build the unit cell leads to the existence of seven different independent unit cell shapes, called crystal systems (Table 2.1).

Table 2.1 The seven crystal systems and respective axes and angles restrictions [6]

Crystal System	Cell constants	Angles
Cubic	a = b = c	$\alpha = \beta = \gamma = 90°$
Rhombohedral (or Trigonal)	a = b = c	$\alpha = \beta = \gamma \neq 90°$
Tetragonal	a = b ≠ c	$\alpha = \beta = \gamma = 90°$
Hexagonal	a = b ≠ c	$\alpha = \beta = 90°$, $\gamma = 120°$
Orthorhombic	a ≠ b ≠ c	$\alpha = \beta = \gamma = 90°$
Monoclinic	a ≠ b ≠ c	$\alpha = \beta = 90°$, $\gamma \neq 90°$
Triclinic	a ≠ b ≠ c	$\alpha \neq \beta \neq \gamma \neq 90°$

Depending on the atoms' arrangement and packing within the crystal, different reflection patterns arise. The pattern formed by PXRD is unique for a specific compound as it is the reflection of the d-spacing present in the crystal [4]. Unknown samples can be identified by comparing the observed diffraction pattern against a reference diffractogram provided by a database organization. Several databases are available however the Inorganic Crystal Structure Database (ICSD) is the world's largest database for completely identified inorganic crystal structures, provided by FIZ Karlsruhe GmbH for the scientific community [7]. Relevant structural information can be found in these references. Analysis of the PXRD pattern allows determining unit cell parameters, atomic positions, atom occupancies, strain, preferential orientation, among others.

Two main full pattern methods can be employed for the determination of unit-cell parameters from polycrystalline diffraction data: the Rietveld and the Le Bail method.

The Rietveld method involves the computation of reflection intensities from a structural model, while the Le Bail approach refers to a whole-powder pattern decomposition method in which the space group and initial unit-cell parameters are also determined however the reflection intensities are treated as arbitrary unknowns [8].

The Rietveld quantitative analysis method is usually used to characterise the crystalline structure of a compound [9]. This method uses a least square approach to refine a theoretical line profile until it matches the measured profile, by gradually refining the unit-cell and structural parameters of the model used. Other parameters can be taken into account such as line widths, angular shifts, atomic displacement, etc [9]. This method is based on the fact that the intensity diffracted by a crystalline phase is proportional to the quantity of the diffraction material, with suitable corrections. The Le Bail method is usually applied to full patterns when structures are not known or are difficult to describe, such as with disordered structures [8]. The refinement of this parameters using either method provides the best agreement between observed and calculated diagrams including all structural and instrumental parameters

The parameter goodness-of-fit (χ^2) serves as a measure of the quality of the fit to a powder diffraction pattern, while the ratio of the weighted profile R-factor (R_{wp}) and expected R factor (R_{exp}) is a good measure of how well the data are fitted [10]. During the refinement process, the value of χ^2 starts large once the model is poor and decrease as the model produces agree more and more with the data. It should be noted that the smallest value which χ^2 can be equivalent is 1 and the smallest that R_{wp} can never be is R_{exp} [10], [11]. Indeed, the normalised χ^2 function can be calculated by the square of the ratio of R_{wp} and R_{exp} (Equation 2.2) [10]:

$$\chi^2 = \left(\frac{R_{wp}}{R_{exp}}\right)^2 \tag{2.2}$$

To do an appropriate Rietveld refinement, the powder diffraction data must be collected appropriately. Geometry of the diffractometer, most suitable radiation (conventional X-rays, synchrotron X-ray or neutron) and necessary counting time are just some of the factors to consider before data collection [12]. Heavily absorbing samples can be a problem when data is collected in a transmission set-up due to the incident beam penetrating the sample or when the surface roughness is not considered when in

reflection geometry. In both cases, errors can happen to lead to anomalously low thermal parameters in the refinement [12].

PXRD data of the as-prepared material were collected at ambient temperature using a Smartlab diffractometer (Rigaku Corporation) equipped with a 9 kW Cu rotating anode (λ= 1.54056 Å) and a D/teX-ULTRA 250 high-speed position sensitive detector system. For the measurement, samples were loaded into borosilicate capillaries (0.6 mm diameter) in an Ar-filled glovebox (MBraun; (H_2O and O_2 < 0.1 ppm), then capillaries were removed from the glovebox and immediately flame-sealed in air. Data were collected in the 10-90° 2θ range at a scan rate of 0.1° min^{-1}. Crystallographic data were fit with the Rietveld and Le Bail method [13] using the GSAS software suite with the EXPGUI and Fullprof [14] software interface [15].

2.2 Electron Microscopy

2.2.1 Field-emission scanning electron microscopy and Energy-dispersive X-ray spectroscopy

Field-emission scanning electron microscopy (FESEM) is a type of surface electron microscopy that produces images of a specimen surface by hitting it with a focused high-energy electron beam. A beam of electrons is produced by an electron gun at the top of the microscope in the cathode (generally tungsten) and accelerated towards the sample at high voltage (0.2 – 30 kV). An electric field is then created between the cathode and anode within a vacuum atmosphere. The electron beam is then focused by a condenser and passes through several scan coils and objective lens which deflect the beam to scan the surface of the sample [16] (Figure 2.3). The electrons interact with the sample producing secondary electrons, backscattered electrons, Auger electrons and X-rays. Primary electrons hit the material, interacting with the sample, and causing the displacement of inner electrons (secondary electrons.) In FESEM, the surface of a material is investigated using two types of signals, secondary and backscattered electrons. Both types of electrons are constantly being produced from the surface of the specimen however they result in two separate types of interaction [16]. Secondary electrons result from inelastic collision and scattering of incident electrons with the specimen electrons. Characterized by their low energies (less than 50 eV), these

electrons are mainly used to reveal the surface structure of the material with a resolution of around 10 nm. On the other hand, backscattered electrons are a result of an elastic collision and scattering event occurring between the incident electrons and specimen electrons and nuclei. This type of electrons can be generated further from the surface and provide a topographical contract and atomic number contrast of the sample with a resolution of > 1 micron [16].

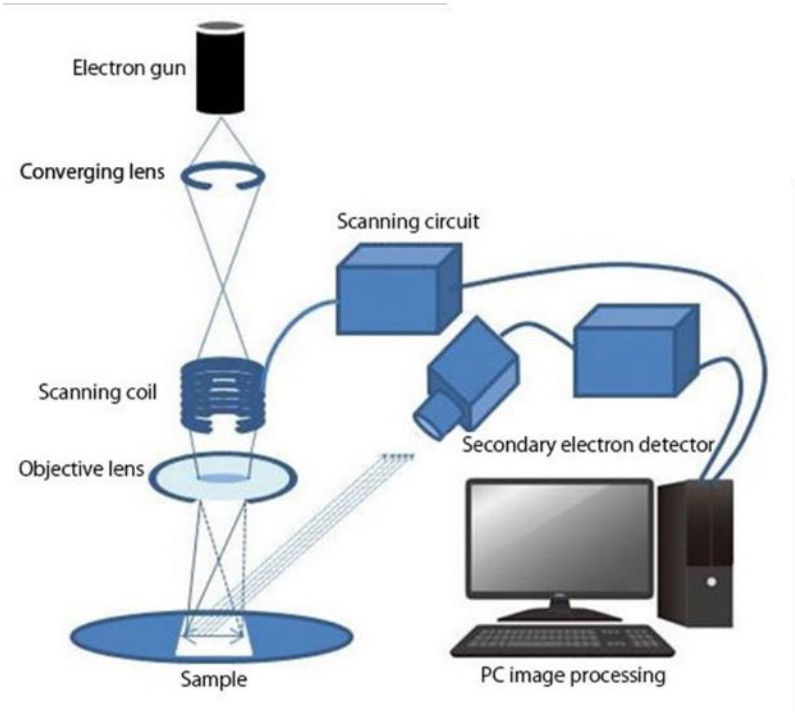

Figure 2.3 - A schematic of a typical SEM instrument with a secondary electron detector [17]

Electrons are detected in a detector located above the sample stage inside the specimen chamber. Specimens are usually mounted and secured onto the stage inside the staging chamber and is controlled by a goniometer which allows xyz movements in a 360° rotation and 90° tilt. The electrons are then detected forming an image of the specimen. Backscattered electrons are considered high-energy electrons as they result of elastic interactions between primary beam electrons and specimen electrons and need a circular type detector to be detected. Once the beam hits the sample, signals are ejected from it as a result of the electron-sample interaction containing information about the sample's surface topography such as morphology and structure [16].

Energy-dispersive X-ray spectroscopy (EDX) is a microanalytical technique used to obtain information about the chemical composition of a sample (qualitative and quantitative) [18]. EDX relies on the interaction of an electron beam with a sample. When electrons interact with the sample, electrons from the inner electronic shells are displaced, leading to their ejection, and creating a vacancy in the shell where the electron was [18]. This state is unstable and therefore an electron from a higher-level fall, filling that gap and the energy difference is released in the form of an X-ray which is characteristic for the element present in the sample [18]. EDX X-ray detectors measure the energy and number of emitted x-rays and data can be presented as a spectrum of the X-ray counts against energy, a line profile or an elemental map. Mapping and line profiles allow determining the elements and their distribution within a sample if the elemental composition of the sample is priorly known.

In this work, the microstructure of the as-synthesised material was characterised using scanning electron microscopy (SEM) (JEOL JSM-7800f, Japan) operating at 10.0 kV. Elemental analysis was performed using Energy Dispersive X-ray Spectroscopy (EDX) (Oxford Instruments, UK) at 12.0 kV. Samples were prepared by coating a uniform layer of the material onto carbon conductive tape.

2.2.2 High-resolution transmission electron microscopy

High-resolution transmission electron microscopy (HRTEM) is a microscopy technique used to assess crystal size and morphology, crystal orientation, surface structures and crystal defects of samples [19]. One of the main advantages of this technique is that it can directly show local structures on an atomic scale or a nanometer scale. Four parameters affect the amount and scale of information that can be extracted from TEM: i) the resolving power of the microscope, ii) the energy spread of the electron beam, iii) the thickness of the sample and iv) the composition and stability of the sample [20]. Parameters i) and ii) are mainly money dependent as the more expensive the better the microscope parameters. Averages microscopes have a resolving power smaller than 0.3 nm and an energy spread in the range of several eV which can be adapted to most of the samples analysed [20]. The thickness of the sample influences

the quality of results obtained and is usually correlated to the experimental skills of the person preparing the samples, the more experienced, the better the preparation of the sample and as a consequence the data quality. On the other hand, the stability of the sample depends on the choice of the system studied, depending on the charge capacity of the sample, the compound may or not react under the beam leading to worse quality data [20]. This technique requires the use of an electron beam that is transmitted through a specimen (usually less than 100 nm thick). The electron is usually produced in a tungsten wire shaped like a hairpin (filament) or a crystal of lanthanum hexaboride, and accelerated under vacuum by a high voltage electric field (200 – 300 kV) away from the filament and focused by a magnetic lens [21]. The electrons that are transmitted through the sample are magnified by lenses and detected by a fluorescent screen/camera to form an image (Figure 2.4).

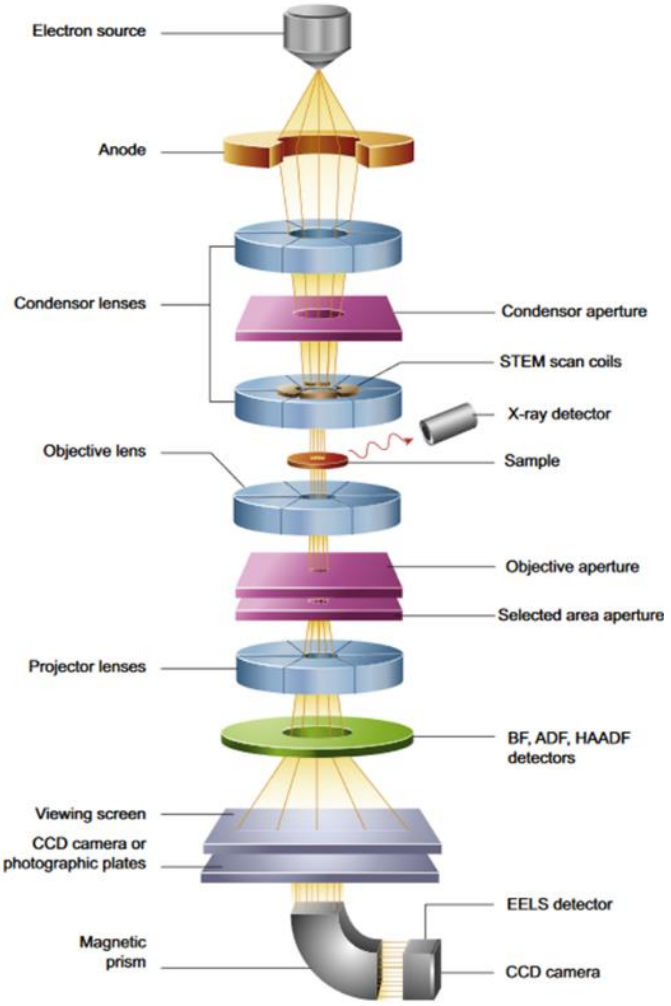

Figure 2.4 - A schematic of a typical TEM instrument [22]

The contrast in TEM images depends mainly on three aspects: (i) the geometry of the electron illumination, (ii) the electron scattering within the specimen and (iii) the path of the transmitted electrons through the post specimen area (lenses, apertures and detection system) [22]. Two types of TEM can be distinguished depending on the way the specimen is addressed: conventional TEM (CTEM) and scanning TEM (STEM). CTEM is a wide-beam technique that consists of a close-to-parallel electron beam flooding the entire area of interest. In this type, the data are collected in parallel and the image acquired is formed by an imaging (objective) lens after the thin specimen (around 106 pixels) [20]. In STEM, a finely focused beam formed by a probe forming lens located before the specimen addresses each pixel in series as the probe scans the specimen (a fine spot with the typical spot size 0.05 – 0.2 nm) [22]. In both types, information related to a small region is collected which depends on the diameter of the beam and thickness of the specimen [20]. The STEM mode is the most used TEM type as it allows to carry out sequential chemical analysis across areas of the specimen.

In this thesis, high-resolution transmission electron microscopy (HR-TEM) was performed using an EFTEM Jeol 2200 FS microscope (Jeol, Japan). A 200 keV acceleration voltage was used for measurement. Elemental maps and EDX spectra were acquired with SDD detector X-MaxN 80 TS from Oxford Instruments (England). Sample preparation was attained by drop-casting the suspension (1 mg mL^{-1} in water) on a TEM grid (Cu; 200 mesh; Formvar/carbon) and dried at 60 °C for 12 h.

2.3 Spectroscopic Techniques

2.3.1 Raman Spectroscopy

Raman spectroscopy is a non-destructive complementary method to infrared spectroscopy that provides information about crystalline structure and crystallinity of macromolecules as well as changes of inorganic solids and polymeric structures in membranes [23]. This analytical technique is used to observe low-frequency modes such as rotational and vibrational modes [24], providing a structural fingerprint by which molecules can be identified [23]. Two types of light scattering can result from the irradiation of a molecule with monochromatic light: elastic (Rayleigh) and inelastic

(Raman) scattering. In elastic or Rayleigh scattering, no changes in photon frequency, wavelength or energy occurs. In this process, when the light focuses on a molecule, an interaction with the molecule occurs but no net exchange of energy occurs ($E = E_0$) [25]. This type of scattering does not provide useful structural information about the material.

The principle of Raman is based on the inelastic scattering of photons (Raman scattering or Raman effect) of monochromatic laser light that ranges from visible to near-ultraviolet [24]. Raman scattering is the result of the light scattering (1×10^{-7} %) of laser light onto the sample which results in a transfer of energy between the excitation light and the sample [26]. A shift in energy results from the photon excitation in the molecules from the ground state to an excited energy state [24]. The emission and return of a photon to the ground state are done in a different rotational or vibrational state, once the light scattered possesses a different frequency from that of the incident light [23]. This difference in frequency is associated with a change in source-induced molecule dipole moment (polarization) known as inelastic scattering [24]. This change in the molecular polarization potential (either gain or loss of energy) concerning the initial vibrational coordinate is essential for a molecule to exhibit a Raman effect [26]. If an energy vibrational gain is observed, then the frequency of the scattered light will be higher than that of the incident light ($E = E_0 + E_v$) and is known as anti-Stokes Raman scattering. Contrarily, if the interaction causes a molecular energy gain, then the frequency of the scattered light will be lower than that of the incident light ($E = E_0 - E_v$) and is known as Stokes Raman scattering [25] (Figure 2.5). The intensity of the anti-Stokes line is usually much less intense compared with the Stokes signal; this is because only molecules that are vibrationally excited before irradiation can give rise to anti-Stokes lines. For that reason, only the more intense Stokes lines are measured in Raman spectroscopy.

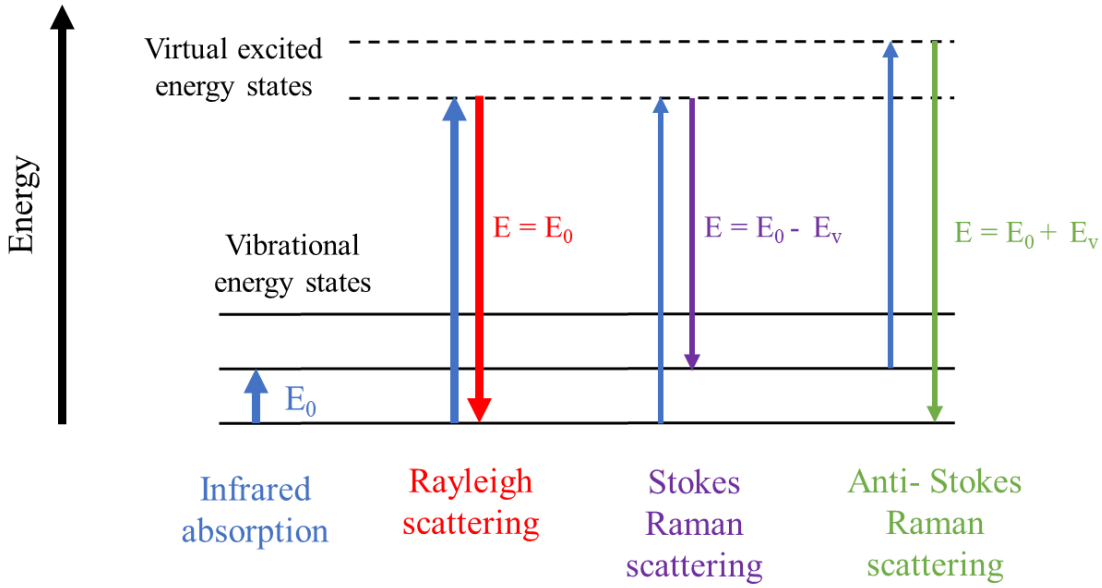

Figure 2.5 - Schematic diagram of the Rayleigh and Raman phenomena in terms of energy transfer. Adapted from [27]

The magnitude of the Raman effect on a molecule is correlated with the polarizability of the electrons in that molecule. If a molecule has a change in polarizability during the vibration, then it can be considered as Raman active [26]. The number of molecules in each energy level scattered during the process is proportional to the intensity of the Raman signal and follow the Boltzmann distribution (Equation 2.3):

$$\frac{N_1}{N_2} = \left(\frac{g_1}{g_2}\right) e^{\frac{-\Delta E}{KT}} \tag{2.3}$$

where N_1 and N_2 represent the number of molecules in the higher and lower energy level, respectively, g_1 and g_2 are the degeneracy of higher and lower energy levels, ΔE represents the change in energy during the scattering process, K is the Boltzmann's constant (1.380649×10^{-23} J K^{-1}) and T stands or the temperature (in K) [26].

A Raman spectrum relates to the intensity of the scattered light with the reciprocal of the wavelength, called wavenumber [28]. The frequency shift in the spectrum of scattered light compared to the incident light is known as the Raman shift (cm^{-1}) and is determined by Equation 2.4:

$$Raman\ shift = \left(\frac{1}{\lambda_{incident}} - \frac{1}{\lambda_{scattered}}\right) x\ 10^{-7} \quad (2.4)$$

where, $\lambda_{incident}$ and $\lambda_{scattered}$ represent the wavelengths of the incident light and scattered light (nm), respectively. The wavenumber is usually correlated in a linear way to the energy of the incident and scattered light, turning the Raman shift independent of the incident wavelength [28].

2.4 Electrochemical Methods

To assess the electrochemical properties of the anode materials described in this thesis, various electrochemical techniques such as galvanostatic cycling, cyclic voltammetry and electrochemical impedance were used.

2.4.1 Galvanostatic cycling

Secondary batteries are defined by their ability to discharge and charge multiple times. The number of complete discharge-charge cycles that a battery cell can perform within 80 % of its original nominal capacity, is given the name of cycle life [29]. There are two ways to discharge and charge a battery cell, either by applying a constant current (called galvanostatic cycling) or by applying a constant potential (referred to as potentiostatic cycling), however, the first one is generally preferred [29], [30].

Galvanostatic cycling characterization is a very useful method to assess the electrochemical performance of an electrode [29]. This method determines the amount of charge stored within an electrode (specific capacity) as well as its voltage profile, life expectancy and stability [29]. The specific capacity (mAh g^{-1}) of an electrode can be obtained by the following Equation:

$$\text{Specific Capacity} = \frac{\text{Current Density } (mA) \text{ x Max duration of (dis)charge (h)}}{\text{Amount of active material (g)}} \quad (2.5)$$

In anode materials, galvanostatic cycling measurements consist of applying a negative specific current to a battery cell until it reaches a minimum value of voltage or capacity

(discharge process), the moment when the sign of the current is inverted, and the cell starts to charge [31]. This current value is often expressed as mA/g, being *g* the amount of active material present in the electrode. Alternatively, the current can also be expressed in terms of the C-rate, where 1 C represents the theoretical amount of charge or discharge that can be obtained in one hour [29].

The maximum voltage that certain material can be charged to is usually called high cut-off potential. This value represents the maximum allowable voltage of a specific material and generally defines the "empty" state of the battery (or fully charged state) [32]. By contrast, the minimum is usually called low cut-off potential. The voltage response of the cell gives us information about the kinetics and electrochemical reactions that are taking place in the system, as well as the cell's load capability [31]

In a two-phase electrochemical reaction, depending on the overall composition of the system, two different variations of the electrical potential can be ascribed, plateau and slope [31]. The potential plateau (segment α+β and β+ γ in Figure 2.6) appears at the point where the charge or discharge reaction leads to the formation of a new phase on one of the electrodes [31]. At that moment, the co-existence of the two species forces the potential of the cell to remain the same if both the initial and final phase exists in the electrode [31]. The slope (segment α, βand γ in Figure 2.6) occurs when charging or discharging mechanisms led to the formation of a non-stoichiometric compound and gradual change of its compositions. In that case, just one of the species exists on the electrode being characterised by a change in the potential over time [31].

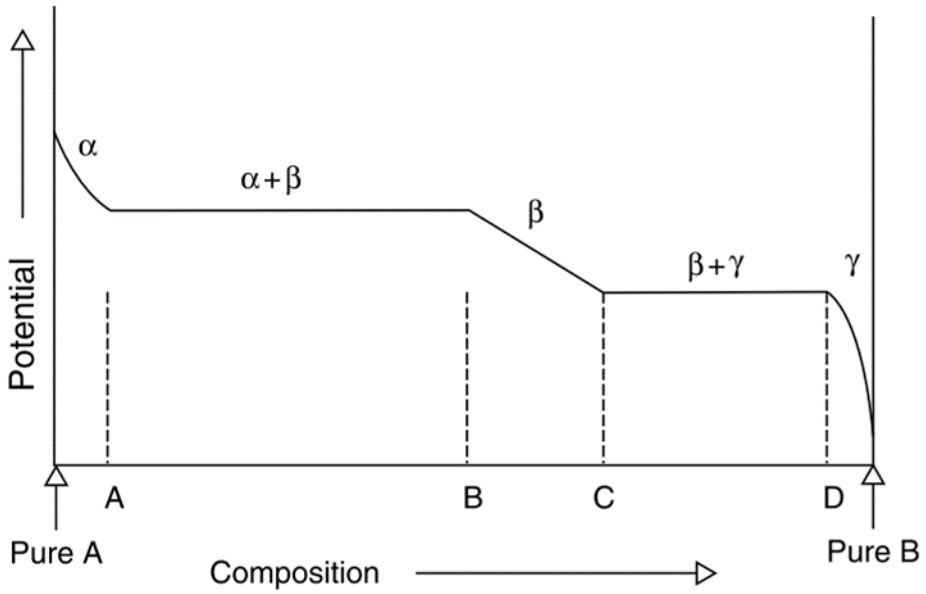

Figure 2.6 - Schematic variation of electrical potential with composition across the binary phase diagram [31]

The total amount of electrical energy that a battery can deliver is directly related to the cell's voltage and capacity, which depend on the chemistry of the system.

The energy stored in a specific system can be described in terms of energy density and volumetric density. Gravimetric energy density is described as the energy stored per mass unit and defines battery capacity in weight (Wh kg^{-1}), while volumetric density or energy density is related to the energy stored per volume unit (Wh l^{-1}) [33]. Along with the energy consumption of a system, it determines the battery weight or volume required to achieve a given electric range [33]. This value is directly related to the electrochemical capacity and operation potential of the battery being used as a characteristic of the battery chemistry and packaging [33]. The value of the gravimetric energy density (or specific energy) (*Eg*) of a half-cell is calculated from the chemical cell information and the weights of the reactants using the following Equation:

$$Eg = \frac{v\ x\ m_a\ x\ C}{\sum w_i} \tag{2.6}$$

Where v represents the average cell operating voltage (V), m_a the area of active material (in g cm^{-2}), C (mAh g^{-1}) represents the capacity and w_i area of individual cell components (in g cm^{-2}).

The stability in each cycle of a battery can be calculated by the ratio between the specific capacity obtained during the charge and the one obtained during discharge and it is given the name of Coulombic efficiency [34]. A value of 1 (or 100 % in percentage) means that the capacity obtained during intercalation and de-intercalation of ions (discharge and charge process) is the same, indicating perfect reversibility of the electrochemical process [30].

In this thesis, the electrochemical properties of each material were assessed by using stainless steel (2032-type) coin cells (Tob Energy) with a Belleville spring, a stainless-steel spacer disk (1 mm thickness), a plastic gasket and a glass microfiber separator (Whatman). Electrode preparation and coin cell assembly were carried out in an Argon-filled atmosphere glovebox (H_2O < 0.1, O_2 < 0.1 ppm).

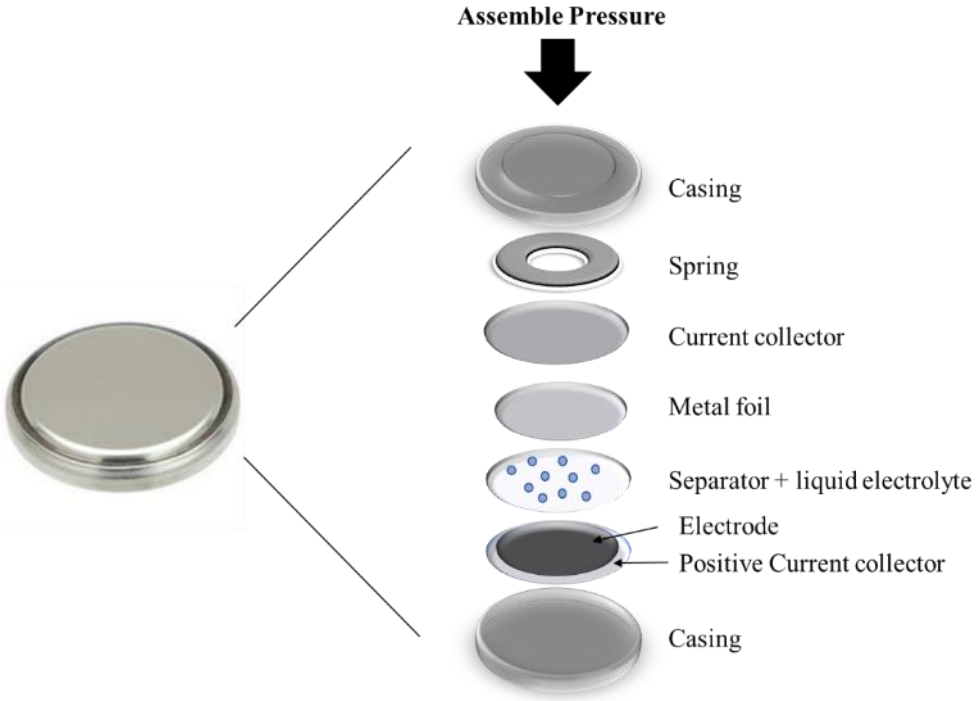

Figure 2.7 - Schematic illustration of the coin cell assembly.

Electrode slurries (300 mg total) were prepared by mixing 70 wt % active material (electrode), 20 wt % carbon black (> 99.0 %, Alfa Aesar) and 10 wt % polyvinylidene fluoride (PVDF, Kynar) (> 99.0 %, Alfa Aesar) and then adding ca. 1.6 ml of N-Methyl-2-pyrrolidone (NMP) (anhydrous, > 99.0 %, Sigma Aldrich) to the mixture. Slurries were left under constant stirring for 7 h and then cast onto aluminium or copper foil using a doctor blade (TOB-KTQ-150S) with an aperture of 30 µm in the glovebox. The film was dried in the antechamber of the glovebox at room temperature for 12 h under vacuum. Once dried, the film was pressed under 5 tons cm^{-2} and electrodes of 19 mm diameter were punched out of the film using a disc cutter. The electrodes were prepared with a typical active material mass loading of 1.5 –2.6 mg cm^{-2}. Metal disks of lithium or sodium (diameter of 14 mm) (Alfa Aesar Merck) were used as reference and counter electrode and 1M $LiPF_6$ or $NaPF_6$ (Sigma Aldrich) in the organic solution of ethylene carbonate/dimethyl or diethyl carbonate (EC: DMC or DEC, 1:1 v/v %, respectively) (Gotion) as the liquid electrolyte.

The electrolyte was dried for several days using activated molecular sieves (0.4 nm porosity, Merck) before use. Galvanostatic charge/discharge measurements were carried out on a Neware battery tester (Neware battery system, current range: 1mA-10mA, China) in the voltage window 0.1 – 3.0 V *vs* Li^+/Li or Na^+/Na at a various current rate (current density range: 10 mA g^{-1} – 500 mA g^{-1}).

2.4.2 Cyclic Voltammetry (CV)

Cyclic Voltammetry (CV) is a popular electrochemical technique commonly used to investigate and correlate the reduction and oxidation processes of species involved in a reaction with the change in the oxidation state of the transition metal present in the electrode [35]. This gives us information about the redox reactions happening during charge and discharge that can then be related to the galvanostatic profiles. This technique requires that the electrode is connected to a potentiostat to control the voltage/ potential applied to each electrode, in a specific range [36]. If the experiment consists of changing the electrode potential in only one direction and stop it is referred to as "linear sweep voltammograms" [36]. However, if the potential sweep

is reversed after reaching a certain value of potential and returns to the starting potential one or more times it is described as "cyclic voltammetry" [36].

During a CV experiment, the electrode potential is ramped linearly with time and the corresponding current is recorded [36], [37]. The type of graphs obtained by CV are called voltammograms or cyclic voltammograms. A typical CV voltammogram presents a series of positive and negative peaks usually associated with oxidation and reduction processes, respectively [37]

The equilibrium between two species A^+ and A can be described using the Nernst Equation (Equation 2.7). This Equation relates the potential of an electrochemical cell (E) to the standard potential of a species ($E^{0'}$) and the relative activities of the oxidized (A^+) and reduced (A) analyte in the system at the equilibrium [36]. For a one-electron reduction process from A^+ to A, activities can be replaced by the concentration of each analyte which is more experimentally accessible, and the standard potential (E^0) can be replaced with the formal potential ($E^{0'}$):

$$E = E^{0\prime} + \frac{RT}{F}\ln\frac{[A^+]}{[A]} \tag{2.7}$$

where *F* is the Faraday's constant (96 485 C mol^{-1}), *R* is the ideal gas constant (8.314 J K^{-1} mol^{-1}), *n* is the number of electrons exchanged and *T* is the temperature (in K). The Nernst Equation allows predicting how the system will respond to a change of concentration of species in solution or a change in the electrode potential [36]. The number of peaks that appear in each redox process will depend on the number of electrons exchanged in the electrochemical reaction. If the reaction is reversible, a symmetrical pair of redox peaks will appear when the potential is ramped in different directions in a redox reaction [36]. However, if the reaction is completely irreversible no peak will be produced when the direction is changed and an unsymmetrical voltammogram is shown. A middle ground between these two extreme cases can also be observed called a 'quasi-reversible' voltammogram [38] (Figure 2.8).

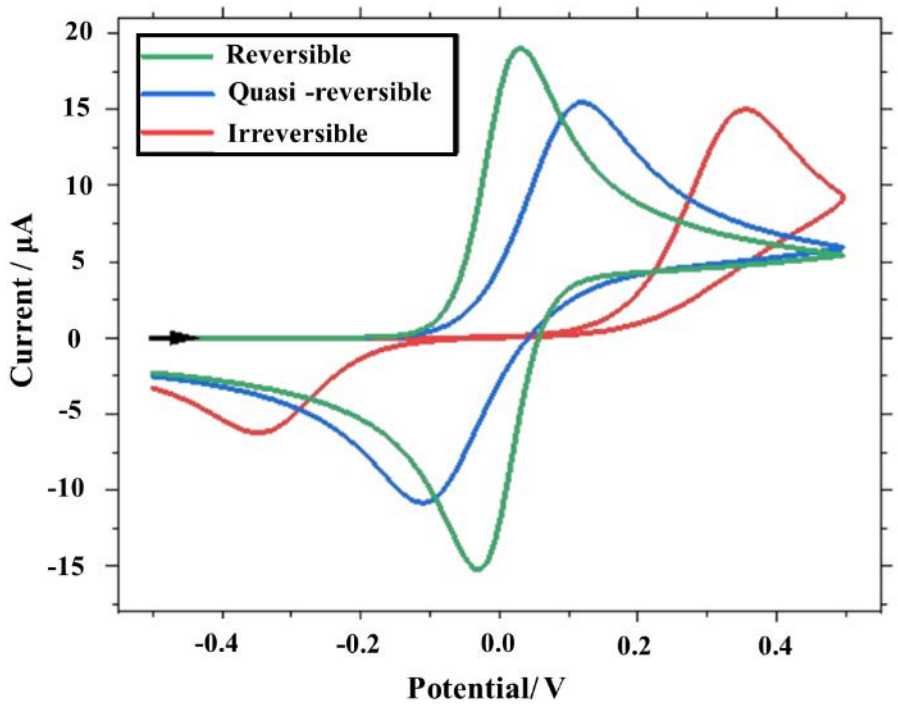

Figure 2.8 – Simulated CV curves of reversible, quasi-reversible and irreversible electron transfer reactions. Adapted from [38]

A crucial parameter to be aware of in CV experiments is the value of scan rate, which represents the change of potential as a function of time, in other words, controls how fast the applied potential is scanned [29]. The relationship between the peak current (i_p) and the square root of scan rate (v) is linear if the electron transfer process happening involves free diffusing redox species and that information can be obtained by the Randles-Sevcik Equation:

$$i_p = 0.446nFAC^o \left(\frac{nFvD_o}{RT}\right)^{1/2} \quad (2.8)$$

where n is the number of electrons transferred during the redox reaction, *F* is the Faraday constant (96485 C mol^{-1}), *A* is the electrode surface area in cm^2, D_o is the diffusion coefficient in $cm^2\ s^{-1}$, *C* is the concentration of the analyte in a molar, *R* is the gas constant (8.314 J K^{-1} mol^{-1}) and *T* is the temperature in K [29]. In ion batteries, the

Randles-Sevcik Equation can be adapted to determine the diffusion coefficient within the compound studied [35], [39]–[41].

Correlations between current, scan-rate and potential can also be obtained using a CV technique allowing a better understanding of the electrochemical reaction occurring in the system [35]. Equation 2.9 expresses the power law which current obeys:

$$i = av^b \tag{2.9}$$

where i represents the current (A), v is the scan rate (mV s^{-1}) and b represents an adjustable value. Depending on the scan rate used, two boundary conditions should be considered to obtain the exact diffusivity of the ion: (i) a semi-infinite diffusion process (fast scan-rate) and (ii) a finite diffusion process (slow scan-rate) [29], [37]. The value of b can be explained as the sum of the diffusion-controlled (Faradaic) and capacitive (non-Faradaic) currents within the material [29], [35]. Depending on the type of electrochemical reactions occurring in the electrode, b can have values between 0.5 (diffusion-controlled reaction) and 1.0 (capacitive reaction) [29], [35]. The value of b can this way be obtained by the variation of the scan-rate experiment and can be compared to the diffusivity of ions. In case that only diffusion-controlled reactions occur, the observed current is proportional to the square root of the scan rate. On the other hand, the capacity current follows linearly to the scan rate (Equation 2.10):

$$|i_c| = AC_d v \tag{2.10}$$

where i_c is the current for the capacitive current, A is the surface area of the electrode, C_d represents the capacitance of electric double-layer and v the scan rate. The above equation shows that the capacitive current is proportional to the scan rate, therefore this is dominantly measured at a fast scan rate, while a diffusion-controlled reaction is recorded at a slow scan rate [29].

In this work, cyclic voltammetry was performed in a two-electrode system using Li or Na metal and the anode material as the working electrode. The experiments were conducted using an Iviumstat instrument (Ivium model, Alvatek, UK), at a scan rate of 0.1 mV s^{-1} and a voltage step of 0.1 mV in the voltage window 0.1 – 3.0 V *vs* Li^+/Li or Na^+/Na.

2.4.3 Electrochemical Impedance Spectroscopy (EIS)

Electrochemical impedance spectroscopy (EIS) is an important experimental technique used to test the inner resistance of ion batteries. EIS is an excellent tool to analyse interfacial processes and variations in internal resistance. In batteries, this technique is mostly used to study the electrochemical processes occurring within the electrode (bulk) and at the electrode-electrolyte interface [42]. The fast, accurate and non-destructive nature of this method makes it ideal for the modelling and diagnosis of batteries [42].

Electrical resistance (R) is the ability of a circuit element to resist the electrical current flow and is defined by Ohm's Law (Equation 2.11) as a ratio between voltage (V) and current (I) [43], [44].

$$R = \frac{V}{I} \tag{2.11}$$

If this relationship is verified, the circuit is limited to a single element – an ideal resistor [43]. However, most electrical circuits are more complex and do not verify this law, leading us to adopt the concept of impedance to analyse them [42], [44]. Like resistance, impedance measures the ability of a circuit to resist the flow of electrical current [44]. Electrochemical impedance (Z) is the response of an electrochemical system (cell or battery) to an applied potential. In this technique, an AC (Alternating Current) potential is applied to an electrochemical cell and the current that passes through that cell is measured [45]. EIS consists of the application of a small excitation signal (between 1 and 10 mV) that destabilizes the electrode's charge state from a given steady-state [43]. Changes in ion transport and charging mechanisms of different time scales, response times and frequencies result from this small deviation allowing us to explore charging kinetics in battery electrodes in a non-destructive and easy-to-use experiment. By measuring the AC equivalent of the Ohmic resistance in a DC circuit, several frequency-dependent conduction processes can be studied [44]. In impedance spectroscopy, the internal resistance, inductance and capacitance of a sample can be measured in a wide range of frequency (10^{-2} to 10^{7} Hz) [44].

The current response to a sinusoidal potential will be a sinusoid at the same frequency but shifted in phase [44]. The frequency dependence of conductivity in most circuits leads to a phase shift (Ø) between the applied potential E(t) and the resulting current I(t) [43]. For this reason, the response of systems is pseudo-linear and always frequency-dependent [44]. Two components can be determined using impedance: resistive and reactive (capacitive/resistive) components [46]. Depending on the region of the sample studied different elements placed in parallel or series are used. In energy storage devices, the electrolyte region is usually characterized by a resistance (R), the existence of an electrical double layer on the interphase between the electrode and the electrolyte led to a capacitor (C), while diffusion mechanisms result in a Warburg (W) impedance. The product of RC results in the characteristic relaxation time or time constant (τ) of each element of the circuit. Impedance can then be expressed in terms of magnitude (Z_0) and a phase shift (Ø) through the following Equation [43]:

$$Z = \frac{E_t}{I_t} = \frac{E_0 \sin(wt)}{I_0 \sin(wt + \emptyset)} = Z_0 \frac{\sin(wt)}{\sin(wt + \emptyset)} \quad (2.12)$$

Using Euler's relationship (Equation 2.13), each sinus can be represented by a complex exponential, giving a real and an imaginary part of the impedance [43]:

$$Z = Z_0 \exp(i\emptyset\emptyset) = Z_0(\cos(\emptyset) + isin(\emptyset)) \quad (2.13)$$

Impedance data can then be represented in the form of an imaginary, Z'' (capacitive) against real, Z' (resistive) impedances by a 'Nyquist' plot [46]. In this plot, the conduction processes showing a phase shift between potential and current are represented as semicircles above the Z'' axis [46]. Low frequencies are usually on the right side of the arc and high frequencies on the left side [46] Analysis of the impedance spectrum from an electrochemical cell is typically approached by modelling data with an electrical circuit [44] (Figure 2.9). This circuit is usually described using simple components (resistors, inductors and capacitors) assembled in series or parallel [42]. The construction of a theoretical circuit allows fitting the data to the model to yield parameters for each circuit element [44]. The simplest way to model the electrochemical interface is to use the Randles circuit, where R_W represents the wiring resistance, whereas R_{CT} models the charge-transfer resistance [42]. R_W is measured in every experiment and is usually low compared to the inner device effects being located at high

frequencies [46]. R_{CT} is dependent on the voltage and is related to the state of charge of the electrode and consequent heterogeneous kinetics which gives information about the kinetic processes and double-layer capacitance of the cell [46]. The diffusion of the electroactive material in the electrode surface is modelled using a 'Warburg element' (W), which is placed in series with the R_{CT} [46]. The corresponding impedance spectrum of a cell consists of a semicircle at high frequency and a linear tail at low frequency [42]. The semicircle is attributed to the charge-transfer resistance (diameter = R_{CT}) whereas the intercept corresponds to the wiring resistance R_W [43]. The diffusion of ions into the bulk electrode material from the electrolyte is expressed by the linear tail in the graph and is dependent on W [43]. At high frequency (> 1 kHz), the spectra are mostly dominated by the electrolyte resistance [45]. The interpretation of the EIS frequencies, therefore, indicates the timescale of processes occurring in the electrochemical cell [42].

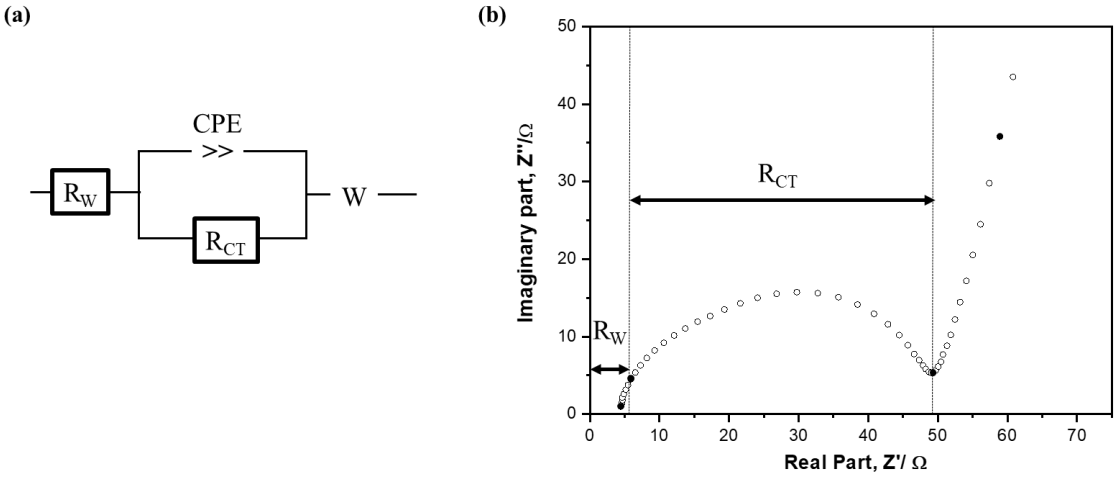

Figure 2.9 - a) Randles circuit with parameters shown. b) Simulated EIS Nyquist plot using the parameters in a).

Electrochemical impedance spectroscopy (EIS) measurements were conducted using an Iviumstat instrument (Ivium model, Alvatek, UK). Data were collected at OCV and at the end of discharge on the 1st, 2nd, 5th and 10th cycles. EIS spectra were obtained by performing at constant potential over a frequency range of 0.01 Hz to 100 kHz using an amplitude of the signal of 0.01 V in a current range of 10 mA.

2.5 Synchrotron-based techniques

Over the past few decades, synchrotron-based X-ray techniques have provided substantial information to better study the working mechanism of battery materials.

Synchrotron radiation consists of light (that can be 10 billion times brighter than the sun) generated by electrons travelling around a large circular accelerator. This radiation is based on a theorem of classic electrodynamics which says that if an electrically charged particle (electrons) changes direction at a relativistic speed (acceleration), the production and emission of electromagnetic radiation occurs as a narrow cone tangent to the path of the moving particle [47], [48]. Synchrotron facilities (Figure 2.10) are composed of: (i) an electron gun where the electrons are generated, (ii) a linear accelerator (or linac) and a booster which compose a series of three particle accelerators where the electrons are filled, accelerated, and (iii) a storage ring where the electrons travel close to the speed of light at final energy of about 1.5 – 8 GeV [47]–[49]. Particles maintain fixed energy as they are accelerated around the storage right by a radio frequency alternating field in a microwave cavity. Moving electrons creates a centrifugal acceleration generating electromagnetic radiation that covers a broad energy range (e.g. infrared, visible, ultraviolet and X-ray) [48]. Powerful magnets present in the storage ring force the electrons' path to bend, leading to a loss of energy in the form of light. This light is then channelled out of the storage ring and into the experimental stations (beamlines), the only part of the synchrotron accessible to scientists [48]. The beamlines contain three sections: (i) the optics hutch where the light is filtered and focused, (ii) the experimental hutch, where the experiment is carried out and the sample is placed and (iii) the control cabin, where the experiment is controlled by scientists [48], [49].

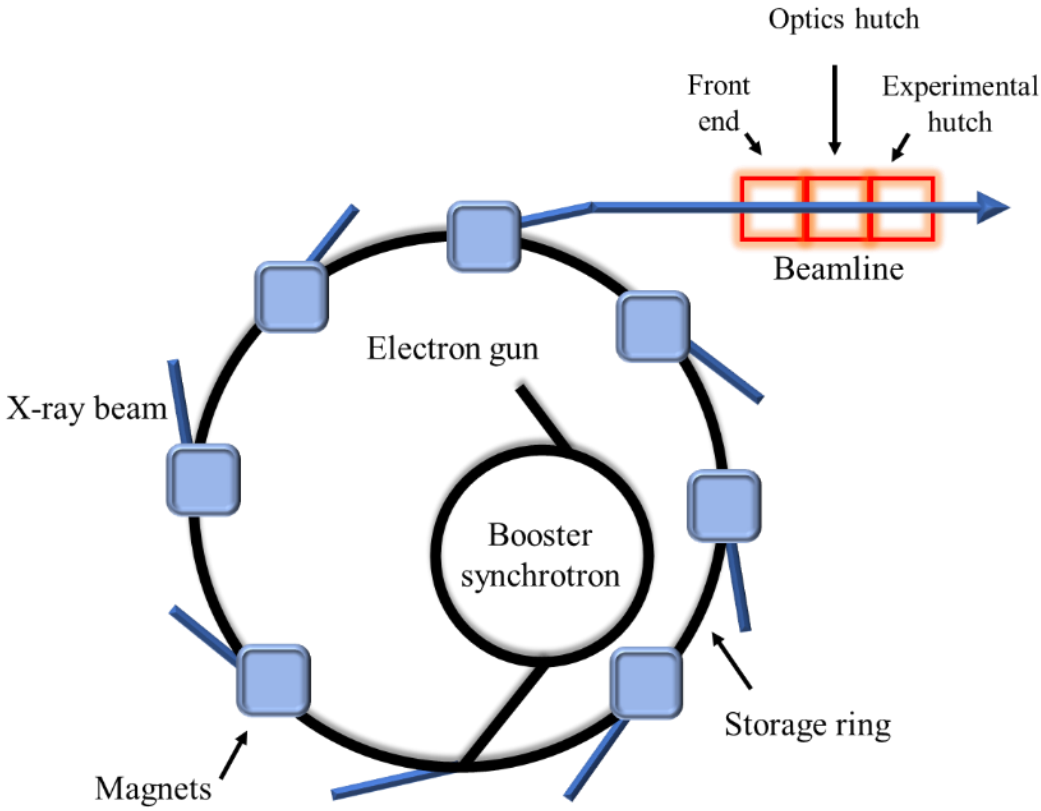

Figure 2.10 - A schematic diagram showing the essential components of a synchrotron facility. Adapted from [49]

Synchrotron radiation possesses several unique properties such as high flux, high brilliance, high stability, polarization, pulsed time structure and continuous wavelength [50]. One of the main advantages of synchrotron radiation compared with conventional laboratory X-ray sources is their extreme high brilliance. Brilliance is defined as the number of photons emitted per unit source area over a unit angle of emission and per unit energy [48], [50]. The high intensity and directionally of synchrotron radiation enables the existence of X-ray micro and nanobeams with high flux densities ($> 10^{13}$ photons s^{-1}). This characteristic offers the opportunity to perform *in situ*/ operando experiments with various techniques to study dynamic properties and time-dependent reaction processes.

The combination of synchrotron radiation with another scattering, spectroscopy (e.g. XANES, see section 2.5.2) and imaging techniques allows a comprehensive study of complicated issues that arise during ion-battery operation [51]. One of the main

advantages of using synchrotron-based techniques is to be able to collect data *in situ* or *operando*. In spectroscopy, the terms "*in situ"* and "operando" are employed to express the way data is collected [52]. Both terms come from Latin where "*in situ*" means "on-site" and "*operando"* means "working" or "operating". An "*in situ* reaction" refers to measurements done under reaction conditions, where the spectra are taken under conditions relevant to the reaction operation (transient or steady-state) [52]. The term "operando" has recently been introduced and expresses a methodology where the spectroscopic characterization of materials undergoing reactions is coupled simultaneously with kinetic measurements. *In situ/operando* approaches have significant advantages over *ex situ* characterization such as explore reactions taking place at specific locations, providing reliable and high precision for data analysis [51]. O*perando* measurements can be used to continuously monitor electrochemical, chemical, and physical processes [51]. Only one sample is used for *in situ/operando* measurements, instead of multiple *ex situ* samples, which saves time in sample preparation and provides closer to real-time operation information. Non-equilibrium and fast-transient processes occurring during electrochemical or chemical reactions can be investigated using this method, while short-lived intermediate states or species cannot be studied by *ex situ* characterizations [47]. The use of *in situ/operando* techniques lowers the possibility for contamination, relaxation, and irreversible changes of highly reactive samples during preparation and handling [47]. In conclusion, more reliable data can be obtained when using *in situ/operando* methods.

The design of an *in situ/operando* cell is the main step to conduct this kind of experiment successfully. A poorly designed cell can result in collecting data with artefacts and signals from inactive parts of the cell (such as casing) [51]. To avoid this complication during the experiment, the *in situ* cell should be designed to fit the specific experimental technique used [51]. Many *in situ* cells have been reported to be successfully used for *in situ/operando* experiments such as modified coin cell and pouch cells, capillary-type cells, Swagelock cells, Argonne's multipurpose *in situ* X-ray (AMPIX) cell [53] and radially accessible tubular *in situ* X-ray (RATIX) cell [54]. Whatever cell is used, it is important to ensure that the cell is highly reproducible for electrochemical testing, easy to assemble/disassemble at synchrotron facilities and that can be incorporated into the existing beamline setup. In battery research, the existence of an oxygen-free

environment is crucial for the good electrochemical performance of electrodes [51]. This requires the design of a closed-cell which still allows the X-ray beam to reach the sample and the detector. *In situ/operando* cells usually possess one hole for reflection or two holes for transmission mode to act as a window [51]. An ideal window should be impermeable to oxygen and moisture, chemically and electrochemically stable during cell operation and stiff to apply uniform pressure to ensure a uniform electrochemical reaction [51]. Beryllium was for several years the main material used for windows, however concerns related to its toxicity and easy oxidation during battery charging lead to the use of other solutions [51]. Polyamide films, especially Kapton films, are the most widespread material used for *in situ/operando* cells due to their versatile performance and easy handling [51]. Kapton has one main disadvantage when applying constant pressure for a long period [51]. Due to its softness, Kapton usually causes the sample underneath the window to react abnormally sometimes [51]. Interference with inactive cell components such as current collectors should be considered when using *in situ/operando* cells, especially in transmission mode [51]. Cell components or material in the X-ray beam path should be selected carefully as they can attenuate the X-rays and result in a poor signal-to-noise ratio [51].

2.5.1 Operando synchrotron X-ray Diffraction

The battery properties such as energy density, cyclic life and rate capability are closely related to the crystal structure of the electrode materials used. Therefore, the in-depth understanding of structural changes (such as lattice parameters, phase transition and atomic occupancy) of electrode materials during the electrochemical process is very important. *In situ/operando* X-ray diffraction (XRD) is a very powerful technique that provides information about the crystal structure and phase transformation of crystalline materials under cycling conditions [47].

Although both synchrotron-based XRD and conventional XRD have the same basic principles (see section 2.1.1), several advantages occur from the use of a synchrotron facility [47]. The high intensity of X-ray sources (at least 5 orders of magnitude more intense when compared with a Cu-source) provided by synchrotron facilities compared with laboratory X-ray sources offers the opportunity to study dynamic properties and

time-resolved reaction processes [47]. *In situ* and *operando* experiments can be performed in the laboratory however, several problems can arise which compromise data quality such as high signal/noise ratio. The high-photon wavelength resolution and tuneable photon energy of synchrotron XRD allow acquiring fluorescence-free diffraction data as well as a better diffraction peaks separation [47].

2.5.2 X-ray Near Edge Absorption Spectroscopy

The use of X-ray absorption spectroscopy (XAS) in the study of the structure of materials has been widely used in energy storage and has had significant progress since the early 1980s [55]. It is a widely used technique for determining the local geometry and electronic structure of matter as well as study changes in the oxidation state of certain elements. XAS measures the X-rays absorption of a material as a function of their energy [47], [55]. This technique can be classified as inner-shell spectroscopy. In an XAS experiment, a sample of interest is bombarded with X-rays of specific energy [56]. Some of these X-rays are absorbed by the atoms of the sample and a photon interact with a deep-core electron causing the excitation or ejection of a core-electron with kinetic energy as well as changes as a function of photon energy [57]. The promotion to some unoccupied state above the Fermi energy leaves behind a core-hole [57]. This causes a higher-lying electron to decay and takes the place into the core-hole (in 1 or 2 femtoseconds) emitting a photon (fluorescent X-ray or an Auger electron) [57]. The comparison between the intensity of the incident beam to that of the transmitted beam allows quantifying this absorption [56]. This can be done by measuring the fluorescence given off by the excited atoms as the core-hole is occupied by another electron (the *core hole*) or by measuring the ejected electrons as the core hole is filled (*Auger electrons*) [56]. When the incident X-ray photon energy scans through the threshold to excite core electrons, a sharp increase of absorption can be identified as the absorption edge. Unlike X-ray diffraction, the XAS technique can provide information on bond-length, coordination number and oxidation states for materials with or without long-range ordering [47].

XAS experiments are usually performed at synchrotron facilities using transmission or fluorescence detection modes. In transmission mode, the sample is placed between initial intensity (I_0) and transmitted intensity (I_t) detection chambers [56]. The intensity of the X-ray beam travelling through the sample is recorded by both detectors, respectively. The Bouger Lambert-Beer law (Equation 2.14) can then be used to calculate the absorption coefficient (μ) of the material. Depending on the thickness and concentration of the element being probed the detection of the signal can be done by fluorescent or transmission mode.

$$I = I_0 \exp(-\mu x) \tag{2.14}$$

The XAS spectrum can be divided into two parts: the X-ray Near-Edge Structure (XANES) and the Extended X-ray Absorption Fine structure (EXAFS) [47] (Figure 2.11). XANES refers to the part of the spectrum in the high-energy range (between 30 – 50 eV) near the absorption edge. This region contains information about the shape of the XANES spectrum, the edge energy position and the pre-edge features. A common XANES spectrum is characterized by the pre-edge (between the Fermi energy and the threshold), the edge (the main rising part) and the near edge (possesses characteristic features above the edge) [57]. The edge energy position is chosen at the inflexion point on the spectrum. This is used to quantitatively identify the oxidation state of the probed atom using reference compounds with known oxidation states [57]. The local geometric structure around the central absorbing atom influences the shape of the XANES spectrum. The introduction of shoulder features on the edge can be a result of interactions of the photon absorber with ligand atoms, which reflects the electronic structure of the system [47]. The pre-edge structures are sensitive to the coordination environment of the probed atom which can be used as a probe for the geometry of a sample [47], [55]. The extended EXAFS part comprises the region starting at 20-30 eV above the absorption edge [55]. In this technique, excited electrons are scattered by a near neighbour, interfering constructively or destructively. Depending on the interference, information about characteristic distances between atoms, coordination number and species of neighbours can be obtained [47].

One of XAS main advantages is the fact that it is possible to carry out fast *in situ* or *operando* XANES and EXAFS measurement during battery cycling. This offers a good

chance to observe structural changes while simultaneously observing the intercalation and deintercalation of ions. Researchers have increasingly recognized the complementary nature of the XAS technique to XRD, and it has been widely applied in structural studies for battery materials [47].

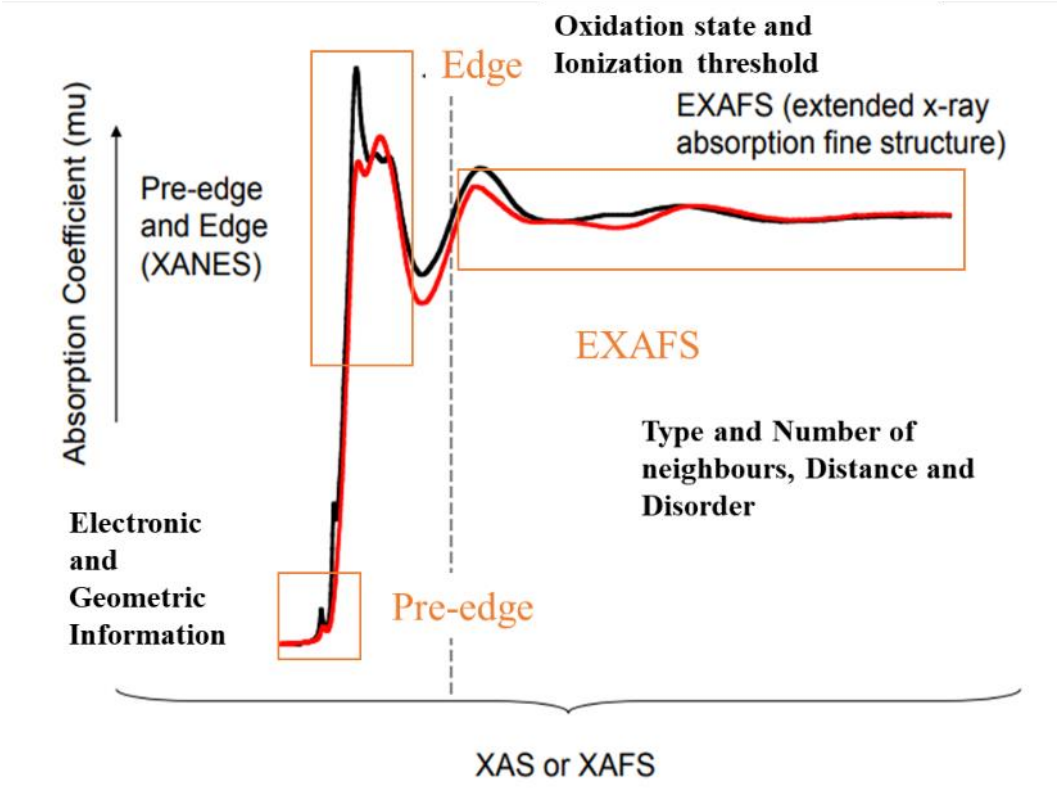

Figure 2.11 – Diagram of a typical XAS spectrum. Adapted from [56]

2.6 References

[1] M. Sabat, "Crystallography made crystal clear. A guide for users of macromolecular models by G. Rhodes," *Acta Crystallogr. Sect. D Biol. Crystallogr.*, vol. 51, no. 6, pp. 1103–1103, 1995, doi: 10.1107/s0907444995007098.

[2] M. Von Laue, "Concerning the detection of X-ray interferences," *Nobel Lect.*, pp. 347–355, 1915, doi: 10.1038/090410b0.

[3] C. Suryanarayana and M. G. Norton, *X-Ray Diffraction: A Practical Approach*.

New York: Springer, 1998.

[4] J. Kacher, C. Landon, B. L. Adams, and D. Fullwood, “Bragg’s Law diffraction simulations for electron backscatter diffraction analysis,” *Ultramicroscopy*, vol. 109, no. 9, pp. 1148–1156, 2009, doi: 10.1016/j.ultramic.2009.04.007.

[5] C. Giannini, M. Ladisa, D. Altamura, D. Siliqi, T. Sibillano, and L. De Caro, “X-ray Diffraction: A powerful technique for the multiple-length-scale structural analysis of nanomaterials,” *Crystals*, vol. 6, no. 8, pp. 1–22, 2016, doi: 10.3390/cryst6080087.

[6] T. H. E. International, U. Of, and C. R. Raphy, *International Tables of Crystallography Vol C*. 2010.

[7] “PDR: NIST Inorganic Crystal Structure Database (ICSD).” https://data.nist.gov/od/id/mds2-2147 (accessed Jun. 11, 2020).

[8] V. K. Peterson, “Lattice parameter measurement using Le Bail versus structural (Rietveld) refinement: A caution for complex, low symmetry systems,” *Powder Diffr.*, vol. 20, no. 1, pp. 14–17, 2005, doi: 10.1154/1.1810156.

[9] X. Orlhac, C. Fillet, P. Deniard, A. M. Dulac, and R. Brec, “Determination of the crystallized fractions of a largely amorphous multiphase material by the Rietveld method,” *J. Appl. Crystallogr.*, vol. 34, no. 2, pp. 114–118, 2001, doi: 10.1107/S0021889800017908.

[10] W. I. F. David, “Powder diffraction: Least-squares and beyond,” *J. Res. Natl. Inst. Stand. Technol.*, vol. 109, no. 1, pp. 107–123, 2004, doi: 10.6028/jres.109.008.

[11] B. H. Toby, “ R factors in Rietveld analysis: How good is good enough? ,” *Powder Diffr.*, vol. 21, no. 1, pp. 67–70, 2006, doi: 10.1154/1.2179804.

[12] L. B. Mccusker, R. B. Von Dreele, D. E. Cox, D. Louër, and P. Scardi, “Rietveld refinement guidelines,” *J. Appl. Crystallogr.*, vol. 32, no. 1, pp. 36–50, 1999, doi: 10.1107/S0021889898009856.

[13] J. L. F. A. Le Bail , H. Duroy, “Ab-initio structure determination of LiSbWO6 by X-ray powder diffraction,” *Mat. Res. Bull.*, vol. 23, no. c, pp. 447–452, 1988.

[14] J. Rodríguez-Carvajal, “Recent advances in magnetic structure determination by neutron powder diffraction,” *Phys. B Phys. Condens. Matter*, vol. 192, no. 1–2, pp. 55–69, 1993, doi: 10.1016/0921-4526(93)90108-I.

[15] R. B. Von Dreele and A. C. Larson, “General Structure Analysis Sytem (GSAS),” *Los Alamos Natl. Lab*, vol. LAUR, pp. 86–748, 1994, [Online]. Available: https://permalink.lanl.gov/object/tr?what=info:lanl-repo/lareport/LA-UR-86-0748_REV.

[16] D. McMullan, “Scanning electron microscopy 1928–1965,” *Scanning*, vol. 17, no. 3, pp. 175–185, 1995, doi: 10.1002/sca.4950170309.

[17] “Evaluation of materials using scanning electron microscope (SEM) | The global standard for mixing, defoaming, dispersing, and pulverizing THINKY CORPORATION.” https://www.thinkymixer.com/en-gl/library/report/evaluation-of-materials-using-scanning-electron-microscope-sem/ (accessed Jun. 11, 2020).

[18] J. I. Goldstein, D. C. Joy, L. C. Sawyer, and D. E. Newbury, *Scanning Electron Microscopy and X-ray Microanalysis*, 3 Edition. Springer Science+Business Media, 2007.

[19] W. Zhou and H. F. Greer, “What Can Electron Microscopy Tell Us Beyond Crystal Structures ?,” *Eur. J. Inorg. Chem.*, pp. 941–950, 2016, doi: 10.1002/ejic.201501342.

[20] P. Goodhew, “General Introduction to Transmission Electron Microscopy (TEM),” in *ABberration-Corrected Analytical Transmission Electron Microscopy*, 2011, pp. 1–19.

[21] W. T. Gunning and E. P. Calomeni, “A Brief Review of Transmission Electron Microscopy and Applications in-Pathology,” *J. Histotechnol.*, vol. 23, no. 3, 2000.

[22] B. J. Inkson, *Scanning Electron Microscopy (SEM) and Transmission Electron Microscopy (TEM) for Materials Characterization*. Elsevier Ltd, 2016.

[23] P. P. Kalantri, R. R. Somani, and D. T. Makhija, “Raman spectroscopy : A

potential technique in analysis of pharmaceuticals," *Der Chem. Sin.*, vol. 1, no. 1, pp. 1–12, 2010.

[24] P. S. Goh, A. F. Ismail, and B. C. Ng, "Raman Spectroscopy," in *Membrane Characterization*, 2017, pp. 31–46.

[25] R. S. Das and Y. K. Agrawal, "Raman spectroscopy: Recent advancements, techniques and applications," *Vib. Spectrosc.*, vol. 57, no. 2, pp. 163–176, 2011, doi: 10.1016/j.vibspec.2011.08.003.

[26] G. S. Bumbrah and R. M. Sharma, "Raman spectroscopy – Basic principle, instrumentation and selected applications for the characterization of drugs of abuse," *Egypt. J. Forensic Sci.*, vol. 6, no. 3, pp. 209–215, 2016, doi: 10.1016/j.ejfs.2015.06.001.

[27] K. J. I. Ember *et al.*., "Raman spectroscopy and regenerative medicine: a review," *npj Regen. Med.*, vol. 2, no. 1, pp. 1–9, 2017, doi: 10.1038/s41536-017-0014-3.

[28] Z. Xu *et al.*., "Topic review: Application of raman spectroscopy characterization in micro/nano-machining," *Micromachines*, vol. 9, no. 7, 2018, doi: 10.3390/mi9070361.

[29] T. E. Keyes and R. J. Forster, *Handbook of Electrochemistry*, Fisrt Edit. Oxford: Elsevier, 2007.

[30] M. E. V. Team, "A Guide to Understanding Battery Specifications," *Current*, no. December, pp. 1–3, 2008, doi: 10.3390/en7084895.

[31] R. A. Huggins, *Advanced batteries: Materials science aspects*. 2009.

[32] A. J. Bard, L. R. Faulkner, N. York, C. @bullet, W. Brisbane, and S. E. Toronto, *Electrochemical Methods: Fundamentals and Applications*. 1944.

[33] D. Linden, "Basic Concepts," in *Handbook of Batteries*, 4 edition., M.-H. Education, Ed. New York: McGraw-Hill Education, 2004, pp. 1.1-1.18.

[34] D. Deng, "Li-ion batteries: Basics, progress, and challenges," *Energy Sci. Eng.*, vol. 3, no. 5, pp. 385–418, 2015, doi: 10.1002/ese3.95.

[35] T. Kim *et al.*., "Applications of Voltammetry in Lithium Ion Battery Research,"

J. Electrochem. Sci. Technol., vol. 11, no. 1, pp. 14–25, 2020, doi: 10.33961/jecst.2019.00619.

[36] N. Elgrishi, K. J. Rountree, B. D. McCarthy, E. S. Rountree, T. T. Eisenhart, and J. L. Dempsey, "A Practical Beginner's Guide to Cyclic Voltammetry," *J. Chem. Educ.*, vol. 95, no. 2, pp. 197–206, 2018, doi: 10.1021/acs.jchemed.7b00361.

[37] J. Heinze, "Cyclic Voltammetry—Electrochemical Spectroscopy," *Angew. Chemie Int. Ed. English*, vol. 23, no. 11, pp. 831–847, 1984, doi: 10.1002/anie.198408313.

[38] L. A. Avaca, S. Kaufmann, K. Kontturi, L. Murtomäki, and D. J. Schiffrin, "Theory of Cyclic Voltammetry for Quasi-Reversible Electrodeposition Reactions with insoluble Products," *Berichte der Bunsengesellschaft für Phys. Chemie*, vol. 97, no. 1, pp. 70–76, 1993, doi: 10.1002/bbpc.19930970114.

[39] Y. Qu *et al.*., "Wafer Scale Phase-Engineered 1T- and 2H-MoSe2/Mo Core–Shell 3D-Hierarchical Nanostructures toward Efficient Electrocatalytic Hydrogen Evolution Reaction," *Adv. Mater.*, vol. 28, no. 44, pp. 9831–9838, 2016, doi: 10.1002/adma.201602697.

[40] A. H. Loo, A. Bonanni, A. Ambrosi, and M. Pumera, "Molybdenum disulfide (MoS2) nanoflakes as inherently electroactive labels for DNA hybridization detection," *Nanoscale*, vol. 6, no. 20, pp. 11971–11975, 2014, doi: 10.1039/c4nr03795b.

[41] J. Li, S. Xiong, Y. Liu, Z. Ju, and Y. Qian, "Uniform LiNi1/3Co1/3Mn1/3O2hollow microspheres: Designed synthesis, topotactical structural transformation and their enhanced electrochemical performance," *Nano Energy*, vol. 2, no. 6, pp. 1249–1260, 2013, doi: 10.1016/j.nanoen.2013.06.003.

[42] H. Dai, B. Jiang, and X. Wei, "Impedance characterization and modeling of lithium-ion batteries considering the internal temperature gradient," *Energies*, vol. 11, no. 1, 2018, doi: 10.3390/en11010220.

[43] Gamry, *The Basics of Electrochemical Impedance Spectroscopy*. 2017.

[44] H. Dehghani and N. K. Soni, “Electrical Impedance Spectroscopy: Theory,” in *Alternative Breast Imaging*, 2005, pp. 85–105.

[45] N. Bonanos *et al.*., “Applications of Impedance Spectroscopy,” *Impedance Spectrosc.*, no. March, pp. 175–478, 2018, doi: 10.1002/9781119381860.ch4.

[46] D. Irvine, J. Sinclair and W. Anthony, “Electroceramics Characterization by Impedance Spectroscopy,” *Adv. Mater.*, vol. 3, pp. 132–138, 1990.

[47] F. Lin *et al.*., “Synchrotron X-ray Analytical Techniques for Studying Materials Electrochemistry in Rechargeable Batteries,” *Chem. Rev.*, vol. 117, no. 21, pp. 13123–13186, 2017, doi: 10.1021/acs.chemrev.7b00007.

[48] G. P. Williams, “A general review of synchrotron radiation, its uses and special technologies,” *Vacuum*, vol. 32, no. 6, pp. 333–345, 1982, doi: 10.1016/0042-207X(82)93826-X.

[49] “About Us - - Diamond Light Source.” https://www.diamond.ac.uk/Home/About.html (accessed Jun. 11, 2020).

[50] F. C. Adams, *X-ray absorption and Diffraction | Overview*, Third Edit., vol. 10, no. 1. Elsevier, 2019.

[51] S. M. Bak, Z. Shadike, R. Lin, X. Yu, and X. Q. Yang, “*In situ*/operando synchrotron-based X-ray techniques for lithium-ion battery research,” *NPG Asia Mater.*, vol. 10, no. 7, pp. 563–580, 2018, doi: 10.1038/s41427-018-0056-z.

[52] M. A. Bañares, “Operando methodology: Combination of *in situ* spectroscopy and simultaneous activity measurements under catalytic reaction conditions,” *Catal. Today*, vol. 100, no. 1–2, pp. 71–77, 2005, doi: 10.1016/j.cattod.2004.12.017.

[53] O. J. Borkiewicz, B. Shyam, K. M. Wiaderek, C. Kurtz, P. J. Chupas, and K. W. Chapman, “The AMPIX electrochemical cell: A versatile apparatus for *in situ* X-ray scattering and spectroscopic measurements,” *J. Appl. Crystallogr.*, vol. 45, no. 6, pp. 1261–1269, 2012, doi: 10.1107/S0021889812042720.

[54] H. Liu *et al.*., “A radially accessible tubular *in situ* X-ray cell for spatially resolved operando scattering and spectroscopic studies of electrochemical energy

storage devices," *J. Appl. Crystallogr.*, vol. 49, no. 5, pp. 1665–1673, 2016, doi: 10.1107/S1600576716012632.

[55] S. J. Gurman, "Amorphous Materials : X-ray Absorption," in *Encyclopedia of Materials: Science and Technology*, 2001, pp. 256–259.

[56] S. Calvin, *XAFS for Everyone*. 2013.

[57] B. Ravel, *Introduction to x-ray absorption spectroscopy*. 2015.

3 A study on the charge compensation mechanisms on T_d-WTe_2 polytype as an anode in SIBs

3.1 Introduction

Among the TMD family, several compounds have attracted attention due to their specific characteristics. VI-group MX_2 materials, including MoX_2 and WX_2 (X = S, Se and Te) are widely investigated due to their different characteristics resulting from different synthetic methods. Due to the way that non-bonding orbitals can be filled with d-electrons, TMDs can display a more metal (partially filled d-orbitals) or semiconductor conductive feature (filled d-orbitals). Changes from a 2H semiconducting structure to a 1T metallic phase make this type of MX_2 highly appealing.

Tungsten ditelluride (WTe_2) is a unique TMD as it possesses a large interlayer spacing, an orthorhombic lattice structure and a semi-metal electronic structure [1], [2]. This structure represents the combination of the two heaviest elements in common TMDs. WTe_2 crystallizes in an orthorhombic lattice when at ambient conditions displaying the space group $Pmn2_1$ [2] (Figure 3.1).

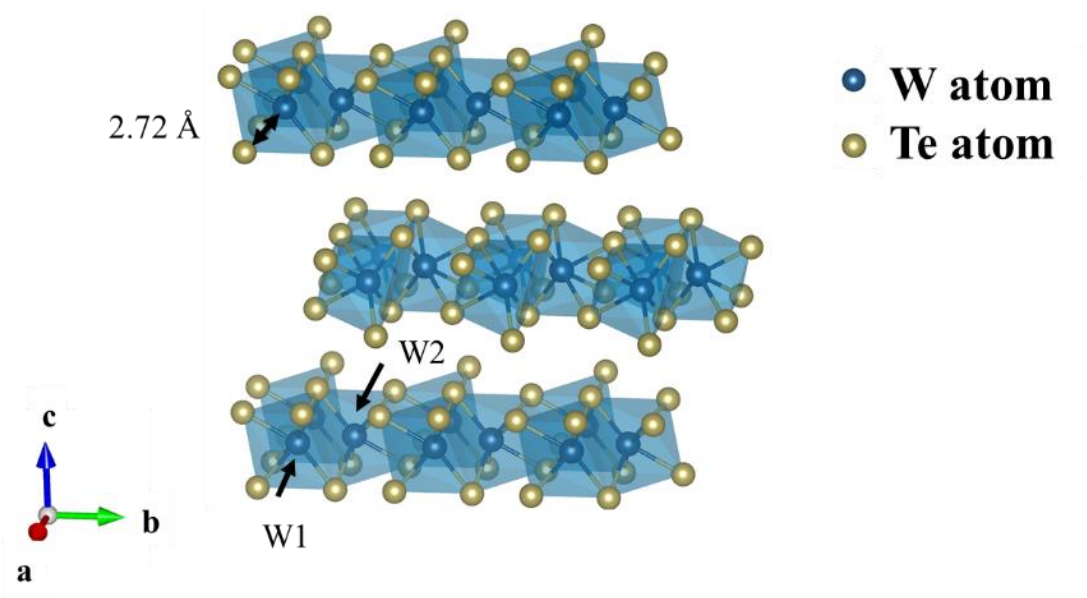

Figure 3.1 - Polyhedral representation of crystal structure of T_d-WTe_2 with a space group *Pmn*2_1 plotted using VESTA 3.4 [3]. W and Te atoms are shown in blue and yellow, respectively. The unit cell contains two tungsten atoms and four tellurium atoms. Each W atom is surrounded by eight neighbours, six Te atoms and two W atoms. The structure is composed of several W layers each separated by two layers of Te stacked along the c-axis.

The unit cell contains two Te-W-Te sheets being that tungsten atoms are coordinated in an octahedral environment by tellurium atoms. From the two sheets composing the unit cell, one is rotated 180° with respect to the other in a stacking sequence referred to as T_d-WTe_2 (distorted 1T structure) [2] (Figure 3.2). This phase corresponds to a distorted 1T phase and has proven to have the lowest energy in the T_d-polytype, exhibiting a semi-metallic character [4]. This additional structural distortion is caused by the W atoms located in zigzag chains along the crystallographic axis which produce a quasi-one-dimensional arrangement. WTe_2's crystal structure can be regarded as a distortion of MoS_2 along the a-axis (W chains) [5]. This structure can be compared to graphite as they both are composed of many layers and the separation between the W layers is done by two layers of Te staked along the z-axis [5]. The large size of W turns the lattice structure sensitive to small changes, resulting in enormous differences in the overall structure formed. WTe_2 was recently discovered as a type-II Weyl semimetal (WSM) [6]. Weyl semimetal is a new state of matter in condensed matter physics that contains

Weyl fermions acting as emergent quasiparticles [7]. As with other TMDs, WTe_2 also possesses a strong metallic nature which can be considered as a semimetal with a reduced density of states at the Fermi level [8]. In the family of 2D TMDs, this is a unique feature of WTe_2 as its metallic phase is more stable than its semiconducting phase [9]. The lattice structure of tungsten dichalcogenides is very similar to that of molybdenum compounds but with a slightly larger cation. For that reason, conventional characterization techniques are not very efficient to differentiate between WX_2 and MoX_2. Raman spectroscopy is usually used for a better distinction between structures. Although they show similar $E_{2g}{}^1$ and A_{1g} peaks, Raman spectroscopy allows estimating the number of layers in the 2D structure by considering the intensity of the substrate peak [10], [11]. Dichalcogenides with larger ions such a WX_2 tend to have lower symmetry in-plane anisotropy when compared with MoX_2. A strong anisotropy is observed in this structure which results from the fact that the distance between adjacent W atoms is smaller along the x-axis compared with the y and z-axis. This feature implies potential spintronic applications of mono and few-layered WTe_2. Differences such as thickness-dependency characteristics can be revealed by subtle differences in Raman spectra [11].

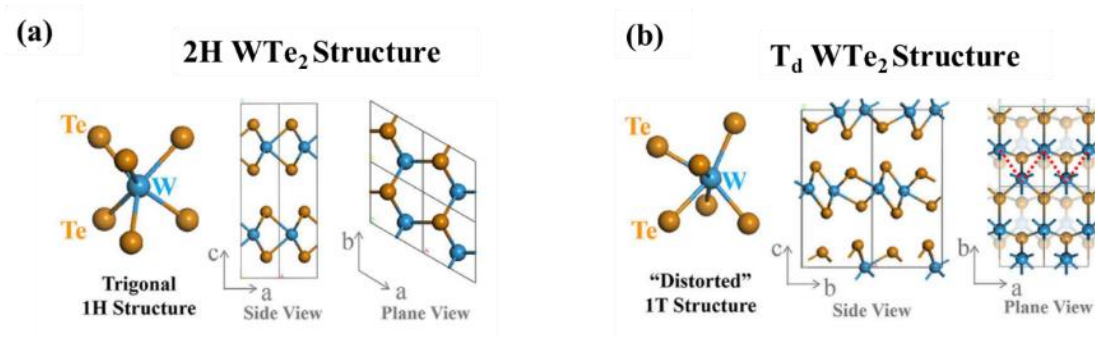

Figure 3.2 - Comparison of the tungsten-tellurium coordination (side and plane views) of (a) 2H-WTe_2 and (b) distorted "1T", or T_d-WTe_2. Adapted from [4]

Due to this unusual structure, several studies were performed to better understand the T_d-WTe_2. *In situ* synchrotron X-ray measurements (SXRD) were performed at high pressure (33.8 GPa) and results show that upon compression, there is a shrinkage of the T_d-WTe_2 lattice [12]. The structure was compressed with pressure from 6.0 to 33.8 GPa and it was described that in the pressure range 6.0 – 15.5 GPa, two different phases can

be observed. XRD profiles show the existence of a low and high-pressure phase. The continuous compression to 33.8 GPa leads to a progressive shift of all peaks to higher angles representing a shrinkage in the unit cell parameters [12]. Rietveld refinement allowed to identify both phases as a single T_d (low-pressure pattern) and 1T' (high-pressure pattern). When decompressing the structure back to the initial pressure, results show that the initial XRD pattern is recovered, evidencing that the pressure-driven structural transition is reversible [12].

WTe_2 has triggered great interest among the TMD family due to its extremely large positive non-saturating spin-mixing magnetoresistance (XMR). The XMR effect observed in the diamagnetic WTe_2 single crystal is unique to this material as it is not observed in other TMDs [1]. Magnetoresistance (MR) describes the change in electrical resistance of a material (usually ferromagnetic) when applied to an external magnetic field. This phenomenon is useful for the development of magnetic memory devices, magnetic sensors and spintronics [13]. First-row magnetic transition metals (such as Fe compounds) are the primary candidates to use, however, WTe_2 has recently been intensively studied [14]. As referred previously, WTe_2 crystallizes in a T_d orthorhombic phase at ambient conditions and displays an extremely large uniaxial positive magnetoresistance. This behaviour is attributed to the perfect balance of electron-hole populations and is then responsible for the high MR effect observed [1], [15]. Das *et al.* studied the role of W and Te atoms using angle and spin-resolved photo-emission spectroscopy in the electronic behaviour of WTe_2 [8]. The results obtained show that this behaviour requires at least three layers of Te-W-Te to rich the perfect balance of electron and hole states. DFT calculations support these results allowing us to conclude that the MR effect observed is not strictly two-dimensional [8]. Bulk monolayered WTe_2 was studied and was shown to deliver extraordinary MR response due to the high mobility of the charge carriers present in the structure [16]. WTe_2 has also been investigated in other areas such as superconductivity [17], quantum spin hall effect and electrocatalysis [18].

As discussed previously (Chapter 1), TMD 2D materials have gained a lot of attention due to their notable electrochemical properties. The fact that they can accommodate large volume expansion and possess a large effective surface area turns them into suitable materials to use in rechargeable ion batteries. Successful application of WTe_2

compounds for Li-ion storage led researchers to study the application of this TMD in sodium storage systems. Highly crystalline semi-metallic 1T' WTe_2 nanorods (NRs) and nanoflowers (NF) were reported for the first time as anode materials for SIBs by H.Chang *et al.* in 2018 [19]. The two WTe_2 structures were synthesized through a novel two-step process with hydrothermal-derived WO_3 transformed into WTe_2 after a chemical vapour deposition process. TEM images reveal some degree of sintering after the chemical vapour deposition process for both materials, however, WTe_2 NRs possess a smaller grain diameter when compared to the WTe_2 NFs, which reflect the difference in the crystal growth process [19]. CV curves show almost identical processes happening in WTe_2 NRs and NFs during the first 5 cycles, indicating that the energy storage mechanism is the same. The first cathodic scan is characterized by the presence of two peaks related to the alloying and phase inversion reaction happening in WTe_2 during Na^+ ion intercalation. The formation of the SEI layer happens simultaneously with the conversion of WTe_2 into W metal and Na_2Te [19]. This reaction is inverted during the oxidation process when the desodiation of Na_2Te leads to the reconstitution of the original WTe_2. The performance of the WTe_2 NRs and NFs in SIB was evaluated by cycling over a voltage range of 0.01 – 3.0 V at a current density of 0.1 A g^{-1}. WTe_2 NRs exhibit an initial discharge/charge capacity of 442/324 mAh g^{-1} against sodium versus 318/254 mAh g^{-1} for WTe_2 NFs. The difference between the first specific discharge and charge capacity is attributed to the formation of the SEI layer and electrolyte decomposition. After 100 cycles, WTe_2 NRs discharge capacity remains at 221 mAh g^{-1} while WTe_2 NFs show a capacity of 260 mAh g^{-1} after 40 cycles [19]. Long cycling studies show a worse performance of WTe_2 NFs electrode compared to WTe_2 NRs due to the irreversible structural damage suffered by WTe_2 NFs during the cycling tests. This damage can be ascribed to the successive intercalation/ deintercalation of Na^+ ions into the layered structure and alloying/dealloying reactions. This study concludes that the performance of the WTe_2 SIB anode is highly influenced by WTe_2 morphology [19].

A detailed study was carried out to characterise the as-synthesized WTe_2 before the investigation of its electrochemical performance as Na-ion anode. These included morphological and structural analysis (PXRD, SEM/EDX, TEM and Raman) and structure evolution analysis (XANES and synchrotron operando PXRD) in conjunction

with electrochemical analysis (galvanostatic cycling, cyclic voltammetry and electrochemical impedance spectroscopy). This study highlights the structural mechanism behind the reversible intercalation of Na^+ ions into the WTe_2 structure.

3.2 Experimental part

3.2.1 Synthesis and structure characterisation

10 g of tungsten telluride (WTe_2) was synthesised by Dr Zdenek Sofer from the University of Chemistry and Technology Prague in Czech Republic following the methods reported in [20]. For the synthesis, stoichiometric amounts of tungsten and tellurium (1:2.1) were added in a quartz ampoule (100 × 15 mm; 2 mm wall thickness) which was evacuated to 1 x 10^{-3} Pa. The quartz ampoule was flame sealed with an O_2/H_2 torch and this was heated to 600 °C for 48 h, 800 °C for 48 h and then to 850 °C for 12 h, with mechanical mixing after each heating step.

The Raman spectrum of the as-prepared sample was collected in backscattering geometry at ambient conditions using a Euromex equipment microscopy equipped with a 532 nm solid-state laser, 100 x objective with a 400 mm numerical aperture and a grating of 1800 gr mm^{-1}. Two data acquisitions were collected with a total acquisition time of 240 s. The laser power was kept under 40 µW during the measurements to avoid possible heating and sample damage.

3.2.2 Operando synchrotron X-ray diffraction

Operando synchrotron PXRD measurements were carried out at the MSPD BL04 beamline of the ALBA synchrotron (Spain). The samples were measured at room temperature in fluorescence geometry using a 13 keV X-ray beam energy (λ $K_{\alpha 1}$ = 0.4195 Å) and a Mythen 6 K detector. Data were recorded in the 2 to 40° 2θ range. To reduce the effect of the preferred orientation of crystallites on the diffracted intensities, a concentric rocking of ± 15° of the whole setups within the Eulerian cradle was used. Each powder X-ray diffraction pattern was collected for 130 s. To verify the reliability of the cell positioning and overall data quality, a capillary (0.5 mm diameter

borosilicate) with WTe_2 powder was used as a reference. Custom-made CR2032 coin cells with a glass window of 8 mm diameter and 130 µm thickness [21] were used for the operando measurement. The electrochemical cell contained *ca.* 7.10 mg of a homogenous powdered electrode mixture (70 wt % active material, 20 wt % carbon black (super P) and 10 wt % Polyvinylidene fluoride (PVDF, Kynar)), Na metal as the counter and reference electrode and a glass fibre separator soaked in 1 M $NaPF_6$ in ethylene carbonate/dimethylene carbonate (EC: DMC 1:1 v/v %) organic electrolyte. The cell was cycled within the voltage range of 0.1 -3.0 V *vs* Na^+/Na at a rate of 40 mA g^{-1}. Electrochemical data were collected using a Biologic (SP200 model) potentiostat and data were processed using the EC-Lab software V11.20 [22].

3.2.3 *Ex situ* synchrotron X-ray absorption spectroscopy

XANES measurements were performed at the B18 Core EXAFS beamline at the Diamond Light Source (UK). For the measurement, cast electrodes were cycled at different states of charge and then extracted from the coin cells and rinsed three times with DMC (ca. 5 ml) in an argon glovebox. The electrodes were sealed under vacuum in aluminium laminated pouches before the measurements. Spectra of the charged electrodes at the W L_{III}-edge and Te K-edge were measured at ambient temperature in fluorescence mode at energies above and below the absorption edges of 10205 and 31807 eV, respectively. Three spectra were collected for each sample for 5 minutes. Te metal and TeO_2 were used as references for Te^0 (31814 eV) and Te^{4+} (31816.4 eV) ions [23], [24] and W metal and WO_2 were used as references for W^0 (10211.3 eV) and W^{4+} (10211.8 eV), respectively [25]. Absorption spectra of the reference samples were collected in transmission mode. The Athena software in the Demeter package [26], [27] was used to average the scans collected, calibrate, and normalise the data.

3.3 Results and Discussion in SIBs

3.3.1 Structural and morphological characterisation of T_d-WTe_2

3.3.1.1 Powder X-ray Diffraction

Powder X-ray diffraction (PXRD) data of the as-synthesized WTe_2 material is shown in Figure 3.3. The sharpness and well-defined shape of the peaks suggest the high crystallinity of the synthesized compound. The experimental diffraction pattern matches the simulated powder pattern of the distorted tetrahedral WTe_2 (T_d-WTe_2) phase with the orthorhombic space group $Pmn2_1$ [ICSD- 73323]. No impurities such as oxides or metals were observed.

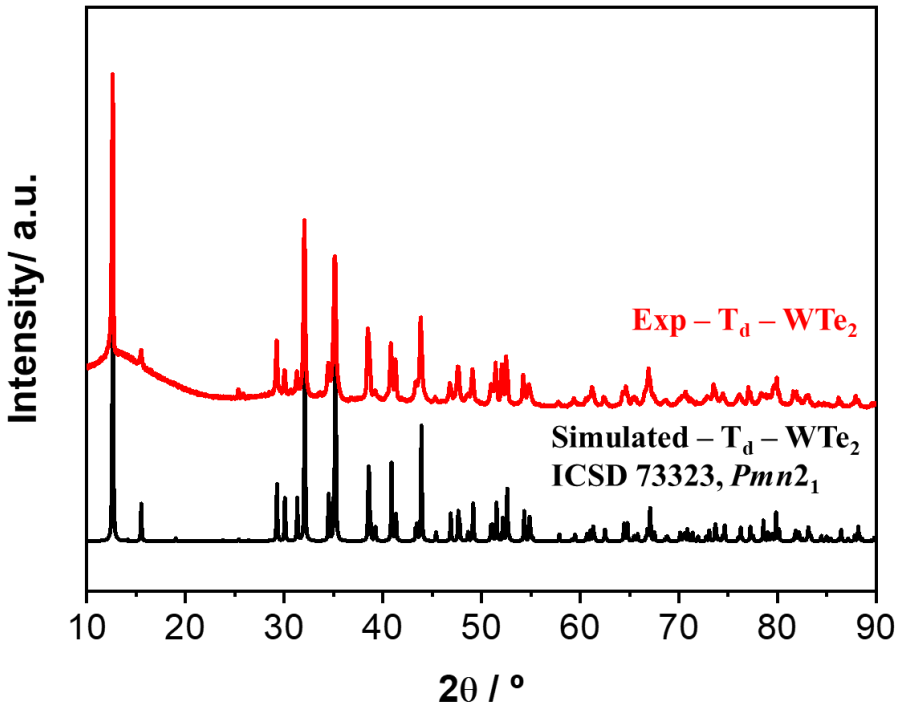

Figure 3.3– X-ray diffraction pattern of as-prepared T_d-WTe_2. The solid red line corresponds to the experimental data and the solid black line corresponds to the simulated pattern (ICSD 73323).

The lattice parameters of the material were obtained using Rietveld refinement (Figure 3.4). The refined parameters included the zero, lattice and profile parameters, atomic positions, and isotropic displacement parameters (U_{iso}). The lattice parameters were

found to be *a* = 3.481(8) Å, *b* = 6.257(1) Å, *c* = 14.036(4) Å, α = 90 °, β = 90 ° and γ = 90 °, which are in agreement to the unit cell parameters reported in the literature [28]. The refined parameters can be found in Table 3.1. The goodness-of-fit, χ^2, was found to be 10.96 and the R factors such as weighted profile R-factor, R_{wp}, and expected R factor, R_{exp}, were found to be 9.63 and 6.74 %, respectively. As mentioned in Chapter 2, the parameter χ^2 serves as a measure of the quality of the fit to a powder diffraction pattern, while the ratio of R_{wp} to R_{exp} R-factors is a good measure of how well the data are fitted [29]. In our case, the data was collected in reflection mode using a conventional Cu $K_{\alpha 1}$ source which influenced the goodness of the refinement. The strong absorption of both W and Te elements hinders an accurate structure refinement, as reflected in the relatively high value of χ^2 obtained.

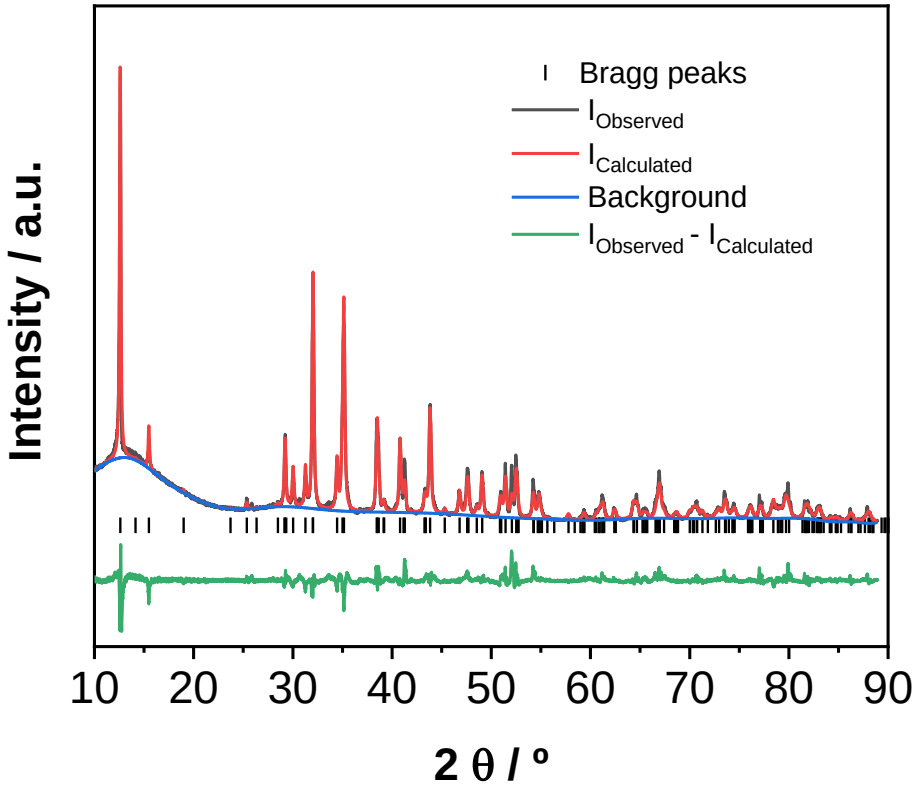

Figure 3.4– Rietveld fit of XRD data of T_d-WTe_2. The solid black line corresponds to the observed data, the solid red line indicates the calculated profile, the solid blue line is the background, and the solid green line corresponds to the difference between the two profiles. Black tick marks indicate Bragg reflections of T_d-WTe_2 (ICSD 73323).

Table 3.1 - Atomic positions, isotropic displacement parameters, occupancies, and reliability factors of WTe_2 determined by Rietveld refinement method from the PXRD data acquired at room temperature.

Atom	*X*	*Y*	*Z*	Multiplicity	Occupancy	U_{iso} (A^3)
W1	0	0.5942(3)	0.4974(1)	2	1	0.00342(2)
W2	0	0.0458(8)	0.0145(5)	2	1	0.00354(6)
Te1	0	0.8526(4)	0.6541(8)	2	1	0.00430(6)
Te2	0	0.6511(2)	0.1142(9)	2	1	0.00405(3)
Te3	0	0.2990(2)	0.8604(0)	2	1	0.00455(9)
Te4	0	0.2039(2)	0.4054(7)	2	1	0.00430(6)

WTe_2 – Space group $Pmn2_1$

a = 3.481(8) Å, b = 6.257(1) Å, c = 14.036(4) α = 90 °, β = 90 °, γ = 90 °

χ^2 = 10.96, R_{wp} = 9.63 %, R_{exp} = 6.74 %

The unit cell of T_d-WTe_2 contains two tungsten atoms and four tellurium atoms. Each W atom is surrounded by eight neighbours, six Te atoms and two W atoms [30], the W-Te bond distance varies from 2.730(6) - 2.842(5) Å for W(1) and 2.681(6) and 2.839(7) Å for W(2) (Figure 3.5). The values obtained from the Rietveld refinement are in agreement with the literature (2.72-2.85 Å [2]). The W-W distance was calculated to be 2.856(6) Å, which is close enough to the distance reported of 2.87 Å. Furthermore, W-Te-W chains are formed along the *ab* plane and the layers are stacked along the *c* axis [2]. Although the bonds between layers are made of weak van-der-Waals, all W atoms are covalently bonded to neighbouring Te atoms forming a sandwich-like trigonal prismatic structure [9], [30]. Here, the off-centring of the W atoms from their "ideal" octahedral sites led to the formation of a zigzag W-W chain along the a-axis, which changes the charge density wave distortion of each W making the W-W bond shorter

than in the 2H phase [5], [9]. In T_d-WTe_2, the successive Te-W-Te layers are the layers formed by the sequential rotation of the lower layer by 180°. The interlayer spacing can be calculated from the PXRD pattern using the reflection at 12.6° 2θ value which is assigned to the inter-planar d-spacing of the (002) crystal plane [2]. The interlayer spacing for the (002) plane is 0.701nm according to Bragg's condition:

$$n\lambda = 2d_{hkl}\sin\theta \tag{3.1}$$

where d spacing is defined by the indices h, k and l from the corresponding diffracting plane, λ is the wavelength (1.54056 Å), θ is the angle between the incident X-ray and scattering planes and n is the layer index number, usually assuming a value of 1.

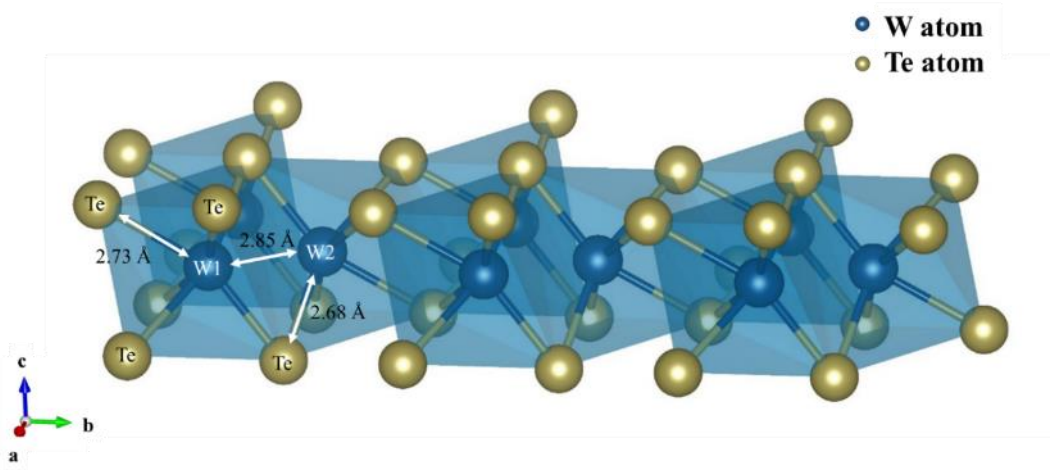

Figure 3.5 – Polyhedral representation of crystal structure of WTe_2 with a space group *Pmn2₁* plotted using VESTA 3.4 [3]. The W and Te atoms are shown in blue and yellow, respectively. Each distance (W(1)-Te, W(2)-Te and W-W) is represented with arrows.

3.3.1.2 Field emission scanning electron microscopy

Field emission scanning electron microscopy (FESEM) analysis was carried out on T_d-WTe_2 after synthesis to assess the morphology, Figure 3.6. The particles consist of monodispersed irregular particle blocks with average lengths of ≈ 3-10 µm consisting of fine plates with thicknesses of ≈ 0.8-2 µm and widths of ≈ 0.9 – 2.4 µm. The SEM view on the edges and the fractured portion of the irregular blocks reveals that these

blocks are composed of stacked nanometre width sheets of T_d-WTe_2 and result in a layered-type material.

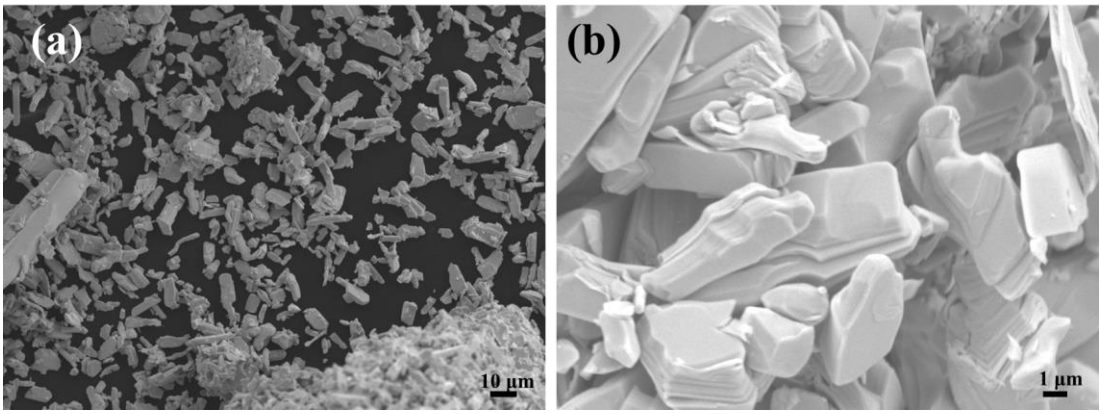

Figure 3.6 - FESEM image of the as-synthesized T_d-WTe_2, at (a) low and (b) high magnification.

Energy-dispersive X-ray spectroscopy (EDX) analysis (Figure 3.7) and elemental distribution mapping indicate a W: Te atomic composition of 1:2 as expected which further confirms the purity and the homogeneous distribution of W and Te components in the as-synthesized material. These findings are consistent with those reported in the literature, in which the solid-state reaction method was used to synthesise T_d-WTe_2 [31].

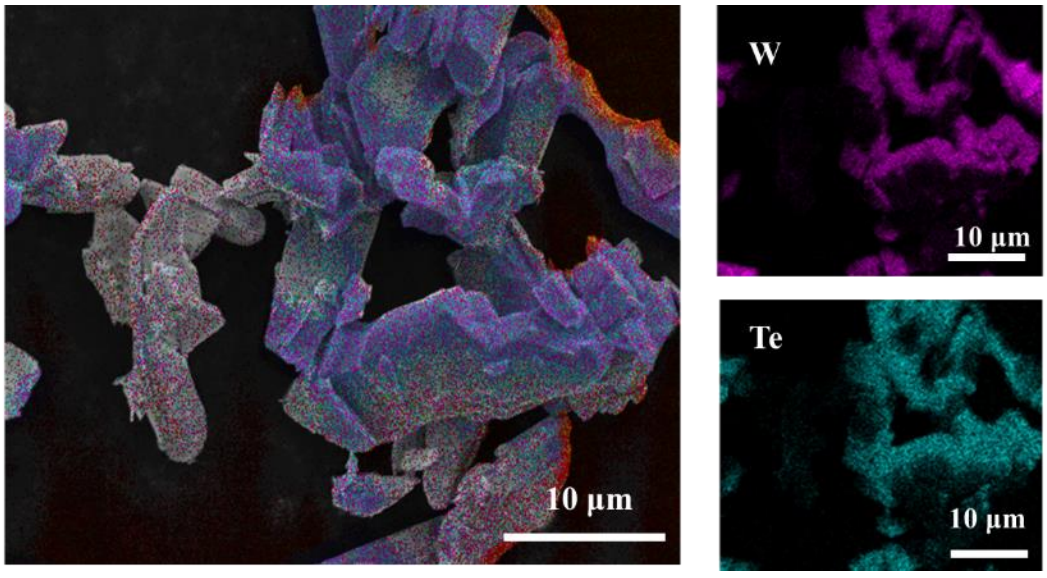

Figure 3.7 - EDX mapping pattern and elemental distribution of W and Te elements in as-prepared T_d-WTe_2.

3.3.1.3 Transmission electron microscopy

The microstructure of T_d-WTe_2 was further analysed with high-resolution transmission electron microscopy (HRTEM). The TEM images are shown in Figure 3.8. These further confirm the layered nature of this material, showing the stacking of a few very thin nanosheets. The darker lines in the high-magnification image (Figure 3.8b) reveal the individual single-layer that form the particles in this specific positioning and can be attributed to a lateral size of ~ 6 nm.

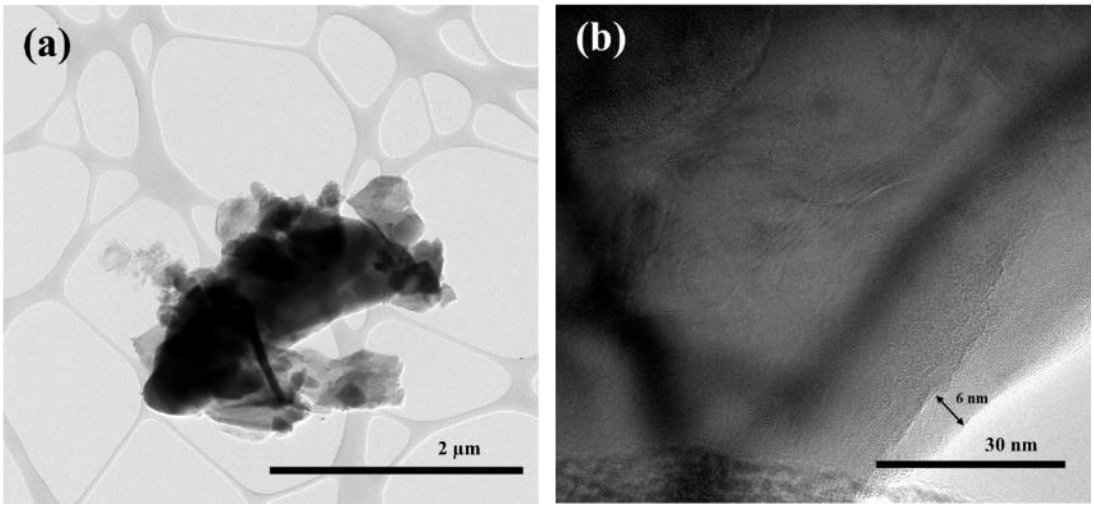

Figure 3.8 – HRTEM image of the exfoliated as-synthesized WTe_2 nanosheets at (a) low and (b) high-resolution of the edges of the WTe_2 nanosheets from the exfoliation process showing a single-layered sheet.

The interplanar spacing of the parallel fringes in the HRTEM image (Figure 3.9a) is 0.301 nm, which agrees well with the (111) plane of the orthorhombic T_d-WTe_2. Furthermore, the corresponding selected-area diffraction (SAED) pattern (Figure 3.9b) is consistent with the crystalline nature of the sample. In the SAED pattern atoms are oriented along the <011> direction, which is perpendicular to the orientation of the layers, and is well-indexed to the (013) and (004) crystal planes.

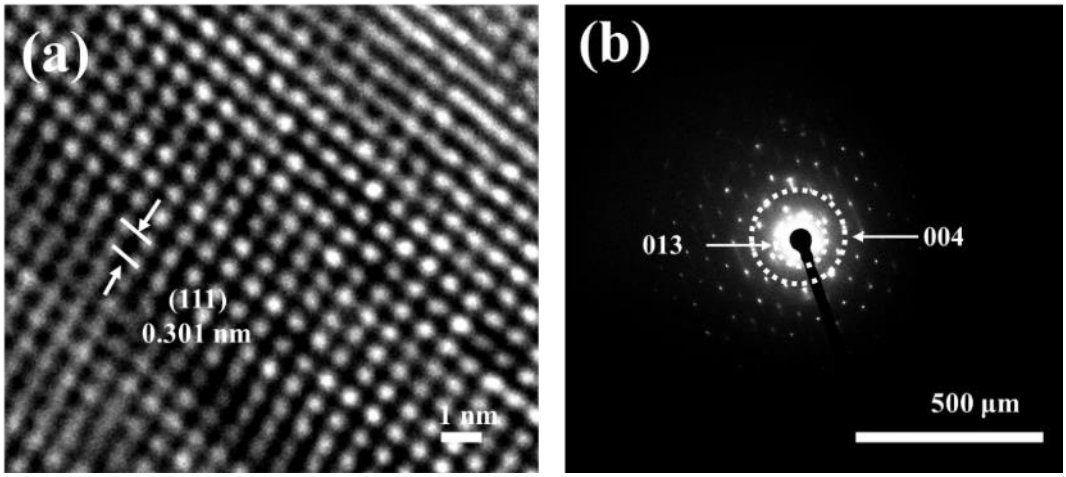

Figure 3.9 – HRTEM image of the exfoliated as-synthesized WTe_2 nanosheets at (a) high-resolution confirming the presence of WTe_2. The interlayer spacing of the WTe_2 nanosheets represents an interatomic spacing length of 0.301 nm and (b) corresponding SAED pattern.

3.3.1.4 Raman spectroscopy

Raman scattering is among the most conventional and fundamental techniques for studying TMDs, allowing to determine in an easy and non-destructive way the structure and layer number [32]–[34]. Raman spectroscopy was used to characterize the electronic energy bands of as-prepared T_d-WTe_2. The Raman spectrum shows five peaks at 112, 118, 134, 164 and 212 cm^{-1} (Figure 3.10), in agreement with the literature [30], which correspond to the A_1^2, A_1^3, A_1^4, A_1^7 and A_1^9 modes, respectively. No Raman modes associated with oxidation species such as WO_x and TeO_x species were observed [35]–[37], confirming the PXRD data.

In TMDs structures, the A vibration modes can be suppressed or shifted depending on the number of layers of the structure or pressure applied [5]. Under the same condition, the higher the crystal symmetry is, the less the Raman modes can be detected [38]. In T_d-WTe_2, the A_1^2 mode is related to the displacement between adjacent W_1 and W_2 atoms [39]. The lattice vibration at 164 cm^{-1} (A_1^7) is related to the direction of the structurally one-dimensional tungsten chains and is mainly independent of the variation of the layer number [5]. The peaks at 118, 134 and 212 cm^{-1} (A_1^3, A_1^4 and A_1^9) in the

spectrum are identified as "tilted" out-of-place A_1 modes and the peaks at 164 and 212 cm^{-1} are stronger in monolayers when compared with the bulk material [40]. The out-of-plane vibrational modes in the T_d-WTe_2 structure are not oriented perpendicularly to the WTe_2 sheets due to the structural distortion induced by the metal-metal bonding in the structure [40]. In contrast to the A_1^g modes of 2H-WTe_2, these Raman-active modes vibrate either along with the W-Te bond or at an angle to the vertical line [40].

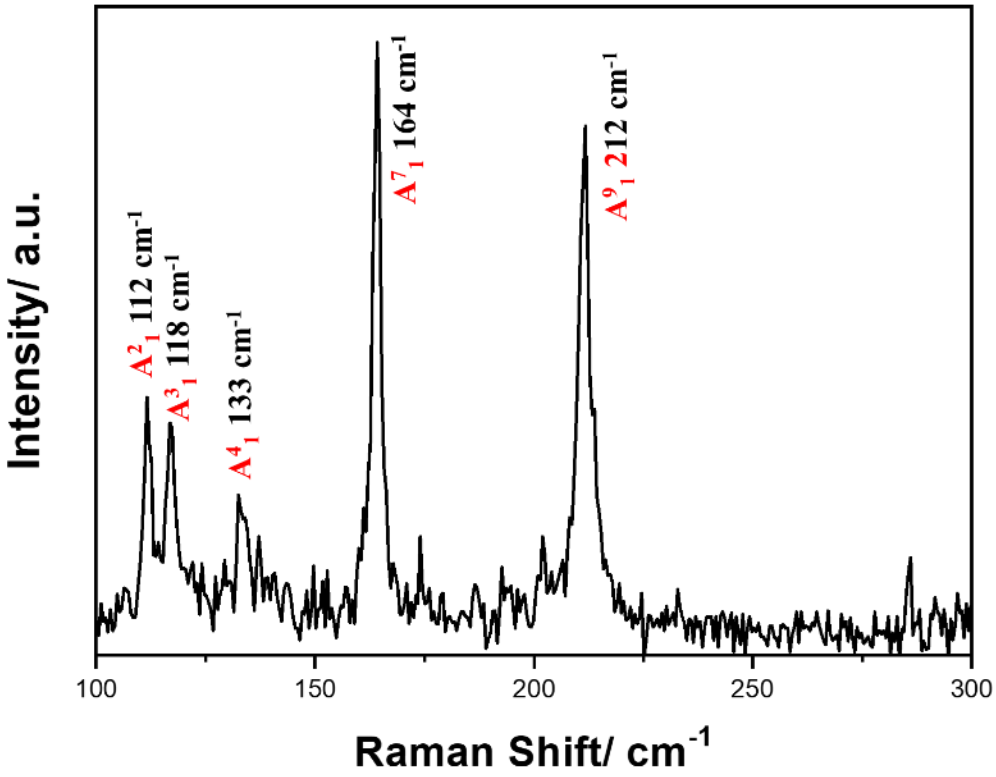

Figure 3.10 - Raman spectrum of as-synthesized bulk T_d-WTe_2.

3.3.2 Electrochemical characterization in SIBs

3.3.2.1 Galvanostatic cycling

The galvanostatic discharge-charge cycling measurements were carried out in the voltage range of 0.1 – 3.0 V *vs* Na^+/ Na at a current density of 10 mA g^{-1}. The voltage profile of different cycles (1^{st}, 2^{nd}, 3^{rd}, 5^{th} and 10^{th}) is displayed in Figure 3.11.

During the initial discharge from the open-circuit voltage (OCV 1.68 V) to 0.1 V, a short and long voltage plateau at 1.2 and 0.6 V are observed, respectively. Followed by

those plateaus, the potential dropped gradually to the cut-off voltage (0.1 V) resulting in a storage capacity of 288 mAh g^{-1} which corresponds to the theoretical insertion of 4.7 Na^+ ions into T_d-WTe_2. Upon charging, the cycling curve is characterized by a voltage plateau in the range of 1.42-1.71 V which then increased monotonously to the cut off voltage, resulting in a charge capacity of 211 mAh g^{-1} with a coulombic efficiency (CE) of 73 %. The extra capacity upon discharge may be attributed to SEI formation, corroborating the CV data (Section 3.3.2.3) and is consistent with previous reports of analogous TMD systems ($MoTe_2$ cycled between 0.01 – 2.5 V at 1 A g^{-1} has a CE of 76 % [41] and MoS_2 cycled between 0.01 – 3.0 V at 40 mA g^{-1} has a CE of 53% [42]). The discharge and charge plateau matched exactly with the cathodic reduction and anodic oxidation peaks of the cyclic voltammogram (Figure 3.16).

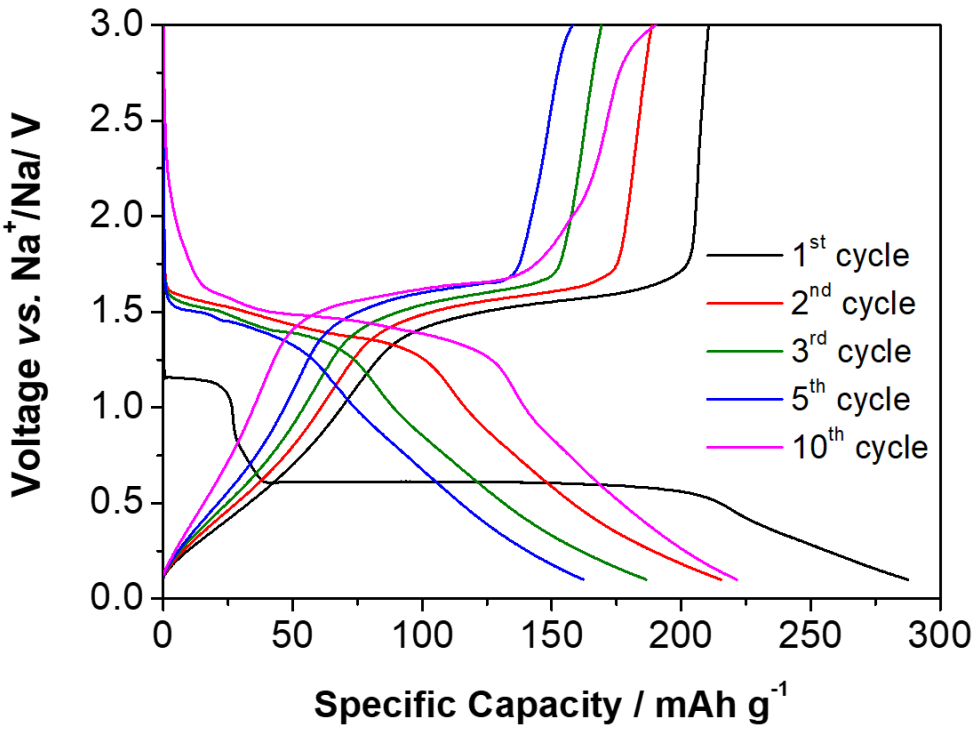

Figure 3.11 - Galvanostatic charge-discharge profiles at a current density of 10 mA g^{-1} of T_d-WTe_2 *vs* Na^+/Na in the voltage range of 0.1-3.0 V.

From the second cycle, the discharge plateau was evidenced from 1.32 V to 1.60 V and the charge plateau from 1.42 V to 1.64 V. An increase in the potential of the discharge plateau (ca. 1.50 V) is observed during this cycle, which mirrors the first charge process,

and is in agreement with the large shift in voltage of the two cathodic peaks observed in the cyclic voltammetry data (Figure 3.16). The increase in voltage has been previously attributed to the formation of ultrafine MTe_2 nanocrystals upon the insertion/extraction and conversion reaction that occurred in the first discharge and the charging process in the literature (MTe_2 (M = Fe, Co, Ni, Cu) materials [41], [43]–[45] and alloying metal tellurides like PbTe (LIBs) [46], SnTe (LIBs and SIBs) [23], [47], [48], Sb_2Te_3 [49], GeTe [48]).

Galvanostatic data show an initial decrease in discharge capacity from 288 to 162 mAh g^{-1} after 5 cycles (Figure 3.12) which then slightly increases to 221 mAh g^{-1} after 10 cycles. This increase in capacity can be attributed to the higher amount of active material exposed upon cycling. As reported in other MTe_2 type materials [42], the successive conversion reactions happening upon discharge and consequent breaking down of the original T_d-WTe_2 structure, as previously reported in [41], exposes the inner active material present in the electrode. The further reaction of extra WTe_2 available with sodium ions leads to an increase in the specific capacity obtained value that stagnates upon the unavailability of new material exposed. The capacity then stabilizes, leading to a discharge capacity of 183 mAh g^{-1} after 20 cycles, which corresponds to a 63.5 % capacity retention with respect to the initial discharge capacity. The capacity loss in other tellurium-based compounds has been previously attributed to the complete pulverisation of the active material upon insertion/extraction of Na^+ ions and exfoliation from the current collector which occurs within the first few cycles and eventually ends up in isolated and broken electrical connections [47].

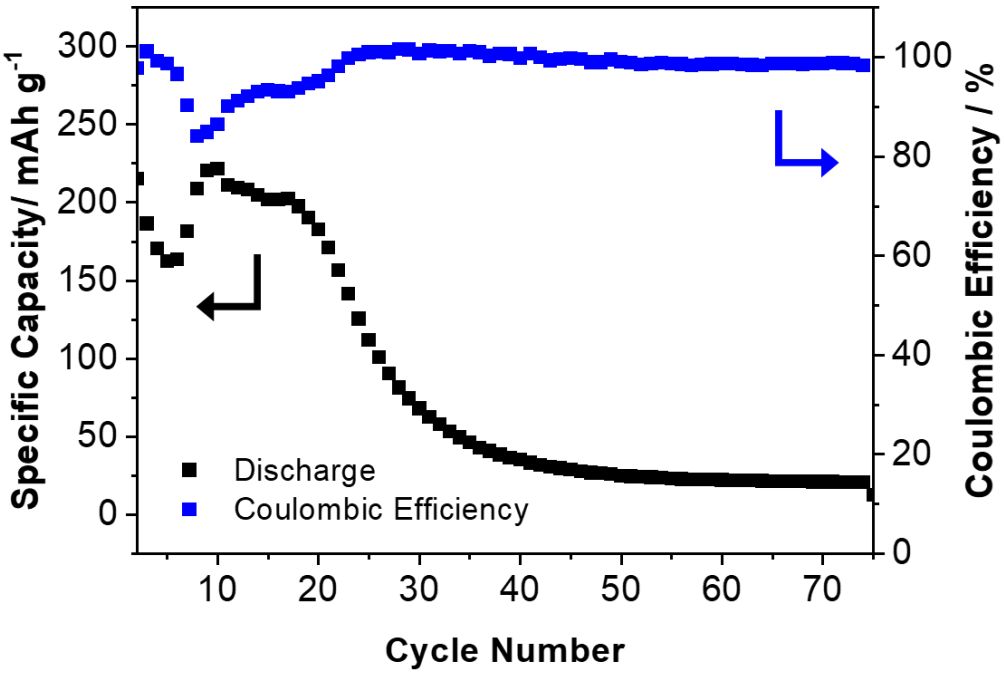

Figure 3.12 - Specific capacity vs cycle number plot with coulombic efficiencies over 75 cycles of T_d-WTe_2 in the voltage range of 0.1-3.0 V at 10 mA g^{-1}.

The rate capability of WTe_2 was tested in the 0.1 - 3.0 V voltage range at different current densities from 10 to 500 mA g^{-1} (5 cycles each) and then returned to 10 mA g^{-1} (Figure 3.13). The electrode shows discharge capacities of 194, 255, 225, 189, 125 and 52 mAh g^{-1} at 10, 20, 50, 100, 200 and 500 mA g^{-1}, respectively. To note that no noticeable decay is observed when the current is increased up to 100 mA g^{-1} (CE of 97 %), however when the current returns to 10 mA g^{-1} a discharge capacity of 147 mAh g^{-1} is achieved, which corresponds to half of the initial specific discharge capacity with a CE of 75 %.

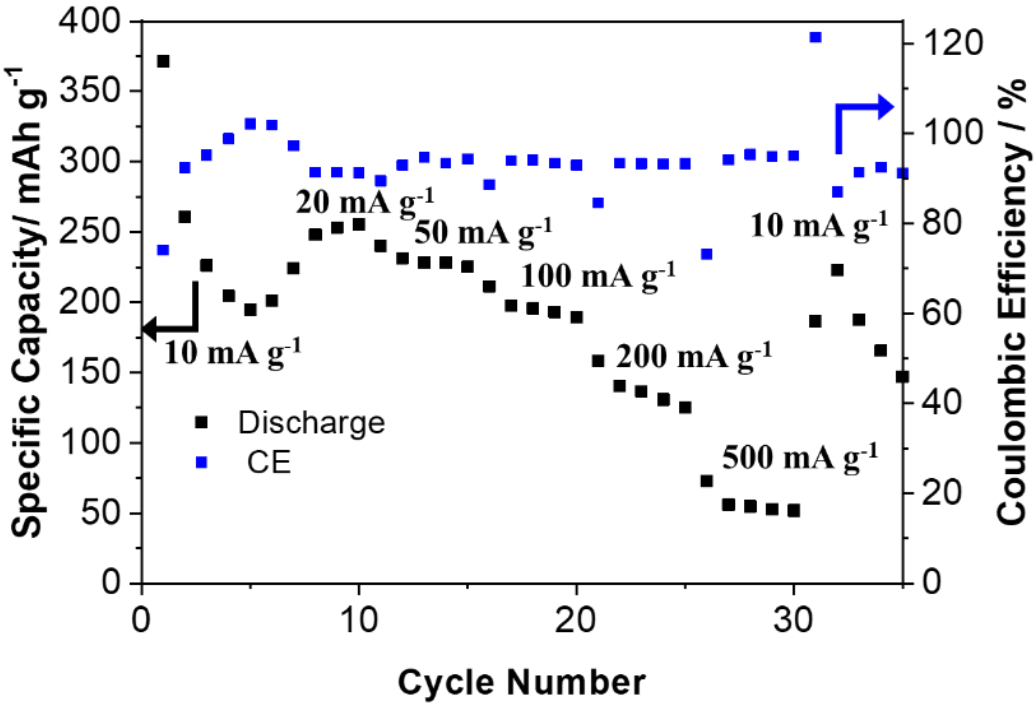

Figure 3.13 - Rate performance at current densities from 10 to 500 mA g^{-1} of T_d-WTe_2 in the voltage range of 0.1-3.0 V.

3.3.2.2 SEM analysis of post-mortem electrodes

The electrode's microstructure stability was studied by analysing long-term cycled electrodes using cycled SEM. WTe_2 microstructure evolution was evaluated by comparing the as-synthesized electrode with the electrode cycled to 25, 50 and 75 cycles (Figure 3.14). To note that in the fresh material (Figure 3.14a) most of the particles are dispersed while the particles are attached to a matrix in the cycled electrodes. This matrix is composed of PVDF, carbon and fibres from the glassfibre separator (evidenced by EDX results, not shown), elements used for the slurry preparation and battery making. In terms of particle size, after 75 cycles the average particle size is 7.8 µm which is twice bigger than the particles size before cycling. This increase in particle size can be related to the agglomeration of particles during the cycling process into the matrix which leads to the formation of bigger size crystals.

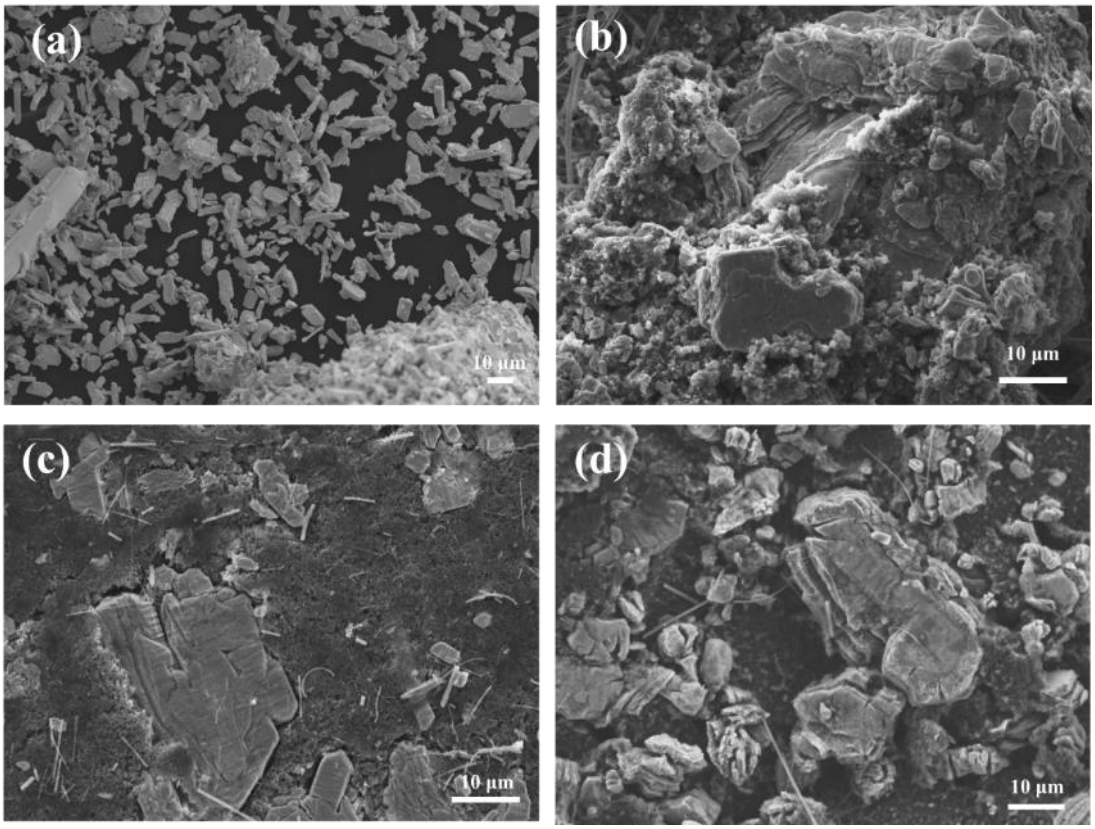

Figure 3.14- Morphology and structure change of the WTe_2 anodes during cycling against Na. The *ex situ* images of SEM were collected at selected cycles (a) pristine, (b) 25 cycles, (c) 50 cycles and (d) 75 cycles.

The formation of cracks and increased porosity as well as lattice breakdowns were previously reported in other MX_2 type materials [50] and can be seen in the SEM imaging of the WTe_2 after 75 cycles (Figure 3.15). Figure 3.15a shows the cracks (labelled with red arrows) formed in the electrode material because of the large strain generated by the removal of Na^+ ions during the charging process. It is worth noting that, although the material cracks, the bulk layered structure associated with WTe_2 is relatively well-preserved during cycling as seen in Figure 3.15b. These results reveal that, even though the insertion of Na^+ ions lead to changes in the material's volume, the crystal structure resists the major changes imposed by this volume expansion maintaining its original layered structure. The increased internal strain during reaction with sodium and consequent cracking of the material results in poor electrochemical performance as previously described (Section 3.3.2.1).

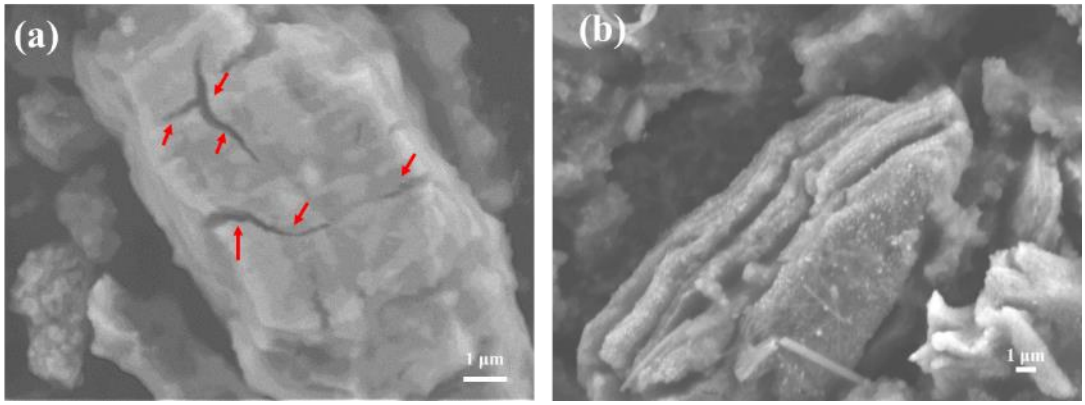

Figure 3.15- *Ex situ* SEM image showing (a) the crack formation in WTe_2 material after 75 cycles; the red arrows indicate the crack locations in the image, and (b) the layered structure of the material.

3.3.2.3 Cyclic Voltammetry

To probe sodium ion (de)intercalation into WTe_2, cyclic voltammetry studies (CV) were performed using Na half-cells in the voltage range of 0.1 – 3.0 V at a scan rate of 0.1 mV s^{-1} for five cycles (Figure 3.16).

The first cathodic scan shows two reduction peaks at 1.01 and 0.40 V which can be attributed to the reduction of the transition metal (W atom) during Na^+ ion intercalation and the corresponding anodic scan shows one oxidation peak at 1.59 V, related to the consequent oxidation of the W atom during Na^+ ion extraction. During the second scan, two new cathodic reduction peaks are observed at 1.47 and 1.22 V with the absence of the cathodic peaks observed in the 1st cycle, followed by the anodic oxidation peak with a gradual positive shift to 1.61 V. A similar trend was observed for the analogous MoX_2 (where X = Te, Se, S) and WTe_2 materials in the first two cycles [19], [41], [51]–[53]. By analogy to these systems, the first cathodic reduction peak observed at 1.01 V can be attributed to the insertion of Na^+ ion into the interlayer spacing of the pristine T_d-WTe_2 and possible formation of a $NaWTe_2$ phase. The second peak at 0.40 V was previously associated in other MTe_2 with the conversion reaction of $NaMTe_2$ to M metal and Na_2Te and the formation of solid electrolyte interphase (SEI) layer due to the irreversible electrochemically driven electrolyte degradation [19], [41]. This Na

insertion/extraction reaction mechanism will be discussed in detail in the following sections. The presence of new peaks in the second and subsequent cycles indicate a different Na^+ insertion mechanism to that observed in the first cycle. Overall, we observed that both cathodic and anodic peaks shift to higher voltages upon cycling, indicating a decrease in the electrochemical polarization [54]. Furthermore, the intensity of the peaks decreases with cycling, which is indicative of capacity loss, as observed in the galvanostatic data.

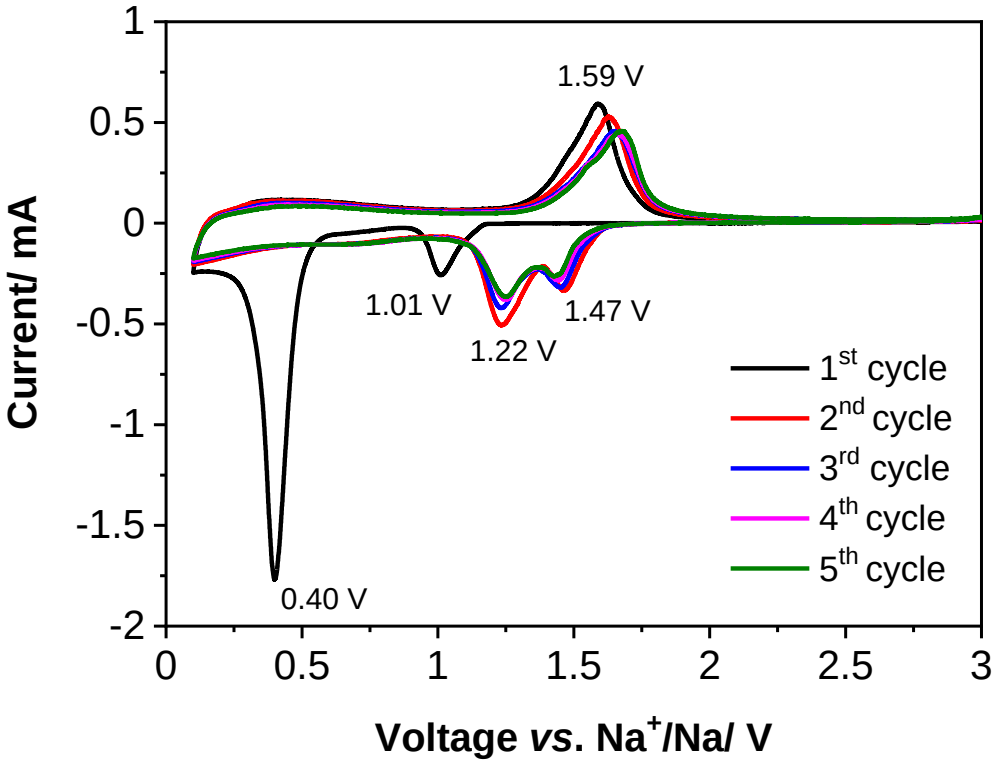

Figure 3.16 - Cyclic voltammogram of T_d-WTe_2 vs Na^+/Na in the voltage range 0.1 – 3.0 V at a scan rate of 0.1 mV s^{-1}.

The kinetics transport mechanism of WTe_2 during sodiation and desodiation processes was studied by performing CV experiments at different scan rates and the second cycle is shown in Figure 3.17. Starting from 0.1 to 1 mV s^{-1}, a peak shift towards higher potential during the charging process was observed when an increased current rate is applied. This indicates, just as stated before, a decrease in the electrochemical polarization of the electrode [54].

Figure 3.18 shows the plot of Log(i_p) *vs* Log(v) which slope corresponds to the values of *b*. The calculated *b* values for the discharge I and II and charge III peaks are estimated to be 0.75, 0.81 and 0.77, respectively which suggested that both surface-controlled and diffusion-controlled reactions are occurring in the WTe_2 electrode during cycling. As reported for $MoTe_2$ (values between 0.743 and 0.961) [41], [55], the pseudocapacitance process in WTe_2 electrodes can be suggested to be the primary process controlling the reaction kinetics in this system which can be related to the superior performance of the electrode at higher current density as observed from the rate capability study (Section 3.3.2.1).

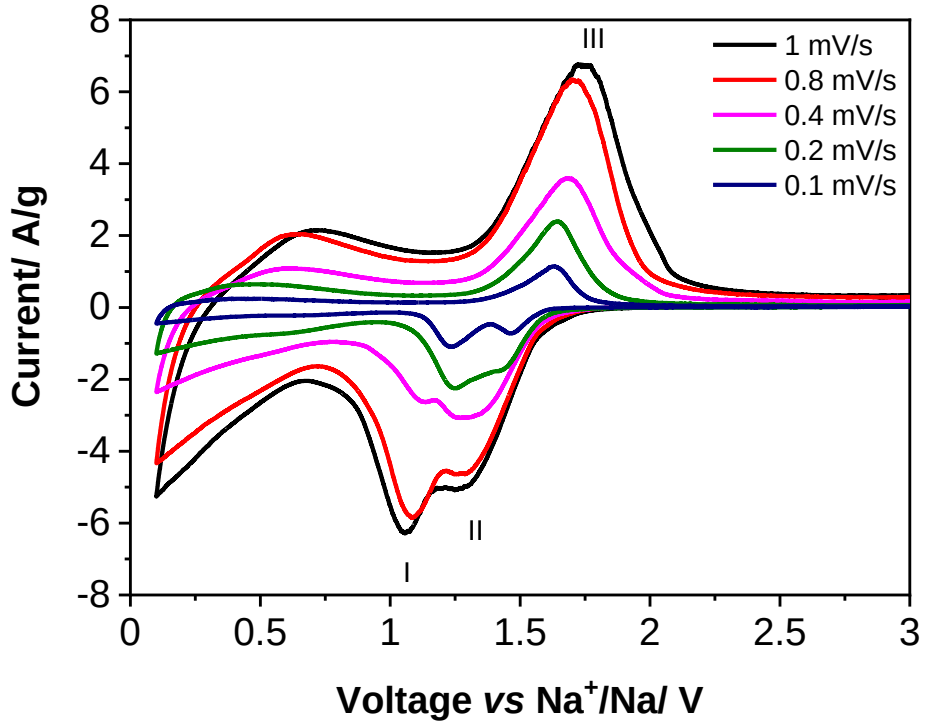

Figure 3.17 - Cyclic voltammogram of the second cycle of the WTe_2 electrode at different scan rates within the potential window 0.1–3.0 V.

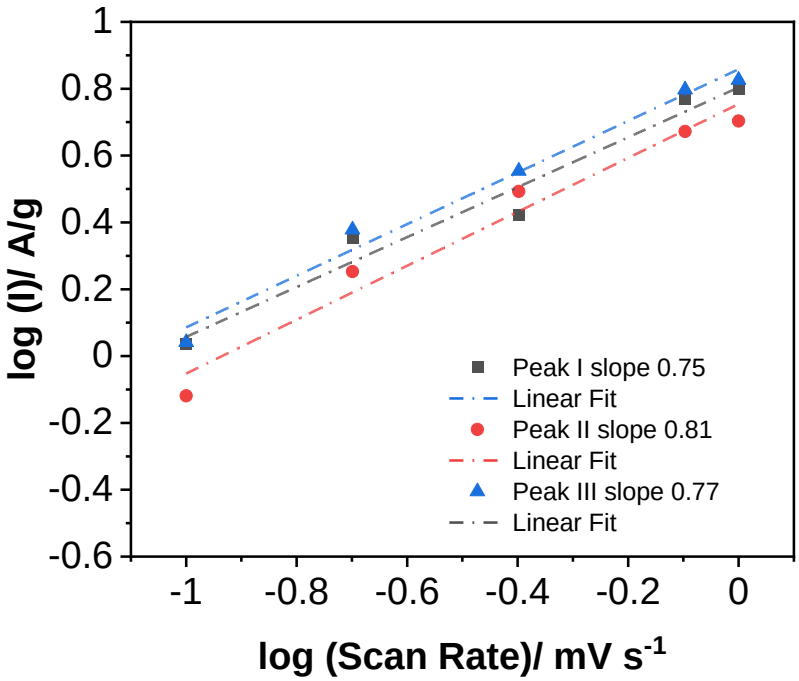

Figure 3.18 - Linear relationship between Log I (logarithm peak currents) and log V (logarithm scan rate) of the reduction peaks (I and II) and oxidation peaks (III) at different scan rates (0.1, 0.2, 0.4, 0.8, and 1.0 mV s^{-1}). R^2 values of 0.952, 0.958 and 0.978, respectively.

A quantitative description of both processes can be achieved by the different sweep rates of the obtained CV results according to the equation:

$$i(V) = k_1 v + k_2 v^{1/2} \quad (3.2)$$

Where i(V) represents the total current and results from the contribution of the surface capacitive process ($k_1 v$) and the diffusion-controlled insertion process ($k_2 v^{-1/2}$) respectively. Figure 3.19a shows the plot of $i(v)/v^{1/2}$ *vs* $v/v^{1/2}$ for the oxidation peak III where the slope corresponds to the value of k_1 and the intercept b value to the value of k_2. The calculation of both k values for every reduction and oxidation peak at various scan rates allows calculating the ratio of pseudocapacitive and diffusion-controlled processes at each scan rate. Figure 3.19b shows the fitted CV curve at 0.1 mV s^{-1} where the pseudocapacitive is represented as the inner coloured graph.

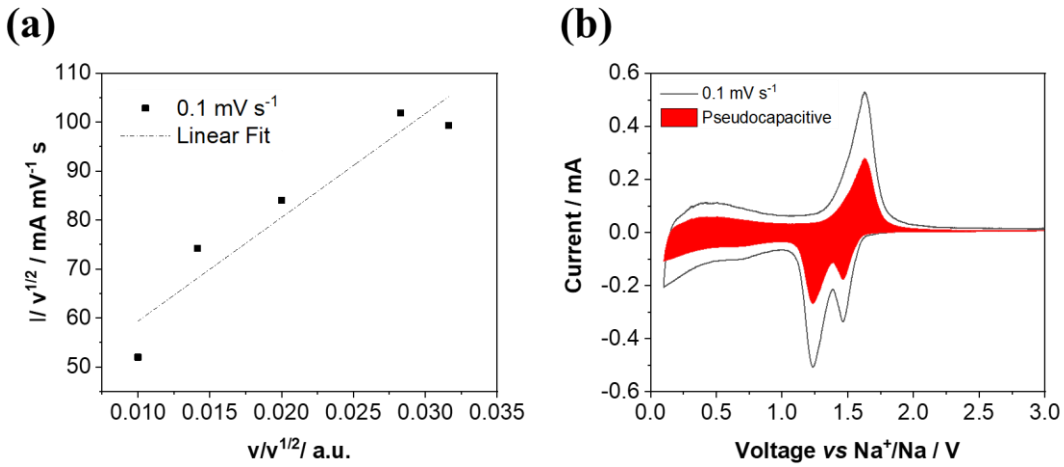

Figure 3.19 – (a) Linear relationship between $I/v^{1/2}$ and $v/v^{1/2}$ at 0.1 mV s^{-1}, R^2 value of 0.908. (b) Fitted pseudocapacitive contribution (red area) of the WTe_2 electrode at a scan rate of 0.1 mV s^{-1} in the potential window, 0.1–3.0 V.

Quantitatively, 53% of the total capacity (highlighted in red in Figure 3.19b) arises from capacitive behaviour at a sweep rate of 0.1 mV s^{-1}. This is lower compared to $MoTe_2$, which presents a value of 61 % at the same scan rate [41]. The difference between the two electrode materials may arise from differences in pseudocapacitive processes occurring during ion intercalation/extraction, however further studies are needed to better understand this idea. Contribution ratios between capacitive and diffusion processes at different scan rates show that the capacitive contribution increases with increasing scan rates (Figure 3.20). The results obtained show that the capacitive contribution of the WTe_2 electrode becomes predominant at higher current densities (see Annexe A - CV Data Calibrations for WTe2 in SIBs for individual k_1 and k_2 data) as a result of faster reversible redox reactions occuring on the electrode material.

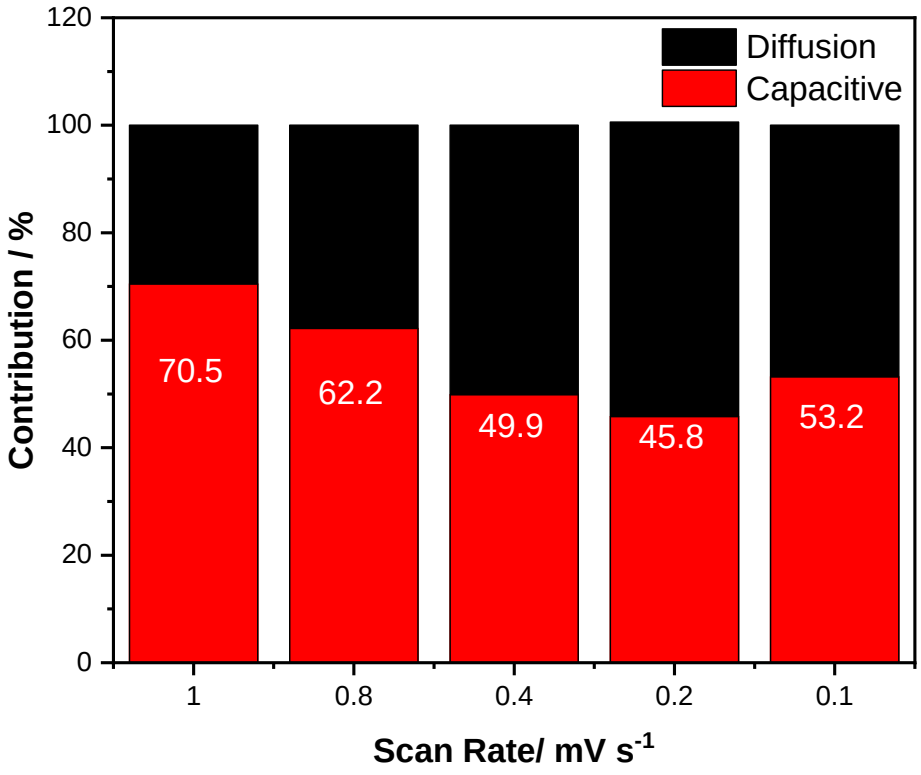

Figure 3.20 - Ratio of pseudocapacitive (red) and diffusion-controlled (black) capacities at various scan rates of WTe_2 electrodes.

The Na^+ ion diffusion coefficients (D_{Na^+}) were calculated using the Randles-Sevcik equation (Chapter 2, Section **Error! Reference source not found.**) [56] and values are shown in Table 3.2. The ion diffusion coefficient in WTe_2 can be extrapolated from the plot representing the relationship between the peak's current and the square root of the scan rate shown in Figure 3.21. As mentioned previously, the complete process of Na^+ ion intercalation and extraction into the layered WTe_2 material is controlled by both capacitive and diffusion, and the linear relationship here presented between the two parameters is only related to the diffusion process occurring. The obtained values for the Na^+ apparent diffusion coefficients at different anodic and cathodic peaks are within the range of $1.02\times10^{-9} - 9.19\times10^{-11}$ cm^2 s^{-1}, as shown in Table 3.2.

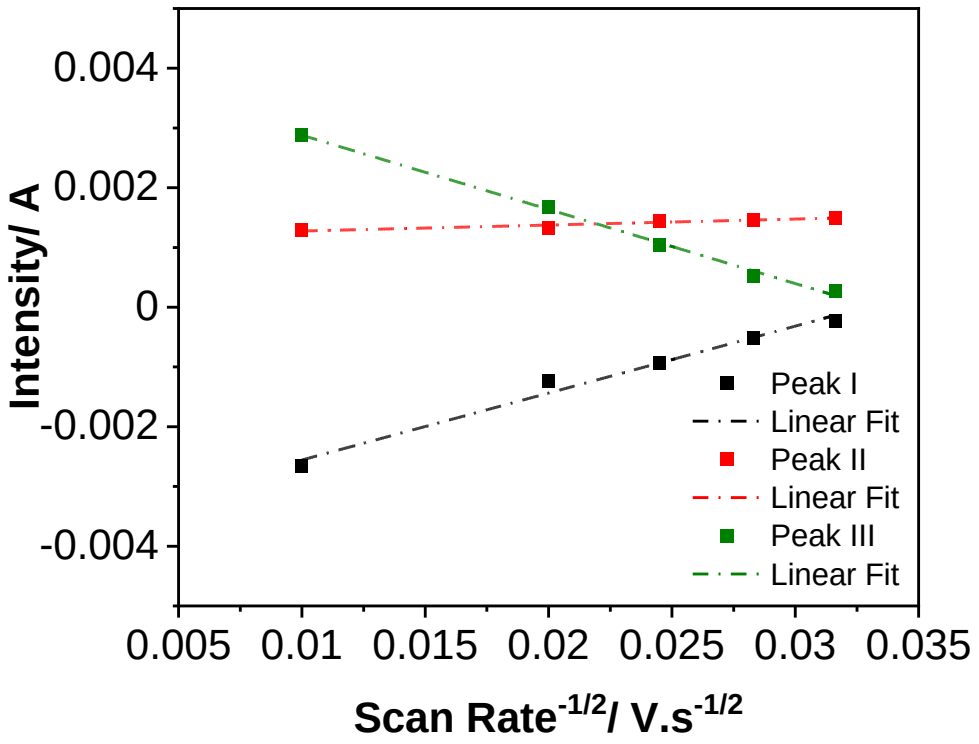

Figure 3.21 - Linear fitting of the peak current versus the square root of the scan rate of the reduction (I and II) and oxidation (III) peaks. R^2 values of 0.979, 0.848 and 0.995, respectively.

Table 3.2 - Diffusion coefficient for each peak calculated from the Randles-Sevcik equation

CV Peak	D_{Na^+} ($cm^2\ s^{-1}$)
I	1.02×10^{-9}
II	9.19×10^{-11}
III	1.14×10^{-9}

The lowest value of the diffusion coefficient is registered for peak II at 1.47 V with a value of 9.19×10^{-11} $cm^2\ s^{-1}$. At the beginning of the discharge process, the insertion of Na^+ ions are controlled by a diffusion process where the ions move from an area of high concentration (counter electrode, Na metal) to an area of low concentration (WTe_2).

Data indicates that the bottleneck step in the cycling process comes from the insertion of Na^+ ions into the WTe_2 material to form a sodiated Na_xWTe_2 phase [19] (associated with the cathodic peak labelled as II in Figure 3.17). Upon further discharge, the value of diffusion coefficient increases to 1.02 x 10^{-9} cm^2 s^{-1} in the second peak I at 1.22 V showing that, once the initial insertion of ions occurs the further insertion of Na^+ ions become easier. The deinsertion of Na^+ ions in charge are shown to be in the same order as for the process related to peak I (1.14 x 10^{-9} cm^2 s^{-1}) indicating that the bottleneck step in the cycling process is during the initial insertion of ions into the WTe_2 layer. These results imply that the material becomes more stable when cycled at voltages under 0.6 V, once the major crystal restructuration is accomplished as a result of ion insertion. Overall, WTe_2 electrodes show similar D_{Na^+} values to other tellurium-based materials ($\approx 10^{-9}$) [41], [57], which are, in turn, higher than other dichalcogenide materials such as $MoSe_2$ and MoS_2 ($\approx 10^{-12}$) [58], [59].

3.3.2.4 Electrochemical Impedance Spectroscopy

Electrochemical impedance spectroscopy is one of the most used techniques to elicit the electrochemical processes occurring at the electrode-electrolyte interface. To further understand the good electrochemical performance and conductivity of the T_d-WTe_2 anode, electrochemical impedance spectroscopy (EIS) analysis was performed. Figure 3.22 shows the impedance spectra of as-prepared T_d-WTe_2 obtained at an open-circuit voltage (OCV) in a frequency ranging from 0.01 Hz to 100 kHz. The spectrum was fitted based on the equivalent circuit in the inset of Figure 3.22. The equivalent-circuit model is a way to describe the electrochemical reaction steps occurring inside the cell [41]. A general Nyquist plot is usually divided into three distinct regions: (i) a small semicircle at high frequencies related to the migration of the ions across the surface of the electrode, (ii) a semicircle at a middle frequency related to the charge-transfer resistance process between the electrolyte and the surface of the electrode and (iii) a step inclined line or curve at low frequencies assigned to the solid-state diffusion kinetics of the ions throughout the active material [60].

The equivalent circuit for the OCV system is composed of a surface resistance (R_S) at high frequencies and a charge-transfer resistance (R_{CT}) along with a constant phase

element (CPE). The intercept at the Z' axis in the high-frequency range, R_S, is dominated by the electrolyte resistance while the high-medium frequency semicircle, R_{CT}, refers to the charge-transfer resistance for electrons and Na^+ ions across the electrode-electrolyte interface [61]. The CPE corresponds to the electrical double layer capacitor that forms on the interface between the electrode and electrolyte, resulting from the adsorption of Na^+ ions from the electrolyte onto the surface of the electrode. The charge transfer resistance in OCV is determined to be 409.2 Ω.

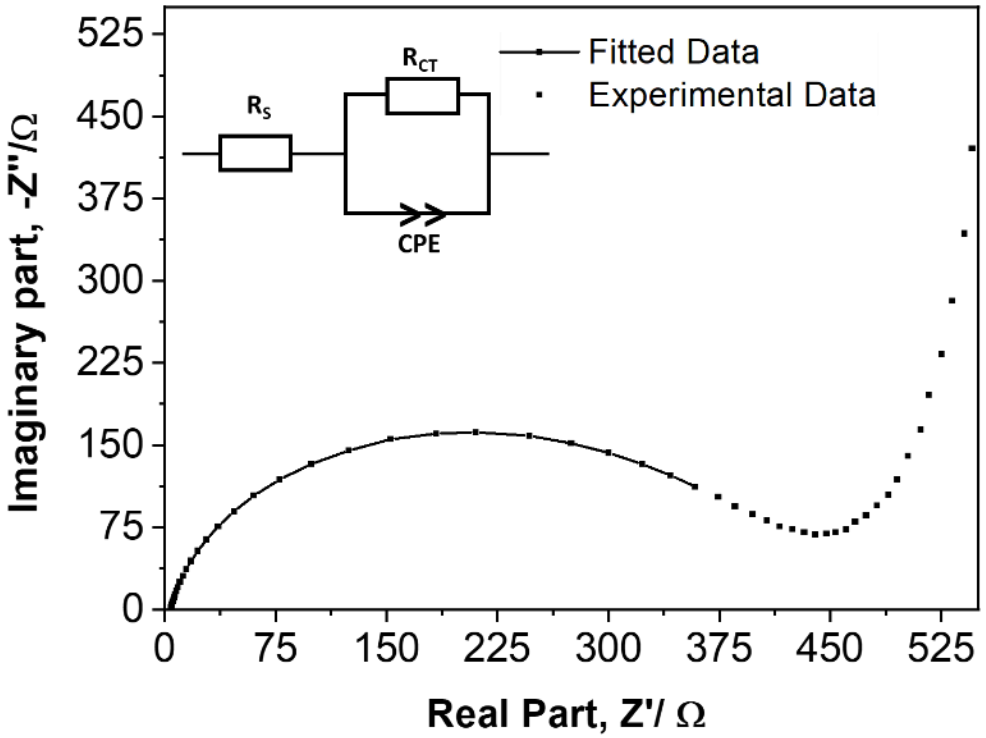

Figure 3.22 - Nyquist impedance plot collected from 0.01 Hz to 100 kHz for WTe_2 in SIBs in OCV.

Figure 3.23 shows the evolution of the impedance spectra during the 1st cycle discharge and charge processes. To note that the arc radius progressively becomes smaller with cycling, suggesting a less resistive interface between the electrolyte and electrode and a smaller charge-transfer resistance. The equivalent circuit used to fit the data of the discharge and charge spectra was composed of, besides an R_s at high frequencies and a charge-transfer resistance R_{CT} along a constant phase element (CPE), of an extra R_{SEI} and correspondent CPE element related to the solid electrolyte interface (SEI) formed after the 1st discharge process. It is observed that the Nyquist graphs for all observations

show discrete semicircles at a higher frequency as a result of the impedance phenomena occurring due to the surface film passivation, electrolyte resistance and the sodium intercalation process [62]. The first discharge process is accompanied by the formation of the SEI layer at the end of the first discharge, which leads to the presence of a single semicircle with the contribution of both the SEI layer and charge-transfer resistance processes. The proximity of the relaxation time constant of both processes results in the observation of a single semicircle as a result of the overlapping of both individual circles, however, both processes can still be distinguished. In this case, the equivalent circuit showed in the inset of Figure 3.23 is the more appropriate to fit the results obtained. The SEI layer and charge transfer resistance were found to be 5.4 and 46.2 Ω, respectively. The arc resistance considering both processes is found to be 51.6 Ω for the 1st discharge process. This abrupt decrease of resistance was registered in other MTe_2 materials and was attributed to the formation of ultrafine nanocrystals upon the conversion reaction of MTe_2 into Na_2Te and M during the 1st discharge [41], [63]. The decrease in arc resistance observed indicates that the material is in a more stable state at the end of the discharge process which agrees with the cyclic voltammetry at different rates presented previously (Section 3.3.2.3). Upon the 1st charge, both the R_{SEI} and R_{CT} values decrease to 3.6 and 10.7 Ω, respectively. The abrupt decrease in R_{CT} value upon deinsertion of Na^+ ions show an increase in the Na^+ diffusion and high stability of the discharge/ charge capacity of the cycled electrode. This is the opposite of the EIS results observed in $MoTe_2$ cycled against Na, revealing that WTe_2 is structurally less stable than other TMDs compounds [41]. The lower R_{CT} value of the charging process compared with the discharging process can be associated with the partial destruction of the SEI upon ion extraction which leads to lower overall resistance in the system and the formation of ultrafine nanocrystals during the 1st discharge process. The value of the different resistances for the 1st cycle can be found in Table 3.3.

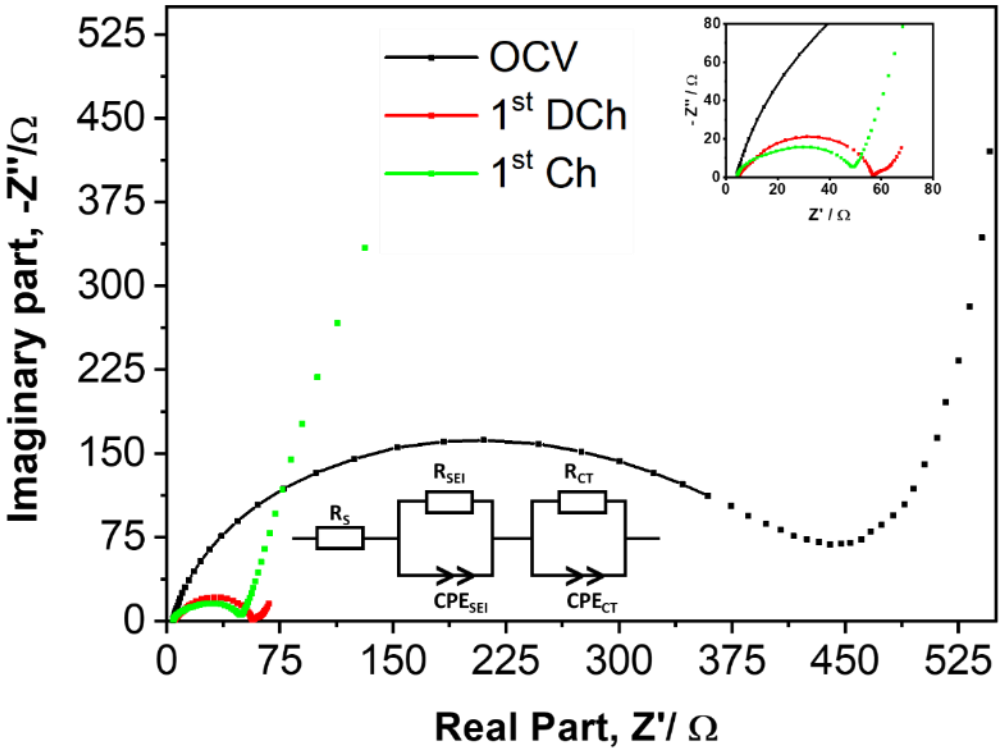

Figure 3.23 - Nyquist impedance plots collected from 0.01 Hz to 100 kHz for WTe_2 in SIBs in OCV, 1st discharge, and 1st charge.

Table 3.3 - Electrolyte, SEI and charge-transfer resistances determined from EIS during the 1st cycle for WTe_2 in SIBs.

Sample	R_S (Ω)	R_{SEI} (Ω)	R_{CT} (Ω)
OCV	3.3		409.2
1st Discharge	4.9	5.4	46.2
1st Charge	4.2	3.6	10.7

The evolution of the EIS spectra was studied up to the 10th cycle to understand the changes in both SEI layer and charge-transfer resistance. Figure 3.24 shows the evolution of the discharge process. To note that the equivalent circuit to fit the EIS data

used was the same as for the 1st discharge composed by an initial R_s at high frequencies, a charge-transfer resistance R_{CT} along with a constant phase element (CPE) and an R_{SEI} and correspondent CPE element at low frequencies.

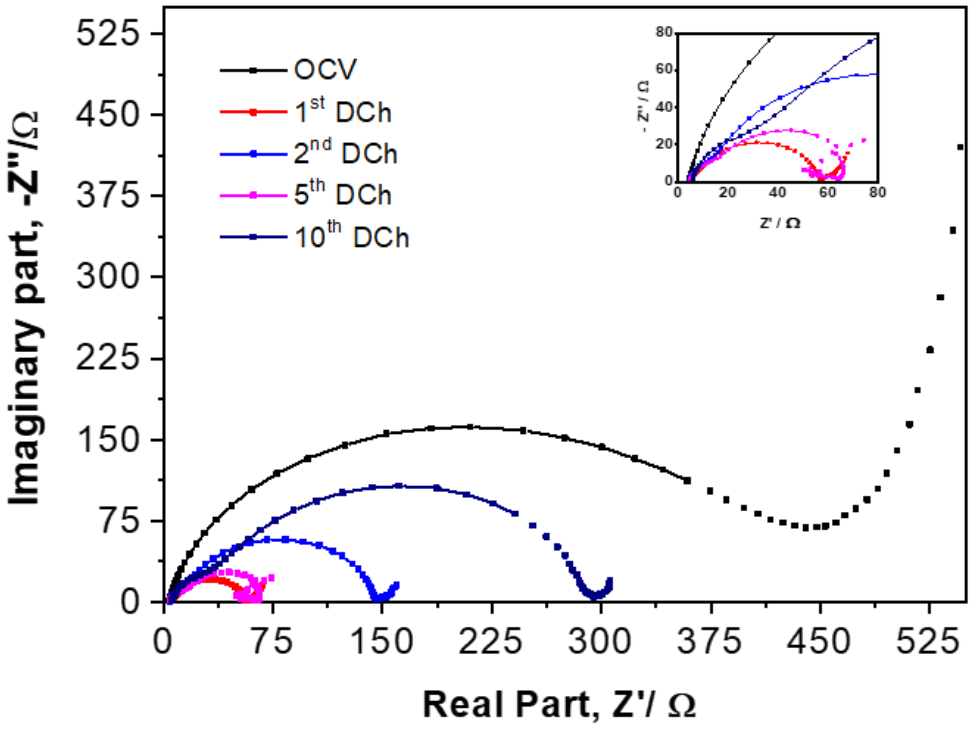

Figure 3.24 - Nyquist impedance plot collected from 0.01 Hz to 100 kHz for WTe_2 in SIBs during the discharge process up to the 10th cycle.

A major increase in total arc resistance from 51.6 Ω for the 1st discharge to 140.9 Ω for the 2nd discharge is observed. The high resistance registered for the 2nd discharge can be associated with the increased resistance linked with the increased interlayer spacing as a result of the extraction of Na^+ ion from the WTe_2 structure during the initial charge process. The relationship between interlayer spacing expansion and charge transfer was previously studied and results show that both R_{SEI} and R_{CT} increase with increasing interlayer spacing especially when the interlayer spacing is larger than 7.3 Å [64]. The increase in R_{SEI} value registered for this cycle (130.0 Ω *vs* 5.4 Ω for the 1st discharge) can be also related to the poor adhesion strength between the electrode material and current collector upon cycling [65]. Further discharge up to the 5th cycle results in a decrease of the overall arc resistance to 72.5 Ω, which can be related to the slight

increase in capacity observed during long cycling as the higher amount of active material exposed upon cycling results in a decrease of resistance and easier insertion of Na^+ ions. Further cycling leads to an increase of impedance again up to the 10th discharge (289.8 Ω). To note the high value of R_{CT} (261 Ω) recorded can be ascribed to the formation of excessive SEI film inside the interlayer related to the increased interlayer spacing [64], [66]. Although the increased resistance recorded upon cycling, the arc resistance continues lower than the registered at the OCV stage. The value of the different resistances is shown in Table 3.4.

Table 3.4 - Electrolyte, SEI and charge-transfer resistances determined from EIS during the discharge processes for WTe_2 in SIBs.

Sample	R_S (Ω)	R_{SEI} (Ω)	R_{CT} (Ω)
OCV	3.3		409.2
1st Discharge	4.9	5.4	46.2
2nd Discharge	4.2	130.0	10.9
5th Discharge	4.6	12.2	60.3
10th Discharge	5.7	28.8	261.0

The same equivalent circuit discussed previously was used to fit the impedance data collected during the charging process upon cycling (Figure 3.25). Contrarily to the trend observed during the discharge process, the charging data suggests a steadier trend of the overall value of arc resistance. The R_{SEI} and R_{CT} calculated up to the 5th charge are similar in every charging process with a slight increase in total resistance from 46.3 Ω to 54.4 Ω from the 1st to the 5th charging process. At the 10th charge, the spectrum shows the presence of two semi-circles that partially overlap in the high-medium frequency range. The arc at high frequency is assigned to the Na^+ ion migration through the SEI layer and the arc at medium frequency is assigned to the charge transfer resistance at the interface between the electrolyte and the electrode. This indicates that the relaxation

time constant of the SEI layer and charge-transfer resistance become significantly different, allowing the observation of their responses. This can be related to the presence of difference resistance species at this moment in time, although further analysis is necessary to confirm this theory. Although the slightly different spectrum observed, the same equivalent circuit used to fit the data of the 1st discharge was used. The SEI layer and charge-transfer resistances were found to be 104.0 Ω and 39.0 Ω, respectively.

Table 3.5 shows the resistance values obtained for the charging process up to the 10th cycle.

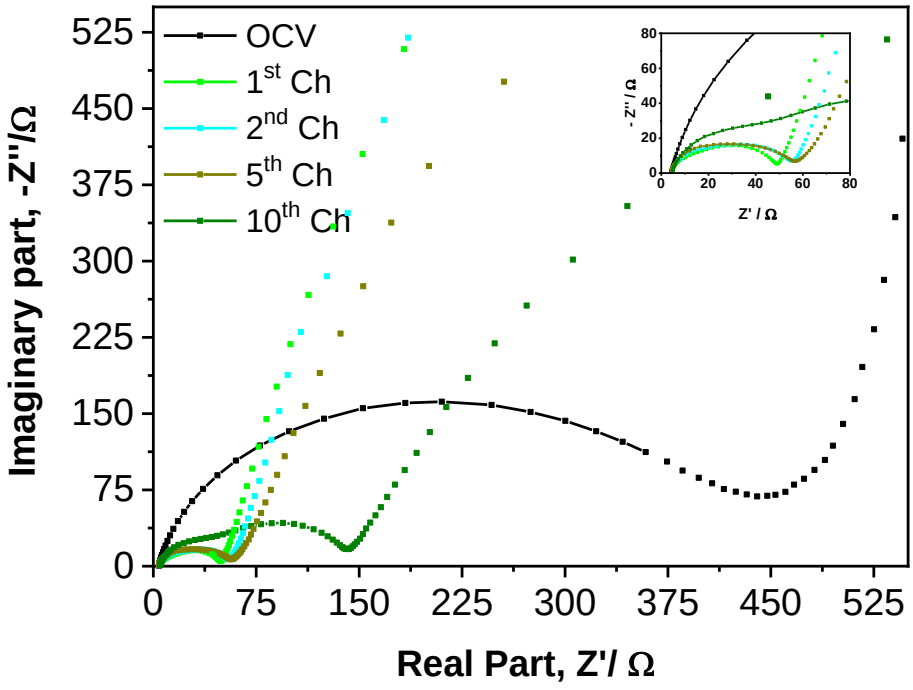

Figure 3.25 - Nyquist impedance plot collected from 0.01 Hz to 100 kHz for WTe_2 in SIBs during the charging process up to the 10th cycle.

Table 3.5 - Electrolyte, SEI and charge-transfer resistances determined from EIS during the charging processes for WTe_2 in SIBs.

Sample	R_S (Ω)	R_{SEI} (Ω)	R_{CT} (Ω)
OCV	3.3		409.2
1st Charge	4.2	35.6	10.7
2nd Charge	4.2	36.5	16.4
5th Charge	4.1	18.9	35.5
10th Charge	4.6	104.0	39.0

Based on the equivalent circuit of the inset of Figure 3.23, the charge-transfer resistance (R_{CT}) was evaluated after 25 and 75 cycles. Figure 3.26 shows an increase in arc radius upon 25 cycles as well as the presence of two semi-circles which can be associated with the increase in overall resistance in the cell upon consecutive Na^+ insertion/ extraction.

Table 3.6 shows the evolution of the R_{SEI} and R_{CT} value upon long cycling. The R_{CT} value after 25 and 75 cycles was registered to be 279.6 and 403 Ω, which is smaller than that registered at OCV (409.2 Ω). The decreases in overall R_{CT} value recorded suggests that the process occurring in the WTe_2 electrode may get faster as the galvanostatic charge-discharge happens due to the lower amount of Na^+ ions that are being intercalated [67]. Furthermore, a major increase in the R_{SEI} value in cycle 25 compared with cycle 10 (562.4 *vs* 104 Ω) is observed. This increase occurs simultaneously with the capacity loss observed in the charge-discharge curves (Section 3.3.2.1). As stated previously, the loss of capacity observed can be related to the pulverization of the active

material upon insertion/extraction of Na^+ ions and exfoliation from the current collector [47]. The movement of Na^+ ions into the WTe_2 conducts to large-volume changes within the crystal structure which is responsible for an increase of the SEI layer. This effect is observed in other high-capacity electrodes as a result of the stress/strain process induced during the first sodiation which can be related to the cell's capacity fading and increase in R_{SEI} value registered [68]–[70]. To note that on the 75th cycle, a single semi-circle is observed similarly to the OCV state, however at this point both SEI layer and charge-transfer processes occur. The similar time constant of the SEI and charge-transfer processes leads to a merge of the semi-circles associated with each process and the visualization of a single semi-circle. This can be accounted to stabilization of the internal resistance from the electrode and interfacial resistance between the active material and current collector [71]. The consecutive charge/discharge cycles lead to the stabilization of the SEI layer, which leads to the presence of a single semi-circle in the EIS spectra.

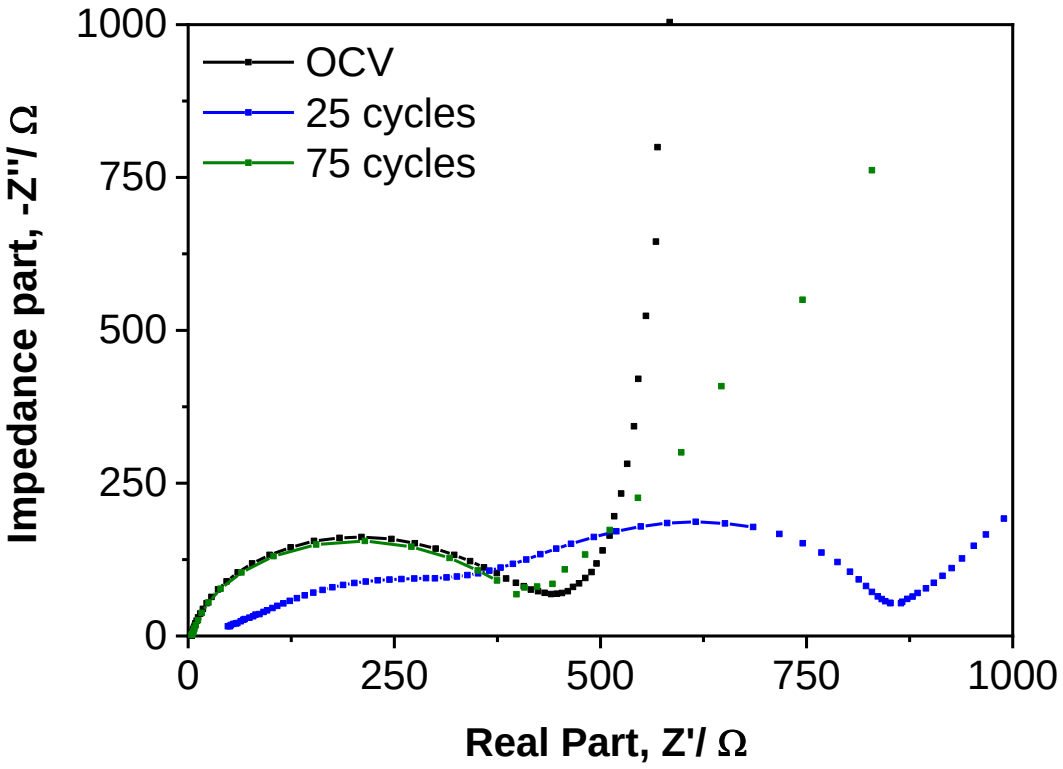

Figure 3.26 - Nyquist impedance plot collected from 0.01 Hz to 100 kHz for WTe_2 in SIBs at OCV, 25th and 75th cycles.

Table 3.6 - Electrolyte, SEI and charge-transfer resistances determined from EIS upon long cycling for WTe_2 in SIBs.

Sample	R_S (Ω)	R_{SEI} (Ω)	R_{CT}(Ω)
OCV	3.29		409.2
25th Cycle	49.2	562.4	279.6
75th Cycle	4.21	(R_{SEI} + R_{CT}) 403	

3.3.3 Structure evolution upon Na^+ ion intercalation

3.3.3.1 X-ray Absorption Near Edge Spectroscopy

To gain more insight into the oxidation state of the W and Te elements in T_d-WTe_2 electrodes at different charge/discharge depths, *ex situ* X-ray absorption spectroscopy measurements were performed. When measuring a XANES spectrum, different absorption edges can be used depending on the element analysed and the information required. The K-absorption edge region depicts the interactions of the inner s shell electrons while the L-edge depicts the interactions occurring in the outer shell electrons (d and f) [72]. The information that is obtained from each electron shell is slightly different. Electron transitions occurring in the s orbital contain more information compared with higher orbital electrons as s electrons are closer to the element's core [73], [74]. L-edges typically provide information regarding the oxidation state of the element as geometric information is harder to extract for the d and f electronic transitions. The appearance of a spectral signal - White Line – as a result of the different partial filled d and f electron transitions occurring is responsible for masking the information of the edge. The white line results from electronic transitions of p electrons into the d and f orbitals and is only observed in heavier elements with partial filled d and f orbitals [75]. To note that L-edges usually contain less information

compared with K-edges due to weaker electronic interactions. When analysing heavier elements (such as W), the L_{III}-absorption edge is usually reported, and the white line signal is analysed. This feature can provide information regarding the structure and composition of the coordination environments in heavier elements [75]. For these experiments, information about the local symmetry, coordination, and valence for the W and Te elements was provided measuring the X-ray absorptions at the L_{III} and K-edge, respectively.

Normalised XAS spectra of the electrodes at the W L_{III} edge show a white line that corresponds to a transition of $2p_{3/2}$ electrons toward unoccupied $5d_{3/2, 5/2}$ orbitals [76] (Figure 3.27). The intensity of the white line for this edge is related to the unoccupied 5d orbitals of the element, providing information about the oxidation state of W. The intensity of the white line provides direct information about the oxidation state of W; the stronger the white line, the less filled the orbitals and the higher the oxidation state is [77]. Contrarily, for the K-edge the edge position is related to the oxidation state of the absorber ion, where lower oxidation states lead to lower energies. By direct comparison with the intensity of the W L_{III} while lines from the W(0) and WO_2 (+4) standards it was inferred that the oxidation state of W is close to +4 (energy of 10207.30 eV). Furthermore, the non-existence of a post-edge feature indicates that the W atom is octahedrally coordinated in the crystal lattice [76], as expected in this material [2], [30].

Three main points were analysed at a voltage of 0.6 V once this is the voltage where the main plateau of T_d-WTe_2 is located and where the conversion reaction is expected to occur. Upon discharge to 0.6 V (insertion of ~0.7 Na^+ ions), the intensity of the white line increases, indicating that electrons are being extracted from the 5d orbitals of W during Na^+ insertion [77] to form a sodiated phase, Na_xWTe_2. The displacement of the electron density from the metal atom towards the Te or Na atoms during the initial insertion of Na^+ into the structure is responsible for the decrease in occupied W 5d orbitals and consequent increase in white line intensity [77]. No major changes in the white line intensity are observed at the middle plateau (0.6 V MP), suggesting that further insertion of 1.3 Na^+ ions (total of 2 Na^+ ions) does not considerably influence the electronic configuration of W. At the end of the plateau (0.6 V EP), a decrease in white line intensity is observed, with values similar to the OCV state, implying that the electrons occupy the 5d orbitals in this process. A decrease in oxidation state is expected

at this point as a result of the following insertion of 1.3 ions during the second part of the plateau. This decrease in white line intensity can be accounted for by the changes in valence bond and coordination environment of the metal atom as the Na^+ ions surge into the system [25]. The exact oxidation state of W cannot be accessed at this point, but it is believed to be between 4-x and 0. From 0.6 V to 0.1 V, an increase in white line intensity is observed as an initial reduction of the telluride bonds occur which increases the oxidation state of the W atom. During this step, the formation of NaTe phases and W metal is expected as reported in other ditelluride materials [2], [30]. The white line intensity of the fully discharged electrode is always larger than the W metal spectrum, showing that the d electrons of the W deviate towards the Na or Te atom during the charge and discharge process. This effect was observed during the (de)lithiation of WS_2 and explained by the formation of weak bonds between W and Li_2S (or S) [77]. The changes in the trend of the white line intensity can be attributed to the change in the coordination environment as well as the geometry of the metal atom resulting from the two-step transformation of W ion from T_d-WTe_2 to Na_xWTe_2 and disintegration of T_d-WTe_2 to W and Te/$NaTe_2$ upon insertion of Na^+ ion [25].

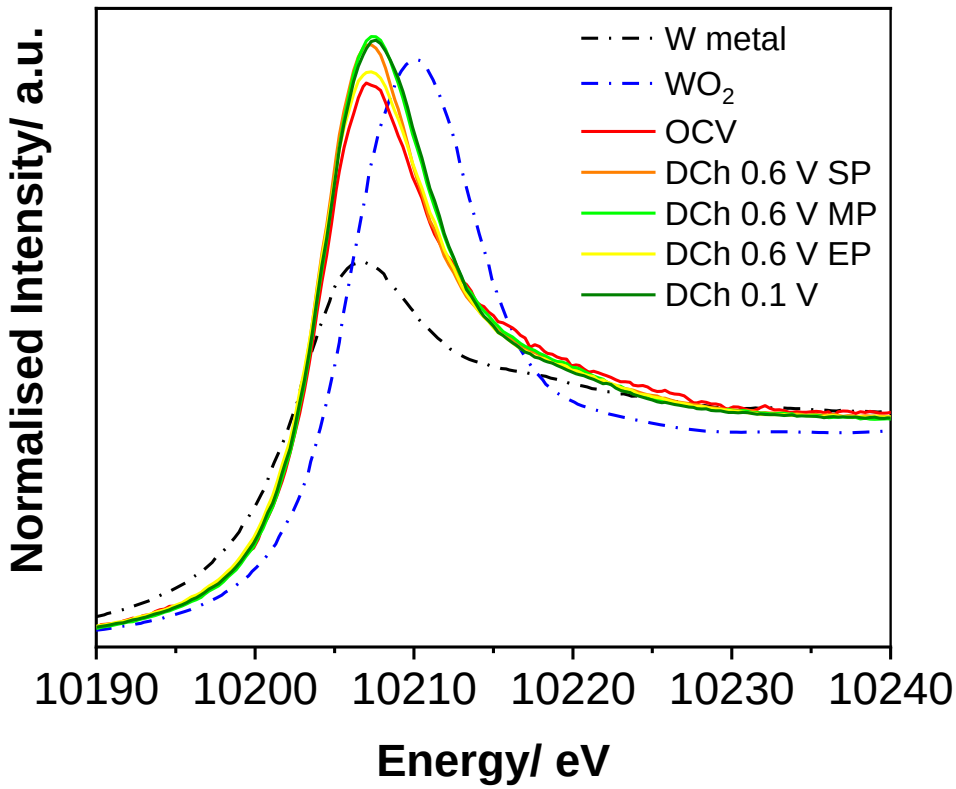

Figure 3.27 - Normalized W L_{III}-edge XANES spectra of WTe_2 electrode during the 1st discharge process along with standard W metal and WO_2 powder used as reference.

Upon charging (Figure 3.28), a decrease in the W white line intensity is observed from the discharge state down up to 3.0 V. We explain this decreasing trend with the filling of d orbitals upon Na^+ extraction due to the reformation of the WTe_2 phase. To note that at the end of 1st charging process the white line intensity is slightly lower than the one registered at OCV state which suggests that the W atom is in a more reduced state upon ion deinsertion compared with pristine, however further data needs to be collected to corroborate this point.

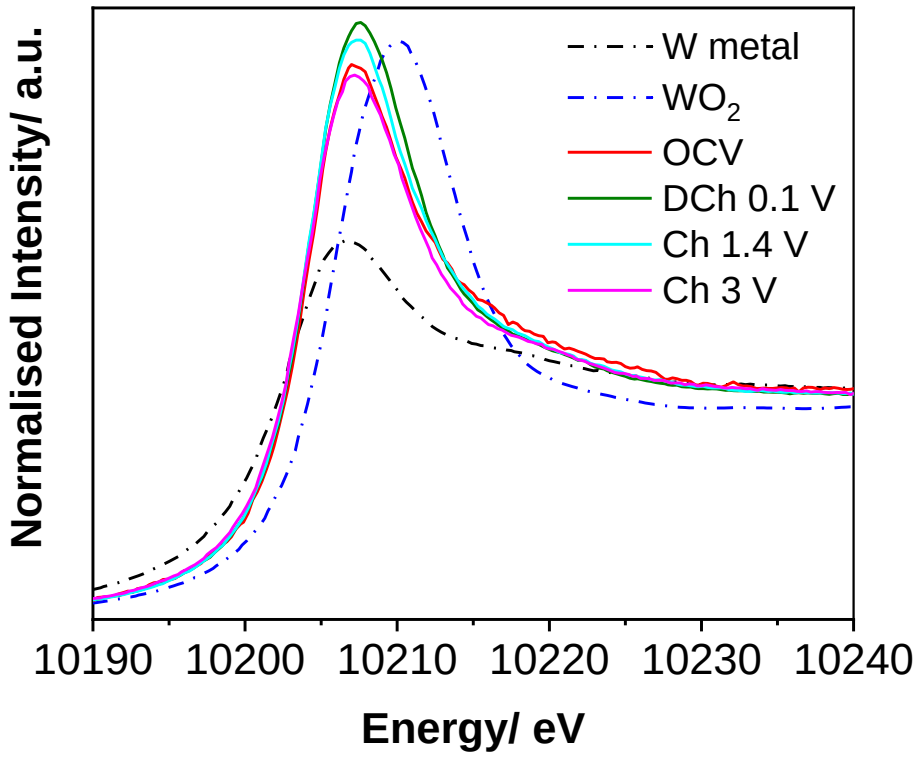

Figure 3.28 - Normalized W L_{III}-edge XANES spectra of WTe_2 electrode during the 1st charge process along with standard W metal and WO_2 powder used as reference.

For further clarity, the area under the white line upon cycling for the charged and discharged samples is represented in Figure 3.29. The changes in white line intensity visibly translate into the changes occurring in the W oxidation state during insertion and deinsertion of Na^+ ions. To note that, for the initial discharge/ charge process, the intensity of the white line is always stronger than that of metal W and WTe_2 at the OCV state (with exception of the charged sample).

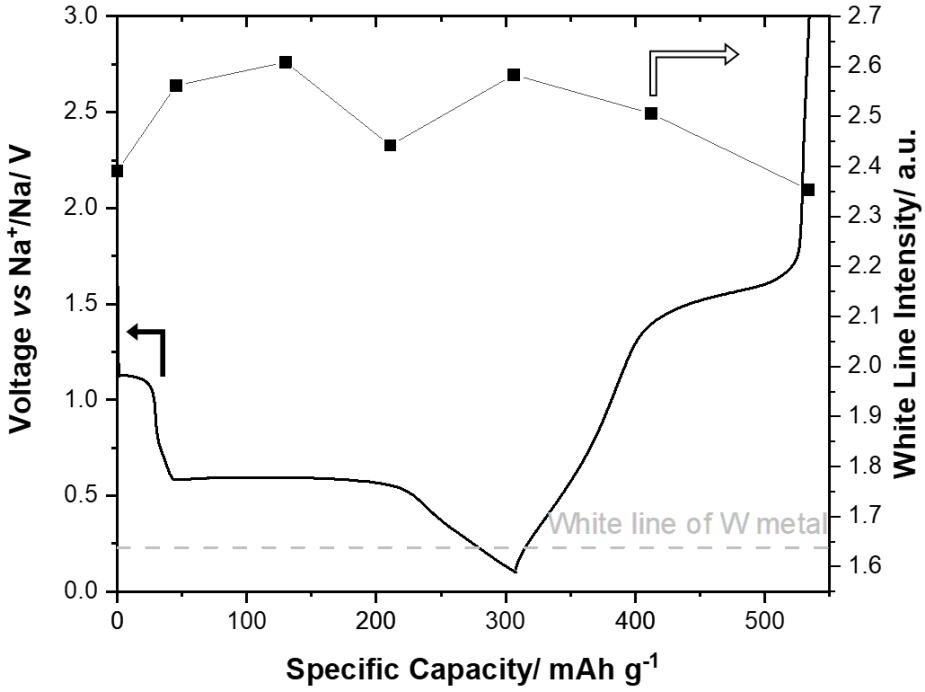

Figure 3.29– The change in the maximum intensity of the white-line of the W L_{III}-edge XANES for the WTe_2 in the initial discharge/charge processes.

Figure 3.30 show the normalised Te K-edge of selected electrodes at different charge/discharge depths with Te (0) metal and TeO_2 (+2) used as standards. In the Te K-edge spectra, the feature of high energy peak position originated from the transition of electrons between the $2p_{3/2}$ and the anti-bonding 5s states in the metal [78]. The K-absorption edge was analysed for the Te element where the position of the edge reflects the local short and intermediate-range structure as well as the oxidation state of the central atom [79]. By direct comparison with the first derivative of the white line of Te metal, it was evidenced that the pristine electrode shows a lower oxidation state than 0, in agreement with the expected nominal oxidation state in WTe_2 (-2). During the discharge process, the insertion of Na^+ ions into the crystal structure leads to the movement of the edge to higher energies, reaching 31814.6 eV at the middle of the plateau phase (0.6 V MP) (Figure 3.30). The movement of the edge towards higher energies has been formally attributed to an increase in the oxidation state for the studied element. Therefore, in this case, it might be attributed to the oxidation of Te^{2-} to Te^{-2+x}.

We explain these changes in the oxidation state with electron donation from Te to W during sodiation. Alternatively, the shift in edge energy can also be related to the higher electropositive bonding of the Na^+ ion (compared to W^{4+}) when forming Na_2Te. Furthermore, data shows a broadening and flattening of the Te edge at higher energies, which suggests the existence of a different coordination environment for Te in the discharged phases when compared to WTe_2. Therefore, these features support the formation of other tellurium-based phases such as Na_2Te (as expected from the conversion reaction occurring at lower voltages). Further discharge of the electrode to 0.1 V, results in a shift of the edge to higher energies (3181.7 eV) indicating further electronic transformations occurring in Te, possibly due to the occurrence of all the Te present in the form of Na_2Te. The spectra of the sample discharged at 0.1 V coincides in energy of the K-edge with that of Te metal and therefore one should not rule out the existence of a more metallic like component in the electrode sample. The *operando* XRD data collected (Section 3.3.3.2) suggests a decrease in crystallinity of the structure upon discharge which could be associated with the presence of amorphous Te metal.

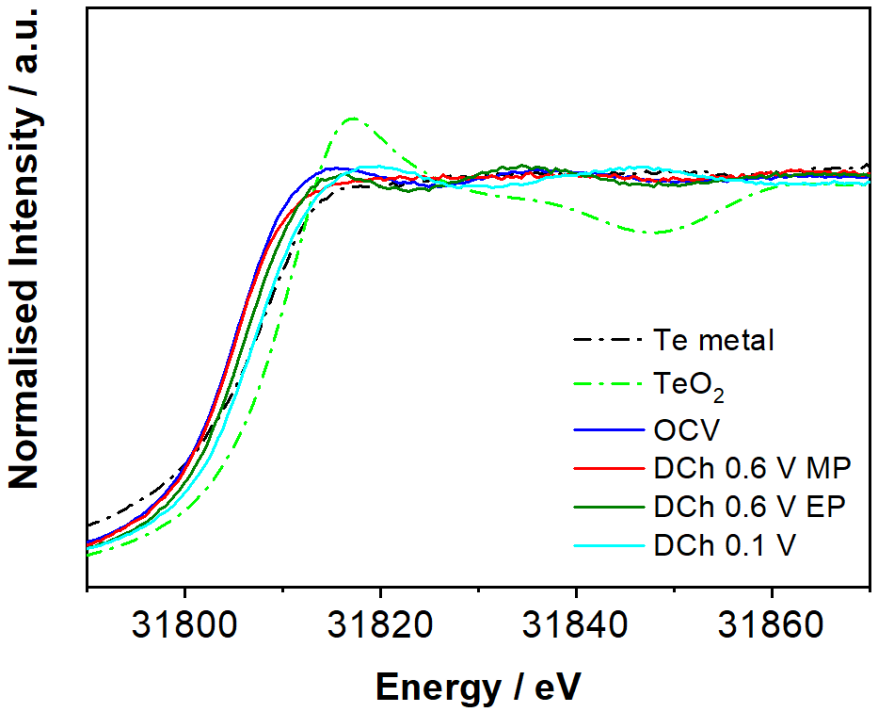

Figure 3.30 - Normalized Te K-edge XANES spectra of WTe_2 electrode during the 1st discharging process along with standard Te metal and TeO_2 powder used as reference.

On the other hand, during the charging (Figure 3.31), the Te K-edge moves towards lower energies (31817.0 eV) as a result of the reduction of the Te atom upon Na^+ ion extraction. The return of the initial edge feature (wave-like) also corroborates the existence of initial Te^{-2} which implies the reformation of the initial WTe_2.

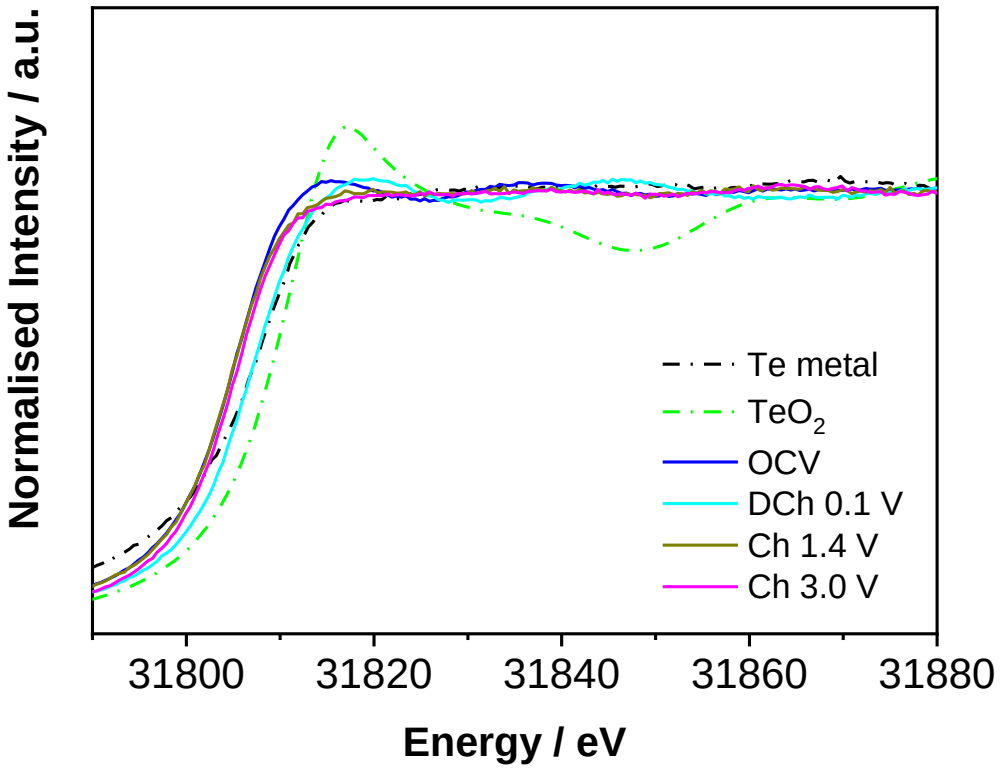

Figure 3.31- Normalized Te K-edge XANES spectra of WTe_2 electrode during the 1st charging process along with standard Te metal and TeO_2 powder used as reference.

3.3.3.2 *Operando* PXRD studies during the first (de)sodiation cycle

Operando powder synchrotron X-ray diffraction was used to better understand the structural changes and phase evolution of WTe_2 during the first charge/discharge process. The evolution of the synchrotron X-ray diffraction patterns along with the cycling profile is shown in Figure 3.32. All diffraction peaks of the electrode before cycling can be indexed to the T_d-WTe_2 phase (*Pmn*2_1, [ICSD- 73323])

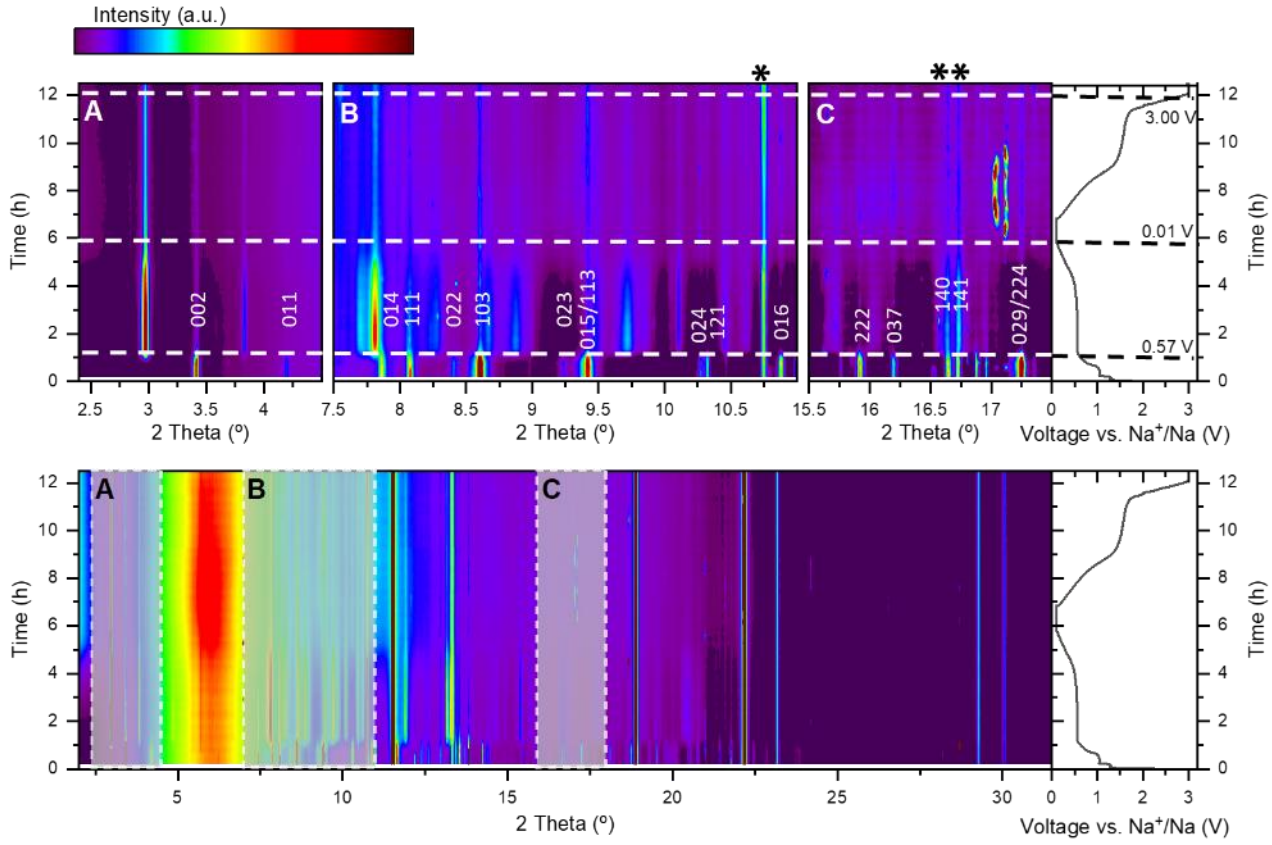

Figure 3.32 - *Operando* synchrotron X-ray diffraction patterns of the WTe_2 electrode material, recorded during the first charge/discharge cycle with corresponding cycling profile. Cu current collector peaks marked with *.

No significant changes in the diffraction peaks concerning 2θ degree position/intensity were observed in region 1, highlighted with a dashed line in Figure 3.32. Upon reaching the first discharge plateau at 0.57 V correspondent to the insertion of 0.65 Na^+ mol ($Na_{0.65}WTe_2$), the main phase peaks lose their intensity but the presence of the WTe_2 phase remains constant throughout the whole cycling, indicating a partially irreversible reaction. This decrease in intensity can be related to the gradual disorder of the interlayer spacing upon Na^+ ion intercalation and consequent fewer van-der-Waals interaction between the crystal layers [83]. This behaviour indicates that Na^+ ion insertion into the crystal induces slight expansion of the lattice parameter in the layered T_d-WTe_2 structure along the c-axis and consequently the increase in interlayer spacing. Concomitantly with the intensity decay of the diffraction peak correspondent to the

WTe_2 phase, several new peaks appear at 2.97°, 3.83° and 7.81° 2θ values, indicating a biphasic reaction mechanism (Figure 3.33).

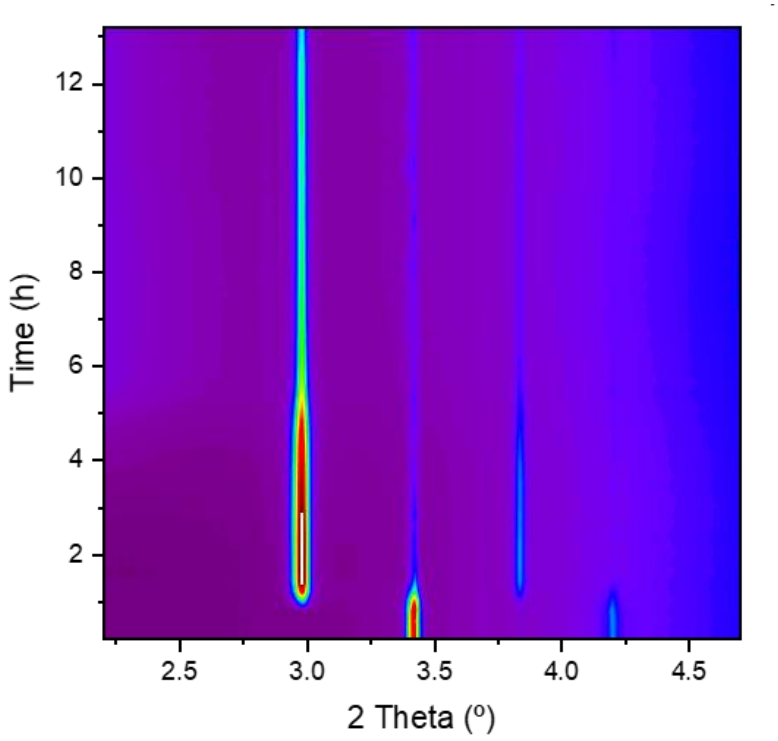

Figure 3.33 - Zoomed region showing (002) and (010) reflection in T_d-WTe_2.

These peaks were identified to a sodiated WTe_2 structure (Na_xWTe_2) and cell parameters can be found in Table 3.7. To note the high expansion in the c parameter of the unit cell from 13.899 to 15.959 Å. An increase of the background signal is also detected at 0.57 V, which can be related to an amorphization of the present phases and/or the appearance of greatly disordered phases. Therefore, the use of techniques that can investigate amorphous phases such as Raman and atomic force microscopy (AFM) are necessary to complement these studies. The appearing peaks are indeed broader than those of the pristine material, suggesting a decrease in crystallite size by cracking or disordering of the crystal structure. Other possible amorphous candidates present in this reaction are WO_2, Te metal or TeO_2 based on the elements in the electrode.

Table 3.7 - Crystallographic data for WTe_2 compounds at pristine and plateau stage

h	k	l	2 Theta (°)	d (Å)	c (Å)	b (Å)	a (Å)	from CIF of WTe_2	Step
0	0	2	2.97	7.9793	15.959				Plateau
0	0	2	3.41	6.9499	13.899			14.018	Pristine
0	1	1	3.83	6.1880		6.713			Plateau
0	1	1	4.19	5.6566		6.193		6.249	Pristine
1	1	1	7.81	3.0364			3.485		Plateau
1	1	1	8.08	2.9350			3.433	3.477	Pristine

The maximum intensity of the sodiated WTe_2 phase is reached at t ~ 3h (correspondent to 1.8 mol Na^+ inserted). When discharging from 0.57 V down to 0.1 V, a gradual albeit slight decrease of the maximum intensity of the sodiated WTe_2 phase peaks can be observed, which is especially apparent after the plateau is finished (t > ~5 h). This suggests that a limiting step in the expansion of the interlayer spacing of the structure is reached during plateau. There is however no shift in the position of the present diffraction peaks, reflecting a robust structure with no changes in the cell parameters upon sodium insertion. This indicates that the formed Na_xWTe_2 structure has an amorphous nature, which corroborates the theory that the initial T_d-WTe_2 disintegrates into W and Te/$NaTe_2$ upon insertion of Na^+ ion [47], [48]. During the constant voltage period at 0.1 V, no changes in the overall pattern intensity are observed. Interestingly, during charge, there are no meaningful changes nor in the intensity nor the peaks' position, a behaviour that has been registered in other layered dichalcogenides materials [84], [85]. This suggests that upon deinsertion of ions, the initial interlayer spacing of the crystal structure is not recovered. That is, the intensity of the peaks of the sodiated phase formed during the first plateau at 0.57 V are by the end of the charge more intense than those of the initial structure. The appearance of two extra high-intensity peaks at $2\theta \approx 17.01^{\circ}$ and 17.12° were observed during the charging which is not related to the studied system as no possible product of the conversion reaction appears at this 2θ value. For this *operando* experiment, a Cu current collector was used instead of the usual Al foil which could have led to the formation of impurities during the ion

deintercalation. However, the peaks could not be matched with any possible impurity resulting from the reaction with the Cu current collector such as CuO (*C*12/*c*1, [ICSD-69094]). Cu_2O (*Pn*-3*mZ*, [ICSD- 63281] and *F*222, [ICSD- 54126]) and CuTe (*PmmnS*, [ICSD- 42591]) or any other possible Na impurity such as NaF (*Fm*-3*m*, [ICSD-26837]). Other possibilities for these peaks may be related to phases formed from a combination of the elements present in the samples such as Na, Cu, Te and W, however more experiments are needed to confirm this (Figure 3.34).

The fact that the initial WTe_2 phase is not recovered after charging the cell back, evidences the partial irreversibility of this compound during the first cycle. Nonetheless, a slight increment of the WTe_2 (002) peak's intensity can be seen during the charging process, which could be associated with the *operando* cell design, however, more studies have to be done to confirm this theory.

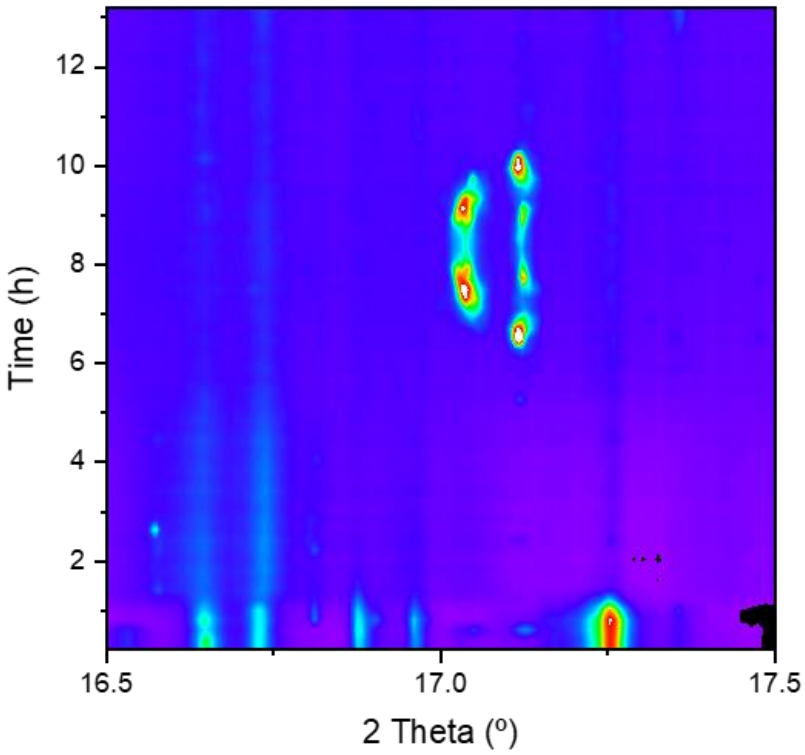

Figure 3.34 - Operando powder X-ray diffraction of T_d-WTe_2 showing some extra phase.

3.4 Conclusions

In summary, WTe_2 was successfully synthesized and further analysed via XRD, Raman and electron microscopy analysis. XRD data show an experimental diffraction pattern that matches the simulated powder pattern of the tetrahedral WTe_2 (T_d-WTe_2) phase with the orthorhombic space group $Pmn2_1$. The lattice parameters were found to be a = 3.481(8) Å, b = 6.257(1) Å, c = 14.036(4) Å, α = 90 °, β = 90 ° and γ = 90 °, which are in agreement to the unit cell parameters reported in the literature indicating that the material was pure, and no extra phases were present. These results are corroborated by Raman data where no Raman modes associated with oxidation species such as WO_x and TeO_x species were observed. Cross-section analysis in SEM and TEM show that the pristine material consists of monodispersed irregular particle blocks consisting of the stacking of a few very thin nanosheets.

Similarly, to other MTe_2 electrodes, the insertion of Na^+ ions is believed to lead to the conversion of WTe_2 into Na_2Te and W metal and consequent reformation of initial WTe_2 upon ion extraction. Electrochemical measurements were performed using WTe_2 electrodes as anode material for SIBs, and the cyclic voltammogram confirmed the expected stepwise insertion of sodium with the existence of matching plateau/slopes and redox peaks, respectively. Galvanostatic discharge-charge cycling shows that the anode material can be cycled reversibly, with an initial discharge capacity of 288 mAh g^{-1} and 63.5 % of the initial discharge capacity still delivered after 20 cycles. The rate capability tests show that the WTe_2 anode does not recover the total of its initial discharge capacity after cycling (50 % retention) which can be related to irreversible damage caused to the electrode's structure during cycling, indicating the poor flexibility of the structure (as shown in the SEM images of the post-mortem electrodes).

The electrochemical results were supported with CV and EIS measurements. The presence of several redox peaks in the cyclic voltammogram corroborates the multiphase reaction occurring in WTe_2 when cycled against Na. The decrease in intensity peaks upon cycling reflects the less stable and reversible electrochemical behaviour of the electrode after the initial sodium intercalation and SEI layer formation. The calculated b values for the redox peaks were estimated to be between 0.75 and 0.81, suggesting both surface-controlled and diffusion-controlled processes occur on the

WTe_2 electrode during ion movement. These results show the dominance of capacitive contribution at higher scan rates as a result of faster redox reactions happening on the electrode material (70.5 % at 1.0 mV s^{-1} *vs* 53.2 % at 0.1 mV s^{-1}). The Na^+ ion diffusion coefficient was found to be in the order of 10^{-10} (ranging from 1.02 x 10^{-9} to 9.19 x 10^{-11} cm^2 s^{-1}). A bottleneck step is encountered during the initial insertion of Na^+ ions to form the WTe_2 to form a sodiated phase. The values obtained for WTe_2 electrodes indicate a similar Na^+ diffusion in comparison with other dichalcogenides materials.

EIS measurements collected at different cycles show a progressive reduction of the total arc radius during cycling, suggesting a less resistive interface between the electrolyte and electrode upon Na^+ intercalation. An abrupt decrease in charge-transfer resistance was observed upon cycling from the EIS measurement collected at OCV, which can be associated with an increase in the Na^+ diffusion and stability of the discharge/ charge capacity of the cycled electrode. This is the opposite of the EIS results observed in other TMDs compounds cycled against Na, revealing that WTe_2 is structurally less stable. At the same time, an increase in R_{SEI} is observed which can be related to the pulverization of the active material upon insertion/extraction of Na^+ ions and exfoliation from the current collector, leading to the capacity loss observed in the charge-discharge curves.

Structure evolution upon Na^+ ion insertion was studied by XANES and operando PXRD measurements. The W L_{III}-edge XAS spectra showed the decrease in the oxidation state of the W atom upon Na^+ intercalation ($W^{4+ - x)}$) to form a sodiated phase (Na_xWTe_2). During the initial insertion of Na^+ ions, a displacement of electron density from the metal atom towards the Te or Na atoms is observed, which is responsible for the decrease in occupied W 5d orbitals and consequent increase in white line intensity. The exact oxidation state of W couldn't be accessed at the end of the discharge process; however, the white line intensity of the fully discharged electrode is always larger than the W metal spectrum, showing that the d electrons of the W deviate towards the Na or Te atom during the charge and discharge process. No W metal was observed, suggesting that the structure of WTe_2 does not convert to W metal upon Na insertion and that some initial WTe_2 or some Na_xWTe_2 phase is still present. At the same time, the movement of the Te K-edge towards higher energies was associated to the higher electropositive bonding of the Na^+ ion (compared to W^{4+}) when forming Na_2Te. Furthermore, data shows a broadening and flattening of the Te edge at higher energies, which suggests the

existence of a different coordination environment for Te in the discharged phases when compared to WTe_2 and consequent formation of a Na_2Te phase. During desodiation, the decrease in W white line intensity suggests the oxidation of the W atom explained by the filling of d orbitals upon Na^+ extraction due to the reformation of the WTe_2 phase. The lower intensity recorded at this point compared with pristine suggests that the W atom is in a more reduced state, however further data needs to be collected to emphasize this point. The Te K-edge moves towards lower energies as a result of the reduction of the Te atom upon Na^+ ion extraction from the Na_2Te phase formed during the discharge process and consequent reformation of WTe_2.

The XAS data is corroborated by the synchrotron operando X-ray diffraction data. At the OCV state, all diffraction peaks can be indexed to the T_d-WTe_2 phase. During the discharge process, a decrease in WTe_2 intensity peaks is observed indicating a gradual disorder of the interlayer spacing upon Na^+ ion intercalation and consequent fewer van der Waals interaction between the crystal layers. This disorder is accompanied by the slight expansion of the lattice parameters layered along the c-axis in the T_d-WTe_2 structure. Several new peaks are also identified and can be attributed to the formation of a sodiated WTe_2 structure (Na_xWTe_2). No meaningful changes nor in the intensity nor the position of the peaks are visible during the charging process, suggesting that some initial WTe_2 does not suffer any kind of restructuring upon ion deinsertion. These results were corroborated by the cycled SEM data. The cycled SEM data after 75 cycles also shows the formation of cracks and particle agglomeration upon continuous ions insertion/extraction which is related to the structure expansion upon ion insertion.

Altogether, the results obtained show that WTe_2 can be successfully used as anode material for SIBs.

3.5 References

[1] M. N. Ali *et al.*., “Large, non-saturating magnetoresistance in WTe2,” *Nature*, vol. 514, pp. 5–10, 2014, doi: 10.1038/nature13763.

[2] B. E. Brown, “The crystal structures of WTe $_2$ and high-temperature MoTe $_2$,”

Acta Crystallogr., vol. 20, no. 2, pp. 268–274, 1966, doi: 10.1107/S0365110X66000513.

[3] K. Momma and F. Izumi, "VESTA 3 for three-dimensional visualization of crystal, volumetric and morphology data," *J. Appl. Crystallogr.*, vol. 44, no. 6, pp. 1272–1276, 2011, doi: 10.1107/S0021889811038970.

[4] C. H. Lee *et al.*., "Tungsten Ditelluride: A layered semimetal," *Sci. Rep.*, vol. 5, pp. 1–8, 2015, doi: 10.1038/srep10013.

[5] Y. Kim, Y. I. Jhon, J. Park, J. H. Kim, S. Lee, and Y. M. Jhon, "Anomalous Raman scattering and lattice dynamics in mono- and few-layer WTe2," *Nanoscale*, vol. 8, no. 4, pp. 2309–2316, 2016, doi: 10.1039/c5nr06098b.

[6] A. McCreary *et al.*., "Distinct photoluminescence and Raman spectroscopy signatures for identifying highly crystalline WS2 monolayers produced by different growth methods," *J. Mater. Res.*, vol. 31, no. 7, pp. 931–944, 2016, doi: 10.1557/jmr.2016.47.

[7] Y. Wu *et al.*., "Observation of Fermi arcs in the type-II Weyl semimetal candidate WTe2," *Phys. Rev. B*, vol. 94, no. 12, pp. 1–5, 2016, doi: 10.1103/PhysRevB.94.121113.

[8] P. K. Das *et al.*., "Layer-dependent quantum cooperation of electron and hole states in the anomalous semimetal WTe2," *Nat. Commun.*, vol. 7, pp. 1–7, 2016, doi: 10.1038/ncomms10847.

[9] N. Lu *et al.*., "Atomic and Electronic Structures of WTe2 Probed by High Resolution Electron Microscopy and ab Initio Calculations," *J. Phys. Chem. C*, vol. 120, no. 15, pp. 8364–8369, 2016, doi: 10.1021/acs.jpcc.6b01044.

[10] E. Corro *et al.*., "and Bulk WSe2 Observed by Resonant Raman Spectroscopy," *ACS Nano*, vol. 8, no. 9, pp. 9629–9635, 2014.

[11] A. Berkdemir *et al.*., "Identification of individual and few layers of WS2 using Raman Spectroscopy," *Sci. Rep.*, vol. 3, pp. 1–8, 2013, doi: 10.1038/srep01755.

[12] Y. Zhang *et al.*., " Pressure-induced Td to 1T′ structural phase transition in WTe 2 ," *AIP Adv.*, vol. 6, no. 7, p. 075008, 2016, doi: 10.1063/1.4959026.

[13] R. V. Coleman and A. Isin, "Magnetoresistance in iron single crystals," *J. Appl. Phys.*, vol. 37, no. 3, pp. 1028–1029, 1966, doi: 10.1063/1.1708320.

[14] E. Torun, H. Sahin, S. Cahangirov, A. Rubio, and F. M. Peeters, "Anisotropic electronic, mechanical, and optical properties of monolayer WTe2," *J. Appl. Phys.*, vol. 119, no. 7, 2016, doi: 10.1063/1.4942162.

[15] I. Pletikosić, M. N. Ali, A. V. Fedorov, R. J. Cava, and T. Valla, "Electronic structure basis for the extraordinary magnetoresistance in WTe2," *Phys. Rev. Lett.*, vol. 113, no. 21, pp. 1–5, 2014, doi: 10.1103/PhysRevLett.113.216601.

[16] H. Y. Lv, W. J. Lu, D. F. Shao, Y. Liu, S. G. Tan, and Y. P. Sun, "Perfect charge compensation in WTe2 for the extraordinary magnetoresistance: From bulk to monolayer," *Epl*, vol. 110, no. 3, 2015, doi: 10.1209/0295-5075/110/37004.

[17] D. Kang *et al.*., "Superconductivity emerging from a suppressed large magnetoresistant state in tungsten ditelluride," *Nat. Commun.*, vol. 6, pp. 6–11, 2015, doi: 10.1038/ncomms8804.

[18] H. Xiang *et al.*., "Quantum spin Hall insulator phase in monolayer WTe2 by uniaxial strain," *AIP Adv.*, vol. 6, no. 9, 2016, doi: 10.1063/1.4962662.

[19] M. Hong, J. Li, W. Zhang, S. Liu, and H. Chang, "Semimetallic 1T′ WTe2 Nanorods as Anode Material for the Sodium Ion Battery," *Energy and Fuels*, vol. 32, no. 5, pp. 6371–6377, 2018, doi: 10.1021/acs.energyfuels.8b00454.

[20] J. Luxa *et al.*., "Layered Transition-Metal Ditellurides in Electrocatalytic Applications - Contrasting Properties," *ACS Catal.*, vol. 7, no. 9, pp. 5706–5716, 2017, doi: 10.1021/acscatal.7b02080.

[21] M. Herklotz *et al.*., "A novel high-throughput setup for *in situ* powder diffraction on coin cell batteries," *J. Appl. Crystallogr.*, vol. 49, pp. 340–345, 2016, doi: 10.1107/S1600576715022165.

[22] "Potentiostats - Biologic." https://www.biologic.net/product_category/potentiostats-galvanostats/ (accessed Jul. 30, 2021).

[23] M. G. Kim *et al.*, "Unusual Li-ion storage through anionic redox processes of bacteria-driven tellurium nanorods," *J. Mater. Chem. A*, vol. 3, no. 33, pp. 16978–16987, 2015, doi: 10.1039/c5ta04038h.

[24] K. T. Bennett *et al.*, "Large-Scale Production of 119mTe and 119Sb for Radiopharmaceutical Applications," *ACS Cent. Sci.*, vol. 5, no. 3, pp. 494–505, 2019, doi: 10.1021/acscentsci.8b00869.

[25] U. Jayarathne *et al.*, "X-ray absorption spectroscopy systematics at the tungsten L-edge," *Inorg. Chem.*, vol. 53, no. 16, pp. 8230–8241, 2014, doi: 10.1021/ic500256a.

[26] B. Ravel and M. Newville, "ATHENA, ARTEMIS, HEPHAESTUS: Data analysis for X-ray absorption spectroscopy using IFEFFIT," *J. Synchrotron Radiat.*, vol. 12, no. 4, pp. 537–541, 2005, doi: 10.1107/S0909049505012719.

[27] M. Newville, "IFEFFIT: Interactive XAFS analysis and FEFF fitting," *J. Synchrotron Radiat.*, vol. 8, no. 2, pp. 322–324, 2001, doi: 10.1107/S0909049500016964.

[28] A. Mar, S. Jobic, and J. A. Ibers, "Metal-Metal vs Tellurium-Tellurium Bonding in WTe2 and Its Ternary Variants TaIrTe4 and NbIrTe4," *J. Am. Chem. Soc.*, vol. 114, no. 23, pp. 8963–8971, 1992, doi: 10.1021/ja00049a029.

[29] W. I. F. David, "Powder diffraction: Least-squares and beyond," *J. Res. Natl. Inst. Stand. Technol.*, vol. 109, no. 1, pp. 107–123, 2004, doi: 10.6028/jres.109.008.

[30] M. K. Jana *et al.*, "A combined experimental and theoretical study of the structural, electronic and vibrational properties of bulk and few-layer Td-WTe2," *J. Phys. Condens. Matter*, vol. 27, no. 28, 2015, doi: 10.1088/0953-8984/27/28/285401.

[31] Z. Sofer *et al.*., "Universal Method for Large-Scale Synthesis of Layered Transition Metal Dichalcogenides," *Chem. - A Eur. J.*, vol. 23, no. 42, pp. 10177–10186, 2017, doi: 10.1002/chem.201701628.

[32] A. C. Ferrari and D. M. Basko, "Raman spectroscopy as a versatile tool for studying the properties of graphene," *Nat. Nanotechnol.*, vol. 8, no. 4, pp. 235–246, 2013, doi: 10.1038/nnano.2013.46.

[33] X. Zhang, X. F. Qiao, W. Shi, J. Bin Wu, D. S. Jiang, and P. H. Tan, "Phonon and Raman scattering of two-dimensional transition metal dichalcogenides from monolayer, multilayer to bulk material," *Chem. Soc. Rev.*, vol. 44, no. 9, pp. 2757–2785, 2015, doi: 10.1039/c4cs00282b.

[34] X. Zhang, Q. H. Tan, J. Bin Wu, W. Shi, and P. H. Tan, "Review on the Raman spectroscopy of different types of layered materials," *Nanoscale*, vol. 8, no. 12, pp. 6435–6450, 2016, doi: 10.1039/c5nr07205k.

[35] J. G. Howell, Y. P. Li, and A. T. Bell, "Propene Metathesis over Supported Tungsten Oxide Catalysts: A Study of Active Site Formation," *ACS Catal.*, vol. 6, no. 11, pp. 7728–7738, 2016, doi: 10.1021/acscatal.6b01842.

[36] A. K. Thakur *et al.*., "Controlled synthesis of WO3 nanostructures: Optical, structural and electrochemical properties," *Mater. Res. Express*, vol. 6, no. 2, 2019, doi: 10.1088/2053-1591/aae991.

[37] J. C. Champarnaud-Mesjard, S. Blanchandin, P. Thomas, A. Mirgorodsky, T. Merle-Méjean, and B. Frit, "Crystal structure, Raman spectrum and lattice dynamics of a new metastable form of tellurium dioxide: γ-TeO2," *J. Phys. Chem. Solids*, vol. 61, no. 9, pp. 1499–1507, 2000, doi: 10.1016/S0022-3697(00)00012-3.

[38] Q. Song *et al.*., "The polarization-dependent anisotropic Raman response of few-layer and bulk WTe2 under different excitation wavelengths," *RSC Adv.*, vol. 6, no. 105, pp. 103830–103837, 2016, doi: 10.1039/c6ra23687a.

[39] Y. C. Jiang, J. Gao, and L. Wang, "Raman fingerprint for semi-metal WTe2

evolving from bulk to monolayer," *Sci. Rep.*, vol. 6, pp. 1–7, 2016, doi: 10.1038/srep19624.

[40] C. H. Lee *et al.*., "Tungsten Ditelluride: A layered semimetal," *Sci. Rep.*, vol. 5, pp. 1–8, 2015, doi: 10.1038/srep10013.

[41] M. R. Panda *et al.*., "Blocks of molybdenum ditelluride: A high rate anode for sodium-ion battery and full cell prototype study," *Nano Energy*, vol. 64, no. July, p. 103951, 2019, doi: 10.1016/j.nanoen.2019.103951.

[42] K. Chang *et al.*., " Ultrathin MoS 2 /Nitrogen-Doped Graphene Nanosheets with Highly Reversible Lithium Storage ," *Adv. Energy Mater.*, vol. 3, no. 7, pp. 839–844, 2013, doi: 10.1002/aenm.201201108.

[43] J. S. Cho, S. Y. Lee, J. K. Lee, and Y. C. Kang, "Iron Telluride-Decorated Reduced Graphene Oxide Hybrid Microspheres as Anode Materials with Improved Na-Ion Storage Properties," *ACS Appl. Mater. Interfaces*, vol. 8, no. 33, pp. 21343–21349, 2016, doi: 10.1021/acsami.6b05758.

[44] G. Zhang, K. Liu, and J. Zhou, "Cobalt telluride/graphene composite nanosheets for excellent gravimetric and volumetric Na-ion storage," *J. Mater. Chem. A*, vol. 6, no. 15, pp. 6335–6343, 2018, doi: 10.1039/c8ta01265b.

[45] E. Yang, H. Ji, and Y. Jung, "Two-Dimensional Transition Metal Dichalcogenide Monolayers as Promising Sodium Ion Battery Anodes," *J. Phys. Chem. C*, vol. 119, no. 47, pp. 26374–26380, 2015, doi: 10.1021/acs.jpcc.5b09935.

[46] X. Wang, I. Veremchuk, M. Bobnar, U. Burkhardt, J. T. Zhao, and Y. Grin, "Sodium Substitution in Lead Telluride," *Chem. Mater.*, vol. 30, no. 4, pp. 1362–1372, 2018, doi: 10.1021/acs.chemmater.7b05091.

[47] A. R. Park and C. M. Park, "Cubic Crystal-Structured SnTe for Superior Li- and Na-Ion Battery Anodes," *ACS Nano*, vol. 11, no. 6, pp. 6074–6084, 2017, doi: 10.1021/acsnano.7b02039.

[48] K. H. Nam, G. K. Sung, J. H. Choi, J. S. Youn, K. J. Jeon, and C. M. Park, "New high-energy-density GeTe-based anodes for Li-ion batteries," *J. Mater. Chem.*

A, vol. 7, no. 7, pp. 3278–3288, 2019, doi: 10.1039/C8TA12094C.

[49] K. H. Nam, J. H. Choi, and C. M. Park, "Highly reversible Na-ion reaction in nanostructured Sb 2 Te 3 -C composites as Na-ion battery anodes," *J. Electrochem. Soc.*, vol. 164, no. 9, pp. A2056–A2064, 2017, doi: 10.1149/2.1161709jes.

[50] T. S. Sahu and S. Mitra, "Exfoliated MoS <inf>2</inf> Sheets and Reduced Graphene Oxide-An Excellent and Fast Anode for Sodium-ion Battery," *Sci. Rep.*, vol. 5, no. June, pp. 1–13, 2015, doi: 10.1038/srep12571.

[51] N. Ma, X. Y. Jiang, L. Zhang, X. S. Wang, Y. L. Cao, and X. Z. Zhang, "Novel 2D Layered Molybdenum Ditelluride Encapsulated in Few-Layer Graphene as High-Performance Anode for Lithium-Ion Batteries," *Small*, vol. 14, no. 14, pp. 1–8, 2018, doi: 10.1002/smll.201703680.

[52] F. Niu *et al.*., "MoSe2-Covered N,P-Doped Carbon Nanosheets as a Long-Life and High-Rate Anode Material for Sodium-Ion Batteries," *Adv. Funct. Mater.*, vol. 27, no. 23, pp. 1–11, 2017, doi: 10.1002/adfm.201700522.

[53] Y. Li, Y. Liang, F. C. Robles Hernandez, H. Deog Yoo, Q. An, and Y. Yao, "Enhancing sodium-ion battery performance with interlayer-expanded MoS2-PEO nanocomposites," *Nano Energy*, vol. 15, pp. 453–461, 2015, doi: 10.1016/j.nanoen.2015.05.012.

[54] J. Zhang *et al.*., "Biomass derived activated carbon with 3D connected architecture for rechargeable lithium - Sulfur batteries," *Electrochim. Acta*, vol. 116, pp. 146–151, 2014, doi: 10.1016/j.electacta.2013.11.035.

[55] M. R. Panda *et al.*., "High Performance Lithium-Ion Batteries Using Layered 2H-MoTe2 as Anode," *Small*, vol. 2002669, pp. 1–16, 2020, doi: 10.1002/smll.202002669.

[56] T. Kim *et al.*., "Applications of Voltammetry in Lithium Ion Battery Research," *J. Electrochem. Sci. Technol.*, vol. 11, no. 1, pp. 14–25, 2020, doi: 10.33961/jecst.2019.00619.

[57] J. Cui, H. Zheng, Z. Zhang, S. Hwang, X. Q. Yang, and K. He, "Origin of anomalous high-rate Na-ion electrochemistry in layered bismuth telluride anodes," *Matter*, vol. 4, no. 4, pp. 1335–1351, Apr. 2021, doi: 10.1016/j.matt.2021.01.005.

[58] P. Guo, H. Song, and X. Chen, "Electrochemical performance of graphene nanosheets as anode material for lithium-ion batteries," *Electrochem. commun.*, vol. 11, no. 6, pp. 1320–1324, 2009, doi: 10.1016/j.elecom.2009.04.036.

[59] Y. Li *et al.*., "Powder exfoliated MoS2 nanosheets with highly monolayer-rich structures as high-performance lithium-/sodium-ion-battery electrodes," *Nanoscale*, vol. 11, no. 4, pp. 1887–1900, 2019, doi: 10.1039/c8nr08511k.

[60] C. D. Snyders and E. E. Ferg, "Electrochemical Impedance Spectroscopy (EIS) study of doped spinel manganese cathode oxide materials synthesized for Li-ion batteries," *Mater. Today Proc.*, vol. 5, no. 4, pp. 10450–10459, 2018, doi: 10.1016/j.matpr.2017.12.376.

[61] M. D. Levi and D. Aurbach, "Simultaneous measurements and modeling of the electrochemical impedance and the cyclic voltammetric characteristics of graphite electrodes doped with lithium," *J. Phys. Chem. B*, vol. 101, no. 23, pp. 4630–4640, 1997, doi: 10.1021/jp9701909.

[62] Y. Xu, Y. Zhu, Y. Liu, and C. Wang, "Electrochemical performance of porous carbon/tin composite anodes for sodium-ion and lithium-ion batteries," *Adv. Energy Mater.*, vol. 3, no. 1, pp. 128–133, 2013, doi: 10.1002/aenm.201200346.

[63] J. S. Cho, Y. J. Hong, and Y. C. Kang, "Design and synthesis of bubble-nanorod-structured Fe2O3-Carbon nanofibers as advanced anode material for li-ion batteries," *ACS Nano*, vol. 9, no. 4, pp. 4026–4035, 2015, doi: 10.1021/acsnano.5b00088.

[64] B. Chen, D. Chao, E. Liu, M. Jaroniec, N. Zhao, and S.-Z. Qiao, "Transition metal dichalcogenides for alkali metal ion batteries: engineering strategies at the atomic level," *Energy Environ. Sci.*, vol. 13, no. 4, pp. 1096–1131, 2020, doi: 10.1039/c9ee03549d.

[65] Y. Guo, Y. Wei, H. Li, and T. Zhai, "Layer Structured Materials for Advanced Energy Storage and Conversion," *Small*, vol. 1701649, p. 1701649, 2017, doi: 10.1002/smll.201701649.

[66] Y. Lu, X. Yao, J. Yin, G. Peng, P. Cui, and X. Xu, "MoS2 nanoflowers consisting of nanosheets with a controllable interlayer distance as high-performance lithium ion battery anodes," *RSC Adv.*, vol. 5, no. 11, pp. 7938–7943, 2015, doi: 10.1039/c4ra14026e.

[67] A. Lasia, *Electrochemical impedance spectroscopy and its applications*, vol. 9781461489, no. July. 2014.

[68] Y. Liu, J. Wang, Y. Xu, Y. Zhu, D. Bigio, and C. Wang, "Lithium-tellurium batteries based on tellurium/porous carbon composite," *J. Mater. Chem. A*, vol. 2, no. 31, pp. 12201–12207, 2014, doi: 10.1039/c4ta02075h.

[69] C. Luo *et al.*., "Selenium@Mesoporous carbon composite with superior lithium and sodium storage capacity," *ACS Nano*, vol. 7, no. 9, pp. 8003–8010, 2013, doi: 10.1021/nn403108w.

[70] Z. Chen and J. R. Dahn, "Methods to obtain excellent capacity retention in LiCoO2 cycled to 4.5 V," *Electrochim. Acta*, vol. 49, no. 7, pp. 1079–1090, 2004, doi: 10.1016/j.electacta.2003.10.019.

[71] E. Frackowiak, "Electrode Materials with Pseudocapacitive Properties," *Supercapacitors Mater. Syst. Appl.*, pp. 207–237, 2013, doi: 10.1002/9783527646661.ch6.

[72] Scott Calvin, *XAFS for Everyone - 1st Edition - Scott Calvin - Routledge Book*. 2013.

[73] R. G. Jones, "X-ray absorption: Principles, applications, techniques of EXAFS, SEXAFS, and XANES," *Endeavour*, vol. 12, no. 4, p. 195, 1988, doi: 10.1016/0160-9327(88)90177-9.

[74] N. Kerr del Grande, J. Hubbell, and J. Mallett, "Compilation of x-ray cross sections, sec 1," vol. 444, no. January, pp. 443–444, 1969.

[75] S. N. Reifsnyder and H. H. Lamb, “Characterization of silica-supported Pd-Au clusters by X-ray absorption spectroscopy,” *J. Phys. Chem. B*, vol. 103, no. 2, pp. 321–329, 1999, doi: 10.1021/jp982893b.

[76] P. Charton, L. Gengembre, and P. Armand, “TeO2-WO3 glasses: Infrared, XPS and XANES structural characterizations,” *J. Solid State Chem.*, vol. 168, no. 1, pp. 175–183, 2002, doi: 10.1006/jssc.2002.9707.

[77] X. Fang *et al.*., “Synthesis and electrochemical performance of graphene-like WS2,” *Chem. - A Eur. J.*, vol. 19, no. 18, pp. 5694–5700, 2013, doi: 10.1002/chem.201204254.

[78] A. Ibanez, T. Ericsson, O. Lindqvist, D. Bazin, and E. Philippot, “Local range order of tellurium atoms in TeO2-BaO and TeO 2-BaF2 glassy systems,” *J. Mater. Chem.*, vol. 4, no. 7, pp. 1101–1106, 1994, doi: 10.1039/JM9940401101.

[79] P. V. Grundler *et al.*., “Xocolatlite, Ca2Mn24+ Te2O12·H2O, a new tellurate related to kuranakhite: Description and measurement of Te oxidation state by XANES spectroscopy,” *Am. Mineral.*, vol. 93, no. 11–12, pp. 1911–1920, 2008, doi: 10.2138/am.2008.2870.

[80] X. Ma *et al.*., “Raman scattering in the transition-metal dichalcogenides of 1T′-MoT e2,Td-MoT e2, and Td-WT e2,” *Phys. Rev. B*, vol. 94, no. 21, pp. 43–45, 2016, doi: 10.1103/PhysRevB.94.214105.

[81] J. He *et al.*., “Tellurium-Impregnated Porous Cobalt-Doped Carbon Polyhedra as Superior Cathodes for Lithium-Tellurium Batteries,” *ACS Nano*, vol. 11, no. 8, pp. 8144–8152, 2017, doi: 10.1021/acsnano.7b03057.

[82] T. Vasileiadis and S. N. Yannopoulos, “Photo-induced oxidation and amorphization of trigonal tellurium: A means to engineer hybrid nanostructures and explore glass structure under spatial confinement,” *J. Appl. Phys.*, vol. 116, no. 10, 2014, doi: 10.1063/1.4894868.

[83] C. Ding *et al.*., “Identifying the origin and contribution of pseudocapacitive sodium ion storage in tungsten disulphide nanosheets for application in sodium-

ion capacitors," *J. Mater. Chem. A*, vol. 6, no. 42, pp. 21010–21017, 2018, doi: 10.1039/C8TA07677D.

[84] X. Wang, Z. Guan, Y. Li, Z. Wang, and L. Chen, "Guest-host interactions and their impacts on structure and performance of nano-MoS2," *Nanoscale*, vol. 7, no. 2, pp. 637–641, 2015, doi: 10.1039/c4nr05773b.

[85] J. R. González, R. Alcántara, J. L. Tirado, A. J. Fielding, and R. A. W. Dryfe, "Electrochemical Interaction of Few-Layer Molybdenum Disulfide Composites vs Sodium: New Insights on the Reaction Mechanism," *Chem. Mater.*, vol. 29, no. 14, pp. 5886–5895, 2017, doi: 10.1021/acs.chemmater.7b01245.

4 A study on the charge compensation mechanisms on T_d-WTe_2 polytype as an anode in LIBs

4.1 Introduction

As discussed in the previous chapter, TMD 2D materials have gained a lot of attention due to their notable electrochemical properties. The fact that they can accommodate large volume expansion and possess a large effective surface area turns them into suitable materials to use in rechargeable ion batteries. Atomically thin WTe_2 nanostructures have been studied as a promising anode material for LIBs applications due to their excellent physicochemical properties such as high electrical conductivities [1]. However, TMDs possess low dimensional heterostructure and ionic conductivity, the reason why they are usually interconnected with carbon sources. Carbon nanotubes (CNTs) are usually used as they have lower weight loading in contrast to traditional carbons like carbon black and graphene [2]. Bare carbon materials can deliver a theoretical capacity of 372 mAh g^{-1} however this limits its practical performance in commercial applications. The hybridization of CNT with TMDs allow developing advanced nanocomposites and delivering up to double the performance of both individual counterparts [1]. Srinivaaset *et al.* synthesized WTe_2 nanostars interconnected with multi-walled CNTs (MWCNTs) to form WTe_2@CNT nanocomposites using a facile heating solution-phase synthetic method [3]. This synthesis involved the use of two precursors, first tungsten hexacarbonyl ($W(CO)_6$) was dissolved in oleylamine (precursor A) and then, diphenyl ditelluride($(C_6H_5)_2Te_2$) was dissolved in oleylamine (precursor B). The tungsten precursor (precursor A) was refluxed under vacuum at 120 °C and then heated to 300 °C under an argon atmosphere. Precursor B was then added to the reaction and the temperature was raised to 320 °C and maintained for 24 h to form WTe_2 nanostars. Different masses of MWCNT powers

were then added to the mixture previously heated to obtain the WTe_2@CNT nanocomposites. TEM experiments show that the layered WTe_2@CNT nanocomposites possess an expanded interlayer distance of around 0.78 nm compared with 0.70 nm of the bare WTe_2 nanostars. The larger inter-atomic distance of the carbon composite allows the easiest buffer of the large volume change occurring during lithium intercalation/deintercalation [3]. Both materials were cycled against Li metal in a half-cell in 1 M $LiPF_6$ to evaluate their electrochemical stability and cyclability. WTe_2@MWCNTs nanocomposites exhibit a reversible capacity of 592 mAh g^{-1} at a current density of 500 mA g^{-1} after 500 cycles with a capacity retention of 100 %. Its counterpart WTe_2 nanostars show a big loss of capacity delivering around 85 mAh g^{-1} at the same current density after only 350 cycles [3]. The high cycling performance of WTe_2@MWCNTs can be attributed to the interconnected channels formed between MWCNTs and the abundant active sites of WTe_2 nanostars. This offers the large lattice spacing within the WTe_2 nanostars for Li intercalation and extraction, as well as avoid agglomeration problems.

The use of 2D layered materials-derived non-dimensional quantum dots (0QDs) such as graphene quantum dots (GQDs) and molybdenum disulphide quantum dots (MoS_2QDs) have attracted attention in recent years due to their many novel quantum effects. Quantum dots are man-made nanoscale crystals able to transport electrons. These artificial nanoparticles exhibit a semiconductive character that has been successfully applied in composites, solar cells, and fluorescent biological labels. WTe_2QDs associated with NiSe/C nanowires have been used as anode material for lithium storage in LIBs. Zhu *et al.* were able to construct a flexible free-standing WTe_2QD-doped NiSe/C nanowire structure using electrospinning techniques and a high-temperature selenization process [4]. The initial WTe_2 material was synthesized by a solid phase reaction using stoichiometric amounts of tungsten and tellurium powder (1:2), heated at 800 °C for 3 days. A solvothermal reaction was then performed to prepare the quantum dots. The WTe_2QD-doped NiSe/C nanowires were then prepared using a simple electrospinning method and a high-temperature selenization process. TEM results show a d-spacing of 0.273 nm in the final material and a hexagonal structure. The lithium-ion storage performance of the as-synthesized WTe_2QD-doped NiSe/C nanowires was investigated against a pure Li metal sheet in the potential range

0.005 – 3.0 V at a current density of 1 A g^{-1} [4]. Results show for the first cycle a discharge and charge capacity of 1120 and 667 mAh g^{-1}, respectively for the WTe_2QD-doped NiSe/C nanowires which correspond to a CE of 59.6 %. These values are higher than the ones obtained for naked NiSe/C which shows a first discharge capacity of 845 mAh g^{-1} and charge capacity of 443 mAh g^{-1} (CE of 51.2 %). A capacity of around 620 mAh g^{-1} is maintained after 500 cycles for the WTe_2QD-doped NiSe/C electrode compared with 265 mAh g^{-1} for the NiSe/C electrode [4]. Results show that the WTe_2QD-doped NiSe/C electrode displays better rate capability and cycling performance compared to the NiSe/C electrode. To further understand redox reaction behaviour and structural charge of the electrode during the charge and discharge process, cyclic voltammetry was performed. The first cathodic scan of NiSe/C electrodes shows the formation of an SEI layer and Li_2Se. The intercalation of Li^+ ions into the NiSe/C electrode results in the formation of Li_2Se accompanied by the conversion reaction of NiSe with Li^+ to form Ni metal and Li_2Se. The regeneration of the initial NiSe can be observed during the anodic scan. This behaviour is also observed for the WTe_2QD-doped NiSe/C electrode. This can be attributed to the high electron mobility of the WTe_2QD-doped NiSe/C nanowires which enhances the electrical conductivity of the composite which increases the carrier transport of the material, as proved by EIS. These results indicate that the WTe_2QD doped on NiSe/C nanowires reduce the total resistance of the composite electrode consequently improving the electrical conductivity of the electrode [4]. The doping process also introduces more active edges sites in the NiSe/C nanowires which improve ion diffusion and charge transport dynamics in the electrode. All these aspects result in the reversible lithium storage performance and capacity retention of this material [4].

A detailed study was carried out to characterise the as-synthesized WTe_2 and its electrochemical performance as a Li-ion anode. These included microstructural and structural analysis (PXRD, SEM/EDX and TEM) and structure evolution analysis (XANES and synchrotron operando PXRD) in conjunction with electrochemical analysis (galvanostatic cycling, cyclic voltammetry and electrochemical impedance spectroscopy). This study highlights the structural mechanism behind the reversible intercalation of Li^+ ions into the WTe_2 structure.

4.2 Experimental part

4.2.1 Synthesis and structure characterisation

Tungsten telluride (WTe_2) synthesis and structural characterization were previously reported in Chapter 3.

4.2.2 Operando synchrotron X-ray diffraction

Operando synchrotron PXRD measurements were carried out at the MSPD BL04 beamline of the ALBA synchrotron (Spain). The samples were measured at room temperature in fluorescence geometry using a 13 keV X-ray beam energy (λ $K_{\alpha 1}$ = 0.4195 Å) and a Mythen 6 K detector. Data were recorded in the 2 to 40° 2θ range. To reduce the effect of the preferred orientation of crystallites on the diffracted intensities, a concentric rocking of ± 15° of the whole setup within the Eulerian cradle was used. Each powder X-ray diffraction pattern was collected for 130 s. To verify the reliability of the cell positioning and overall data quality, a capillary (0.5 mm diameter borosilicate) with WTe_2 powder was used as a reference. Custom-made CR2032 coin cells with a glass window of 8 mm diameter and 130 µm thickness [5] were used for the operando measurement. The electrochemical cell contained *ca.* 7.10 mg of a homogenous powdered electrode mixture (70 wt % active material, 20 wt % carbon black (super P) and 10 wt % Polyvinylidene fluoride (PVDF, Kynar)), Li metal as the counter and reference electrode and a glass fibre separator soaked in 1 M $LiPF_6$ in ethylene carbonate/dimethylene carbonate (EC: DMC 1:1 v/v %) organic electrolyte. The cell was cycled within the voltage range of 0.1 -3.0 V *vs* Li^+/Li at a rate of 40 mA g^{-1}. Electrochemical data were collected using a Biologic (SP200 model) potentiostat and data were processed using the EC-Lab software V11.20 [6].

4.2.3 *Ex situ* synchrotron X-ray absorption spectroscopy

XANES measurements were performed at the B18 Core EXAFS beamline at the Diamond Light Source (UK). For the measurement, cast electrodes were cycled at

different states of charge and then extracted from the coin cells and rinsed three times with DMC (ca. 5 ml) in an argon glovebox. The electrodes were sealed under vacuum in aluminium laminated pouches before the measurements. Spectra of the charged electrodes at the W L_{III}-edge and Te K-edge were measured at ambient temperature in fluorescence mode at energies above and below the absorption edges of 10205 and 31807 eV, respectively. Three spectra were collected for each sample for 5 minutes. TeO_2 and H_2TeO_3 were used as references for Te^{4+} (31816.4 eV) and Te^{6+} (31820.9 eV) ions [7], [8] and W metal and WO_2 were used as references for W^0 (10211.3 eV) and W^{4+} (10211.8 eV), respectively [9]. Absorption spectra of the reference samples were collected in transmission mode. The Athena software in the Demeter package [10], [11] was used to average the scans collected, calibrate and normalise the data.

4.3 Results and Discussion in LIBs

4.3.1 Electrochemical characterization in LIBs

4.3.1.1 Galvanostatic cycling

The previous characterization of the bulk T_d-WTe_2 material is shown in Chapter 3, Section 3.3.1.

The Li^+ storage ability of the T_d-WTe_2 anode was tested through galvanostatic discharge-charge cycling. Measurements were carried out in the voltage range of 0.1 – 3.0 V *vs* Li^+/ Li at a current density of 10 mA g^{-1}. The cycling performance over different cycles (1^{st}, 2^{nd}, 3^{rd}, 5^{th} and 10^{th}) is displayed in Figure 4.1.

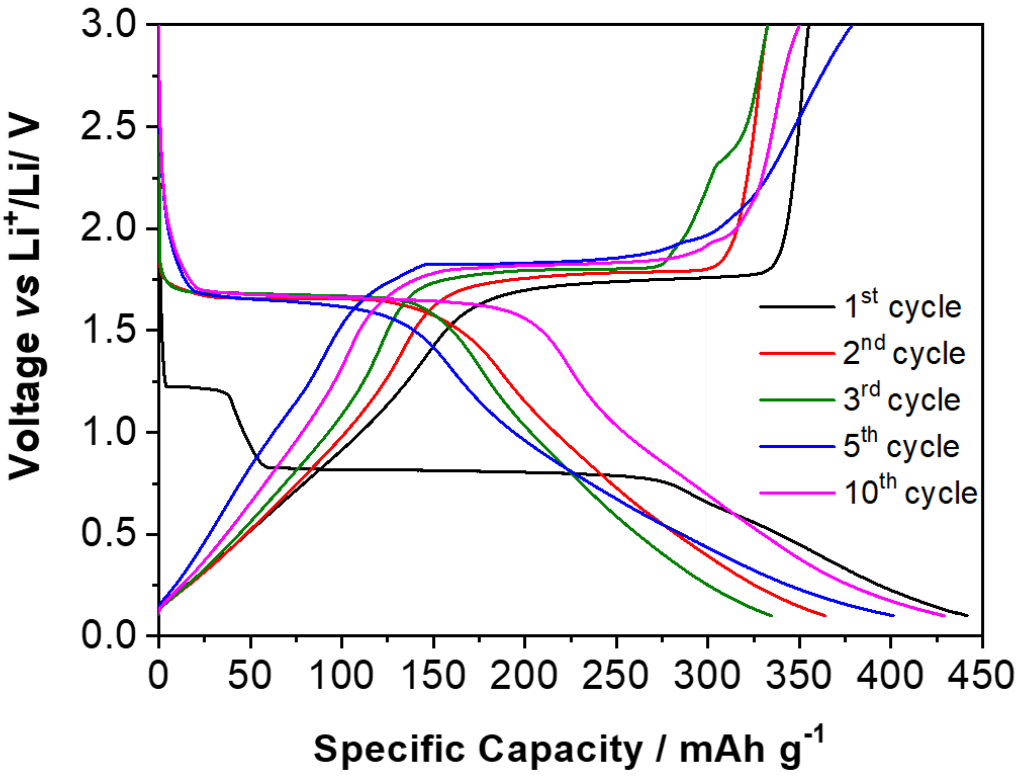

Figure 4.1 - Galvanostatic charge-discharge profiles at a current density of 10 mA g^{-1} of T_d-WTe_2 vs Li^+/Li in the voltage range of 0.1-3.0 V.

The first discharge from OCV to 0.1 V is characterised by a short and a long voltage plateau at 1.22 and 0.80 V, respectively. The anode material displays a first discharge capacity of 442 mAh g^{-1} correspondent to the theoretical insertion of 4 Li^+ ions per T_d-WTe_2 unit (240 mAh g^{-1}) plus the capacity associated with the SEI layer formation (~200 mAh g^{-1}) [12], [13]. Upon charging, a shorter and less defined plateau is observed at 1.71 V followed by an increase to the cut off voltage of 3.0 V, resulting in a charge capacity of 355 mAh g^{-1} corresponding to a coulombic efficiency of 84 %. These results compare with the ones obtained for SIBs (Section 3.3.2.1) both in terms of galvanostatic curve shape and CE obtained, however, the capacity obtained for the 1st cycle is higher for LIBs than SIBs (Figure 4.2). The higher capacity of T_d-WTe_2 *vs.* Li^+ compared with Na^+ ions can be attributed to the smaller size and lighter weight of lithium compared with sodium (0.76 Å *vs* 1.02 Å, respectively). To note that the voltage plateaux identified in the first discharge process also differ depending on if Li^+ or Na^+ ions are

intercalated. Although the first plateaux can be identified at 1.2 V for both SIBs and LIBs, the long plateau at lower voltage is located at a higher potential when Li^+ ions are intercalated comparing with Na (0.8 and 0.6 V, respectively). The difference in ion intercalation potential can be related to the higher standard reduction potential of Na^+/Na than Li^+/Li (ΔE^o = 0.33 V).

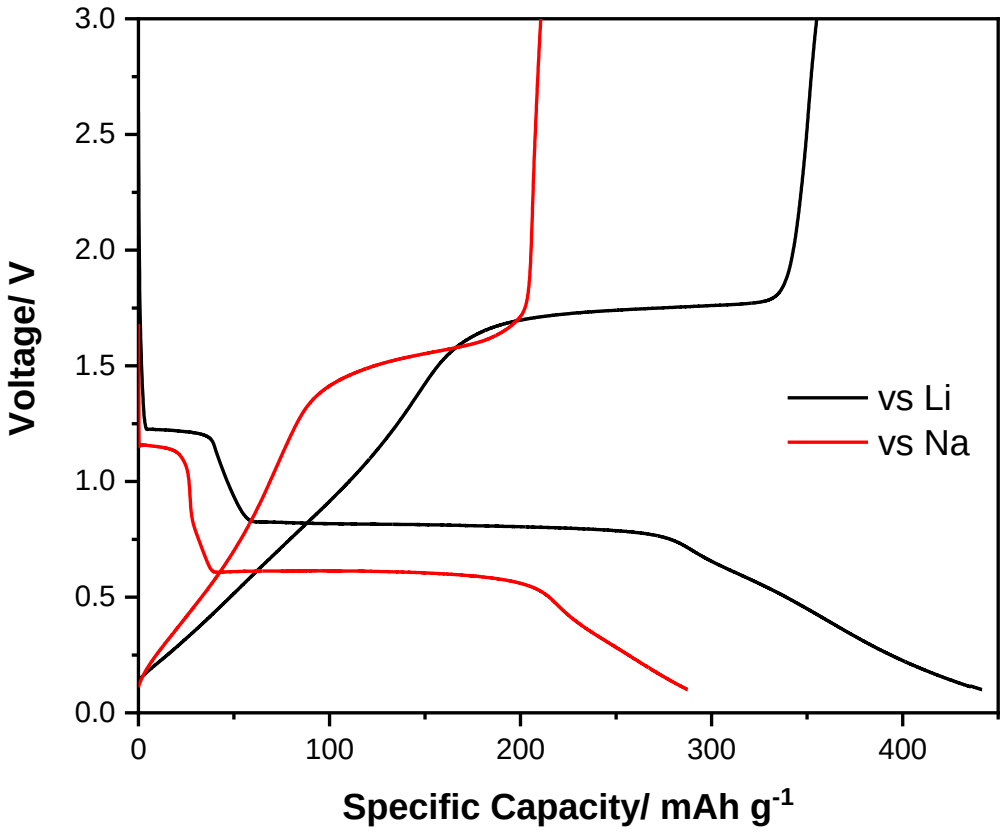

Figure 4.2 - Galvanostatic charge-discharge profiles at a current density of 10 mA g^{-1} of T_d-WTe_2 *vs* Li^+/Li and Na^+/Na in the voltage range of 0.1-3.0 V.

The discharge and charge plateaux matched exactly with the cathodic reduction and anodic oxidation peaks of the cyclic voltammogram (Figure 4.9). The mechanism for Li^+ insertion and extraction in the T_d-WTe_2 structure during the 1st cycle is comparable to the mechanism observed in SIBs with the existence of an intercalation reaction followed by a conversion reaction. The discharge reaction can be separated into two steps: the transformation of T_d-WTe_2 to Li_XWTe_2 during the initial Li^+ intercalation, followed by the disintegration of the crystal structure by the reduction of W^{4+} to W and the alloying reaction of Li^+ ions with tellurium to form Li_2Te. The extended plateau

observed at 0.8 V in the discharge profile of the first cycle is associated with the conversion reaction to form the metal alloy structure and the formation of the SEI layer [14]. The formation of this layer is associated with the consumption of Li^+ ions during the initial discharge and can be attributed to the initial capacity mismatched observed. The final reaction mechanism for LIBs can be described as:

$$WTe_2 + 4\,Li^+ + 4\,e^- \rightarrow W + 2\,Li_2Te \quad (4.1)$$

A shift is observed in the second cycle with a single discharge plateau observed at 1.66 V and the charge plateau at 1.77 V. A similar shift is observed during the cyclic voltammetry experiment (Figure 4.9) which can be attributed to the formation of ultrafine WTe_2 nanocrystals upon insertion and extraction of Li^+ ions. The activation process which occurs in the 1st cycle results in the distortion of the WTe_2 lattice due to a decrease of the electrochemical polarization after the activation process [15]. The plateaux and slopes observed in the electrochemical galvanostatic profiles during discharge and charge are consistent with the redox peaks in the CV curves. Similarly, to what is observed in SIBs (Section 3.3.2.1), a major decrease in specific capacity is observed up to the 5th cycle (390/ 350 mAh g^{-1}), followed by an increase in the subsequent 5 cycles (429/ 379 mAh g^{-1}). This suggests that the capacity decay during the first cycles is related to the electrode material itself and not the intercalant used. The pseudo-capacitive behaviour associated with TMDs at lower potentials is believed to be responsible for this increase in capacity [13], [16].

At a current density of 10 mA g^{-1}, a reversible discharge capacity of 181 mAh g^{-1} is obtained after 20 cycles which correspond to a capacity retention of 40 % (Figure 4.3). This capacity drop is associated with the particle size reduction of the bulk active material upon insertion and extraction of ions into the structure combined with the exfoliation of the active material from the current collector upon cycling [3], [15]. Cycled SEM data collected corroborated this idea (Section 4.3.1.2).

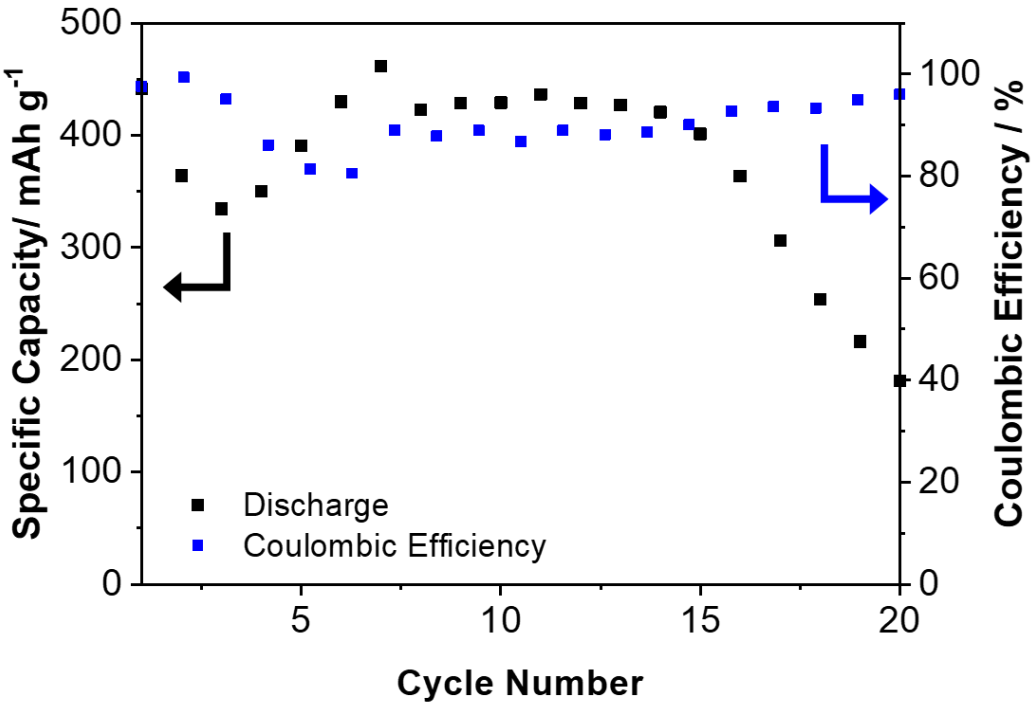

Figure 4.3 - Specific capacity *vs* cycle number plot with coulombic efficiencies over 20 cycles of T_d-WTe_2 in the voltage range of 0.1-3.0 V at 10 mA g^{-1}.

Previous studies report that the kinetics of the WTe_2 system and other layered dichalcogenides are characterized by a pseudocapacitance process, which was also observed against Na [18]. To evaluate the response of the material upon fast Li (de)intercalation, galvanostatic discharge-charge cycling *vs* Li^+/Li in the voltage range of 0.1 – 3.0 V at a current density of 100 mA g^{-1} is shown in Figure 4.4. The T_d-WTe_2 anode material retains 90.4 % of its initial charge capacity after 20 cycles.

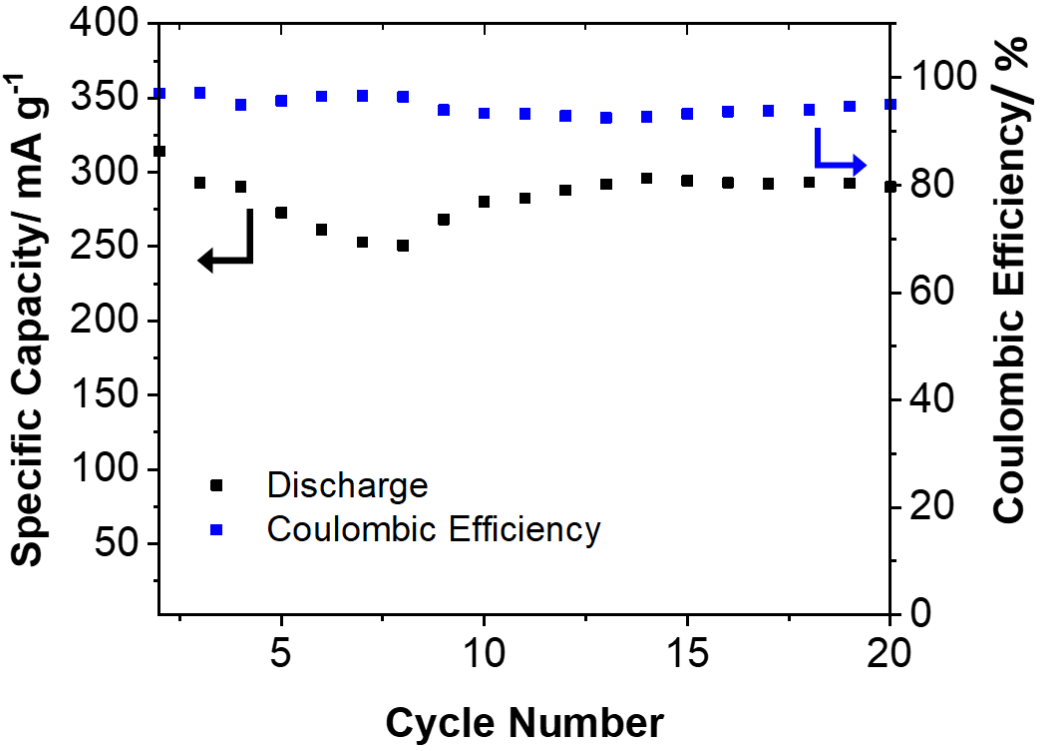

Figure 4.4 - Specific capacity *vs* cycle number plot with coulombic efficiencies over 20 cycles of T_d-WTe_2 in the voltage range of 0.1-3.0 V at 100 mA g^{-1}.

Figure 4.5 shows the long cycling performance of T_d-WTe_2 *vs* Li^+/Li at 10 and 100 mA g^{-1} in the voltage window of 0.1 – 3.0 V. The initial cycling (up to cycle 17) at 10 mA g^{-1} shows a higher discharge specific capacity with higher capacity retention when compared with the electrode cycled at 100 mA g^{-1} (69.4 and 67.4 %, respectively). However, after cycle 18 a major discharge capacity decline is observed for the electrode cycled at 10 mA g^{-1} while the electrode cycled at 100 mA g^{-1} presents a more stable decay. To note that, although both electrodes show different capacity retention patterns during cycling, the capacity obtained after 75 cycles is very similar (89.2 mAh g^{-1} and 85 mAh g^{-1} for 10 and 100 mA g^{-1}, respectively).

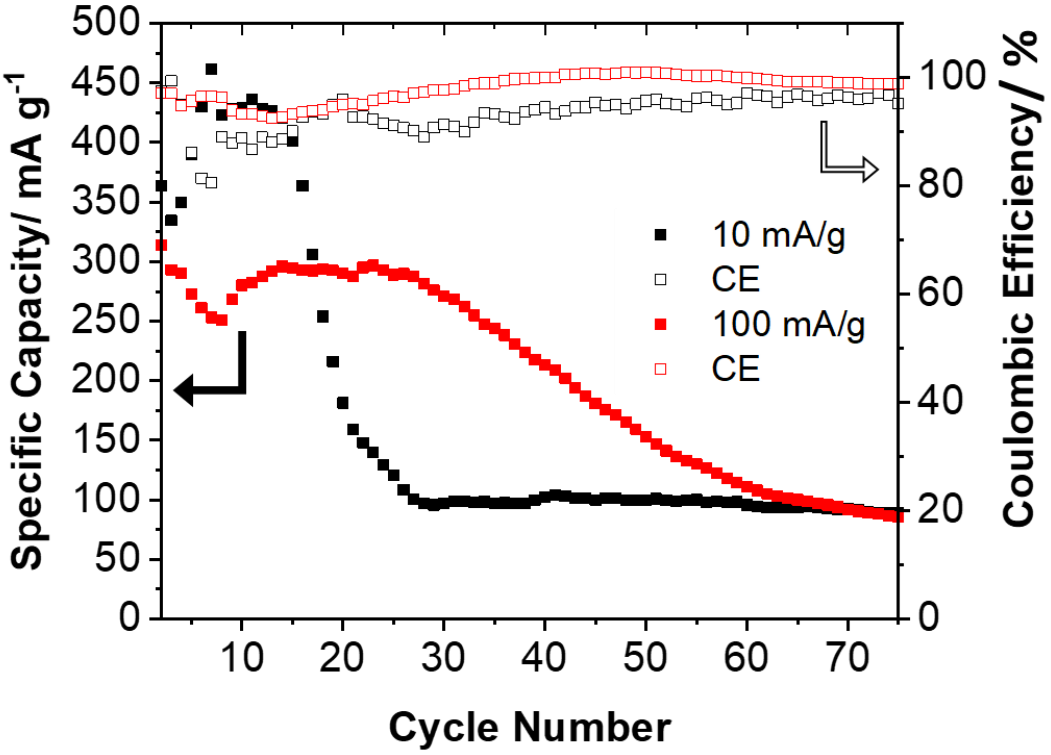

Figure 4.5 – Comparison graph of specific discharge capacity *vs* cycle number plot with coulombic efficiencies over 75 cycles of T_d-WTe_2 in the voltage range of 0.1-3.0 V at 10 and 100 mA g^{-1}.

The rate capability of WTe_2 anode for LIBs was examined at different currents from 10 to 500 mA g^{-1} (5 cycles each) between 0.1 and 3.0 V and then returned to 10 mA g^{-1} and is shown in Figure 4.6. The anode material shows a discharge capacity of 452, 525, 473, 332, 157 and 75 at 10, 20, 50, 100, 200 and 500 mA g^{-1}, respectively. A capacity of 221.2 mAh g^{-1} is achieved when the current density returns to 10 mA g^{-1}, corresponding to 46.4 % of its initial specific discharge capacity (476.3 mAh g^{-1}). The fact that the initial discharge capacity is not totally recovered can be related to the fact that the structure of the WTe_2 electrode material is irreversibly damaged during the cycling tests, indicating a low degree of flexibility of the structure.

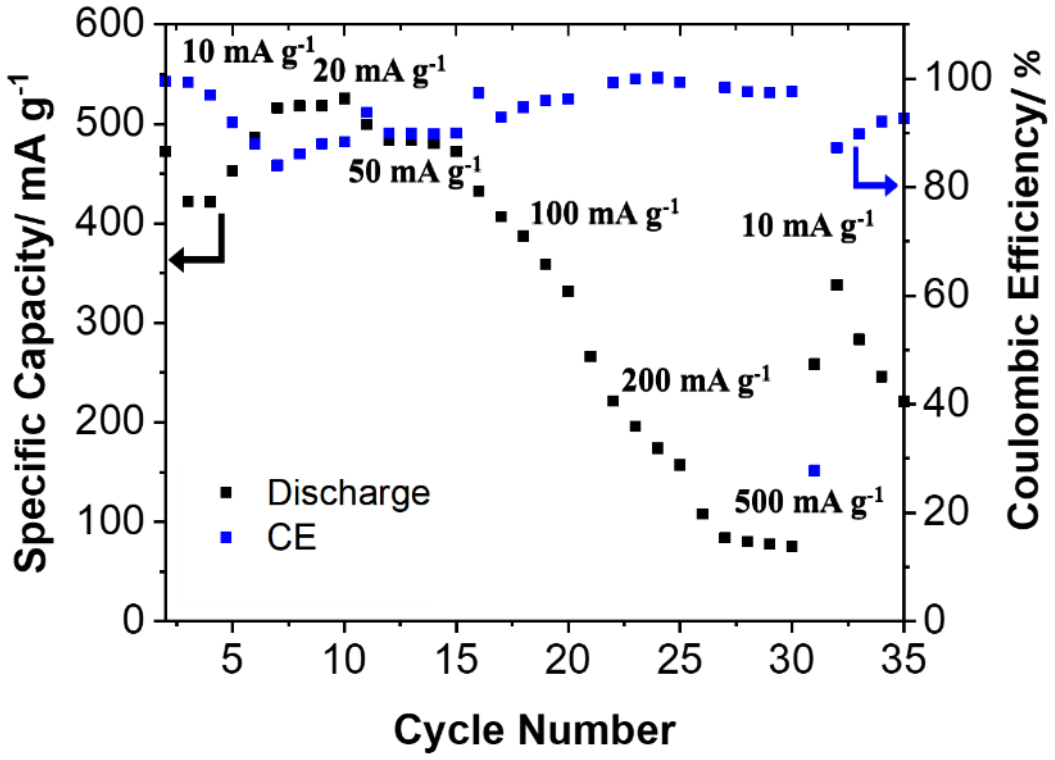

Figure 4.6 - Rate performance at current densities from 10 to 500 mA g^{-1} of T_d-WTe_2 in the voltage range of 0.1-3.0 V.

4.3.1.2 SEM analysis of post-mortem electrodes

Cycled SEM analysis was performed to study the electrode's microstructure evolution upon long-cycling. Figure 4.7 shows the SEM of the as-synthesized material as well as the electrode cycled up to 50 and 75 cycles. By analogy to the Na system (Section 3.3.2.2), a matrix composed of PVDF, carbon and separator's fibres can be seen in the cycled electrodes. This contrasts with the loose particles of the fresh material. In terms of particle size, after 50 cycles the average particle size is 10.8 μm a value which decreases to 9.5 μm after 75 cycles. The particle size is twice the size of the particles before cycling, an increase which can be related to the agglomeration of particles during the cycling process into the matrix which leads to the formation of bigger size crystals.

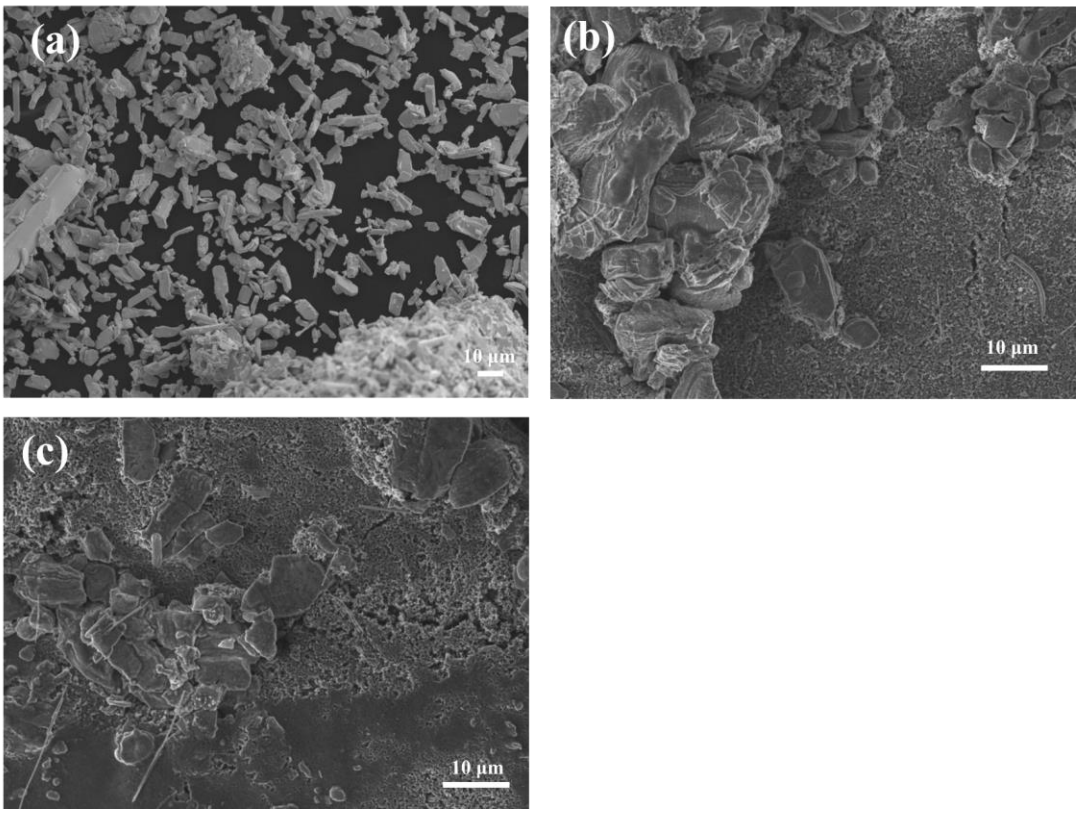

Figure 4.7- Morphology and structure change of the WTe_2 anodes during cycling against Li. The *ex situ* images of SEM were collected at selected cycles (a) pristine, (b) 50 cycles and (c) 75 cycles.

As reported in other MX_2 materials, the continuous insertion and extraction of ions into the structure lead to the formation of cracks and porosities as well as lattice breakdowns [13], [19]. Figure 4.8a shows the cracks formed in the WTe_2 electrode after 75 cycles. To note that the deformations formed upon Li insertion are more subtle compared with the insertion of Na (bigger ion) into the crystal structure, with smaller and softer cracks formed. These deformations are a result of the large stain generated by the removal of Li^+ ions during the charging process. It is worth noting that, although the material cracks, the particular layered structure associated with WTe_2 is well maintained during cycling [20]. The formation of nanoparticles during the cycling process leads to changes in the material's volume as well as aggregation of particles and electrolyte decomposition. These changes result in a gel-like polymeric layer and the formation of a thick SEI layer [15], giving the idea that the layers are fused, which can be seen in

Figure 4.8b. The increased internal strain during reaction with lithium and consequent cracking of the material and less defined morphology can be related to the poor electrochemical performance at long cycling as previously described (Section 4.3.1.1).

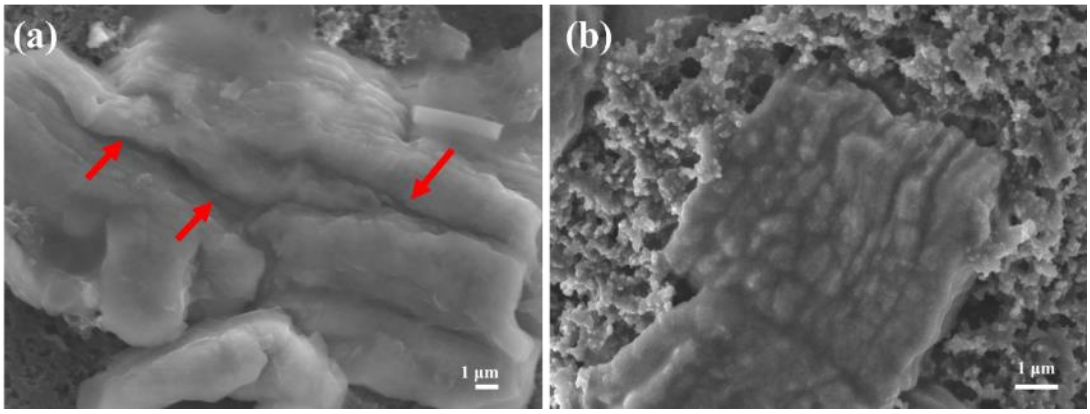

Figure 4.8- *Ex situ* SEM image showing (a) the crack formation in WTe_2 material after 75 cycles – cracks identified with red arrows and (b) the layered structure of the material.

4.3.1.3 Cyclic Voltammetry

The electrochemical performance of WTe_2 powder has been tested against lithium metal in a CR2032 type coin-cell configuration at room temperature. Figure 4.9 shows the CV performance of the WTe_2 anode for the first 5 cycles at a voltage scan of 0.1 mV s^{-1}, in the voltage range between 0.1 and 3.0 V. Two peaks can be observed in the first cathodic scan, a small peak at around 1.06 V and a sharp peak at 0.54 V. The small reduction peak at higher voltage corresponds to the intercalation of Li^+ ions into the anode structure leading to the formation of Li_xWTe_2, while the sharp peak is attributed to the combined formation of an SEI layer, metallic W and Li_2Te compound [15]. This conversion reaction between MTe_2 and metal ions was observed in other TMDs anode materials and is described by the equation below [14], [18]:

$$MTe_2 + 4\,X^+ + 4e^- \rightarrow M + 2\,X_2Te$$

From the second cycle onwards, the spectra are characterized by the presence of a single reduction peak at higher voltages (1.58 V) which, by analogy with its Na analogue, is

attributed to the formation of Li_2Te alloy [18], [21]. During the second scan, a single reduction peak is observed at 1.58 V, which stabilizes at that voltage for the following cycles. A single peak at around 1.82 V is observed in the anodic scans and can be assigned to the re-formation of the initial compound WTe_2, which shifts to higher potentials (1.84 V) during the 2nd scan. It can be observed that the intensities of the redox peaks decrease with the increase in the number of cycles reflecting the less stable and reversible electrochemical behaviour of the electrode after the initial conversion reaction and SEI layer formation. The single oxidation and reduction peak observed after the 1st cycle suggests the reaction mechanism in cycle 2 and subsequent cycles are different from cycle 1 and that from cycle 2 the extraction/insertion of Li^+ ions turns into a single reversible step.

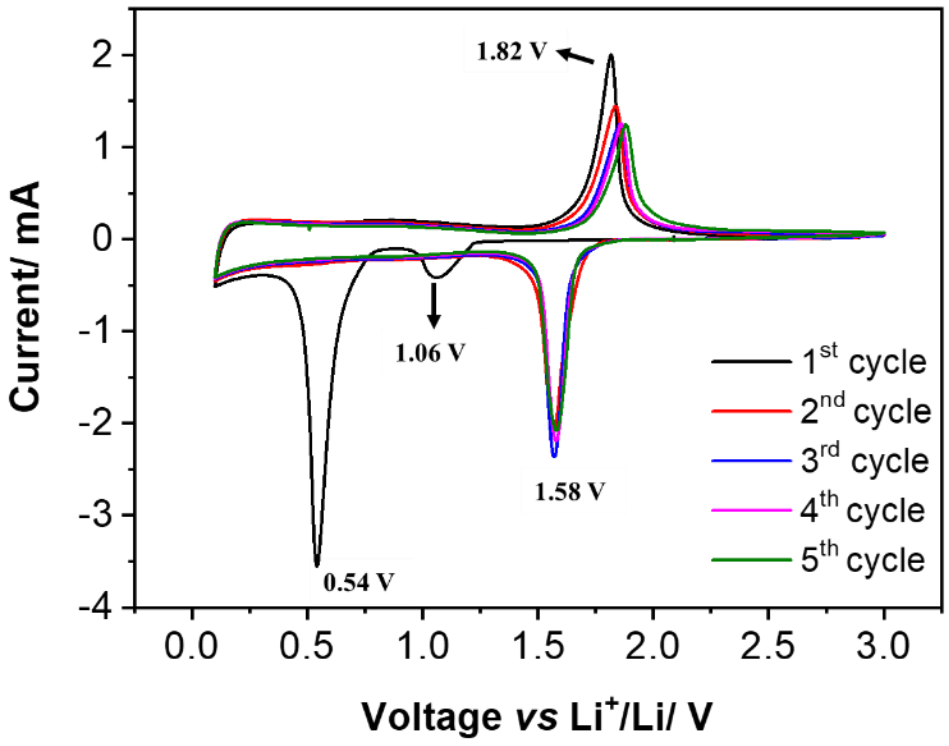

Figure 4.9 - Cyclic voltammogram of WTe_2 electrode *vs* Li^+/Li within the potential window 0.1–3.0 V at 0.1 mV s^{-1}.

The kinetics transport mechanism of WTe_2 during Li^+ ion intercalation and deintercalation processes was assessed by performing CV experiments at different scan rates and the second cycle is shown in Figure 4.10. A peak shift towards lower potential, 1.53 V to 1.45 V, was observed for the reduction peak (I) when an increased current rate from 0.08 to 1 mV s^{-1} is applied, respectively. The opposite is observed for the cathodic peak (II) where we observe the peak to shift from 1.84 V for 0.08 mV s^{-1} to a higher potential of 1.91 V for 1 mV s^{-1}. The calculated *b* values for the discharge I and charge II peaks (Figure 4.11) are estimated to be 0.71 and 0.73, respectively which suggest both surface-controlled and diffusion-controlled processes in the WTe_2 electrode. These results are different from the ones obtained for $MoTe_2$ where a lower value of b was registered (≈0.5689 and ≈0.6634) suggesting a more diffusion-controlled reaction [15]. There are several possible reasons for this discrepancy such as the possible larger surface area of WTe_2 compared with that of $MoTe_2$ or the possible interfacial sites and tellurium vacancies in the $MoTe_2$ blocks [13], [15], [22]. Further studies are necessary to confirm these options.

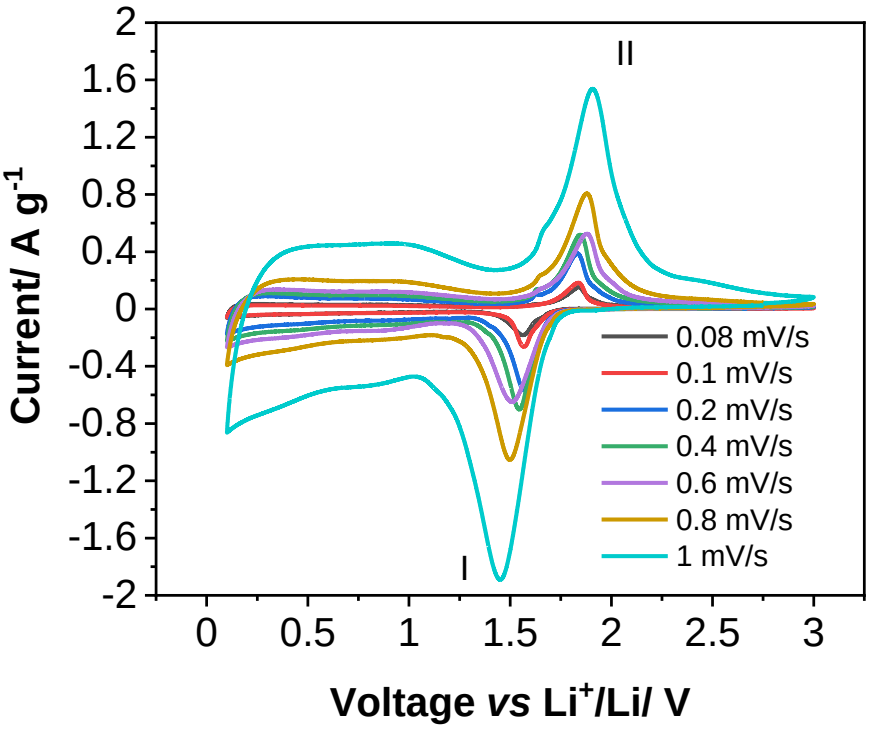

Figure 4.10 - Cyclic voltammograms of the second cycle of the WTe_2 electrode at different scan rates within the potential window 0.1–3.0 V.

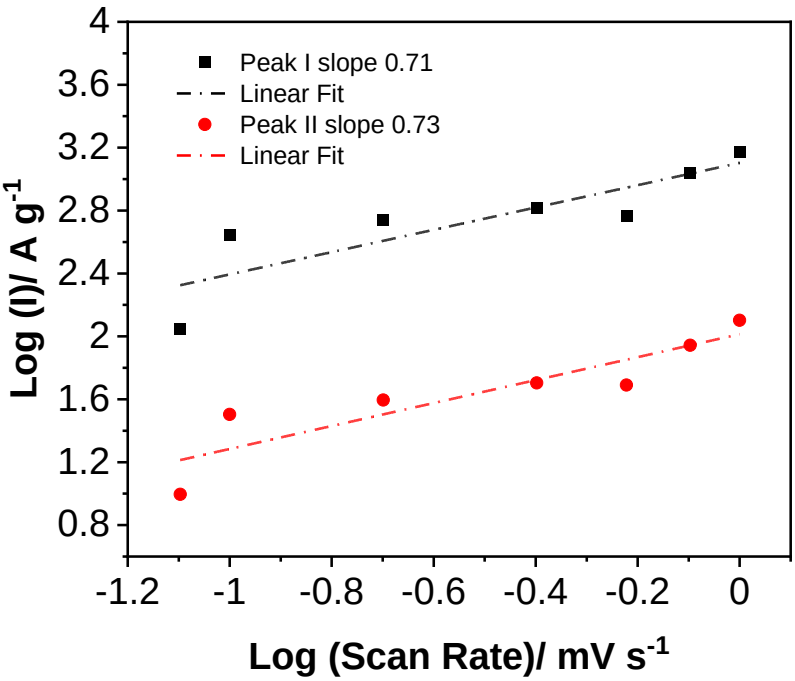

Figure 4.11 - Linear relationship between Log I (logarithm peak currents) and log V (logarithm scan rate) of the reduction peak (I) and oxidation peak (II) at different scan rates (0.08, 0.1, 0.2, 0.4, 0.6, 0.8, and 1.0 mV s^{-1}). R^2 values of 0.75 and 0.82, respectively.

Figure 4.12b shows the fitted CV curve at 0.4 mV s^{-1} where the pseudocapacitive is represented as the inner coloured graph.

From the fitted curve, we can observe that when cycled at 0.4 mV s^{-1} the total Li^+ storage capacity arises mainly from the capacitive behaviour of the WTe_2 electrode with 78.5 %. The electrode exhibits a decrease in capacitive contributions from 1 to 0.08 mV s^{-1} as can be seen in Figure 4.13. Compared with the Na system (50 % at 0.4 mV s^{-1}) and other dichalcogenides such as $MoTe_2$ (61 % at 0.1 mV s^{-1}) [18], the Li system presents the highest capacitive value of 78.5 %.

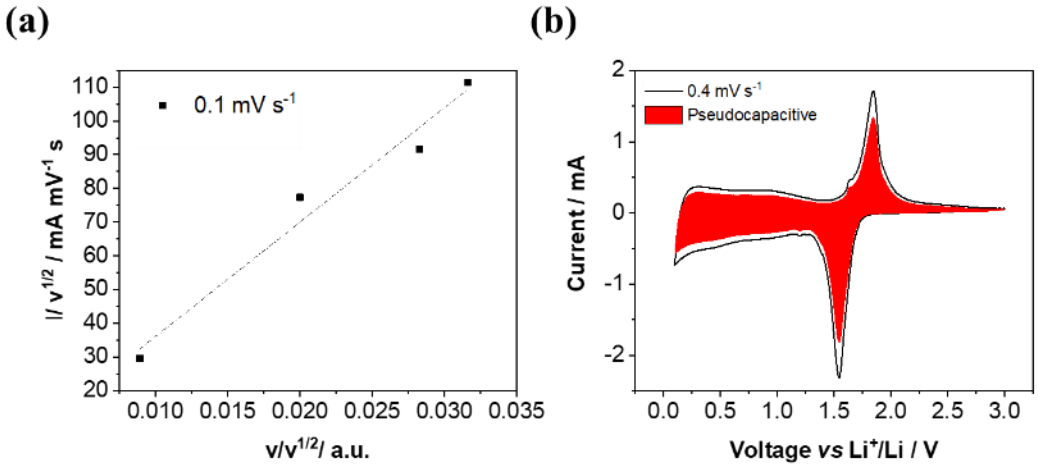

Figure 4.12 – (a) Linear relationship between $I/v^{1/2}$ and $v/v^{1/2}$ at 0.1 mV s^{-1} R^2 value of 0.907. (b) Fitted pseudocapacitive contribution (red area) of the WTe_2 electrode at a scan rate of 0.4 mV s^{-1} in the potential window, 0.1–3.0 V.

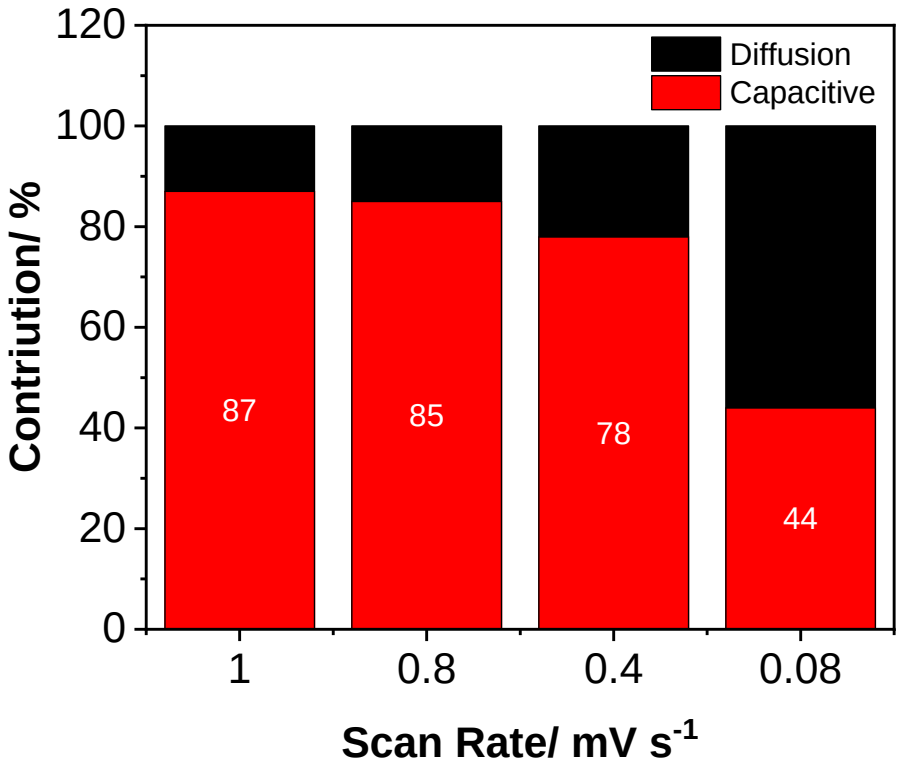

Figure 4.13 - Ratio of pseudocapacitive (red) and diffusion-controlled (black) capacities at various scan rates of WTe_2 electrodes.

The results obtained further confirm that the capacitive contribution of the WTe_2 electrode becomes predominant at the higher current densities.

The CV curves at different scan rates allowed further determination of the Li^+ ion diffusion coefficient using the Randles-Sevcik equation (Section **Error! Reference s ource not found.**). The linear relationship between the peak current and the square root of the scan rate for each peak are shown in Figure 4.14. From the slope of these plots, the average diffusion coefficient in WTe_2 can be determined. As mentioned previously, the (de)lithiation processes into the layered WTe_2 material are controlled by both capacitive and diffusion reactions and therefore the linear relationship here presented between the two parameters is only related to the diffusion process occurring. The obtained values for the Li^+ apparent diffusion coefficients at different anodic and cathodic peaks are within the range of 8.21 x 10^{-10} and 9.89 x 10^{-10} cm^2 s^{-1}, as shown in Table 4.1.

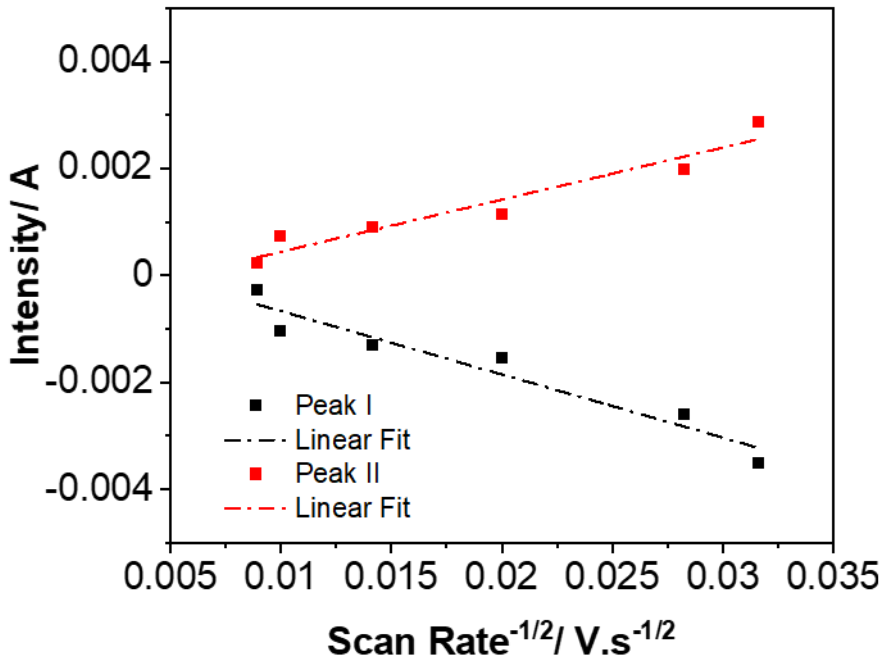

Figure 4.14 - Linear fitting of the peak current versus the square root of the scan rate of the reduction (I) and oxidation (II) peaks. R^2 values of 0.93 and 0.93, respectively.

Table 4.1 – Diffusion coefficient for each peak calculated from the Randles-Sevcik equation

CV Peak	D_{Li^+} ($cm^2\ s^{-1}$)
I	9.89×10^{-10}
II	8.21×10^{-10}

The diffusion coefficient values calculated for both peaks I and II are in the same order of magnitude, showing that the Li^+ ion diffusion is slightly favoured upon lithiation. Contrarily to the Na system where a bottleneck step is observed during the initial insertion of ions into the layered structure, this is not observed in the Li system, where there is a single peak upon reduction only. To note that a slightly higher diffusion coefficient is registered for SIBs compared with LIBs based on the calculated values in Table 4.2, which can be related to the different kinetics of the Na^+ and Li^+ ions. The close diffusion coefficient values obtained can be attributed to the large 2D channels in WTe_2 which allow facile ionic intercalation for both Li^+ and Na^+ ions during the initial charge/discharge cycles (in this case, the 2nd cycle).

Table 4.2 - Diffusion coefficient for Na^+ and Li^+ ion of each peak calculated from the Randles-Sevcik equation

Process	CV Peak	D_{Na^+} ($cm^2\ s^{-1}$)	D_{Li^+} ($cm^2\ s^{-1}$)
Cathodic	I	1.02×10^{-9}	9.89×10^{-10}
	II	9.19×10^{-11}	
Anodic	III	1.14×10^{-9}	(peak II) 8.21×10^{-10}

The values obtained in WTe_2 electrodes indicate a better Li^+ diffusion in comparison with other dichalcogenides materials such as TiS_2 (in the order of 10^{-13} obtained by GITT method) [23] and a similar diffusion compared with other Te-dichalcogenides such as $MoTe_2$ (10^{-9}) [15]. The increased diffusion coefficient is attributed to the

enlarged interlayer spacing in Te materials (0.70 and 0.71 nm for WTe_2 and $MoTe_2$, respectively) compared with TiS_2 (0.57 nm), which facilitates the movement of ions (see Annexe B - CV Data Calibrations for WTe2 in LIBs for deeper data analysis).

4.3.1.4 Electrochemical Impedance Spectroscopy

The impedance spectrum of the as-prepared T_d-WTe_2 was recorded at OCV in a frequency ranging from 0.01 Hz to 100 kHz and is shown in Figure 4.15. The equivalent-circuit model used to fit the OCV spectrum consists of a surface resistance (R_S) at high frequencies plus a charge-transfer resistance (R_{CT}) along with a constant phase element (CPE). The high-frequency range is dominated by the electrolyte resistance while the high-medium frequency range is related to the charge-transfer resistance of electrons and Li^+ ions moving across the electrode-electrolyte interface [24]. The interface between the electrode and electrolyte leads to the formation of an electrical double-layer capacitor (CPE) as a result of ion adsorption onto the surface of the electrode. The equivalent-circuit used allows calculating the charge-transfer resistance by measuring the size of the semi-circle in OCV state which was determined to be 82.5 Ω. The high R_{CT} value at OCV shows the initial barrier of Li^+ reaction to WTe_2 as previously observed for other TMDs [15].

The evolution of the impedance spectra during the 1st cycle during the discharge and charge processes was studied and is shown in Figure 4.16. During the 1st discharge process, we observe the formation of a solid electrolyte interface (SEI) layer onto the electrode surface which affects the resistive interface between the electrolyte and electrode during ion intercalation. The equivalent circuit used to fit the data of the discharge and charge spectra was composed of, besides an R_s at high frequencies and a charge-transfer resistance R_{CT} along with a constant phase element (CPE), an extra R_{SEI} and correspondent CPE element related to the SEI layer formed. This extra feature is identified at high frequencies by a discrete semicircle as a result of the impedance phenomena occurring due to the surface film passivation, electrolyte resistance and the lithium intercalation process [25]. The proximity of the relaxation time constant of both processes does not allow the observation of individual semicircles so the one observed results of the overlapping of both individual circles. Although a single semicircle is

observed as a result of the contribution of both SEI layer and charge-transfer resistance processes, both individual processes can still be distinguished.

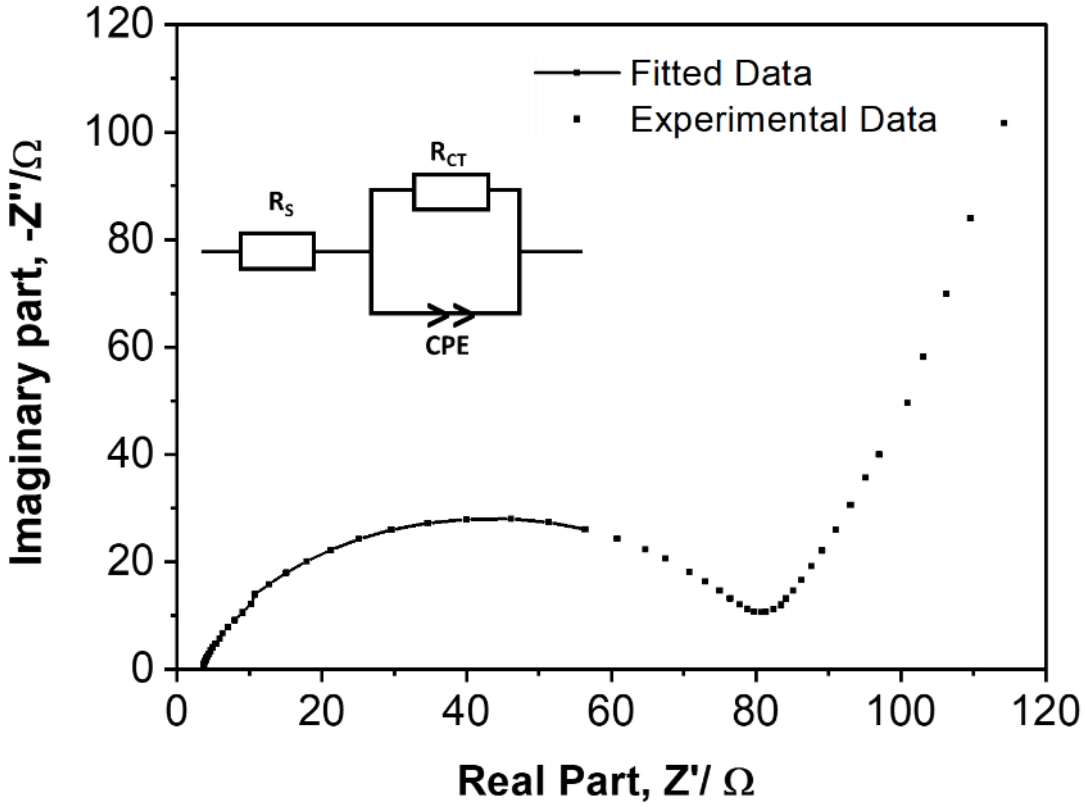

Figure 4.15 - Nyquist impedance plot collected from 0.01 Hz to 100 kHz for WTe_2 in LIBs in OCV.

The equivalent circuit showed in the inset of Figure 4.16 is the most appropriate to fit the results obtained. The R_{SEI} and R_{CT} values for the 1st discharge were found to be 65.4 and 68.1 Ω, respectively, resulting in a total arc resistance of 133.5 Ω. The increase in arc radius upon ion insertion suggests a more resistive interface between the electrolyte and electrode. The high value registered for the SEI layer resistance is the main contributor for the high arc radius observed, however, we observe a slight reduction of the R_{CT} value compared with the OCV state. The reason for this might be the formation of ultrafine nanocrystals upon conversion of WTe_2 into Li_2Te and W during the 1st discharge, which facilitates the movement of Li^+ ions across the electrode-electrolyte interface resulting in a decrease of the charge-transfer resistance [26]. Upon charge, both the R_{SEI} and R_{CT} values decrease to 45.8 and 5.9 Ω, respectively. The abrupt decrease in R_{CT} value upon deinsertion of Li^+ ions show an increase in the Li^+ diffusion and stability of the discharge/ charge capacity of the cycled electrode. This reduction in

R_{CT} value registered during the deinsertion of ions from the WTe_2 structure can be associated with the formation of a less resistive electrode-electrolyte interface upon the reformation of the initial T_d-WTe_2 structure. The fact that the particles become nanosized after the first cycle also facilitates Li^+ transfer by decreasing R_{CT} [15]. The decrease observed in R_{SEI} value can be associated with the dissolution of the SEI layer during Li^+ deintercalation. The value of the different resistances for the 1st cycle can be found in

The changes in both the SEI layer and charge-transfer resistance were studied up to the 10th cycle and the evolution of the EIS spectra upon discharge is shown in Figure 4.17. The equivalent circuit used to fit the EIS data for the 1st was used to fit the data of the 2nd, 5th and 10th discharge processes.

Table 4.3.

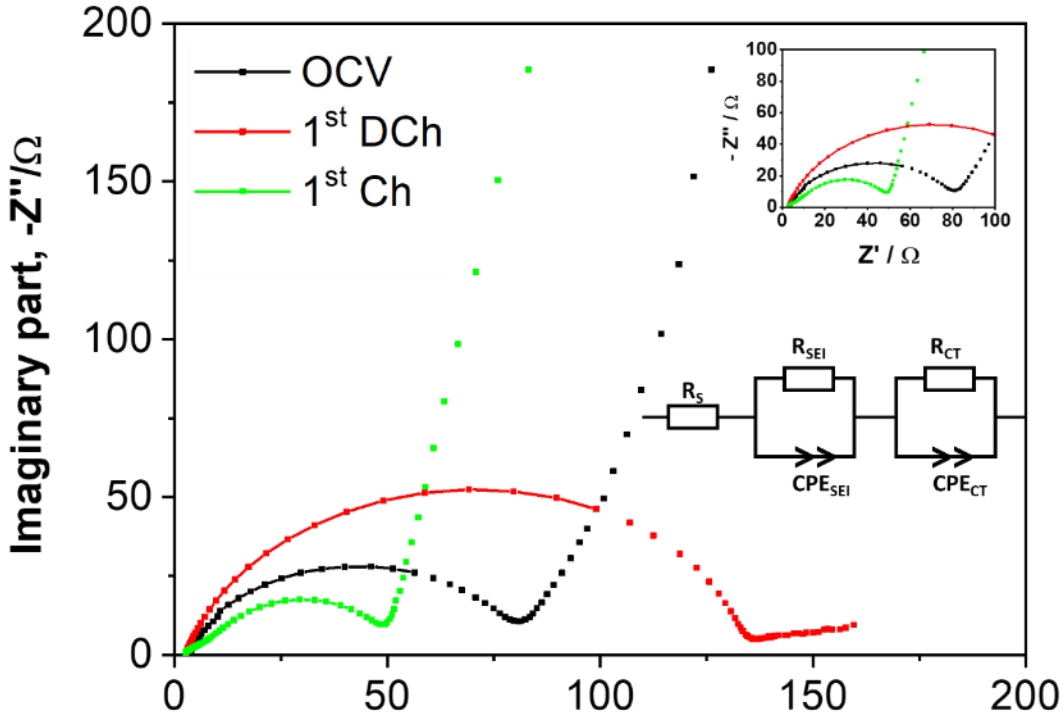

Figure 4.16- Nyquist impedance plots collected from 0.01 Hz to 100 kHz for WTe_2 in LIBs in OCV, 1st discharge, and 1st charge.

The changes in both the SEI layer and charge-transfer resistance were studied up to the 10th cycle and the evolution of the EIS spectra upon discharge is shown in Figure 4.17. The equivalent circuit used to fit the EIS data for the 1st was used to fit the data of the 2nd, 5th and 10th discharge processes.

Table 4.3 - Electrolyte, SEI and charge-transfer resistances determined from EIS during the 1st cycle for WTe_2 in LIBs.

Sample	R_S (Ω)	R_{SEI} (Ω)	R_{CT} (Ω)
OCV	3.2		82.5
1st Discharge	2.6	65.4	68.1
1st Charge	2.1	45.8	5.9

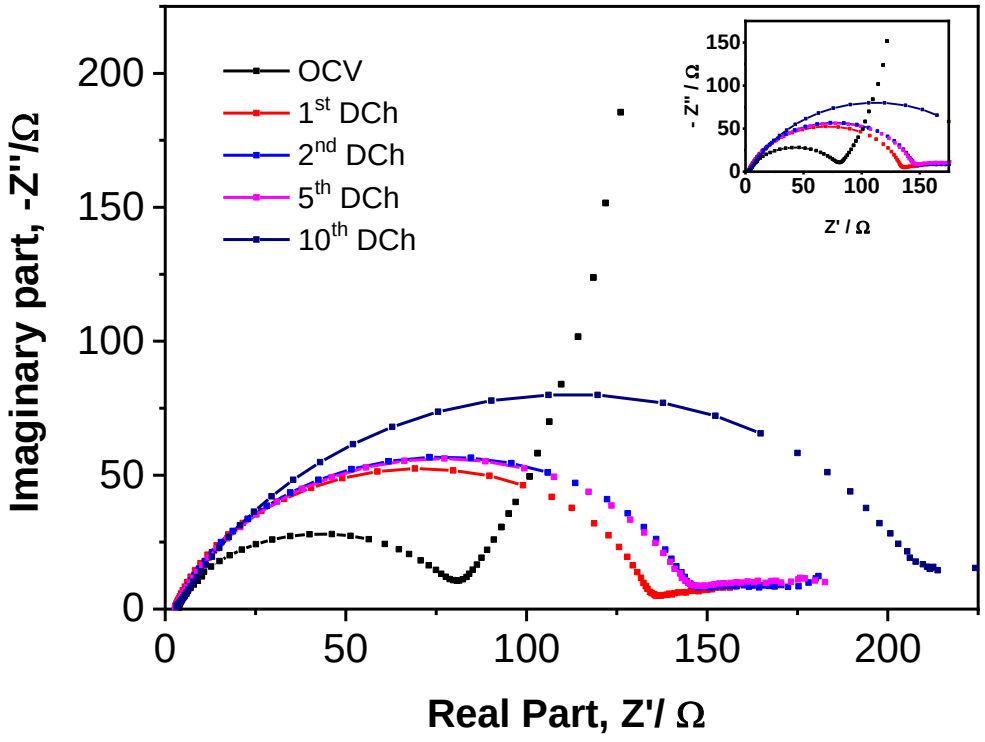

Figure 4.17 - Nyquist impedance plot collected from 0.01 Hz to 100 kHz for WTe_2 in LIBs during the discharge process up to the 10th cycle.

A slight increase in total arc resistance from 133.5 Ω for the 1st discharge to 150.8 Ω for the 2nd discharge is observed. The reformation of WTe_2 during the initial charging process results in an increased interlayer spacing between layers which is associated with an increased internal resistance [27]. The overall arc resistance stays constant during the 5th discharge (153 Ω) while further cycling leads to a major increase of impedance up to the 10th discharge (211 Ω). To note the high value of R_{SEI} (151 Ω) recorded during the 5th discharge can be ascribed to the formation of excessive SEI film inside the interlayer related to the increased interlayer spacing [27], [28]. The continuous decrease of the R_{CT} value with cycling is linked to the nano-sized particles formed after the first cycle and prove that faster Li^+ mobility in the WTe_2 electrode leads to low overpotential after the first cycle. The value of the different resistances is shown in Table 4.4.

Table 4.4 - Electrolyte, SEI and charge-transfer resistances determined from EIS during the discharge processes for WTe_2 in LIBs.

Sample	R_S (Ω)	R_{SEI} (Ω)	R_{CT} (Ω)
OCV	3.2		82.5
1st Discharge	2.6	65.4	68.1
2nd Discharge	3.0	2.1	148.7
5th Discharge	1.1	151.3	1.63
10th Discharge	2.5	208.1	3.2

The impedance data collected during the charging process was fitted using the equivalent circuit used for the 1st charge and is shown in Figure 4.18. The trend observed during the discharge process shows a decrease in overall resistance and consequently in arc radius upon charging. The R_{SEI} and R_{CT} calculated up to the 10th charge are similar in every charging process with a slight decrease in total resistance from 51.6 Ω to 46.4

Ω from the 1st to the 10th charging process. Table 4.5 shows the resistance values obtained for the charging process up to the 10th cycle.

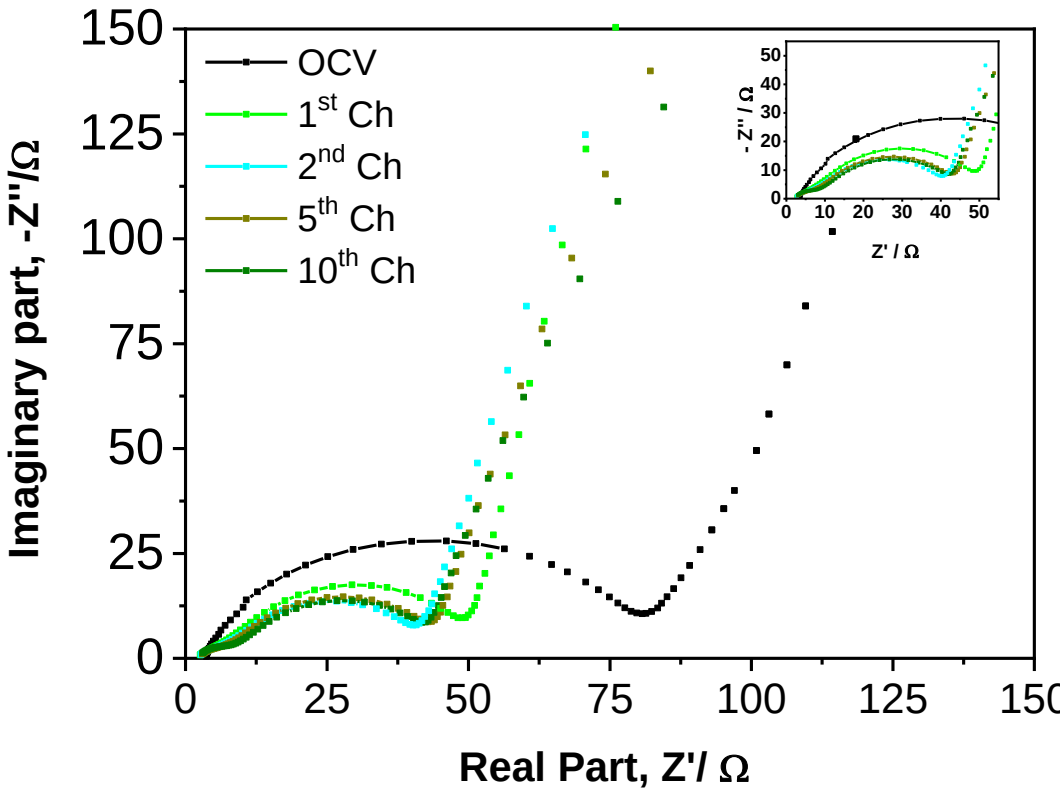

Figure 4.18 - Nyquist impedance plot collected from 0.01 Hz to 100 kHz for WTe_2 in LIBs during the charging process up to the 10th cycle.

Table 4.5 - Electrolyte, SEI and charge-transfer resistances determined from EIS during the charging processes for WTe_2 in LIBs.

Sample	R_S (Ω)	R_{SEI} (Ω)	R_{CT} (Ω)
OCV	3.2		82.5
1st Charge	2.1	45.8	5.8
2nd Charge	2.1	38.4	5.6
5th Charge	2.3	41.8	5.5
10th Charge	2.1	7.0	39.4

The EIS data was recorded upon long cycling to understand the resistance evolution after continuous Li^+ intercalation/ extraction. Figure 4.19 shows the EIS spectra at OCV state and for cycles 50 and 75. The data were fitted using the same equivalent circuit used for cycle 10 and the evolution of the R_{SEI} and R_{CT} value upon long cycling is shown in Table 4.6. To note that no major increase or decrease in overall resistance is registered upon cycling which suggests good stability of the electrode material. However, a major increase in the R_{SEI} value in cycle 50 compared with cycle 10 (7.0 *vs* 76.8 Ω) is registered. This increases in resistance can be associated with an increase in the thickness of the SEI layer created during cycling which can be related to the major capacity fading observed during this phase. The large-volume changes experienced by the Te-based compounds formed during cycling upon Li^+ movement are the main responsible for these SEI layer changes. The relaxation of stress/strain induced by volume expansion is observed in high-capacity electrodes after the first lithiation through deformation of the initial material [29], [30]. The expansion that occurs during lithiation breaks the SEI layer, resulting in more electrolyte to be used to rebuild the layer during cycling and therefore, a thicker SEI layer. This increase leads to a shortened lifetime of a cell as can be observed by the charge-discharge curves (Figure 4.3).

The stability of the R_S value upon cycling suggests a stable intrinsic and interfacial resistance of the electrode upon ion intercalation/ extraction. The slight increases in R_S value upon 75 cycles (6.1 Ω) could suggest a consequent increase in the electrode resistivity as a whole. The constant destruction and reconstruction of the initial WTe_2 electrode material accompanied by the formation of extra phases during cycling may result in damage of the electronic transfer sites at the surface of the electrode [31], which may affect the performance upon cycling.

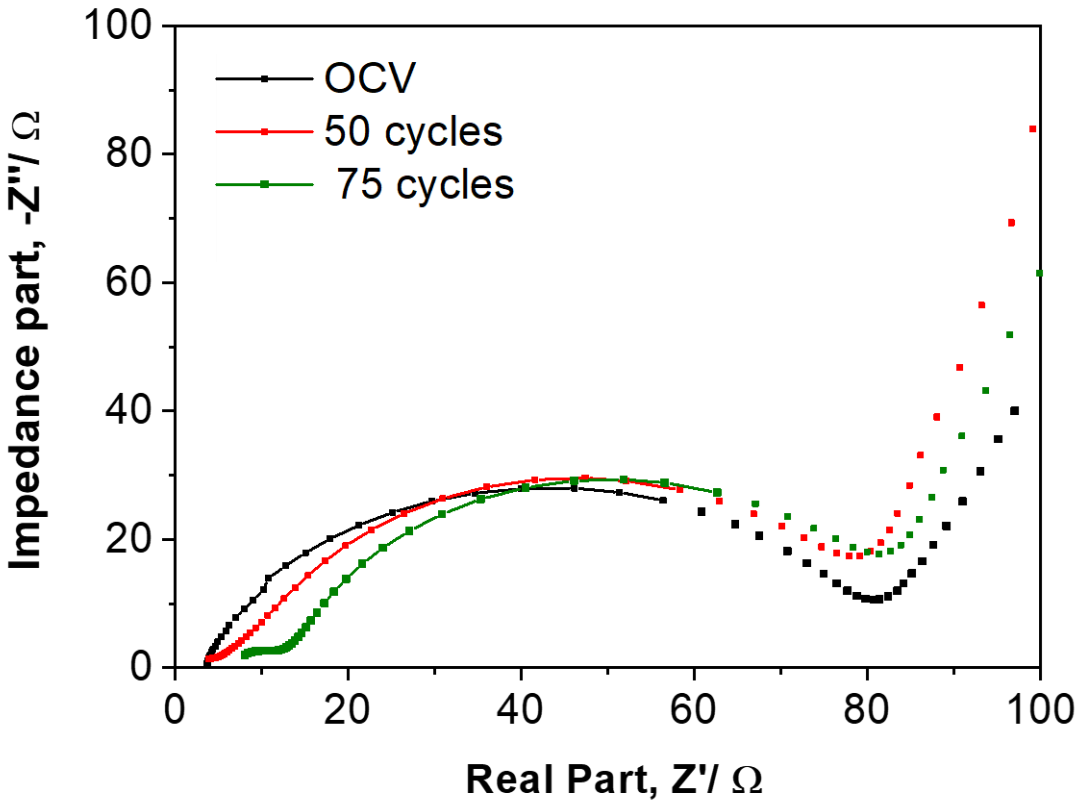

Figure 4.19 - Nyquist impedance plot collected from 0.01 Hz to 100 kHz for WTe_2 in LIBs at OCV, 50th and 75th cycle.

Table 4.6 - Electrolyte, SEI and charge-transfer resistances determined from EIS upon long cycling for WTe_2 in LIBs.

Sample	R_S (Ω)	R_{SEI} (Ω)	R_{CT}(Ω)
OCV	3.2		82.5
50th cycle	3.3	76.8	5.4
75th Cycle	6.1	7.5	74.2

4.3.2 Structure evolution upon Li^+ ion insertion

4.3.2.1 X-ray Absorption Near Edge Spectroscopy

The oxidation state of the transition metal ions in the layered T_d-WTe_2 was evaluated at different states of charge using X-ray absorption near-edge spectroscopy (XANES). The spectra of W and Te were collected from samples extracted from cells stopped at key points during the 1st charge/ discharge cycle. For these experiments, information about the local symmetry, coordination, and valence for the W and Te elements was provided measuring the X-ray absorptions at the L_{III} and K-edge, respectively. The oxidation state for W and Te in the pristine compounds were confirmed to be +4 and 2-, respectively, by comparing the absorption edge energies to standards [32].

The XAS spectra of the W L_{III}-edge (Figure 4.20) show a single white line above the edge centred at an energy of 10207.20 eV for the OCV sample. The non-existence of a post-edge feature can be attributed to the presence of octahedral W^{4+} in the crystal [32]. To understand the changes in oxidation state occurring in the W transition metal during the discharge phase, three main points were analysed during the main plateau at 0.6 V: start, middle and end plateau. When the material is discharged to the beginning of the plateau (0.6 V SP), a decrease in the white line intensity is observed (Figure 4.22). This decrease can be associated with the decrease in the oxidation state of the W atom due to the insertion of ~ 1 Li^+ ions at this stage (presence of a Li_xWTe_2 phase). The initial insertion of Li^+ ions into the WTe_2 structure leads to a displacement of the electron density towards the W atom leading to an increase in occupied W 5d orbitals and a consequent decrease in white line intensity. At the middle plateau (0.6 V MP), a total of 2.7 Li^+ ions are expected to be inserted into the crystal structure (Li_xWTe_2 phase) which is expected to lead to a further decrease in the W oxidation state (W^{4-x}). However, no major changes are observed in the white line intensity at this point, suggesting that the further insertion of ions does not majorly influence the electron density in W as seen for the Na system (Section 3.3.3.1). Further insertion of ions up to the end of the plateau phase (0.6 V EP) results in an additional decrease in white line intensity. At this point, full conversion of WTe_2 to W metal and Li_2Te is expected as the specific capacity obtained reflects the presence of 4.2 Li^+ ions in total, which is more than the 4 ions supported by the crystal structure. At the end of the discharge process (0.1 V), the

intensity of the white line reaches a minimum, however, is to note that the discharge sample does not coincide in energy to the W metal spectrum. This leads us to consider that the structure of the WTe_2 structure does not convert to W metal upon Li insertion and that some initial WTe_2 or some Li_xWTe_2 phase is still present in the electrode

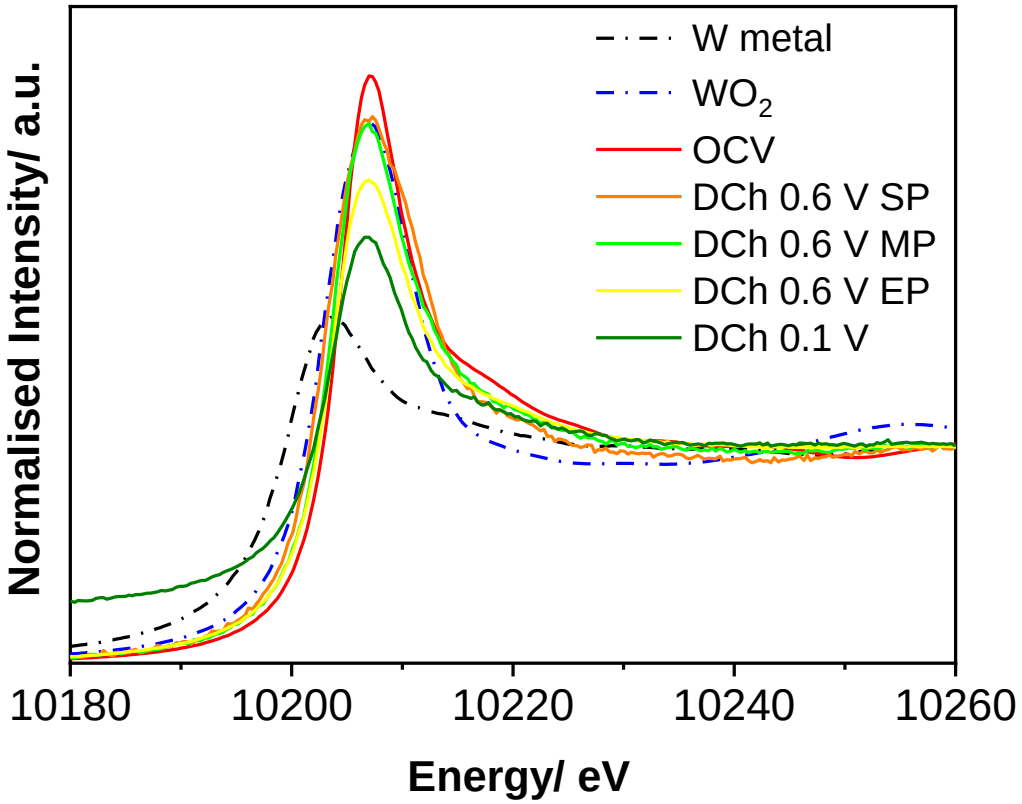

Figure 4.20 - Normalized W L_{III}-edge XANES spectra of WTe_2 electrode during the 1st discharge process along with standard W metal and WO_2 powders used as reference.

The deinsertion of ions leads to an increase in the W white line intensity during the entire charging process (Figure 4.21). The deinsertion of Li^+ ions from the Li_2Te alloy phase leads to the reformation of the initial WTe_2 structure and consequently the oxidation of the W atom back to W^{4+}. The data obtained at the end of the charge corroborate this assumption as an increase in the intensity of the white line is observed as a result of the movement of electrons from the W d orbital upon Li^+ extraction. To note that at the end of 1st charging process the white line intensity is lower than the one registered at OCV state which suggests that the W atom is in a more reduced state upon

ion deinsertion compared with pristine, which agrees with the partial reversibility of the process, as seen in the galvanostatic data.

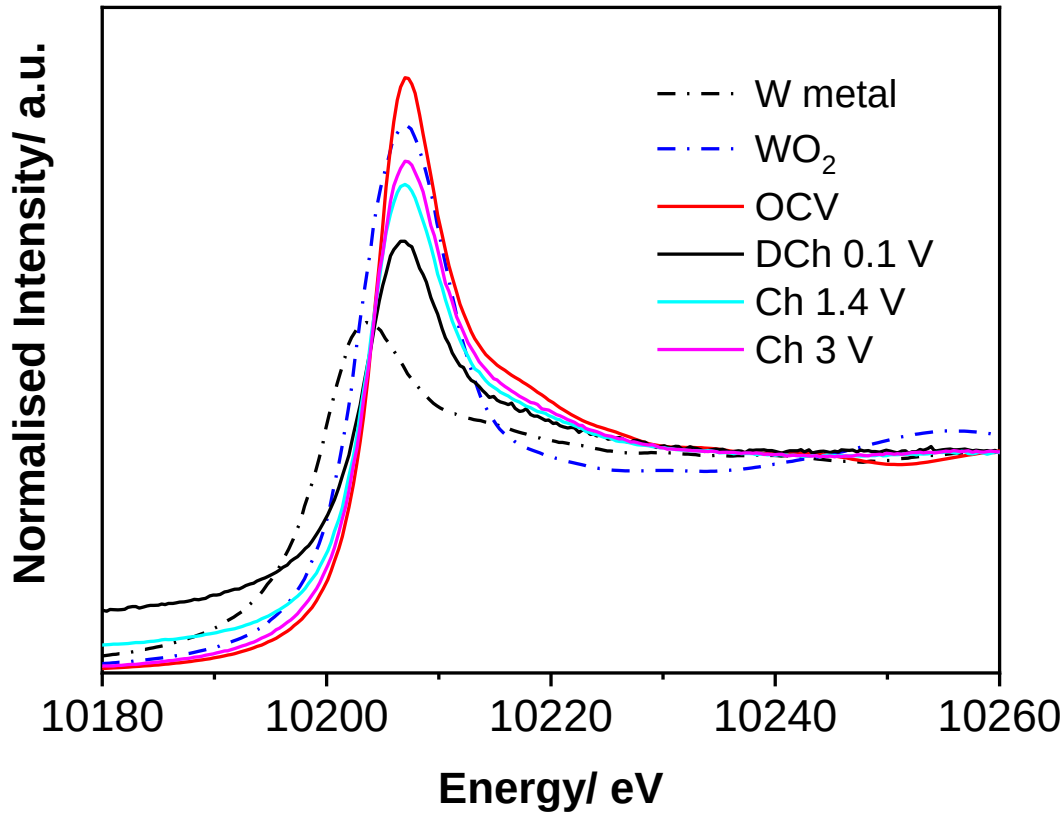

Figure 4.21 - Normalized W L_{III}-edge XANES spectra of WTe_2 electrode during the 1st charge process along with standard W metal and WO_2 powders used as reference.

The integrated white line intensity upon cycling for the charged and discharged samples is represented in Figure 4.22. The changes in white line intensity visibly translate into the changes occurring in the W oxidation state during ion insertion and deinsertion.

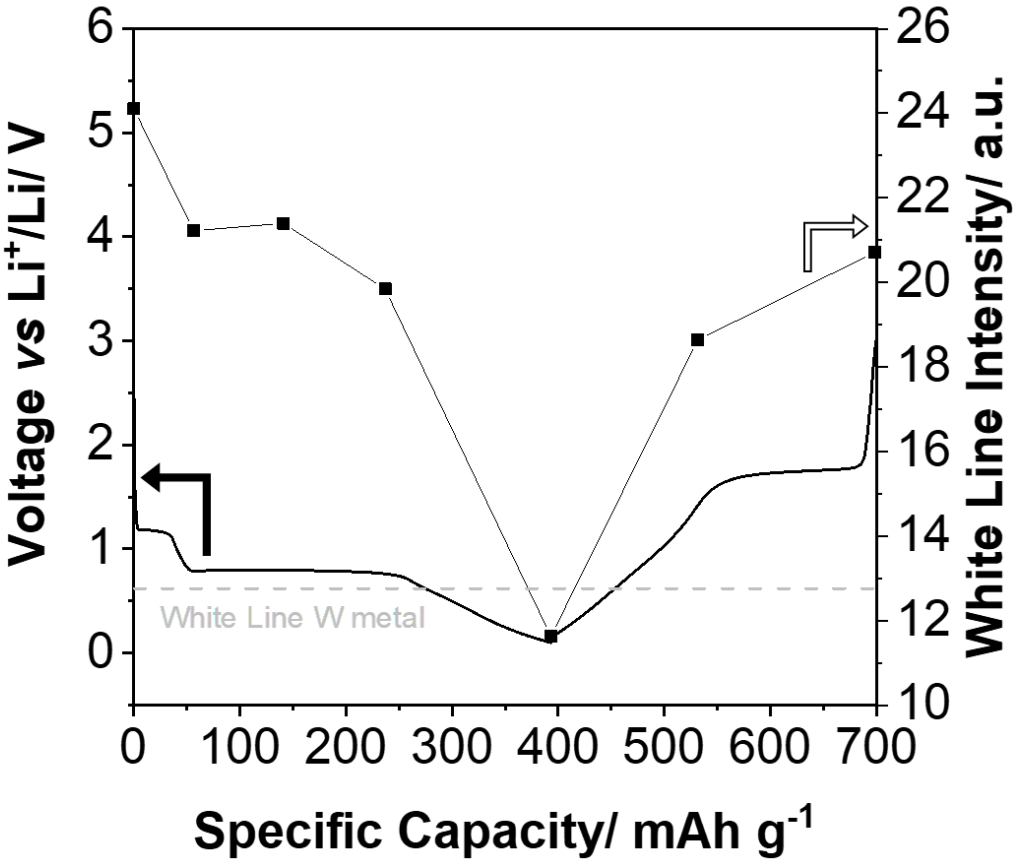

Figure 4.22– The change in the integrated white-line intensity of the W L_{III}-edge XANES for the WTe_2 in the initial discharge/charge processes.

The K-absorption edge was analysed for the Te element where the position of the edge reflects the local short and intermediate-range structure as well as the oxidation state of the central atom [33]. The XAS spectrum of the pristine material shows a single edge at 31808.6 eV which can be associated with the Te^{-2} anion (Figure 4.23).

During the discharge process, the insertion of Li^+ ions into the crystal structure leads to the movement of the edge to lower energies, reaching 31806.82 eV at the middle of the plateau phase (0.6 V MP). The oxidation of the Te atoms leads to the movement of the edge towards lower energies which is consistent with the formation of Te^{-2-x} upon ion insertion. During this phase, a movement of electrons toward the W atom is observed which can be correlated to the formation of the $LiWTe_2$ phase. This shift toward lower energies continues until the end of discharge at 0.1 V (31806.36 eV) accompanied by the broadening and flattening of the Te edge. Both features lead to the conclusion that

metallic tellurium is present during this step. No indication of the presence of Te^{2-} as Li_2Te phase is observed by the XAS spectra of tellurium, however, its existence cannot be denied.

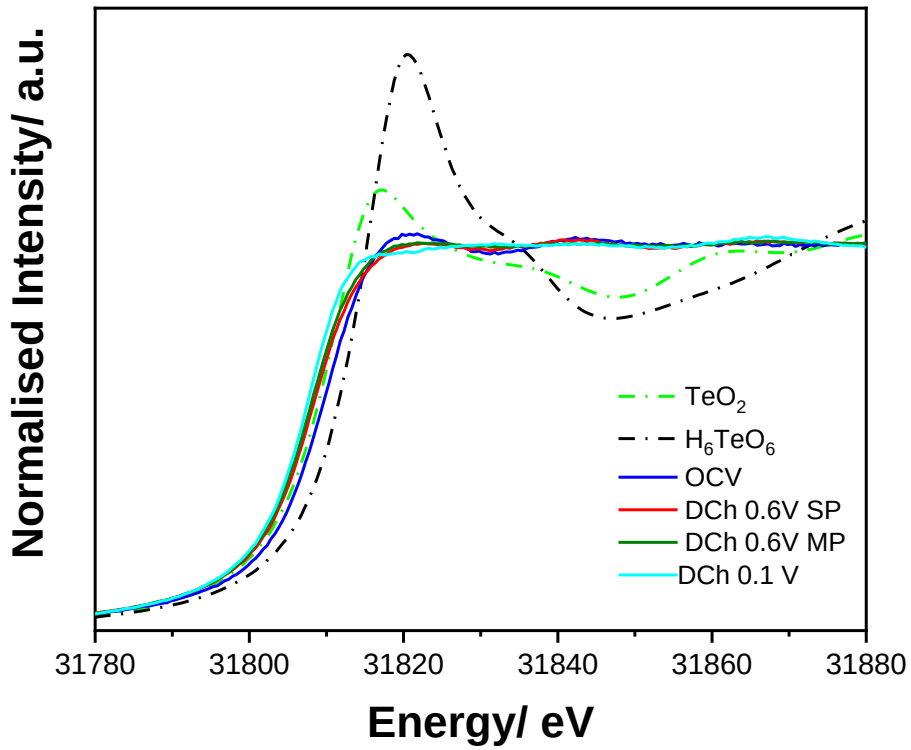

Figure 4.23 - Normalized Te K-edge XANES spectra of WTe_2 electrode during the 1st discharging process along with standard TeO_2 and TeO_6H_6 powders used as reference.

The impact of Li^+ ion extraction during the charging process is shown in Figure 4.24. At 1.4 V in charge, a movement of the Te K-edge towards higher energies (31809.7 eV) is observed as a result of the reduction of the Te atom upon Li^+ ion deinsertion from the Li_2Te phase formed during the discharge process. At this point, around 2.5 Li^+ ions are present in the crystal structure and the presence of some $LiWTe_2$ phase is expected. The return of the initial edge feature (wave-like) during this step corroborates the existence of initial Te^{-2} which implies the partial reformation of the initial WTe_2. At the end of the charging process (3.0 V), the edge is located at an energy below the OCV and DCh 0.1 V points (31803.76 eV) and reveals a flat edge. The deintercalation of Li^+ ions should lead to the movement of the Te edge towards higher energies demonstrating the

reduction of the Te atom. During this step, the presence of Te^{-2} is expected as the initial WTe_2 structure is recovered, which should appear as a wave-like feature in the spectrum. The different results obtained suggest something wrong with the electrode analysed which resulted in erroneous data collected as no explanation can be associated with these results. New data should be acquired for the end of the charge electrode.

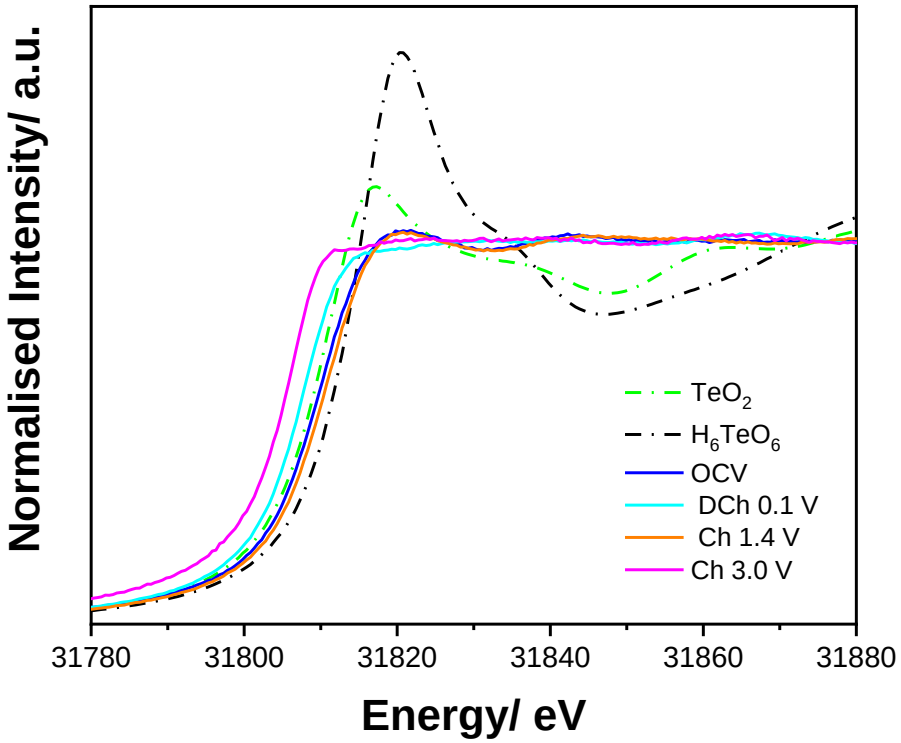

Figure 4.24- Normalized Te K-edge XANES spectra of WTe_2 electrode during the 1st charging process along with standard TeO_2 and TeO_6H_6 powders used as reference.

4.3.2.2 Operando PXRD during the first (de)lithiation cycle

Structural changes and phase evolution of T_d-WTe_2 during the electrochemical process of lithium insertion and extraction was studied by *operando* synchrotron powder X-ray diffraction (PXRD) analysis carried out during the 1st charge and discharge processes. The evolution of the synchrotron X-ray diffraction patterns along with the cycling profile is shown in Figure 4.25. All diffraction peaks of the electrode before cycling can be indexed to the T_d-WTe_2 phase (*Pmn*2_1, [ICSD- 73323]).

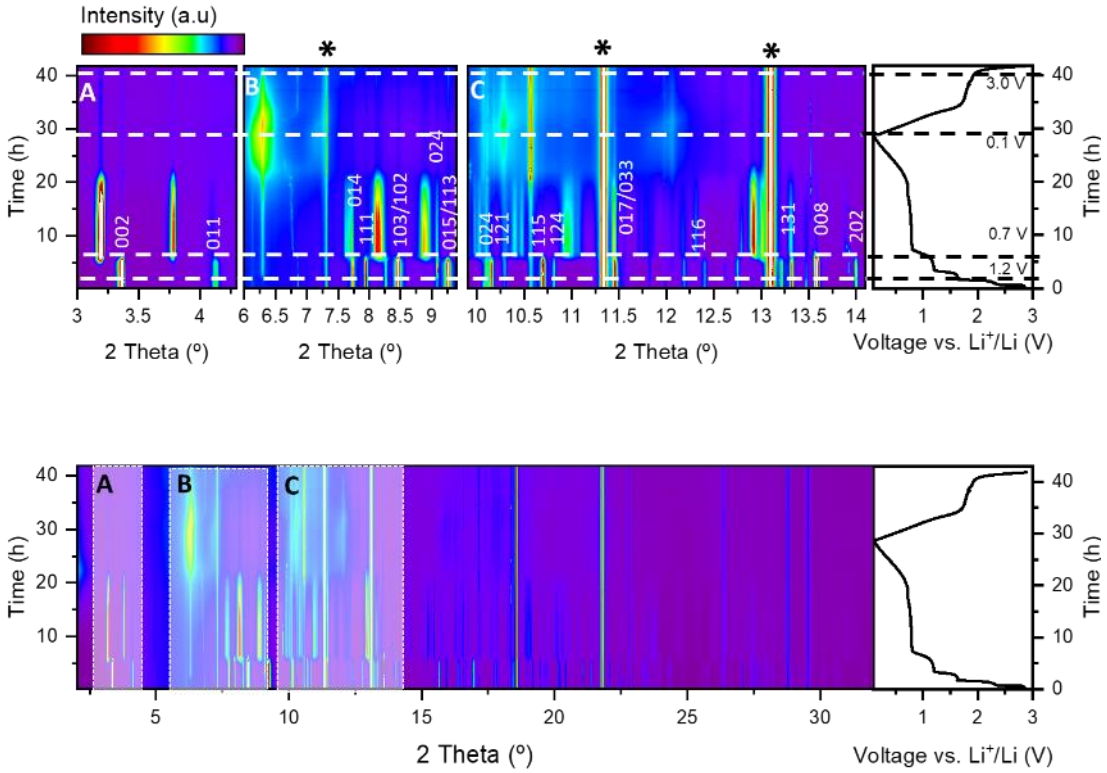

Figure 4.25 - Operando synchrotron X-ray diffraction patterns of the WTe_2 electrode material, recorded during the first charge/discharge cycle with corresponding cycling profile. Cu current collector peaks marked with *.

No significant changes in the diffraction peaks concerning 2θ degree position/intensity were observed in region 1, highlighted with a dashed line in Figure 4.25. Upon reaching the first discharge plateau at 1.2 V (region 2) correspondent to the insertion of 0.82 Li^+ mol ($Li_{0.82}WTe_2$) major intensity loses occur to the peaks corresponding to the WTe_2 phase. These changes are well visible in the (002) and (011) diffraction peaks of the main phase, located at 3.36 º and 4.13 º 2θ values (Figure 4.26). Although with low intensity, the presence of WTe_2 phase peaks remains constant throughout the whole cycling, indicating a partially irreversible reaction. The decrease in intensity observed up to 1.2 V (t ~ 5h) indicates a decrease in the van-der-Waals interactions that stabilize the layered structure and can be related to the gradual disorder of the interlayer spacing upon Li^+ intercalation [34], [35]. This disorder is reflected in a slight expansion of the lattice parameters layered along the c-axis in the T_d-WTe_2 structure upon ion insertion. Alongside the intensity decay of the diffraction peak correspondent to the WTe_2 phase,

several new peaks appear at 3.18°, 3.79° and 8.90° 2θ values at around 0.7 V (the moment when the electrode can be found in a theoretical stoichiometry of $Li_{1.78}WTe_2$).

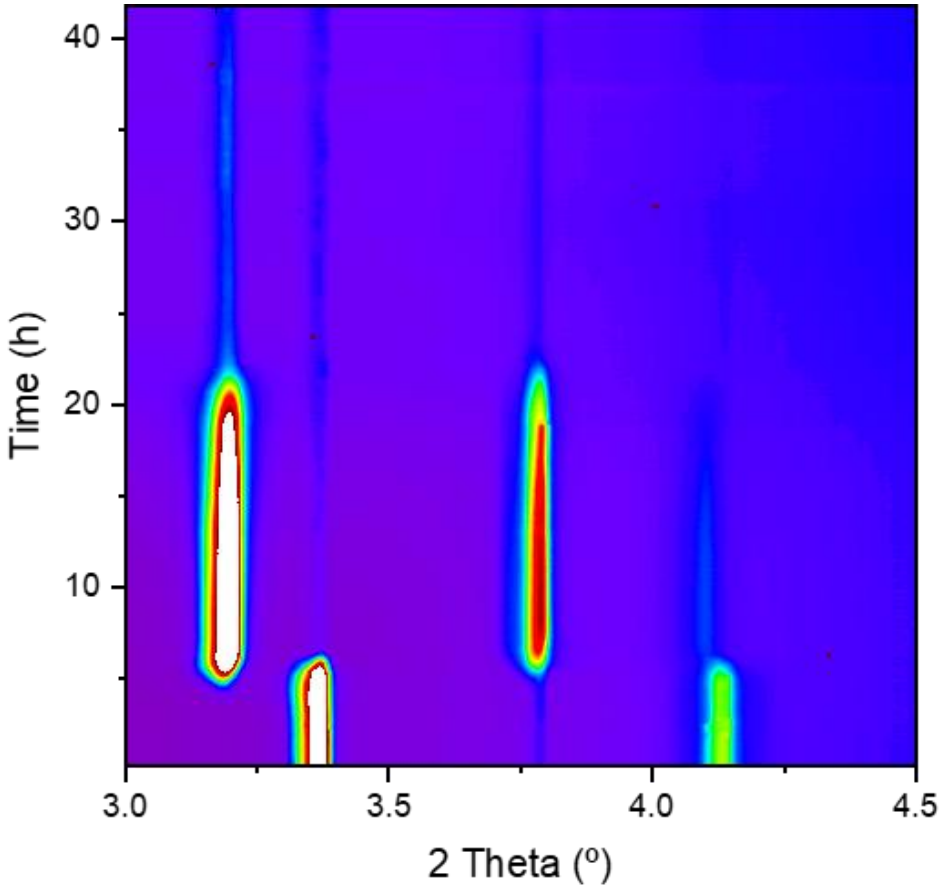

Figure 4.26 - (a) Zoomed region showing (002) and (010) reflection in T_d-WTe_2.

Similarly, to the results described in the sodium system (Section 3.3.3.2), the appearance of new peaks indicates the presence of a biphasic mechanism. These peaks can be ascribed to a lithiated WTe_2 structure (Li_xWTe_2) and the cell parameters for this phase are shown in Table 4.7. An expansion from 14.107 to 14.858 Å is observed in the c parameter of the unit cell. To note that although in both the sodium and lithium systems, an increase in the interlayer spacing is observed upon ion insertion, this expansion is bigger in SIBs (14.858 *vs* 15.959 Å for Li^+ and Na^+ ions, respectively) which could be related to the smaller size and lighter weight of lithium compared with sodium, however, the theory that different amounts of ions are intercalated cannot be disregarded.

Table 4.7 - Crystallographic data for WTe_2 compounds at pristine and plateau stage.

h	k	l	2 Theta (°)	d (Å)	c (Å)	b (Å)	a (Å)	from CIF of WTe_2	Step
0	0	2	3.19	7.4291	14.858				Plateau
0	0	2	3.36	7.0533	14.107			14.018	Pristine
0	1	1	3.78	6.2699		6.916			Plateau
0	1	1	4.13	5.7387		6.282		6.249	Pristine
1	1	1	8.13	2.9171			3.295		Plateau
1	1	1	8.45	2.8068			3.218	3.477	Pristine

The formation of the lithiated phase is accompanied by the appearance of new reflections (at 6.29 °, 7.25 °, 8.10 ° and 10.25 ° 2θ values, Figure 4.28) which can be attributed to the formation of two different phases of LiTe alloys: Li_2Te (*Fm*-3*m*, [ICSD- 60434]) and $LiTe_3$ (*P*-3*c*1, [ICSD- 935]) (Figure 4.27). The formation of these alloys occurs as a result of the weakening of the W-Te bond upon intercalation of Li^+ ion into the crystal structure. The maximum intensity of the lithiated WTe_2 phase is reached at t ~ 10h (correspondent to 2.9 mol Li^+ inserted). A gradual decrease of maximum intensity of the lithiated WTe_2 phase peaks is observed through the plateaux at 0.7 V, with no shift in peak position. These data suggest that the lithiated phase formed is maintained during the plateaux with no changes in the cell parameters upon Li insertion. An increase of the background signal is also detected during the plateau at 0.7 V, which can be related to an amorphization of the phases present and/or the appearance of greatly disordered phases. The presence of broader peaks compared with those of the pristine material suggests a decrease in crystallite size by cracking or disordering of the crystal structure. Other possible amorphous candidates present in this reaction are W metal, WO_2, Te metal or TeO_2 attending to the present elements.

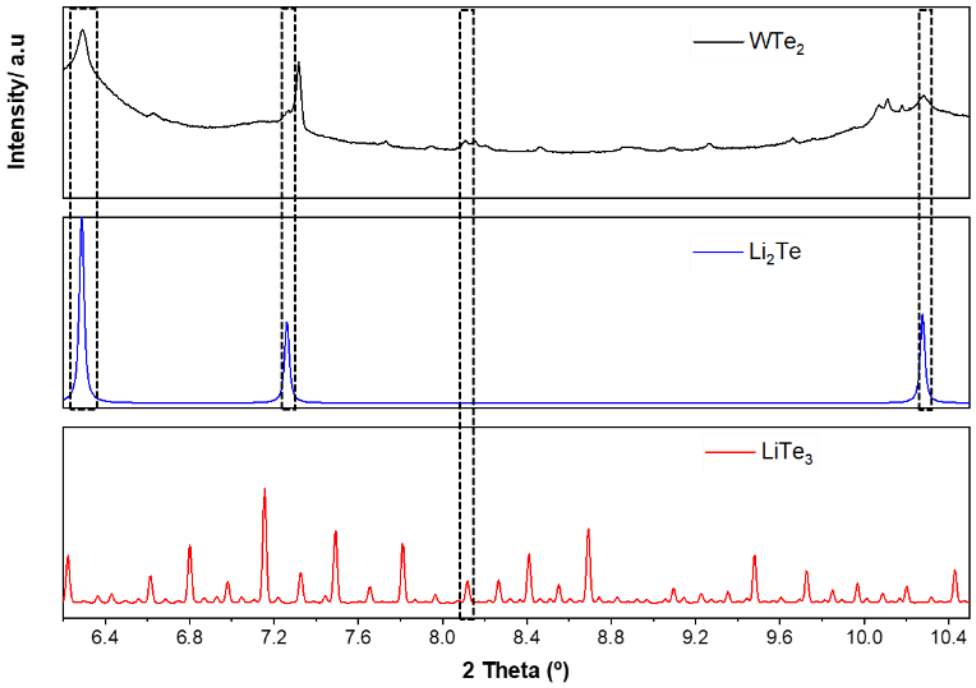

Figure 4.27 - Operando powder X-ray diffraction patterns from T_d-WTe_2 at middle plateau, Li_2Te and $LiTe_3$.

The end of discharge at 0.1 V, is characterized by the presence of small T_d-WTe_2, lithiated WTe_2, Li_2Te and $LiTe_3$ alloys peaks. No meaningful changes nor in the intensity nor the position of the peak are visible during the charging process, suggesting that some initial WTe_2 does not suffer any kind of restructuring upon ion deinsertion. To note that the peak at 10.25º 2θ value assigned to Li_2Te reaches its maximum intensity during the initial charging process (around 31 h) and just starts to lose intensity 2h after (Figure 4.28). The intensity of this peak is expected to reach its maximum at the end of discharge (0.1 V) and then decrease during the deintercalation of Li^+ ions as the ions are removed from the alloy and reintroduced in the initial electrode. The disparity observed can be related to a delay in the data acquisition compared with the electrochemistry occurring. Differences in the kinetics of the system and the recording of the XRD pattern can be the reason why the loss in intensity is just visible 2h into the charging process.

The fact that the initial WTe_2 phase is not recovered after charging the cell back, evidences the high structural irreversibility of this compound during the first cycle. The operando PXRD results obtained for LIBs match the ones obtained for Na, suggesting that the intercalation/extraction process affects the T_d-WTe_2 structure in the same way independently of the intercalant.

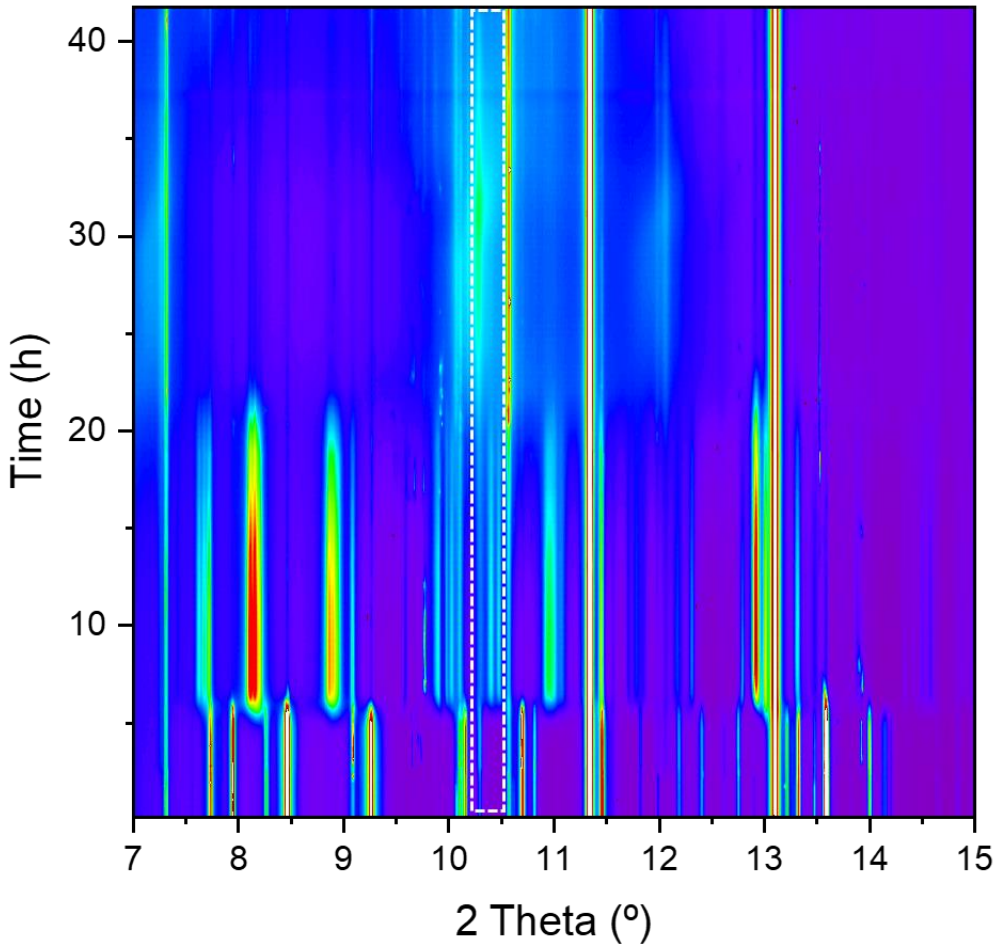

Figure 4.28 - Operando powder X-ray diffraction of T_d-WTe_2 showing the peak of Li_2Te phase at 10.25º.

4.4 Conclusions

WTe_2 electrodes were successfully tested as anode material for LIBs. The Li^+ storage ability of the T_d-WTe_2 anode was tested through galvanostatic discharge-charge cycling. The anode material can be cycled reversibly, with an initial discharge capacity

of 442 mAh g^{-1} and 40 % of the initial discharge capacity still delivered after 20 cycles. The pseudocapacitance behaviour of the electrode was studied by cycling the material at a high current rate (100 mA g^{-1}), where the anode material retains 90.4 % of its initial charge capacity after 20 cycles. Upon long cycling (75 cycles), the capacity values are different for both high and low current cycled electrodes, however, the capacity obtained after 75 cycles is very similar (89.2 mAh g^{-1} and 85 mAh g^{-1} for 10 and 100 mA g^{-1}, respectively). This can be related to the fact that the structure of the WTe_2 electrode material is irreversibly damaged during the cycling tests, indicating a low degree of flexibility of the structure. Similarly, the rate capability tests show that the WTe_2 anode does not recover the total of its initial discharge capacity after cycling (46.4 % retention). These results were corroborated by SEM images of the post-mortem electrodes. Data after 75 cycles also shows the formation of cracks and particle agglomeration upon continuous ions insertion/extraction.

The CV results corroborate the multiphase reaction occurring in WTe_2 when cycled against Li by the presence of several redox peaks in the cyclic voltammogram. The decrease in intensity peaks upon cycling reflects the less stable and reversible electrochemical behaviour of the electrode after the initial conversion reaction and SEI layer formation. The calculated b values for the redox peaks were estimated to be 0.71 and 0.73, suggesting both surface-controlled and diffusion-controlled processes occur on the WTe_2 electrode during ion movement. These results show the dominance of capacitive contribution at higher currents. The Li^+ ion diffusion coefficient was found to be in the order of 10^{-10} (ranging from 8.21 x 10^{-10} to 9.89 x 10^{-10} cm^2 s^{-1}). The values obtained in WTe_2 electrodes indicate a better Li^+ diffusion in comparison with other dichalcogenides materials.

EIS measurements collected at different cycles show no major increase or decrease in overall resistance upon cycling which suggests good stability of the electrode material. An abrupt decrease in charge-transfer resistance was observed upon cycling from the EIS measurement collected at OCV, which can be associated with the formation of a less resistive electrode-electrolyte interface upon the reformation of the initial T_d-WTe_2 structure and the presence of nanosized particles which facilitates the Li^+ transfer. At the same time, an increase in R_{SEI} is observed which can be associated with an increase in the thickness of the SEI layer created during cycling and large volume changes

occurring within the crystal structure. This increase leads to a shortened lifetime of a cell as can be observed by the charge-discharge curves. The stability of the R_S value upon cycling suggests a stable intrinsic and interfacial resistance of the electrode upon ion intercalation/ extraction.

Structure evolution upon Li^+ ion insertion was studied by XANES and operando XRD measurements. The W L_{III}-edge XAS spectra showed the decrease in the oxidation state of the W atom upon Li^+ intercalation ($W^{4+ - x)}$), however, the spectra does not match that of W metal, suggesting that the structure of WTe_2 does not fully convert to W metal upon Li insertion and that some initial WTe_2 or some Li_xWTe_2 phase is still present. At the same time, the Te K-edge suggests the formation of $Te^{-2 - x}$ as the edge moves towards lower energies. The broadening and flattening of the Te edge also suggest the formation of metallic tellurium during this step. During Li^+ extraction, the increase in W white line intensity suggests the oxidation of the W atom back to W^{4+}. The intensity registered is lower than the one registered at OCV state which suggests that the W atom is in a more reduced state upon ion deinsertion compared with pristine and therefore WTe_2 is not fully reformed. The Te K-edge towards higher energies as a result of the oxidation of the Te atom upon Li^+ ion deinsertion from the Li_2Te phase formed during the discharge process.

The XAS data is corroborated by the synchrotron operando X-ray diffraction data. At OCV state, all diffraction peaks can be indexed to the T_d-WTe_2 phase. During the discharge process, a decrease in WTe_2 peaks intensity peaks is observed indicating a decrease in the van-der-Waals interactions that stabilize the layered structure and gradual disorder of the interlayer spacing upon Li^+ intercalation. This disorder is accompanied by the slight expansion of the lattice parameters layered along the c-axis in the T_d-WTe_2 structure. To note that the expansion in the c-axis observed for LIBs is lower than for SIBs. Several new peaks are also identified and can be attributed to the formation of a lithiated WTe_2 structure (Li_xWTe_2) and lithium alloy phases (Li_2Te and $LiTe_3$). No meaningful changes nor in the intensity nor the position of the peak are visible during the charging process, suggesting that some initial WTe_2 does not suffer any kind of restructuring upon ion deinsertion.

Altogether, the results obtained show that WTe_2 can be successfully used as anode material for LIBs.

4.5 References

[1] Y. M. Chen, X. Y. Yu, Z. Li, U. Paik, and X. W. Lou, "Hierarchical MoS2 tubular structures internally wired by carbon nanotubes as a highly stable anode material for lithium-ion batteries," *Sci. Adv.*, vol. 2, no. 7, pp. 1–9, 2016, doi: 10.1126/sciadv.1600021.

[2] Y. Wang, B. Qian, H. Li, L. Liu, L. Chen, and H. Jiang, "VSe2/graphene nanocomposites as anode materials for lithium-ion batteries," *Mater. Lett.*, vol. 141, pp. 35–38, 2015, doi: 10.1016/j.matlet.2014.11.038.

[3] M. Srinivaas, C. Y. Wu, J. G. Duh, Y. C. Hu, and J. M. Wu, "Multi-walled carbon-nanotube-decorated tungsten ditelluride nanostars as anode material for lithium-ion batteries," *Nanotechnology*, vol. 31, no. 3, p. 035406, 2020, doi: 10.1088/1361-6528/ab48b2.

[4] X. Zhu *et al.*., "Free-standing WTe2QD-doped NiSe/C nanowires for highly reversible lithium storage," *Electrochim. Acta*, vol. 295, pp. 22–28, 2019, doi: 10.1016/j.electacta.2018.10.128.

[5] M. Herklotz *et al.*., "A novel high-throughput setup for *in situ* powder diffraction on coin cell batteries," *J. Appl. Crystallogr.*, vol. 49, pp. 340–345, 2016, doi: 10.1107/S1600576715022165.

[6] "Potentiostats - Biologic." https://www.biologic.net/product_category/potentiostats-galvanostats/ (accessed Jul. 30, 2021).

[7] M. G. Kim *et al.*., "Unusual Li-ion storage through anionic redox processes of bacteria-driven tellurium nanorods," *J. Mater. Chem. A*, vol. 3, no. 33, pp. 16978–16987, 2015, doi: 10.1039/c5ta04038h.

[8] K. T. Bennett *et al.*., "Large-Scale Production of 119mTe and 119Sb for Radiopharmaceutical Applications," *ACS Cent. Sci.*, vol. 5, no. 3, pp. 494–505, 2019, doi: 10.1021/acscentsci.8b00869.

[9] U. Jayarathne *et al.*., "X-ray absorption spectroscopy systematics at the tungsten L-edge," *Inorg. Chem.*, vol. 53, no. 16, pp. 8230–8241, 2014, doi: 10.1021/ic500256a.

[10] B. Ravel and M. Newville, "ATHENA, ARTEMIS, HEPHAESTUS: Data analysis for X-ray absorption spectroscopy using IFEFFIT," *J. Synchrotron Radiat.*, vol. 12, no. 4, pp. 537–541, 2005, doi: 10.1107/S0909049505012719.

[11] M. Newville, "IFEFFIT: Interactive XAFS analysis and FEFF fitting," *J. Synchrotron Radiat.*, vol. 8, no. 2, pp. 322–324, 2001, doi: 10.1107/S0909049500016964.

[12] G. K. Sung, K. H. Nam, J. H. Choi, and C. M. Park, "Germanium telluride: Layered high-performance anode for sodium-ion batteries," *Electrochim. Acta*, vol. 331, p. 135393, 2020, doi: 10.1016/j.electacta.2019.135393.

[13] N. Ma, X. Y. Jiang, L. Zhang, X. S. Wang, Y. L. Cao, and X. Z. Zhang, "Novel 2D Layered Molybdenum Ditelluride Encapsulated in Few-Layer Graphene as High-Performance Anode for Lithium-Ion Batteries," *Small*, vol. 14, no. 14, pp. 1–8, 2018, doi: 10.1002/smll.201703680.

[14] M. Hong, J. Li, W. Zhang, S. Liu, and H. Chang, "Semimetallic 1T′ WTe2 Nanorods as Anode Material for the Sodium Ion Battery," *Energy and Fuels*, vol. 32, no. 5, pp. 6371–6377, 2018, doi: 10.1021/acs.energyfuels.8b00454.

[15] M. R. Panda *et al.*., "High Performance Lithium-Ion Batteries Using Layered 2H-MoTe2 as Anode," *Small*, vol. 2002669, pp. 1–16, 2020, doi: 10.1002/smll.202002669.

[16] S. Zhang, G. Wang, J. Jin, L. Zhang, Z. Wen, and J. Yang, "Robust and Conductive Red MoSe2 for Stable and Fast Lithium Storage," *ACS Nano*, vol. 12, no. 4, pp. 4010–4018, 2018, doi: 10.1021/acsnano.8b01703.

[17] M. A. Bissett, S. D. Worrall, I. A. Kinloch, and R. A. W. Dryfe, "Comparison of Two-Dimensional Transition Metal Dichalcogenides for Electrochemical Supercapacitors," *Electrochim. Acta*, vol. 201, pp. 30–37, 2016, doi: 10.1016/j.electacta.2016.03.190.

[18] M. R. Panda *et al.*., "Blocks of molybdenum ditelluride: A high rate anode for sodium-ion battery and full cell prototype study," *Nano Energy*, vol. 64, no. July, p. 103951, 2019, doi: 10.1016/j.nanoen.2019.103951.

[19] Y. Guo, Y. Wei, H. Li, and T. Zhai, "Layer Structured Materials for Advanced Energy Storage and Conversion," *Small*, vol. 1701649, p. 1701649, 2017, doi: 10.1002/smll.201701649.

[20] R. Brec, D. M. Schleich, G. Ouvrard, A. Louisy, and J. Rouxel, "Physical Properties of Lithium Intercalation Compounds of the Layered Transition Chalcogenophosphates," *Inorg. Chem.*, vol. 18, no. 7, pp. 1814–1818, 1979, doi: 10.1021/ic50197a018.

[21] V. L. Chevrier and G. Ceder, "Challenges for Na-ion negative electrodes," *J. Electrochem. Soc.*, vol. 158, no. 9, pp. 10–14, 2011, doi: 10.1149/1.3607983.

[22] T. S. Sahu and S. Mitra, "Exfoliated MoS <inf>2</inf> Sheets and Reduced Graphene Oxide-An Excellent and Fast Anode for Sodium-ion Battery," *Sci. Rep.*, vol. 5, no. June, pp. 1–13, 2015, doi: 10.1038/srep12571.

[23] F. N. Sayed *et al.*., "Li and Na-ion diffusion and intercalation characteristics in vertically aligned TiS2 nanowall network grown using atomic layer deposition," *Mater. Res. Express*, vol. 6, no. 11, 2019, doi: 10.1088/2053-1591/ab3e19.

[24] M. D. Levi and D. Aurbach, "Simultaneous measurements and modeling of the electrochemical impedance and the cyclic voltammetric characteristics of graphite electrodes doped with lithium," *J. Phys. Chem. B*, vol. 101, no. 23, pp. 4630–4640, 1997, doi: 10.1021/jp9701909.

[25] Y. Xu, Y. Zhu, Y. Liu, and C. Wang, "Electrochemical performance of porous carbon/tin composite anodes for sodium-ion and lithium-ion batteries," *Adv.*

Energy Mater., vol. 3, no. 1, pp. 128–133, 2013, doi: 10.1002/aenm.201200346.

[26] J. S. Cho, Y. J. Hong, and Y. C. Kang, "Design and synthesis of bubble-nanorod-structured Fe2O3-Carbon nanofibers as advanced anode material for li-ion batteries," *ACS Nano*, vol. 9, no. 4, pp. 4026–4035, 2015, doi: 10.1021/acsnano.5b00088.

[27] B. Chen, D. Chao, E. Liu, M. Jaroniec, N. Zhao, and S.-Z. Qiao, "Transition metal dichalcogenides for alkali metal ion batteries: engineering strategies at the atomic level," *Energy Environ. Sci.*, vol. 13, no. 4, pp. 1096–1131, 2020, doi: 10.1039/c9ee03549d.

[28] Z. Hu *et al.*, "MoS2Nanoflowers with Expanded Interlayers as High-Performance Anodes for Sodium-Ion Batteries," *Angew. Chemie - Int. Ed.*, vol. 53, no. 47, pp. 12794–12798, 2014, doi: 10.1002/anie.201407898.

[29] Y. Liu, J. Wang, Y. Xu, Y. Zhu, D. Bigio, and C. Wang, "Lithium-tellurium batteries based on tellurium/porous carbon composite," *J. Mater. Chem. A*, vol. 2, no. 31, pp. 12201–12207, 2014, doi: 10.1039/c4ta02075h.

[30] C. Luo *et al.*, "Selenium@Mesoporous carbon composite with superior lithium and sodium storage capacity," *ACS Nano*, vol. 7, no. 9, pp. 8003–8010, 2013, doi: 10.1021/nn403108w.

[31] R. M. Wightman, P. M. Kovach, W. G. Kuhr, and K. J. Stutts, "Methods To Improve Electrochemical Reversibility At Carbon Electrodes.," *Proc. - Electrochem. Soc.*, vol. 84–5, no. 7, pp. 510–524, 1984, doi: 10.1149/1.2115913.

[32] P. Charton, L. Gengembre, and P. Armand, "TeO2-WO3 glasses: Infrared, XPS and XANES structural characterizations," *J. Solid State Chem.*, vol. 168, no. 1, pp. 175–183, 2002, doi: 10.1006/jssc.2002.9707.

[33] P. V. Grundler *et al.*, "Xocolatlite, Ca2Mn24+ Te2O12·H2O, a new tellurate related to kuranakhite: Description and measurement of Te oxidation state by XANES spectroscopy," *Am. Mineral.*, vol. 93, no. 11–12, pp. 1911–1920, 2008, doi: 10.2138/am.2008.2870.

[34] H. Katzke, “Stacking disorder in 2H-NbS2 and its intercalation compounds Kx(H2O)yNbS2 II. Stacking disorder in Kx(H2O)yNbS2,” *Zeitschrift fur Krist.*, vol. 217, no. 4, pp. 149–154, 2002, doi: 10.1524/zkri.217.4.149.20643.

[35] Y. Saito, P. Fons, A. V. Kolobov, and J. Tominaga, “Self-organized van der Waals epitaxy of layered chalcogenide structures,” *Phys. Status Solidi Basic Res.*, vol. 252, no. 10, pp. 2151–2158, 2015, doi: 10.1002/pssb.201552335.

5 A study on the charge compensation mechanisms on $TaTe_2$ polytype as an anode in LIBs

5.1 Introduction

Tellurium compounds have attracted a lot of attention since tellurium behaves rather differently from lighter sulphur and selenium homologues. Many new metal tellurides have demonstrated a so-called "non-classical" behaviour related to the bonding properties of the tellurium element [1], [2]. This means that tellurium can exhibit covalent, ionic, and metallic bonding interaction giving rise to a family of solids with a wide variety of physical and chemical properties [3].

Two-dimensional metallic transition metal dichalcogenides (MTMDs) such as group VB metal tellurides, (VTe_2, $NbTe_2$ and $TaTe_2$) have attracted a lot of attention in the last few years for both fundamental studies and potential technological applications due to their intrinsic magnetic properties [3]. These compounds have been regarded as potential materials for studying fundamental physical phenomena including charge density waves (CWDs), superconductivity, quantum spin Hall effect and electro-catalytic activity.

Among MX_2 systems, tantalum dichalcogenides (TaX_2, X = S, Se or Te) have been investigated to understand the charge modulation properties of TMDs due to their rich and different ground states [4]. The strong electron coupling for all neighbouring M^{4+}-M^{4+} pairs observed in this type of TMDs makes them an interesting category to be further explored [5]. MX_2 crystallize in a structure that consists of vertically stacked layers, held together by weak van-der-Waals-like interactions [6]. Each layer is formed by a sheet of cations, having a 6-fold environment, packed together between two sheets of anions [6]. The two most common structures are the so-called 1T (Ta in octahedral

coordination, space group $P\bar{3}m1$) and 2H (Ta in trigonal prismatic coordination, space group P_{63mmc}) [6]. Most tantalum chalcogenides can crystallize in both types of structure except for tantalum telluride ($TaTe_2$), which can only crystallise in a monoclinic distortion of the 1T type so-called 1T' or T_d (space group $C12/m1$) [7], [8]. This is related to the relationship between the number of electrons available for bonding and the bond length since $TaTe_2$, contrarily to $MoTe_2$ and WTe_2 possesses a metal-metal bonding (Figure 5.1) [7].

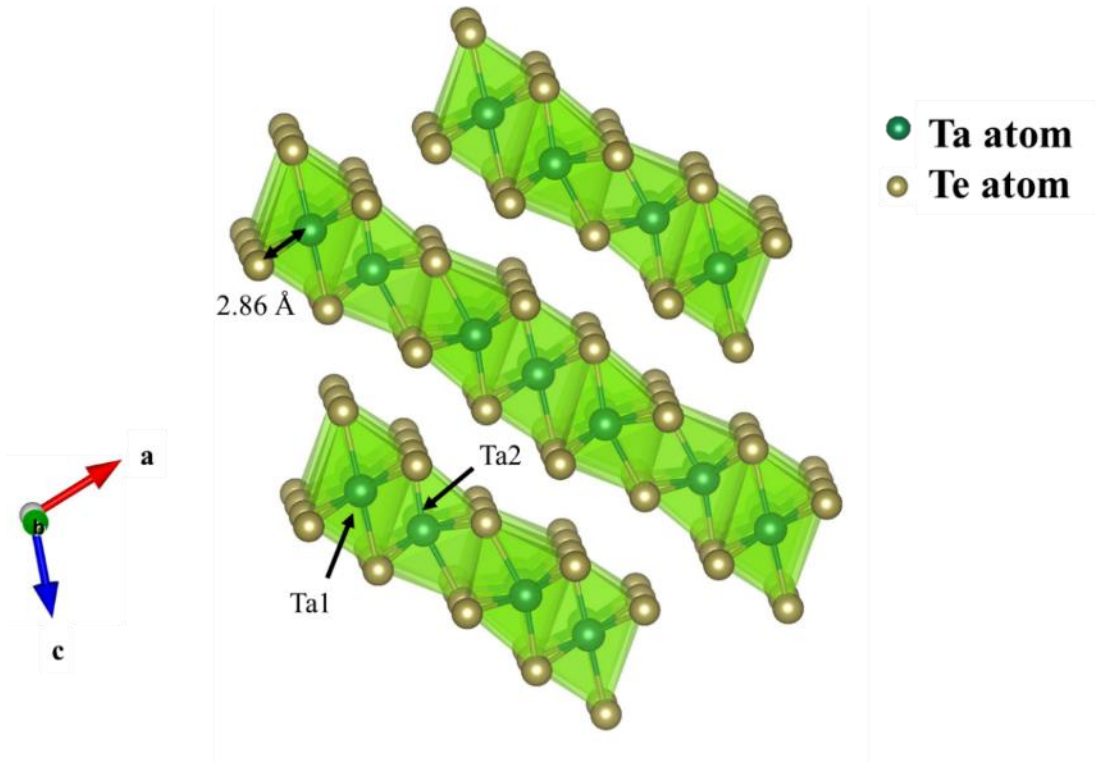

Figure 5.1 - Polyhedral representation of crystal structure of $TaTe_2$ with a space group $C12/m1$ plotted using VESTA 3.4 [9]. The Ta and Te atoms are shown in green and yellow, respectively. Each Ta atom is surrounded by six Te atoms in a distorted octahedral environment forming a $TaTe_6$ octahedron around each central Ta atom. The distorted $TaTe_6$ octahedra are joined via common edges forming slabs [7].

The intrinsic band gap in these TMDs can be easily tuned depending upon the number of layers and choice of elements in the structure, which can, in turn, determine their possible application, such as sensing, photonics devices, and energy harvesting. TaX_2 have been lightly studied as energy storage materials with applications in supercapacitors and metal-ion batteries [10]. $TaTe_2$ nanosheets synthesized using a

microwave-assisted technique have been used as anode materials in supercapacitor cells against platinum metal. The maximum discharge/charge capacity obtained was below 2.4 mV s^{-1} and a coulombic efficiency of 95%, which is a preferable characteristic for achieving supercapacitor behaviour [10]. The electrochemical lithium insertion was evaluated in $TaTe_2$ cathode materials by Guzmán *et al.* [11]. 1T' - $TaTe_2$ was shown to be able to insert Li^+ ions through consecutive pseudo-plateaus with limits at specific x values (x = Li^+ ions in Li_xTaTe_2). A maximum degree of insertion in the voltage window between 1.6 and 1.2 V is observed when x =1, which corresponds to the complete filling of the distorted octahedral sites located in the interlayer space of monoclinic $TaTe_2$ [11]. The formation of ordered superstructures during the intercalation process was identified for an intermediate value of x ($0.33 < x < 0.66$) and correspondent compositions. According to the structural data for $TaTe_2$, two sets of equivalent sites of different symmetry can accommodate alkaline ions: site 2d (symmetry 2/m) and site 4i (symmetry m) [11]. The most symmetrical sites, 2d sites, fall between tantalum atoms displaced from the centre of the Te_6 octahedra, while the 4i sites have tantalum atoms at the centre of the Te_6 octahedron [11]. If lower energy of 2d sites is assumed, the intercalation of ions in this site is favoured against 4i sites as there is less repulsion between Ta and alkali atoms [11]. To our knowledge, no detailed characterization has been done or published regarding the use of $TaTe_2$ as anode materials for LIBs.

A detailed study was carried out to characterise the as-synthesized $TaTe_2$ and its electrochemical performance as a Li-ion anode. These included microstructural and structural analysis (PXRD, SEM/EDX and TEM) and structure evolution analysis (XANES and synchrotron operando PXRD) in conjunction with electrochemical analysis (galvanostatic cycling, cyclic voltammetry and electrochemical impedance spectroscopy). This study highlights the structural mechanism behind the reversible intercalation of Li^+ ions into the $TaTe_2$ structure.

5.2 Experimental part

5.2.1 Synthesis and structure characterisation

6 g of tantalum telluride ($TaTe_2$) were synthesised by Dr Zdenek Sofer from the University of Chemistry and Technology Prague in Czech Republic following the methods reported in [12]. For the synthesis, stoichiometric amounts of tantalum and tellurium (1:2.1) were added in a quartz ampoule (100 × 15 mm; 2 mm wall thickness), which was evacuated to 5 x 10^{-3} Pa. The quartz ampoule was flame sealed with an O_2/H_2 torch and this was heated to 900 °C for 24 h (heating and cooling rate of 5 °C min^{-1}).

5.2.2 Operando synchrotron X-ray diffraction

Operando powder diffraction measurements were carried out at the MSPD BL04 beamline of the ALBA synchrotron, Spain. The samples were measured at room temperature in fluorescence geometry. A Mythen 6K detector with a 13 keV X-ray beam energy (λ $K_{\alpha 1}$ = 0.41273 Å) and an exposure time of 130 s per pattern was used to record the diffraction data covering 40° in 2θ range. To reduce the effect of the preferred orientation of crystallites on the diffracted intensities a concentric rocking of ±15° of the whole setup within the Eulerian cradle was realized. To verify the reliability of the cell positioning and overall data quality, a borosilicate capillary (0.5 mm Ø) with $TaTe_2$ as powder reference material was measured. Custom-made CR2032 coin cells with a glass window of 8 mm diameter and 130 µm thickness were used [14]. The electrochemical cell contained *ca.* 7.10 mg of a homogenous powdered mixture (70 wt % active material, 20 wt % carbon black and 10 wt % Polyvinylidene fluoride (PVDF, Kynar)) as the anode material, Li metal as the counter and reference electrode and a glass fibre separator soaked in 1 M $LiPF_6$ in ethylene carbonate/dimethyl carbonate (EC: DMC 1:1 v/v %) organic electrolyte. The cell was cycled at a rate of 40 mA g^{-1} within the voltage range of 0.1 V-3.0 V *vs* Li^+/Li. Electrochemical data were collected using a Biologic (SP200 model) potentiostat and data was analysed using the EC-Lab software V11.20 [15].

5.2.3 *Ex situ* synchrotron X-ray absorption spectroscopy

Ex situ synchrotron X-ray absorption near-edge spectroscopy (XANES) measurements were performed at the B18 Core EXAFS beamline at the Diamond Light Source (UK). Spectra of Ta at the L_{III}-edge and Te at the K-edge were measured at ambient temperature in fluorescence mode at energies above and below the absorption edges of 9883.2 eV and 31807 eV, respectively. For the characterisation, cast electrodes were cycled at different states of charge and then extracted from the coin cells and rinsed three times with DMC (ca. 5 ml) in an argon glovebox. The electrodes were sealed under vacuum in aluminium laminated pouches before the measurements. Three spectra were collected for each sample for 5 minutes. Te metal, TeO_2 and TeO_6H_6 were used as references for Te^0 (31814 eV), Te^{4+} (31816.4 eV) and Te^{6+} (31820.9 eV) ions [16], [17], respectively. Ta metal and Ta_2O_5 were used as references for Ta^0 (9881.1 eV) and Ta^{5+} (9883.05 eV), respectively. Absorption spectra of the references and samples were collected in transmission and fluorescence mode, respectively. The Athena software in the Demeter package [18], [19] was used to average the scans collected, calibrate, and normalise the data.

5.3 Results and Discussion

5.3.1 Structural and morphological characterisation of $TaTe_2$

5.3.1.1 Powder X-ray Diffraction

Powder X-ray diffraction (PXRD) data of the as-synthesized $TaTe_2$ sample matches the simulated powder pattern of the $TaTe_2$ phase with the monoclinic space group *C*12/*m*1 [ICSD- 86141] (Figure 5.2). The sharpness and well-defined shape of the peaks suggest the high crystallinity of the synthesized compound. No impurities such as oxides, tellurides, tellurium metal and other phases were observed.

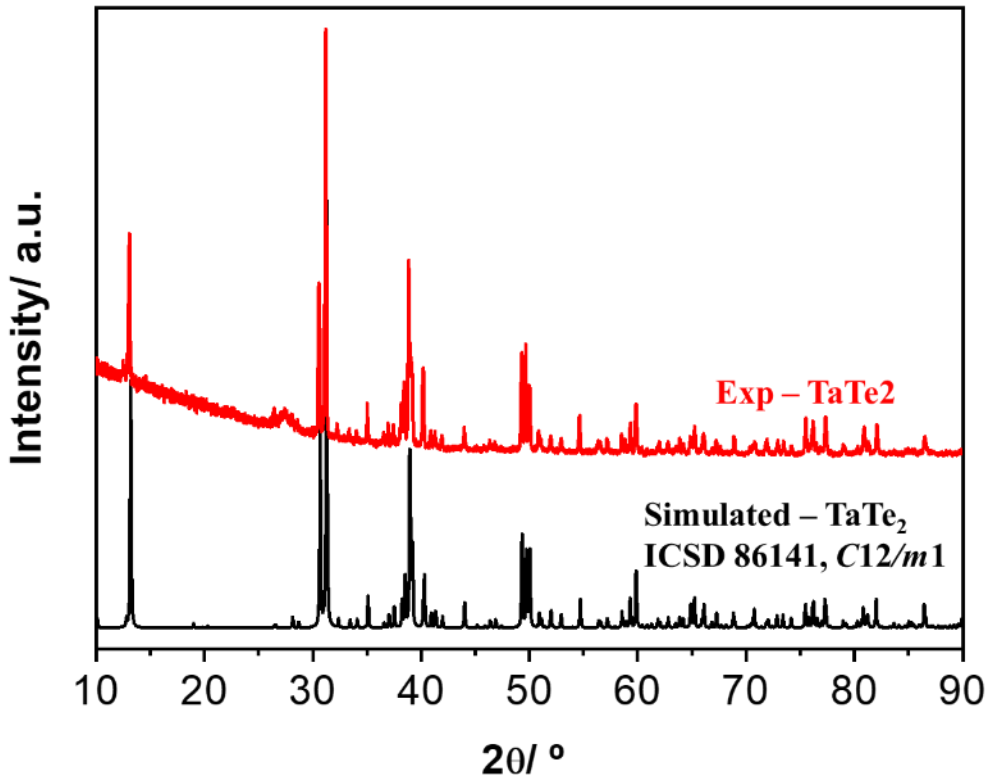

Figure 5.2– X-ray diffraction pattern of as-prepared $TaTe_2$. The solid red line corresponds to the experimental data and the solid black line corresponds to the simulated pattern (ICSD 86151).

Rietveld refinement on the X-ray diffraction data was performed to obtain an accurate structural model on the material (Figure 5.3). The refined parameters included the zero, lattice and profile parameters, atomic positions, and isotropic displacement parameters (U_{iso}) while occupancies were set to 1. The lattice parameters were determined and found to be a = 14.783 (3) Å, b = 3.637 (4) Å, c = 9.346 (2) Å, α = 90°, β = 110.9° and γ = 90°, which are in agreement to the unit cell parameters reported in the literature [7]. The refined parameters can be found in Table 5.1. The goodness-of-fit, χ^2, was found to be 3.84 and the R factors such as weighted profile R-factor, R_{wp}, and expected R factor, R_{exp}, were found to be 15.56 and 10.68 %, respectively.

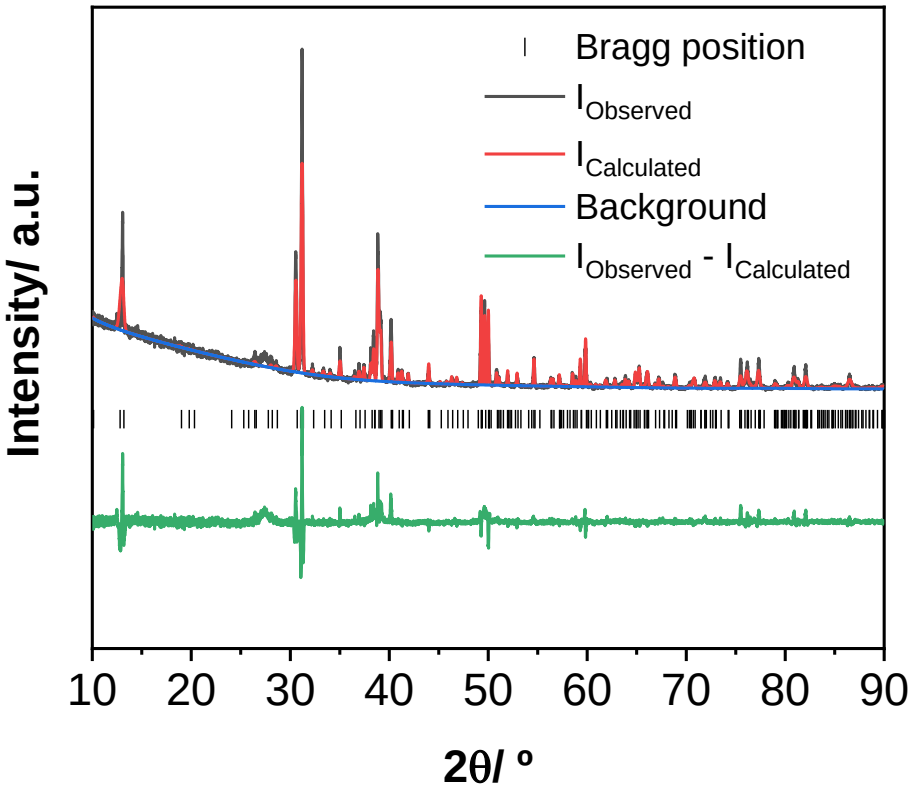

Figure 5.3– Rietveld fit of XRD data of $TaTe_2$. The solid black line corresponds to the observed data, the solid red line indicates the calculated profile, the solid blue line in the background, and the solid green line corresponds to the difference between the two profiles. Black tick marks indicate Bragg reflections of $TaTe_2$ (ICSD 86141).

The data was collected in reflection mode using a conventional Cu $K_{\alpha 1}$ source which influenced the goodness of the refinement fit due to the high absorption of the sample elements (Ta and Te), which affect the peak intensity. Other factors such as preferential orientation can also be related to the mismatch in intensity observed. For that reason, the Le Bail method was also used to refine the X-ray diffraction data, assuming arbitrary values for all the reflection intensity values (Figure 5.4). The goodness-of-fit, χ^2, for this refinement was found to be 2.99.

Table 5.1 Atomic position, isotropic displacement parameters, occupancies, and reliability factors of $TaTe_2$ determined by Rietveld refinement method from the PXRD data acquired at room temperature.

Atom	*X*	*Y*	*Z*	Multiplicity	Occupancy	U_{iso} (Å^3)
Ta1	0	0	0	2	1	0.00022(8)
Ta2	0.8605(7)	0.5000(0)	0.7095(3)	4	1	0.00012(7)
Te1	0.0057(4)	0	0.3077(0)	4	1	0.00012(7)
Te2	0.8510(5)	0.5000(0)	0.0094(9)	4	1	0.00013(9)
Te3	0.7967(7)	0.5000(0)	0.3786(7)	4	1	0.00012(7)

$TaTe_2$ – Space group *C*12/*m*1

a = 14.783 (3) Å, *b* = 3.637 (4)Å, *c* = 9.346 (2) Å, α = 90 °, β = 110.9 °, γ = 90 °

χ^2 = 3.84, R_{wp} = 15.56 %, R_{exp} = 10.68 %

The lattice parameters and agreement factors obtained from the Rietveld and Le Bail fits are shown in Table 5.2. To note that the lattice parameters obtained with both refinements are internally consistent and only differ slightly. The fact that the Le Bail and full-structural Rietveld derived results match almost completely, indicates that both methods are correct.

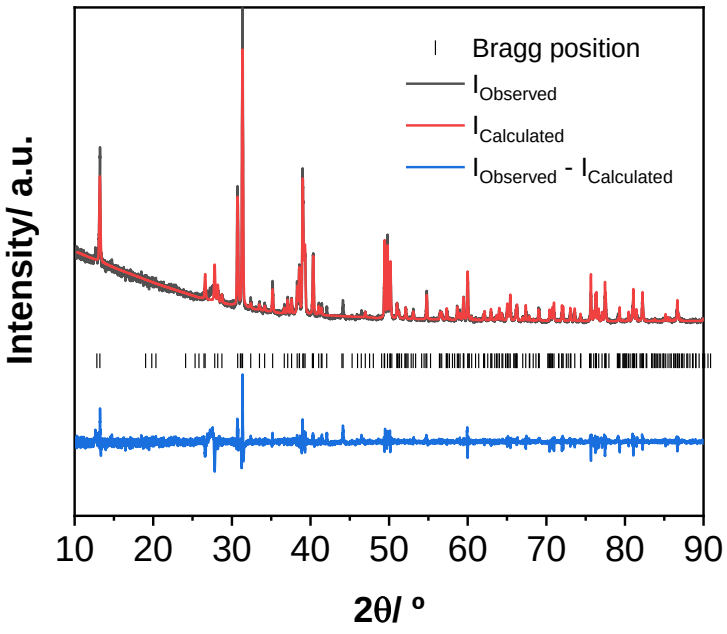

Figure 5.4- XRD Le Bail refinement of $TaTe_2$. The solid black line corresponds to the observed data, the solid red line indicates the calculated profile, and the solid blue line corresponds to the difference between the two profiles. Black tick marks indicate Bragg reflections of $TaTe_2$ (ICSD 86141). Space group *C*12/*m*1, *a* = 14.7663 (1) Å, *b* = 3.633 (0) Å, *c* = 9.336 (0) Å, α = 90 °, β = 110.9 °, γ = 90 °, χ^2 = 2.99, R_{wp} = 35.10 %, R_{exp} = 20.22 %

Table 5.2 – Lattice parameters and reliability factors for representative Le Bail and Rietveld refinement methods from the PXRD data acquired at room temperature.

Parameter	Le Bail	Rietveld
a	14.766 (1)	14.783 (3)
b	3.633 (9)	3.637 (4)
c	9.336 (4)	9.346 (2)
χ^2	2.99	3.84
R_{wp}	35.10 %	15.56 %
R_{exp}	20.22 %	10.68 %

In $TaTe_2$, the two Ta centres are placed in a distorted octahedral environment within the structure with Ta-Te distances ranging from 2.832(5) to 2.846(7) Å for Ta(1) and 2.732(4) to 2.892(3) Å for Ta(2) (Figure 5.5). Although the Rietveld refinement shown previously could have affected the accuracy of the results obtained, due to the high χ^2 reported, these distances agree with the ones reported in the literature ranging from 2.828 to 2.868 Å for Ta(1) and 2.668 to 2.903 Å for Ta(2) [7]. The different distance between both Ta atoms results in the formation of a $TaTe_6$ octahedron around each Ta, which in this case is less distorted for Ta(1) compared with Ta(2) [7]. The distorted $TaTe_6$ octahedra are joined via common edges, forming slabs running parallel to the [201] direction forming two-dimensional uneven slabs [7]. The $TaTe_2$ structure is characterized by a double zigzag chain of the Ta-Ta bond instead of the alternating short and long Ta-Ta distances pattern observed in other transition metal compounds [7]. This zigzag structure is characteristic of metal centres with a d^2 configuration, however, in the case of $TaTe_2$, this pattern results from the d^1 electronic configuration of the Ta centres [7]. The Te-Te distance from the intra-slab distance of the structure range between 3.533(8) and 3.550(6) Å which is in agreement with literature values (usually ranges between 3.551 and 3.642 Å [7]). These inter-slab contacts are shorter than the sum of the van-der-Waals radii of Te^{2-} (around 4 Å) which results in a 'polymeric' Te network inside the structure [7]. This shortened distance is also observed in other structures such as $TiTe_2$ [20] and VTe_2 [20] as a consequence of the charge transfer between Te sp levels and transition metal d level, leading to a net charge of -1.5 per tellurium atom in $TaTe_2$. The low electronegativity of Te atoms leads to complex scenarios of competition between metals and non-metals about the valence electrons resulting in valence electron localization in either sublattice introducing manifold types of homonuclear bonding [21]. If this tellurium-to-tantalum charge transfer did not exist, the Ta would present a +4 oxidation state and d^1 configuration, however, as a consequence, the formal oxidation state of Ta is +3 with a d^2 electronic configuration [22]. A clear dependence of the structural modulations on the d-electron count has been found in group 5 metal ditellurides with the formula MTe_2. The Te-Te interaction resulting from the depopulated antibonding states of the Te p orbital leads to the enhancing of the d-electron count of the metal ions from d^1 to about $d^{4/3}$ [11]. This excess valence electron density available for the M-M bonding creates specific structural distortions. The resulting d-electron count leads to metal-metal interactions

in two different directions within each layer, resulting in metal ribbon-chains running parallel to the layers and defining an in-plane monoclinic *C2/m* supercell [23]. Studies show that these kinds of systems are electronically unstable and distortions due to metal-to-metal bond formation are often observed [20]. The charge transfer mentioned previously results in the formation of a net of metal-metal bonds due to transferred electrons. The Te atoms act as a reservoir, supplying the charge to empty spaces within the structure giving rise to a relatively weak binding between the $TaTe_6$ octahedra [22].

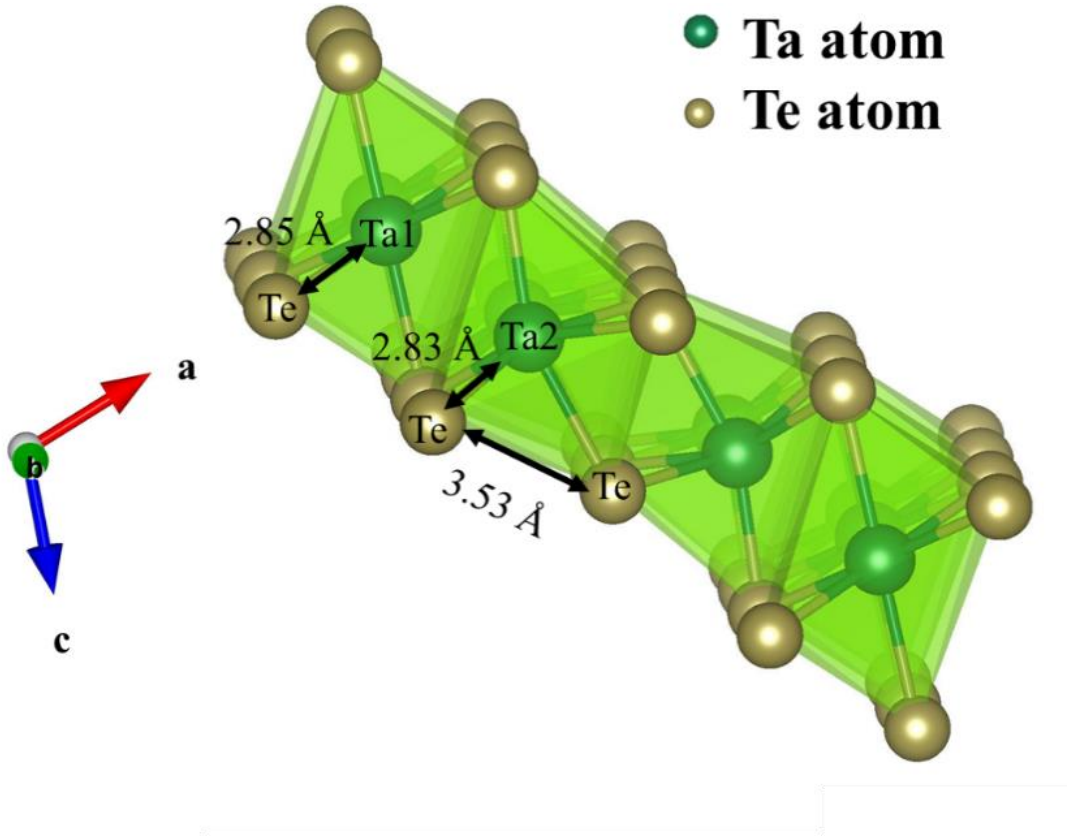

Figure 5.5– Polyhedral representation of crystal structure of $TaTe_2$ with a space group $C_{2/m}$ plotted using VESTA 3.4 [9]. The Ta and Te atoms are shown in green and yellow, respectively. Each distance (Ta(1)-Te, Ta(2)-Te and Te-Te) is represented with arrows.

5.3.1.2 SEM and EDX

The morphology of the sample was evaluated by field emission scanning electron microscopy (FESEM). Figure 5.6 shows that the $TaTe_2$ particles consist of monodispersed irregular blocks mostly in the range of 10 - 27 µm in length (average of 18.8 µm). To note that the particles are formed of stacked fine plates with thicknesses

in the range of 4.5 – 11.4 µm (average of 6.4 µm) which can be observed in the edges and fracture regions of the $TaTe_2$ blocks, demonstrating the layered structure of this material. The particles synthesised using the method described previously are considerably bigger (more than twice the size in length and approximately twice the thickness) compared with reports of the same material [5], [10]. This can be related to the different synthesis route used to synthesize the material described in this thesis, which involved the use of pure metals and high temperatures.

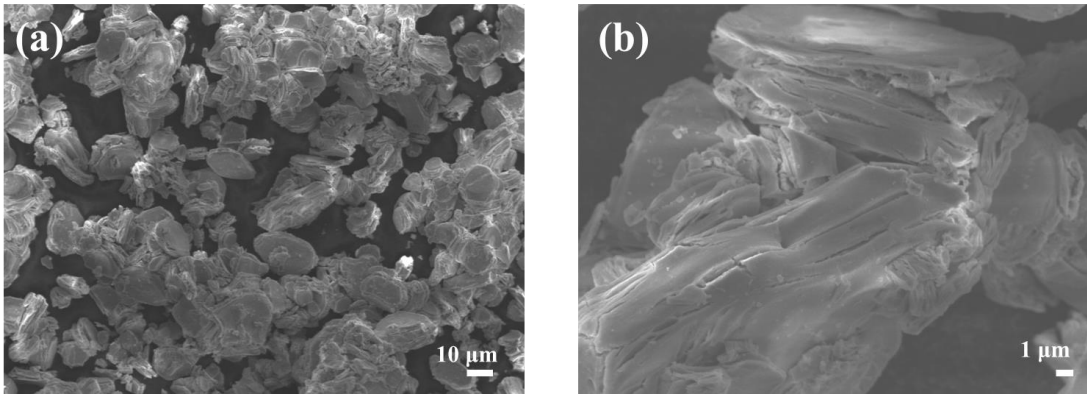

Figure 5.6 - FESEM images of the as-synthesized $TaTe_2$ (a) low magnification and (b) close-up view showing the layered structure of each particle.

Energy-dispersive X-ray spectroscopy (EDX) analysis and elemental distribution mapping of a selected area of a pristine $TaTe_2$ sample are shown in Figure 5.7. Data confirms a homogeneous distribution of Ta and Te components in the as-synthesized material.

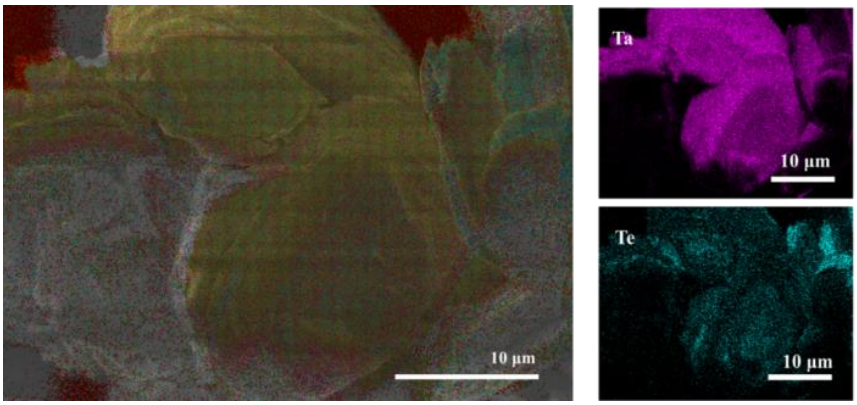

Figure 5.7 - EDX mapping of Ta and Te elements in the as-synthesized $TaTe_2$, showing the homogeneous distribution of both elements.

5.3.1.3 Transmission electron microscopy

The microstructural properties of the as-synthesized material were further analysed using high-resolution transmission electron microscopy (HRTEM). Figure 5.8 shows a low-magnification bright-field image of a single $TaTe_2$ particle evidencing the stacking of thin nanosheets in the material. Darker lines in the TEM images of flake edges are correspondent to individual single layers and from Figure 5.8b it is possible to distinguish the single layers and observe three layers of exfoliated material. TEM analysis revealed that $TaTe_2$ particles contained single- and few-layered exfoliated flakes with lateral sizes of ~ 13 nm.

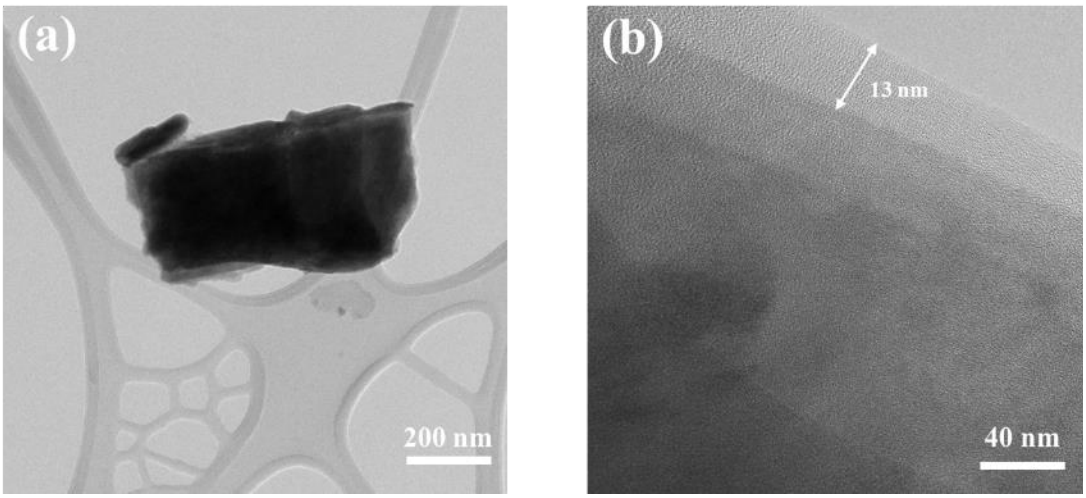

Figure 5.8 – HRTEM image of the exfoliated as-synthesized $TaTe_2$ nanosheets at (a) low and (b) high-resolution of the edges of the $TaTe_2$ nanosheets from the exfoliation process showing a single-layered sheet.

High-resolution TEM images (Figure 5.9a) clearly show lattice fringes with interplanar spacings of about 0.37 and 0.46 nm, which agrees well with the (40-1) and (201) planes of $TaTe_2$. Figure 5.9b shows a typical SAED pattern of the exfoliated $TaTe_2$ confirming the existence of single crystallinity of the stacked thin plates.

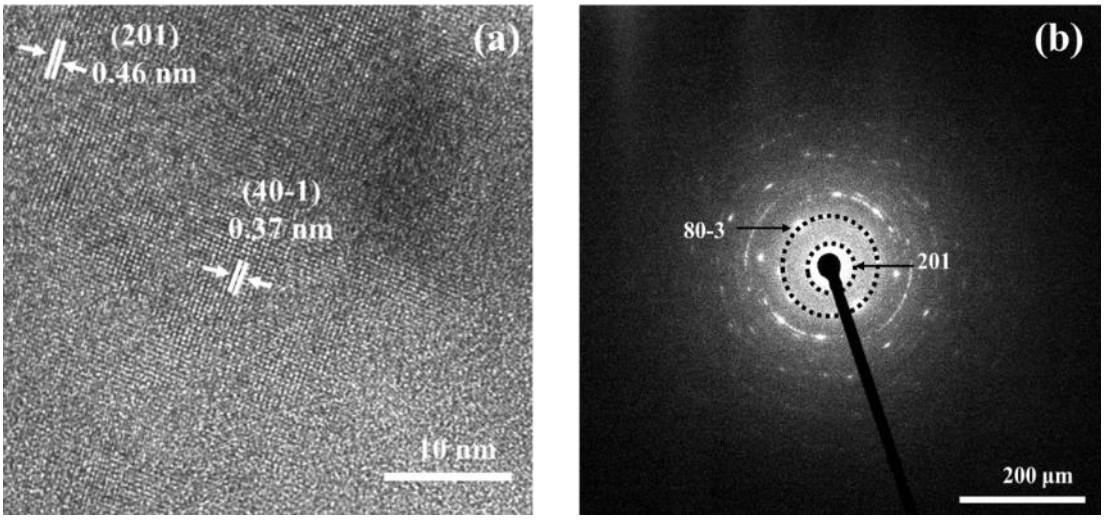

Figure 5.9 – HRTEM image of the exfoliated as-synthesized $TaTe_2$ nanosheets at (a) high-resolution confirming the presence of $TaTe_2$. The interlayer spacing of the $TaTe_2$ nanosheets represents an interatomic spacing length of 0.37 and 0.46 nm and (b) corresponding SAED pattern.

5.3.2 Electrochemical characterisation in LIBs

5.3.2.1 Galvanostatic Cycling

Figure 5.10 shows the load curve of the first cycle of $TaTe_2$ *vs* Li^+/ Li in the voltage window of 0.1 – 3.0 V at 10 mA g^{-1}. Four different voltage plateaus can be observed in the initial discharge from the open-circuit voltage (OCV 2.65 V) to 0.1 V at 1.37 (a), 1.20 (less evident) (b), 0.83 (c) and 0.60 (d) V. Followed by those plateaus, the potential sloped continuously to the cut-off voltage (0.1 V) resulting in a storage capacity of 468.9 mAh g^{-1}. This similar step-like voltage profile mechanism was described in other MTe_2 materials when cycled in LIBs and SIBs [16], [24]–[27]. These works described a multistep process behind the intercalation of Li^+ ions into the interlayer spacing of MTe_2 with the conversion of the initial material and the sequent alloying reaction of $TaTe_2$ to Ta and Li_2Te. The experimental capacity obtained can be matched to the theoretical capacity for the insertion of 7 Li^+ ions into $TaTe_2$ (430 mAh g^{-1}) plus an extra capacity of ~40 mAh g^{-1}. Previous literature in this type of electrode

materials shows an extra capacity of around ~50 mAh g^{-1} which can be associated with the SEI formation [28]–[30].

Upon charging, a slope followed by a voltage plateau at 1.69 V was observed. Then the potential increased monotonously up to the cut off voltage, resulting in a charge capacity of 336.2 mAh g^{-1} corresponding to the deinsertion of ~ 5.5 Li^+ ions and a coulombic efficiency (CE) of 71.9 %. This result indicates the partially reversible mechanism observed. The difference in load curves between the discharge and charge processes confirms that the insertion and deinsertion of Li^+ ions into the structure proceeds following different pathways.

Although, four peaks are observed in the CV curves (Section 5.3.2.3) which match with the number of plateaus observed in the GD curves, the voltage at which each plateau is seen is slightly higher in the GD curves (~ 0.14 V higher on average).

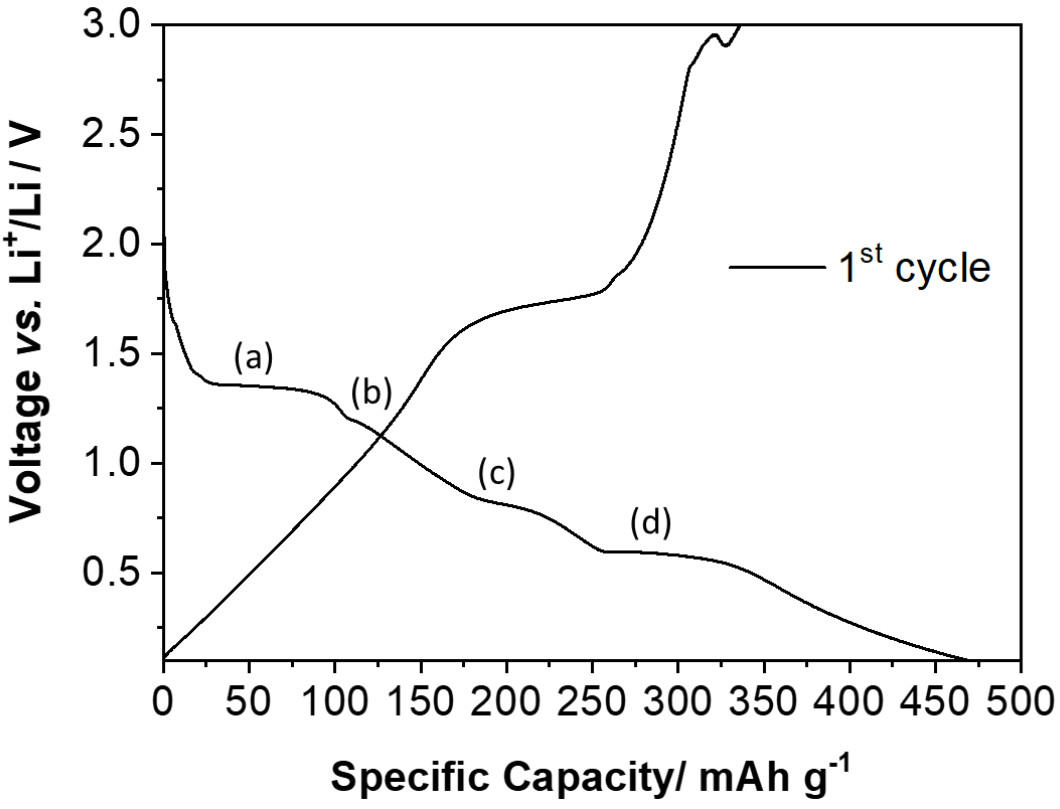

Figure 5.10 - Galvanostatic charge-discharge profile of the first cycle at a current density of 10 mA g^{-1} of $TaTe_2$ *vs* Li^+/Li in the voltage range of 0.1-3.0 V.

Figure 5.11 shows the cycling profile for cycles 1, 2, 3 5, and 10 under the same current and voltage window as in Figure 5.10. From the second cycle, the voltage of the first discharge plateau increases to ~1.6 V and becomes shorter while the other three plateaus at 1.20, 0.83 and 0.60 V disappear, matching with the disappearance of the peaks in the cyclic voltammogram (Section 5.3.2.3). A decrease in capacity is observed in the 2nd cycle with a value of discharge/charge capacity of 351.7/ 301.6 mAh g^{-1}, representing a loss of 15 % compared with the 1st cycle.

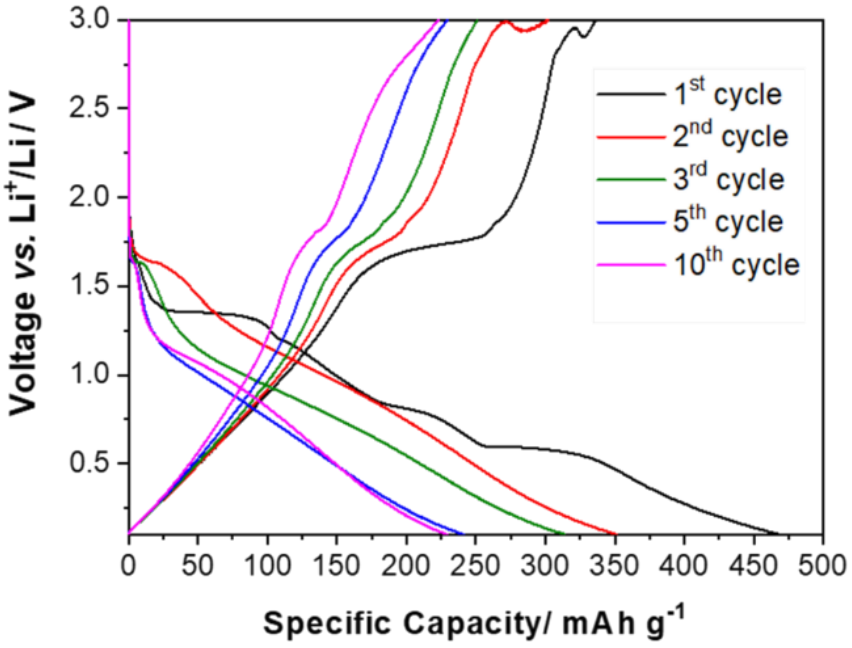

Figure 5.11 - Galvanostatic charge-discharge profiles for cycles 1-3, 5 and 10 at a current density of 10 mA g^{-1} of $TaTe_2$ *vs* Li$^+$/Li in the voltage range of 0.1-3.0 V.

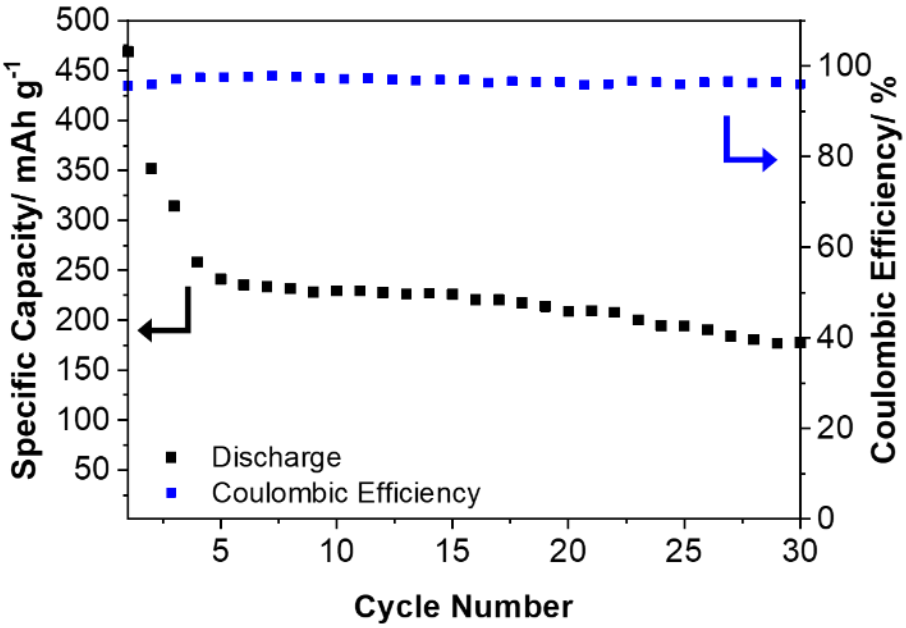

Figure 5.12 – Specific capacity *vs* cycle number plot with coulombic efficiencies over 30 cycles of $TaTe_2$ in the voltage range of 0.1-3.0 V at 10 mA g^{-1}.

A continuous loss of capacity is observed in the $TaTe_2$ anode material upon cycling retaining 68.3 % and 49.4 % of its initial charge capacity after 5 and 30 cycles, respectively (Figure 5.12).

The drastic drop in capacity after 30 cycles can be associated with the complete pulverization of the bulk active materials upon insertion/extraction of Li^+ ions as well as the formation of cracks in the electrode material upon cycling [31]. The images of the particles upon cycling show this result (Section 5.3.2.2). Exfoliation of the anode from the current collector that occurs within the first few cycles can also be related to this capacity loss as it eventually ends up in isolated and broken electrical connections [31], [32].

Owing to their weak van-der-Waals force, ions can diffuse rapidly through the interlayer gap in MX_2 type materials. For that reason, electrodes were cycled at a high current density of 100 mA g^{-1} to examine the ion insertion and deinsertion process in the $TaTe_2$ *vs* Li^+/Li system and the load curves for cycles 1, 2, 3, 5 and 10 are shown in Figure 5.13.

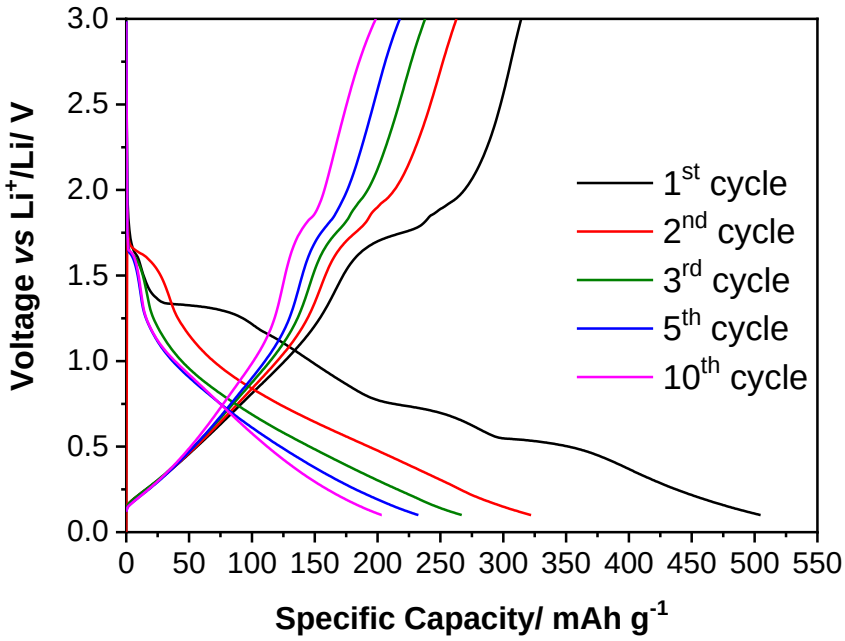

Figure 5.13 - Galvanostatic charge-discharge profiles at a current density of 100 mA g^{-1} of $TaTe_2$ *vs* Li^+/Li in the voltage range of 0.1-3.0 V.

Similarly, to the load curves obtained at lower current density, four different voltage plateaus can be observed during the initial discharge (at 1.31, 1.16 (less evident), 0.71 and 0.51 V) and one less evident during charge (at 1.77 V). A 1st discharge/ charge capacity of 504.7 and 314.3 mAh g^{-1}, respectively, is obtained. The similar load curve obtained for the 100 mA g^{-1} compared with 10 mA g^{-1} (Figure 5.14) shows that the intercalation and deintercalation of Li^+ ions into the $TaTe_2$ structure is independent of the current density applied.

The $TaTe_2$ anode material cycled at 100 mA g^{-1} shows an initial decay of 30.7 % during the first 5 cycles and capacity retention of 53.6 % of its initial charge capacity after 30 cycles (Figure 5.15).

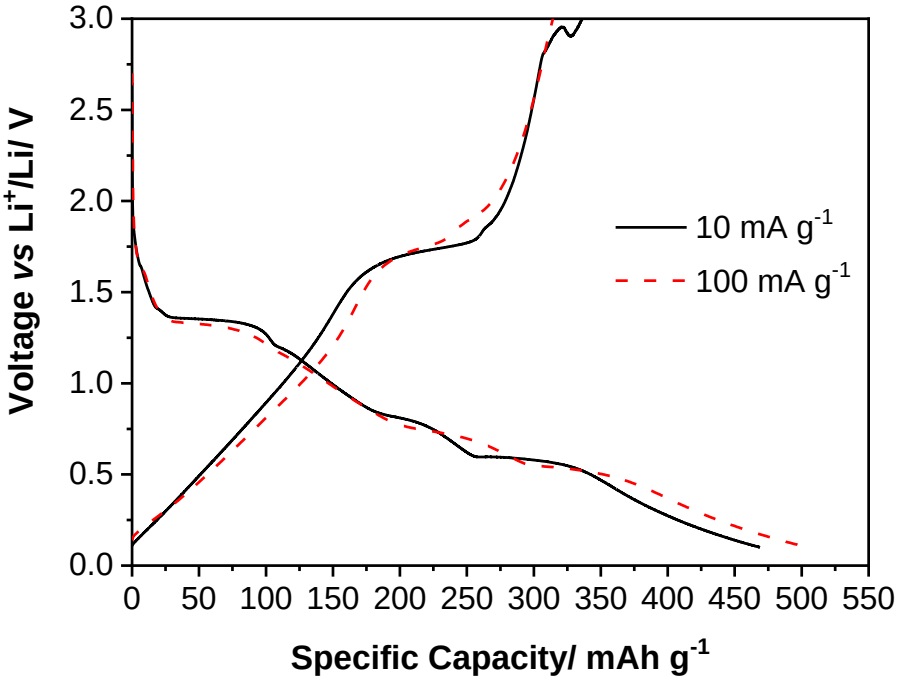

Figure 5.14 - Galvanostatic charge-discharge profile of the 1st cycle at a current density of 10 and 100 mA g^{-1} of $TaTe_2$ *vs* Li^+/Li in the voltage range of 0.1-3.0 V.

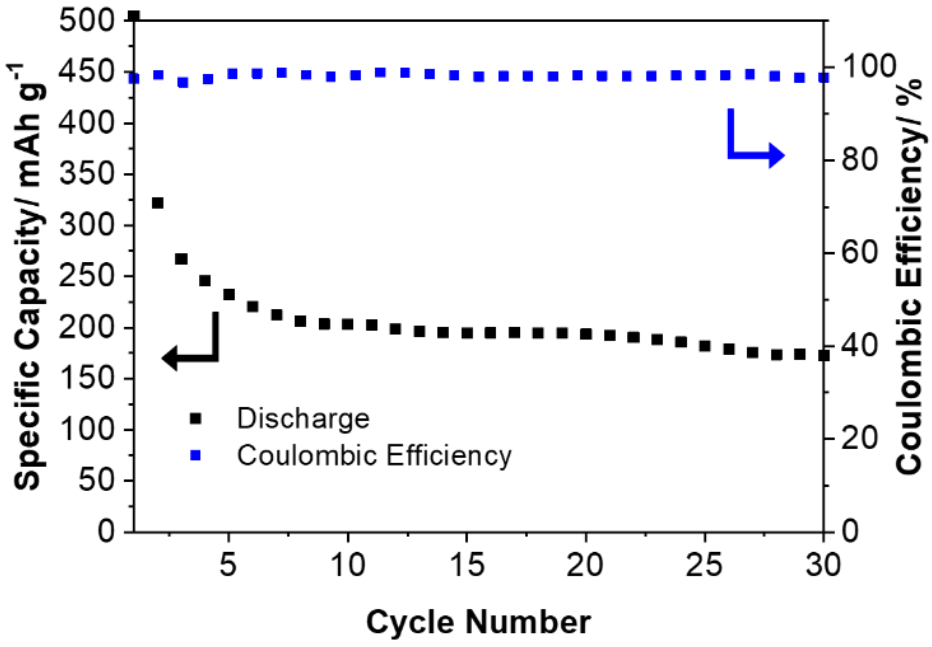

Figure 5.15 – Specific capacity vs cycle number plot with coulombic efficiencies over 30 cycles of $TaTe_2$ in the voltage range of 0.1-3.0 V at 100 mA g^{-1}.

Despite increasing the current density from 10 to 100 mA g^{-1}, comparable capacity retention is achieved with no major capacity lost in neither case over 100 cycles (24.5 % *vs* 25.4 % for 10 and 100 mA g^{-1}, respectively) (Figure 5.16).

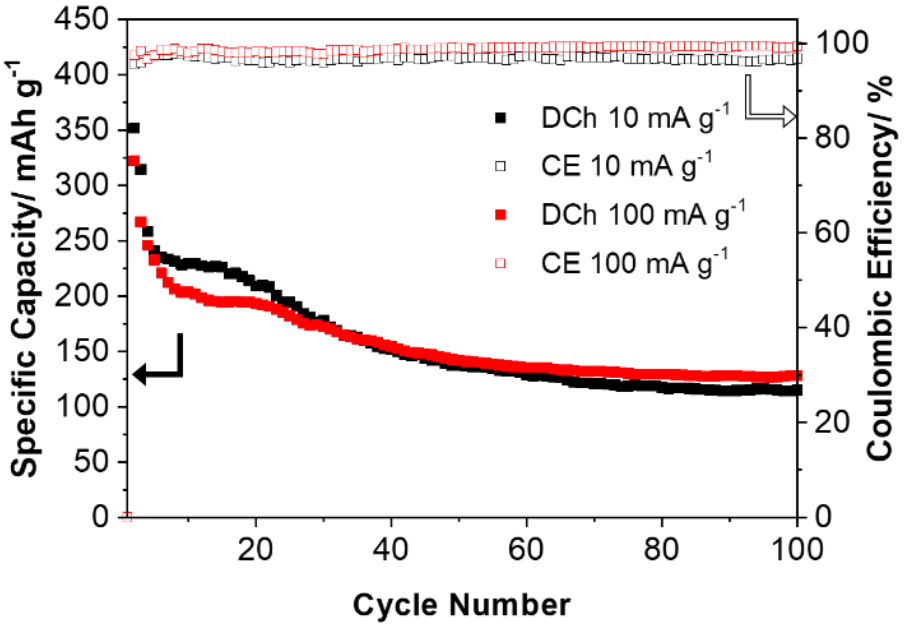

Figure 5.16 – Specific capacity *vs* cycle number plot with coulombic efficiencies over 100 cycles of $TaTe_2$ in the voltage range of 0.1-3.0 V at 10 and 100 mA g^{-1}.

The rate capability of $TaTe_2$ was tested at different currents from 10 to 500 mA g^{-1} (5 cycles each) between 0.1 and 3.0 V and then returned to 10 mA g^{-1} (Figure 5.17). The electrode shows a discharge capacity at the 5th cycle of 200, 162, 137, 107, 85 and 60 mAh g^{-1} at 10, 20, 50, 100, 200 and 500 mA g^{-1}, respectively. When the current returns to 10 mA g^{-1} a discharge capacity of 177 mAh g^{-1} is achieved, which corresponds to half of the initial specific discharge capacity with a CE of 88.5 %.

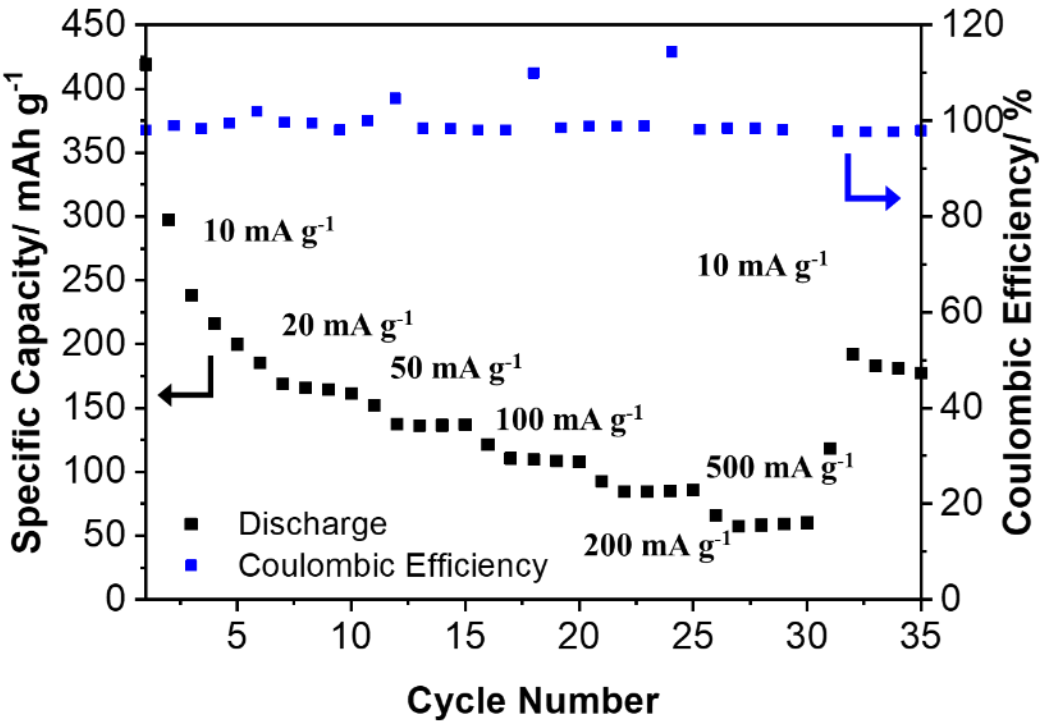

Figure 5.17 – Rate performance of $TaTe_2$ *vs* Li^+/Li in the potential range of 0.1 – 3.0 V at different current densities of 10, 20, 50, 100, 200 and 500 mA g^{-1}.

The electrochemical performance of the $TaTe_2$ electrode as anode material for SIBs was also investigated by galvanostatic driven discharge-charge tests in the voltage range of 0.1 – 3.0 V *vs* Na^+/Na at a current density of 10 mA g^{-1} (Figure 5.18). Due to the poor electrochemical performance observed in SIBs compared to LIBs, we decided to focus solely on the investigation of $TaTe_2$ applied to LIBs.

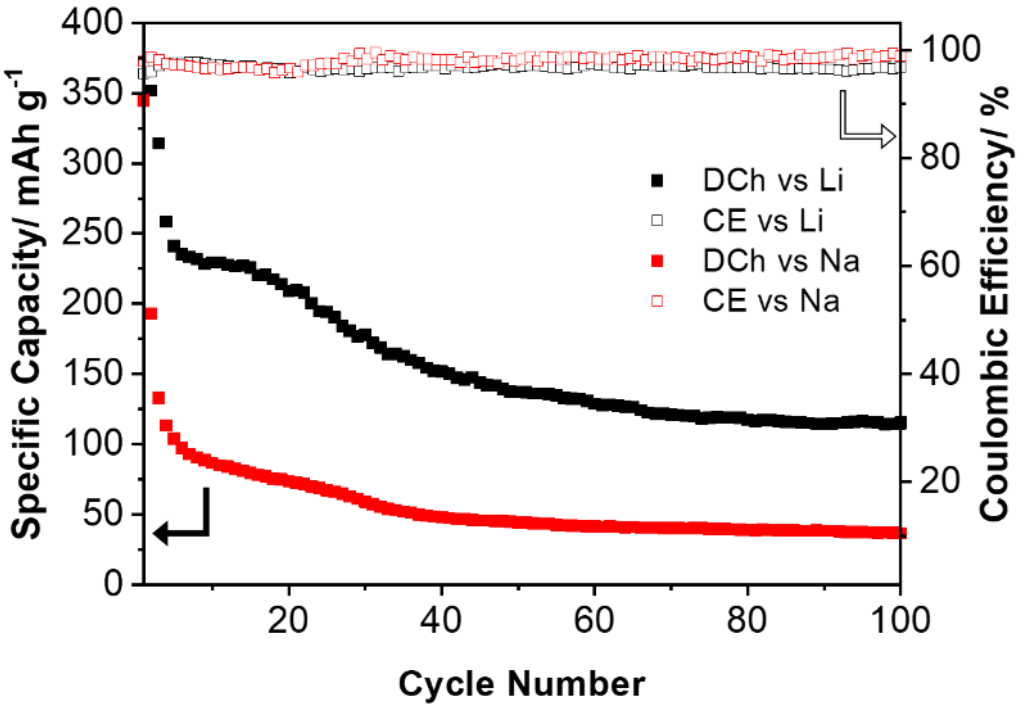

Figure 5.18 – Discharge specific capacity *vs* cycle number plot with coulombic efficiencies over 100 cycles of $TaTe_2$ *vs* Li^+/ Li and Na^+/Na in the voltage range of 0.1-3.0 V at 10 mA g^{-1}.

5.3.2.2 SEM analysis of post-mortem electrodes

To study the electrode's structure stability, cycled SEM analysis was performed to evaluate the morphology evolution of the $TaTe_2$ during long-term cycling. Figure 5.19 shows the SEM images of the as-synthesized electrode, as well as the electrode, cycled to 25, 50 and 75 cycles. The main difference observed is the fact that in the fresh electrode (Figure 5.19a) the particles are dispersed, while the particles in the cycled electrodes are trapped in a carbon and PVDF matrix. The existence of fibres from the glassfibre separators is also present in the cycled electrodes. To note that the longer the cycling (75 cycles, Figure 5.19d), the fewer lose particles are observed which leads us to believe that the continuous cycling increases the matrix thickness. The presence of a thicker SEI layer can also be hypothesised as the reason for this fact. In terms of particle

size, after 25 cycles the average particle size is 27.82 nm which is 1400 times smaller than the particles size before cycling.

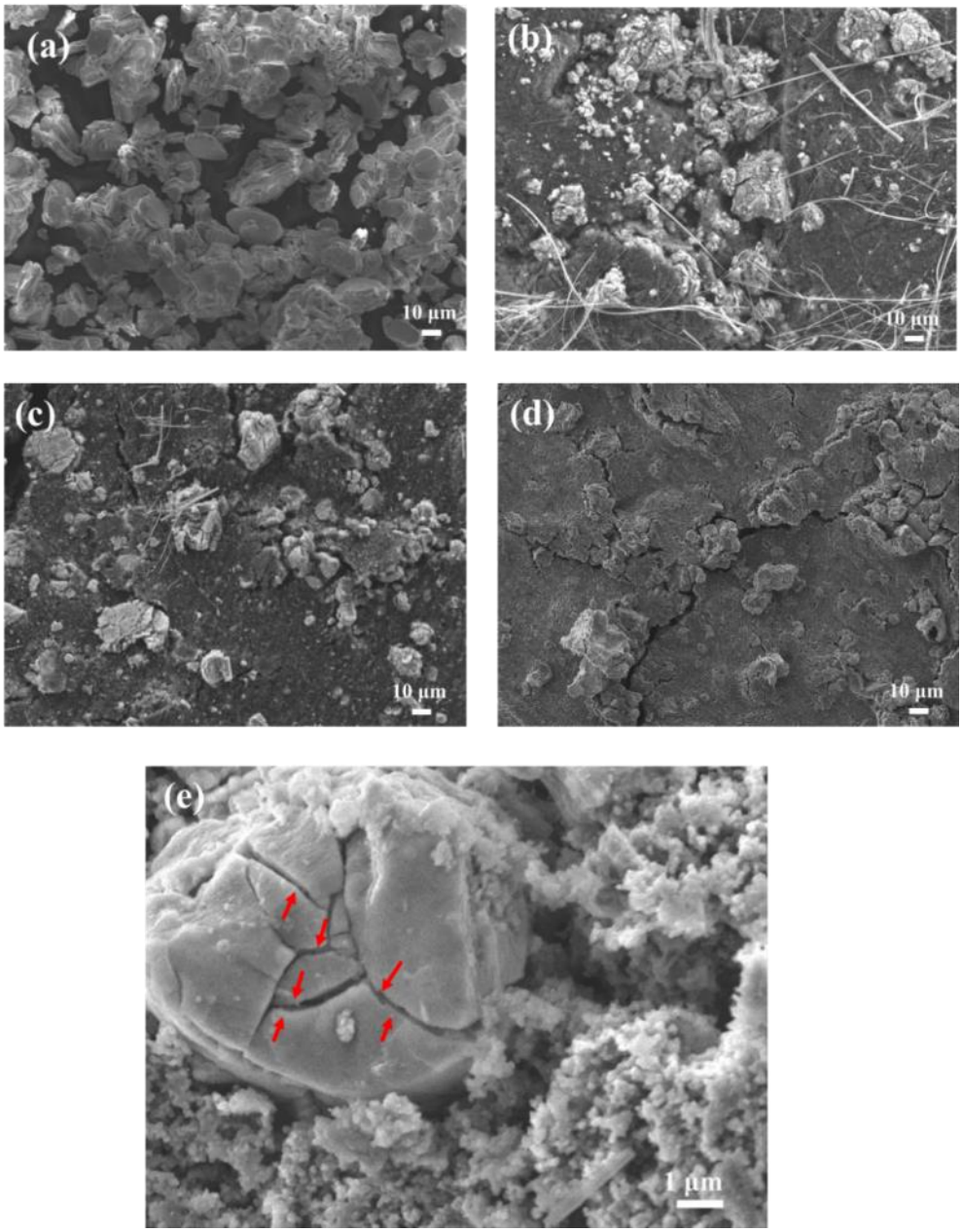

Figure 5.19- Morphology and structure change of the $TaTe_2$ anodes during cycling against Li. The *ex situ* images of SEM were collected at selected cycles (a) pristine, (b) 25 cycles, (c) 50 cycles and (d) 75 cycles. (d) *Ex situ* SEM image showing the crack formation in $TaTe_2$ after 75 cycles; the red arrows indicate the crack locations in the image.

As reported in other MX_2 type materials, the continuous insertion and extraction of ions from the lattice of the layer-structured material lead to lattice breakdown, crack and porosity formation [33]. The results of the SEM imaging in the cycled $TaTe_2$ after 75 cycles is shown in Figure 5.19e. The cracks are labelled with red arrows in the SEM image and show the cracks formed within the particle due to cycling. The large strain generated by the removal of Li^+ ions during charging is believed to be the origin of these crack formations. The increased internal strain during reaction with lithium and consequent cracking of the material results in poor electrochemical performance as previously described (Section 5.3.2.1) as well as an increase in the SEI layer thickness and consequently increase in internal impedance (Section 5.3.2.4).

5.3.2.3 Cyclic Voltammetry

The electrochemical performance of the $TaTe_2$ material was evaluated as an anode material for LIBs in half cells using lithium metal as the counter and the reference electrode. The cyclic voltammetry (CV) curves of the first 5 cycles in the potential window of 0.1 – 3.0 V *vs* Li^+/Li at a scan rate of 0.1 mV s^{-1} are shown in Figure 5.20. The first cathodic scan shows peaks at 1.24, 1.13, 0.62 and 0.41 V and the corresponding anodic scan shows one oxidation peak at 1.80 V. The cathodic and anodic peaks indicate the intercalation and extraction of lithium ions into the interlayer spacing of $TaTe_2$, respectively.

Similarities between this system and other MX_2 compounds allow the identification of CV peaks by comparison [29], [31], [34]. Therefore, we suggest that the cathodic peaks centred at 1.24 and 1.13 V in the first discharge can be attributed to the Li^+ ion intercalation into the crystal structure by conversion reaction of $TaTe_2$ and Li^+ to form a $LiTaTe_2$ compound. At 0.62 V, another reduction peak is observed which, by comparison, can be attributed to the conversion reaction of $LiTaTe_2$ to Ta metal and Li_2Te. Simultaneously, a strong reduction peak at 0.41 V can be observed which corresponds to the formation of solid electrolyte interphase (SEI) layer, which contributes to the irreversible decomposition of the electrolyte [29], [34]. This peak was previously observed in other MTe_2 compounds, such as $MoTe_2$ [29]. The as-obtained

discharge capacity corresponds to the insertion of 7 Li^+ ions into the crystal structure and the mechanism is represented below:

$$1.75\,TaTe_2 + 7\,Li^+ + 7e^- \leftrightarrow 3.5\,Li_2Te + 1.75\,Ta \qquad (5.1)$$

The extraction of Li^+ ions from Li_2Te during the charging process results in the reformation of $TaTe_2$ and a single anodic oxidation peak at 1.80 V. The poor electrical conductivity and large size of $TaTe_2$ particles, observed in the SEM data (Section 5.3.1.2), just as $MoTe_2$, results in slow kinetics and high polarization [29].

During the second scan, a single new cathodic peak is observed at 1.61 V, followed by the anodic oxidation peak a 1.80 V. During the 2nd discharge scan, the region between 1.5 and 0.5 V containing the centred peaks at 1.24, 1.13 and 0.62 V in the 1st discharge, turns into a broader region. The single oxidation and reduction peak observed after the 1st cycle suggests that the extraction/insertion of Li^+ ions turn into a single step. The 2nd to 4th CV curves nearly overlaps, especially upon the charge, however, the intensities of the redox peaks decrease, reflecting the less stable and reversible electrochemical behaviour of the electrode after the initial conversion reaction and SEI layer formation.

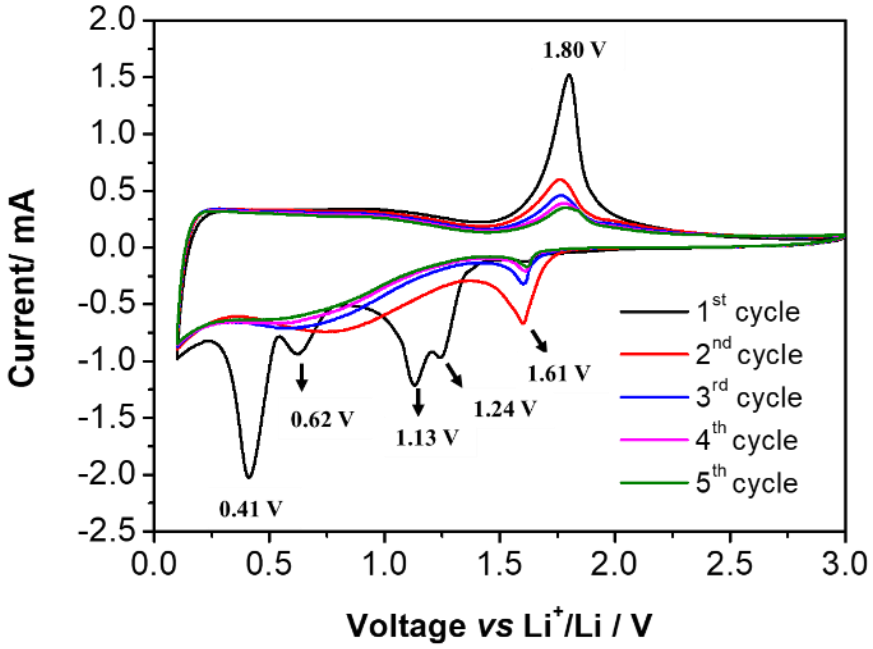

Figure 5.20 - Cyclic voltammograms at a scan rate of 0.1 mV s^{-1} for $TaTe_2$ *vs* Li^+/Li in the voltage range of 0.1 – 3.0 V.

5.3.2.4 Impedance Spectroscopy

EIS measurements were performed in $TaTe_2$ to investigate the electrochemical processes occurring at the electrode-electrolyte interface and within the electrode during cycling. The impedance spectra were collected at an open-circuit voltage (OCV) and charge and discharge point up to the 10^{th} cycle in a frequency range from 0.01 Hz to 100 kHz. Figure 5.21 shows the impedance spectra of the as-prepared $TaTe_2$ obtained at the OCV point and the corresponding equivalent circuit model used to fit the spectra. The equivalent circuit is composed of an R_S at high frequencies and an R_{CT} along with a CPE element. The electrolyte resistance dominates the intercept at the Z' axis in the high-frequency range (R_S). The movement of electrons and Li^+ ions across the electrode-electrolyte interface generates a charge-transfer resistance that is characterised by a semicircle at a high-medium frequency (R_{CT}). The CPE element corresponds to the electrical double layer capacitor that forms on the interface between the electrode and electrolyte, resulting from the adsorption of Li^+ ions from the electrolyte onto the surface of the electrode. The charge transfer resistance in OCV is determined to be 106.5 Ω. The high R_{CT} value at OCV shows the initial barrier of Li reaction to $TaTe_2$ as observed in $MoTe_2$ [35].

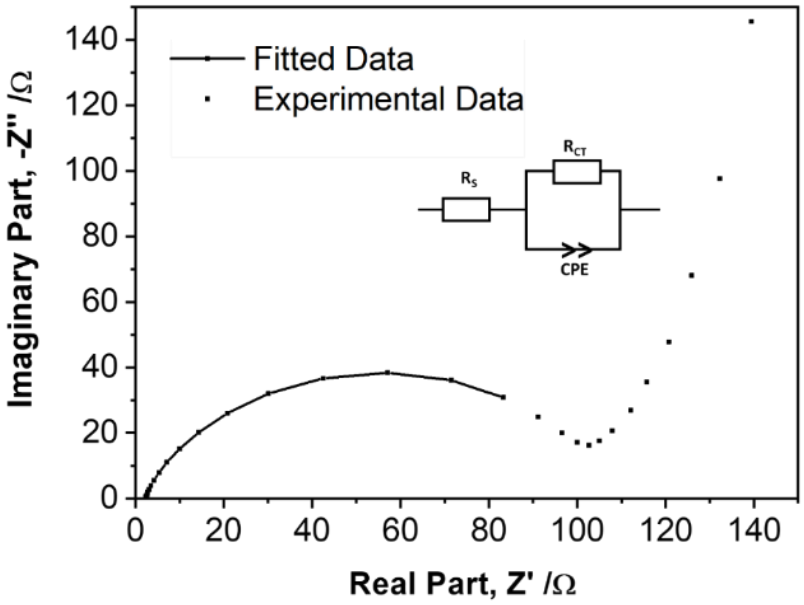

Figure 5.21– Nyquist impedance plots collected from 0.01 Hz to 100 kHz in OCV state and equivalent circuit model used to analyse the EIS spectra acquired for $TaTe_2$ in LIBs.

The evolution of the impedance spectra during the 1st cycle was evaluated and is shown in Figure 5.22. The slight increase of the arc radius upon discharge suggests that the interface between the electrolyte and the electrode becomes more resistive which can be related to the formation of an SEI layer upon Li-ion insertion. Both spectra can be fitted using the equivalent circuit shown in Figure 5.22 composed an R_S element at high frequencies, a charge-transfer resistance (R_{CT}) along with a CPE and an R_{SEI} and correspondent CPE element. The extra resistance present in these spectra compared to the OCV spectrum is associated with the formation of a solid electrolyte interface (SEI) during the 1st discharge process. The first discharge process is accompanied by the formation of the SEI layer, which leads to the presence of a single semicircle with the contribution of both the SEI layer and charge-transfer resistance processes. Although a single semicircle is observed this is a product of the overlapping of the charge-transfer and SEI individual circles due to the proximity of the relaxation time constant of both processes. The equivalent circuit used to fit the results allow distinguishing both processes and respective resistances. The SEI layer and charge transfer resistance were found to be 109.5 and 7.4 Ω, respectively, resulting in a total arc resistance of 116.9 Ω.

Upon the 1st charge, both the R_{SEI} and R_{CT} values decrease to 3.2 and 30.2 Ω, respectively. The abrupt decrease in R_{CT} value upon deinsertion of Li^+ ions show an increase in the Li^+ diffusion and lower stability of the discharge/ charge capacity of the cycled electrodes. The EIS results observed reveal the low structural stability of $TaTe_2$ upon Li intercalation/extraction. The value of the different resistances for the 1st cycle can be found in Table 5.3.

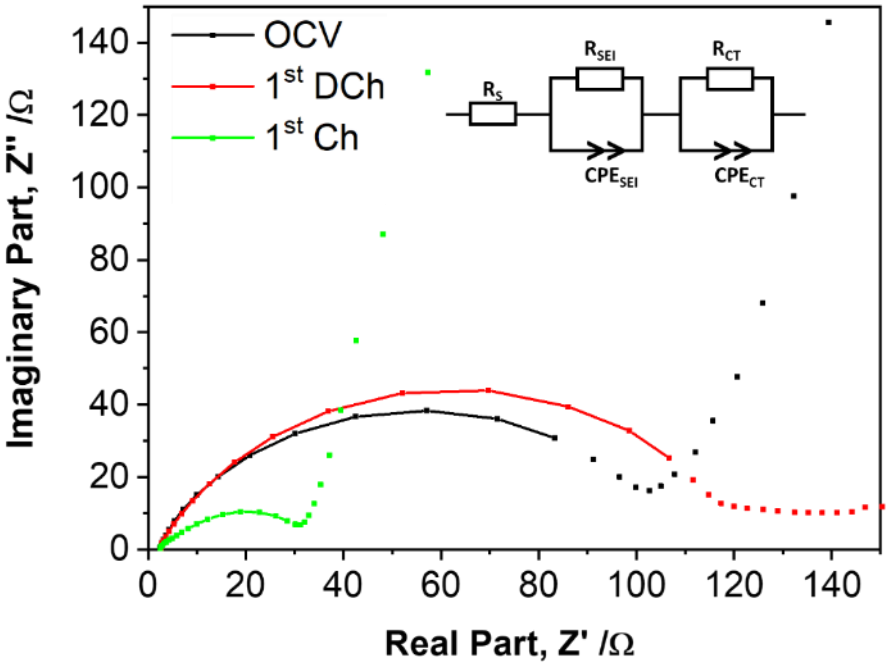

Figure 5.22 - Nyquist impedance plots collected from 0.01 Hz to 100 kHz during the 1st cycle and equivalent circuit model used to analyse the EIS spectra acquired for $TaTe_2$ in LIBs.

Table 5.3 - Electrolyte, SEI and charge-transfer resistances determined from EIS during the 1st cycle for $TaTe_2$ in LIBs.

Sample	R_S (Ω)	R_{SEI} (Ω)	R_{CT} (Ω)
OCV	2.1		106.5
1st Discharge	2.4	109.5	7.4
1st Charge	2.2	3.2	30.2

The evolution of the EIS spectra was studied up to the 10th cycle to understand the changes in both the SEI layer and charge-transfer resistance. Figure 5.23 shows the evolution of the discharge process. To note that the equivalent circuit to fit the EIS data used was the same as for the 1st discharge composed by an initial R_s at high frequencies,

a charge-transfer resistance R_{CT} along with a constant phase element (CPE) and an R_{SEI} and correspondent CPE element at low frequencies.

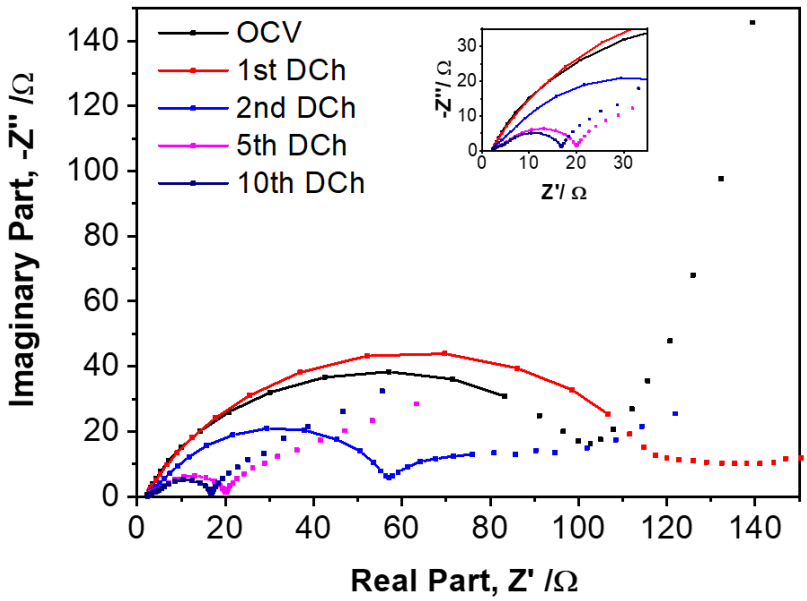

Figure 5.23 - Nyquist impedance plots collected from 0.01 Hz to 100 kHz during discharge states acquired for $TaTe_2$ in LIBs. The inset depicts the high-frequency impedance plot.

A major decrease in total arc resistance from 116.9 Ω for the 1st discharge to 87.5 Ω for the 2nd discharge is observed. The low value of R_{CT} registered for the 2nd discharge can be associated with increasing the number of nanosized particles obtained after the conversion reaction after the first cycle which facilitates Li^+ transfer by decreasing the R_{CT} [35]. To note that in this spectrum, two semicircles can be easily identified indicating that the relaxation time constant of the SEI layer and charge-transfer resistance becomes significantly different, allowing the observation of their responses. The arc at high frequency is assigned to Li^+ ion migration through the SEI layer and the arc at medium frequency is assigned to the charge-transfer resistance at the interface between the electrolyte and electrode. Further discharge up to the 5th cycle results in a decrease of the overall arc resistance to 18 Ω, which can be related to the slight increase in capacity observed during long cycling as the higher amount of active material exposed upon cycling results in a decrease of resistance and easier insertion of Li^+ ions. Further cycling leads to a slight decrease of impedance again up to the 10th discharge

(14.8 Ω). Two separate arcs are observed as a result of two processes (SEI and charge transfer) indicating an increase in the relaxation time constants of both processes. To note that the arc radius becomes progressively smaller as the material is cycled, suggesting that the charge-transfer resistance becomes smaller, which is beneficial to accelerate the charge-transfer process. The continuous decrease of the R_{CT} with cycling proves that faster Li^+ ion mobility in the $TaTe_2$ electrode leads to low overpotential after the first cycle [35], [36]. The value of the different resistances is shown in Table 5.4.

Table 5.4 - Electrolyte, SEI and charge-transfer resistances determined from EIS during the discharge processes for $TaTe_2$ in LIBs.

Sample	R_S (Ω)	R_{SEI} (Ω)	R_{CT} (Ω)
OCV	2.1		107
1st Discharge	2.4	110	7.4
2nd Discharge	3.2	32.9	54.6
5th Discharge	2.4	14.8	3.2
10th Discharge	2.3	3.0	11.8

Contrarily to the trend observed during the discharge process, the charging data suggests a steadier trend of the overall value of arc resistance. The equivalent circuit used to fit the charge EIS data was the same as for the 1st discharge (R_S element at high frequencies, a charge-transfer resistance (R_{CT}) along a CPE at medium frequencies and an R_{SEI} along a CPE at low frequencies) (Figure 5.24). The R_{SEI} and R_{CT} calculated up to the 5th charge are similar in every charging process with a slight increase in total resistance from 33.4 Ω to 34.3 Ω from the 1st to the 5th charging process. At the 10th charge, the spectrum shows the presence of two semi-circles that partially overlap in the high-medium frequency range. Although the slightly different spectrum observed, the same equivalent circuit was used to fit the data of the 1st discharge was used. The SEI layer and charge transfer resistance were found to be 3.1 Ω and 13.5 Ω, respectively.

Table 5.5 shows the resistance values obtained for the charging process up to the 10th cycle.

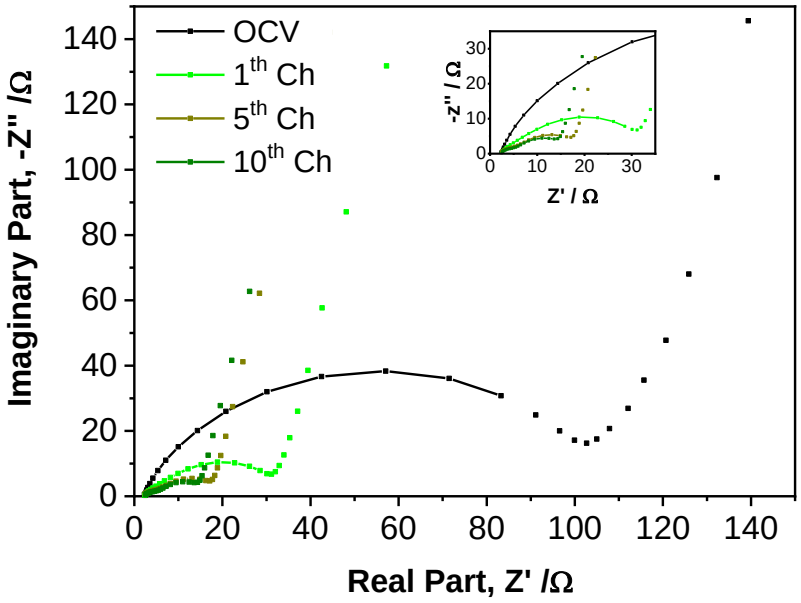

Figure 5.24 - Nyquist impedance plots collected from 0.01 Hz to 100 kHz during charge states acquired for $TaTe_2$ in LIBs. The inset depicts the high-frequency impedance plot.

Table 5.5 - Electrolyte, SEI and charge-transfer resistances determined from EIS during the charging processes for $TaTe_2$ in LIBs.

Sample	R_S (Ω)	R_{SEI} (Ω)	R_{CT} (Ω)
OCV	2.1		107
1st Charge	2.2	3.2	30.2
5th Charge	2.2	30.3	4.0
10th Charge	2.2	3.1	13.5

EIS data was recorded for cycles 25 and 75 to understand the resistance evolution after long cycling. Figure 5.25 shows an increase in arc radius upon cycling which is related

to the increase in overall resistance in the cell. The data were fitted using the same equivalent circuit used for cycle 10. Table 5.6 shows the evolution of the R_{SEI} and R_{CT} value upon long cycling. A major increase in the R_{SEI} value in cycle 25 compared with cycle 10 (3.0 *vs* 65.5 Ω) is observed. The increase of the SEI layer is one of the main reasons for the capacity fading of cells [37]. In the case of $TaTe_2$ cycled against Li, this increase in the SEI layer can be related to the large-volume changes experienced by Te compounds formed during cycling during lithiation and delithiation. The relaxation of stress/strain induced by volume expansion is observed in high-capacity electrodes after the first lithiation through deformation of the initial material [38], [39]. The expansion that occurs during lithiation breaks the SEI layer, resulting in more electrolyte to be used to rebuild the layer during cycling and therefore, a thicker SEI layer.

The increase in SEI layer leads to an increase in SEI resistance with repeated cycling as it can be observed by the R_{SEI} value at cycle 75 (114.6 Ω). This increase leads to a shortened lifetime of a cell as can be observed by the charge-discharge curves.

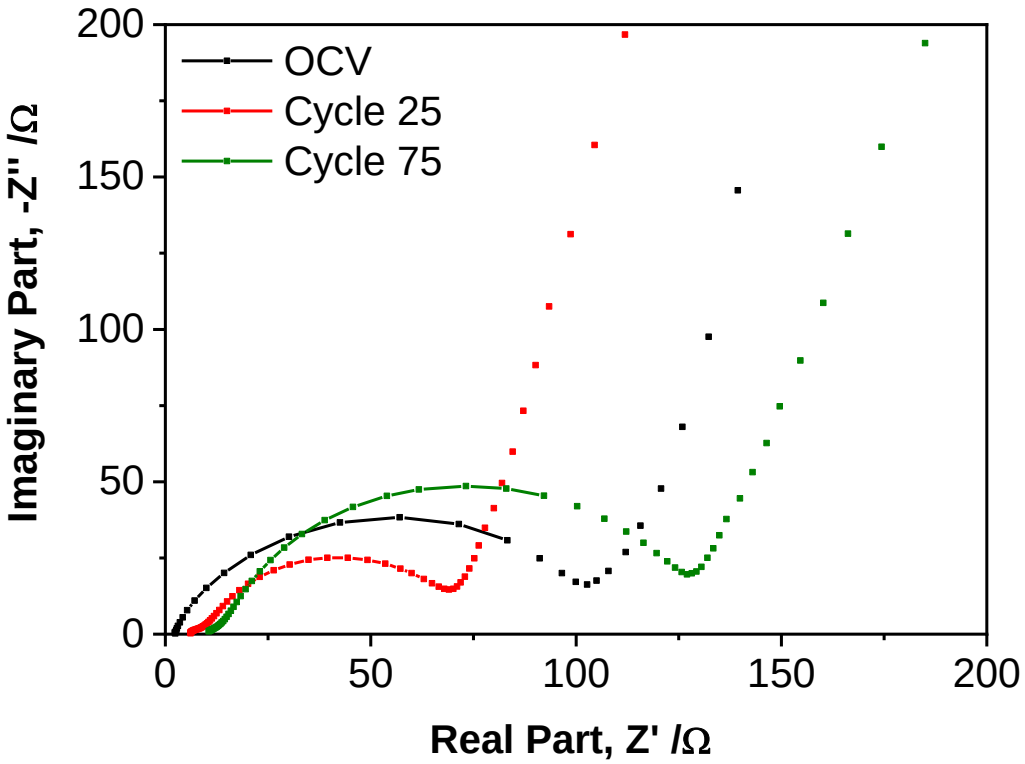

Figure 5.25 - Nyquist impedance plots collected from 0.01 Hz to 100 kHz at the end of discharge in cycles 25 and 75 acquired for $TaTe_2$ in LIBs.

Table 5.6 - Electrolyte, SEI and charge-transfer resistances determined from EIS for long cycling for $TaTe_2$ in LIBs.

Sample	R_S (Ω)	R_{SEI} (Ω)	R_{CT} (Ω)
OCV	2.1		107
10th cycle	2.3	3.0	11.8
25th cycle	5.8	65.5	4.4
75th cycle	10.2	114.6	5.8

Considering that the R_S takes into account contributions from the system, mainly intrinsic resistance from the electrode and interfacial resistance between the active material and current collector [40], the stable value up to the 10th cycle shows the stable intrinsic and interfacial resistance upon ion insertion and deinsertion. The sudden increase in R_S value upon 75 cycles could suggest an increase in the electrode resistivity as a whole. This can be related to the repetitive destruction and reconstruction of the initial $TaTe_2$ accompanied by the formation of extra phases, leading to the damage of the electronic transfer sites at the surface of the electrode [41]. This can be another reason why the performance of the electrode degrades upon cycling.

The Li^+ chemical diffusion coefficient (D_{Li^+}) was calculated from the low-frequency plots of the EIS spectra according to equation 5.2:

$$D_{Li^+} = \frac{R^2T^2}{2A^2n^4F^4C^2\sigma^2} \tag{5.2}$$

where R represents the ideal gas constant (8.314 J mol^{-1} K^{-1}), T is the ambient temperature (298.15 K), A is the surface area of the electrode, n is the number of electrons per molecule during intercalation, F is the Faraday constant (96485 C mol^{-1}), C is the electrolyte concentration (mol cm^{-3}) and σ is the Warburg coefficient (Ω $s^{-1/2}$). Figure 5.26 shows the graphs of real Z' with the inverse of the square root of angular

frequency, from which the Li^+ ion diffusion coefficient was determined for the OCV state.

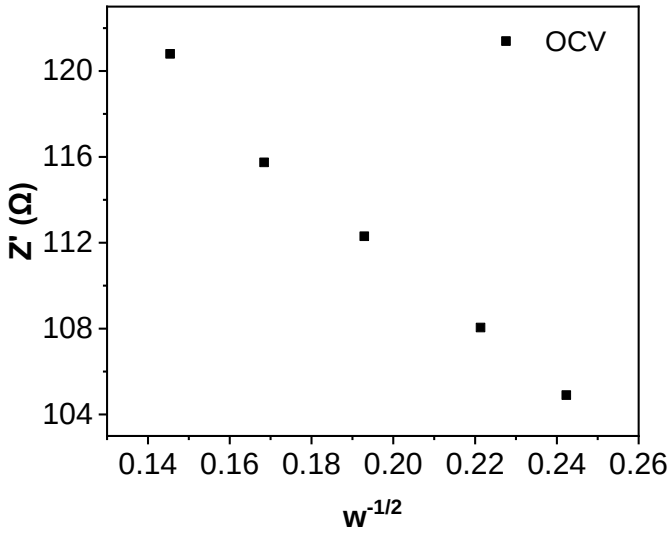

Figure 5.26 - Relationship between Z' and $\omega^{-1/2}$ in the low-frequency range for $TaTe_2$ at OCV state.

Table *5.7* shows the diffusion calculated values for the several points studied during the cycling process. The lithium diffusion coefficient determined at the OCV state was determined to be 1.80 x 10^{-18} cm^2 s^{-1}. To note that the values obtained vary by a couple of order of magnitude between 10^{-16} and 10^{-19}. To note that the diffusion coefficient values obtained are slightly lower than the values obtained by CV methods for Li^+ in $MoTe_2$ (vary from 1.43 x 10^{-11} and 3.83 x 10^{-15} cm^2 s^{-1}) [35]. The lowest diffusion value is registered at the end of the 2nd discharge (5.10 x 10^{-19} cm^2 s^{-1}). Although the highest R_{CT} value is registered at OCV state, the diffusion coefficient at OCV is higher han at the 2nd discharge which registers the second highest R_{CT} value. This can be associated with the high charge-transfer resistance of the material resulting from the reformation of the layered $TaTe_2$ during the charging process. The slight differences in crystal structure upon reformation result in a more difficult intercalation of ions leading to a higher diffusion coefficient.

Table 5.7 - Charge transfer resistance and Li^+ ion diffusion coefficient determined from EIS

Sample	R_{CT} (Ω)	D_{Li^+} ($cm^2\ s^{-1}$)
OCV	106.5	1.80×10^{-18}
1st Charge	30.2	4.30×10^{-17}
2nd Discharge	54.6	5.10×10^{-19}
5th Discharge	3.2	9.10×10^{-18}
5th Charge	4.0	1.20×10^{-16}
10th Discharge	11.8	7.4×10^{-18}
10th Charge	13.5	1.3×10^{-16}

5.3.3 Advanced structural characterization in LIBs

5.3.3.1 X-ray Absorption Near Edge Spectroscopy

Ex-situ X-ray absorption spectroscopy measurements were performed to understand the nature of the redox chemistry upon (de)lithiation of $TaTe_2$. The spectra of Ta and Te at the L_{III} and K-edges were collected from samples extracted from cells stopped at specific points during different discharge/ charge cycles. The intensity of the white line for the L_{III}-edge and the edge position of the K-edge was considered to gather the information needed.

As previously explained (Section 5.3.1.1), although the oxidation states of Ta and Te in $TaTe_2$ is expected to be +4 and -2 respectively, the short Te-Te distance in this compound leads to a charge transfer between the sp levels of the Te atoms and the d level of the transition metal which results in a net charge of -1.5 per tellurium atom. By consequence, the existent Te to Ta charge transfer occurring in the structure leads to a formal oxidation state of Ta of +3 [22].

The XAS spectra of the Ta L_{III}-edge (Figure 5.27) show a single large peak (white line) above the edge that corresponds to the dipolar transition from 2p core levels to unoccupied Ta 5d states. In theory, the white line intensity increases, and the peak position shifts to higher energies when the oxidation state of Ta increases and vice-versa [43]. The XAS spectra of the Ta L_{III}-edge shows a peak maximum at 9880.70 eV for the pristine material which can be attributed to Ta^{3+} in a distorted octahedral environment. Upon initial discharge down to 1.3 V, the white line intensity abruptly drops indicating a decrease in the Ta oxidation state. This can be explained by the movement of electron density from the Ta^{3+} atom to the $Te^{-1.5}$ atom for the Te atom to enter a more stable Te^{2-}. At this stage, the Ta atom is believed to be in a Ta^{4-x} state upon intercalation of Li^+ ions into the initial structure and transformation of $TaTe_2$ to $Li_xTa_{1-x}Te_2$, although a specific oxidation state cannot be accessed. An opposite trend is observed upon continuous discharge of the electrode to 0.1 V as the insertion of Li leads to a movement of electrons from the d orbital of Ta and a consequent increase in white line intensity. From the charge/discharge profiles (Section 5.3.2.1), is possible to assume that a total of 4 Li^+ ions are intercalated around 0.6 V, which leads us to expect the existence of Ta metal (Ta^0) below this voltage. The white line intensity at 0.8 V and 0.4 V is similar, with a slight difference in peak shape, although there are an extra 2.6 ions inserted in this 0.4 V window (3.3 and 5.9 ions for 0.8 and 0.4 V, respectively). This can be related to the change in preferential Li^+ intercalation site from the more stable 2d site to the less stable 4i site, which leads to a change of charge towards the Te atom and consequently the same oxidation state of Ta although more ions are inserted. At this point, we can only assume that the oxidation state of Ta is somewhere between OCV (+3) and 1.3 V (4-x). From 0.4 V to 0.1 V, an increase in white line intensity is observed which increases the oxidation state of the Ta atom. To note that the spectrum of the discharged sample does not coincide in energy to the Ta metal spectrum, which leads us to believe that the $TaTe_2$ structure does not fully convert Ta metal.

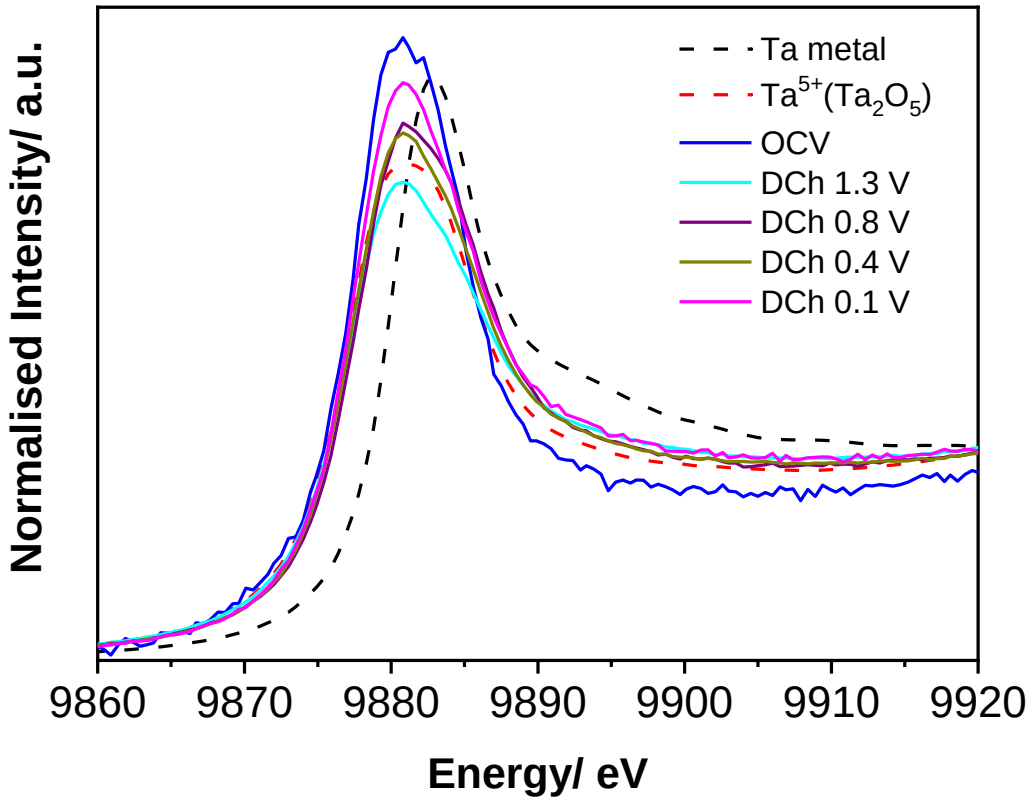

Figure 5.27- Normalized Ta L_{III}-edge XANES spectra of $TaTe_2$ electrode during the 1st discharge process along with standard Ta metal and Ta_2O_5 powders used as reference.

Upon charging (Figure 5.28), the Ta edge white line intensity is expected to lower as a result of the reduction of the Ta atom upon Li^+ deintercalation. The data obtained corroborate this assumption as we observe a decrease in the intensity of the white line as a result of the movement of electrons back into the Ta d orbital upon Li^+ extraction. Although a lower white line intensity is registered at the end of the charge at 3.0 V, the oxidation state of the initial $TaTe_2$ OCV sample is never recovered. This suggests that at the end of the 1st charging process, not all the Li^+ ions are removed and a $Li_xTa_{1-x}Te_2$ phase is still present.

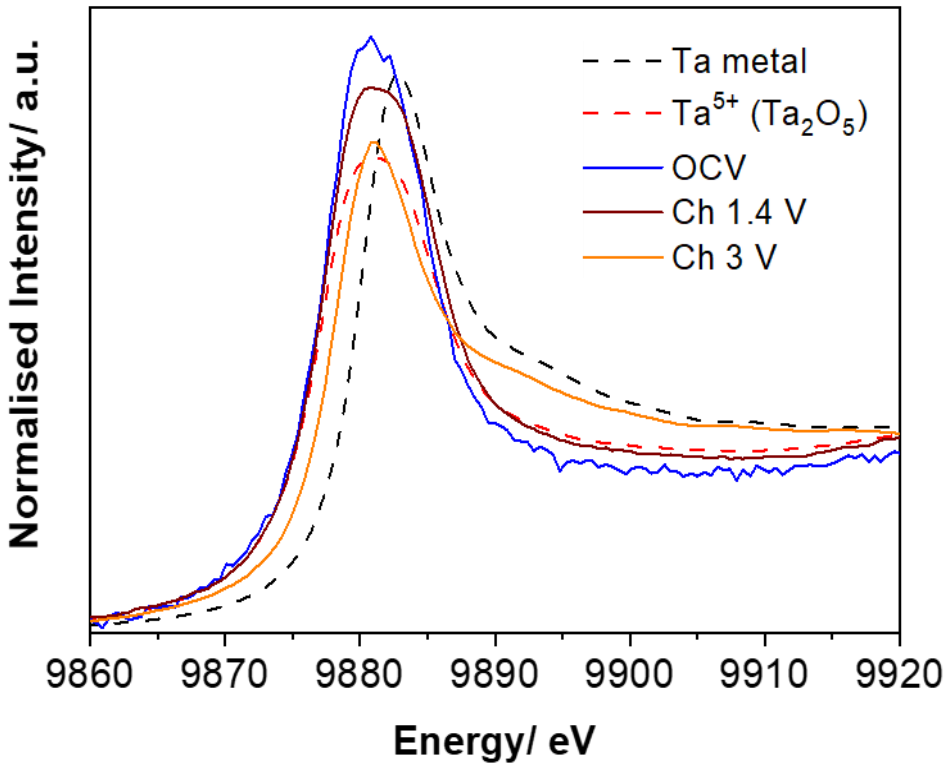

Figure 5.28- Normalized Ta L_{III}-edge XANES spectra of $TaTe_2$ electrode during the 1st charging process along with standard Ta metal and Ta_2O_5 powders used as reference.

The white-line intensity of the XANES spectra changes during the discharge and charge process and the maximum intensity of the white line upon cycling is represented in Figure 5.29. To note that the area of the white line behaves oppositely to the maximum intensity of the white line. The data shows that the white-line area in the various discharge and charge states are always lower than that of the metallic Ta, thus illustrating that the d electrons of the Ta deviate towards $TaTe_2$ instead of $LiTe_2$ during the discharge/charge process, thereby forming a stronger bond between Ta and Te.

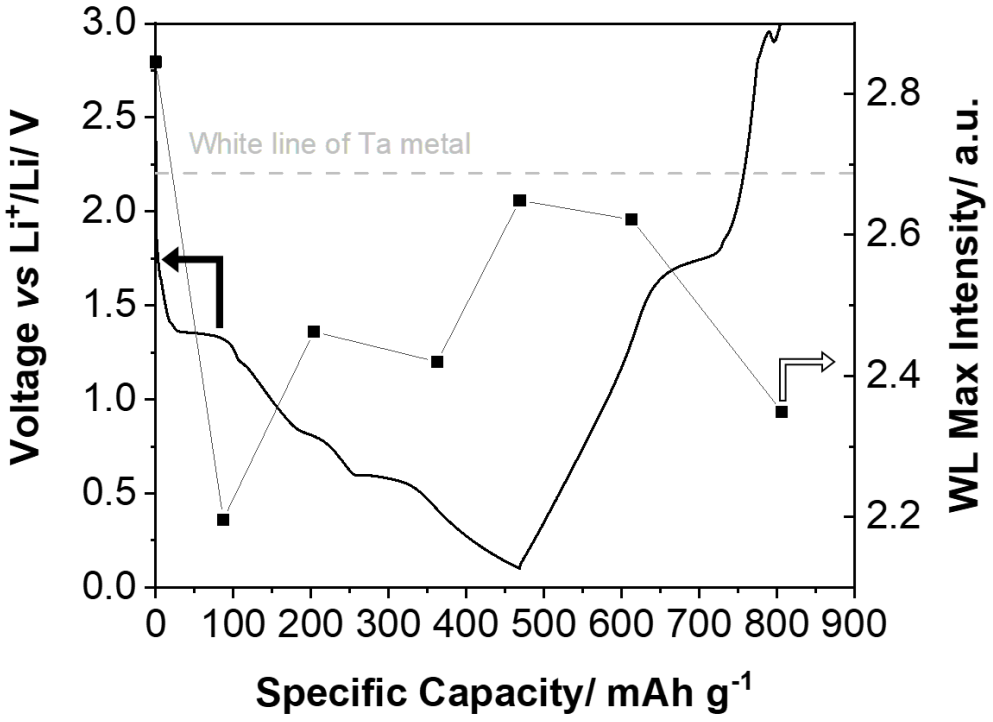

Figure 5.29– The change in the maximum white-line intensities of the Ta L_{III}-edge XANES for the $TaTe_2$ in the initial discharge/charge processes.

The K-absorption edge was analysed for the Te element where the maximum edge is proportional to the unoccupied density-of-states projected on the absorbing atom. The position of the edge reflects the local short and intermediate-range structure as well as the oxidation state of the central atom. The oxidation state of the Te element was analysed depending on the position of the edge [44]. The XAS spectrum of the pristine material shows a single edge at 32812.62 eV which can be associated with $Te^{-1.5}$. During the discharge process, the insertion of Li^+ ions into the crystal structure leads to the movement of the edge to lower energies, reaching 32809.72 eV at the end of discharge (0.1 V) (Figure 5.30). This movement indicates the reduction of the telluride ions, possibly from a $Te^{-1.5}$ state to a Te^{-2} like state. Upon discharge to 0.9 V, the broadening and flattening of the edge are observed which can be related to a change in the local coordination environment around Te. This could therefore explain the formation of Li_2Te.

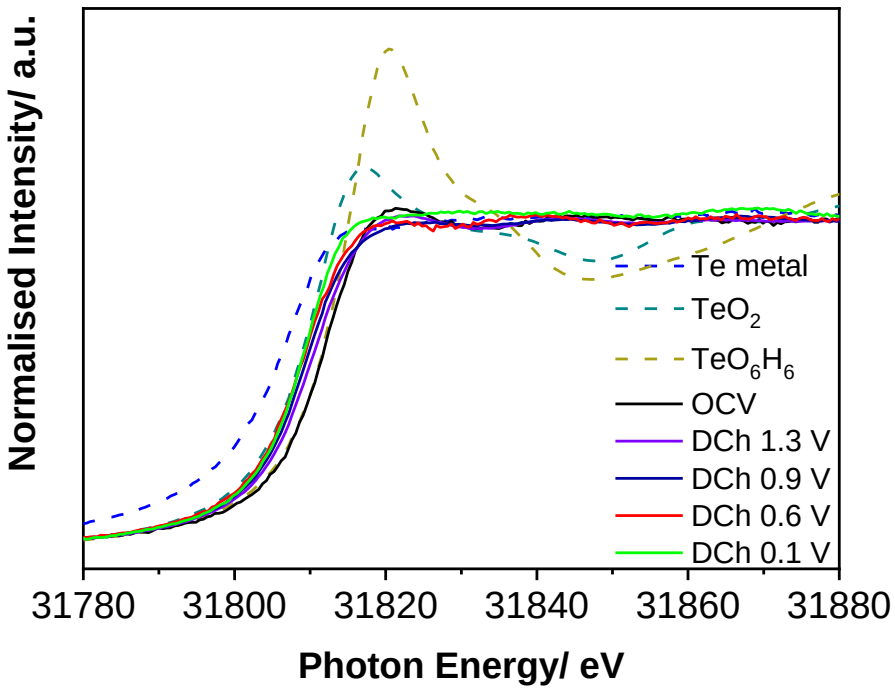

Figure 5.30- Normalized Te K-edge XANES spectra of $TaTe_2$ electrode during the 1st discharging process along with standard Te metal, TeO_2 and TeO_6H_6 powders used as reference.

Upon charge (Figure 5.31), the edge is observed to move towards higher energies (32812.62 eV), coinciding with the energy of the electrode at the OCV state. The return of the initial edge feature (wave-like) also corroborates the existence of $Te^{-1.5}$ which implies the reformation of the initial $TaTe_2$.

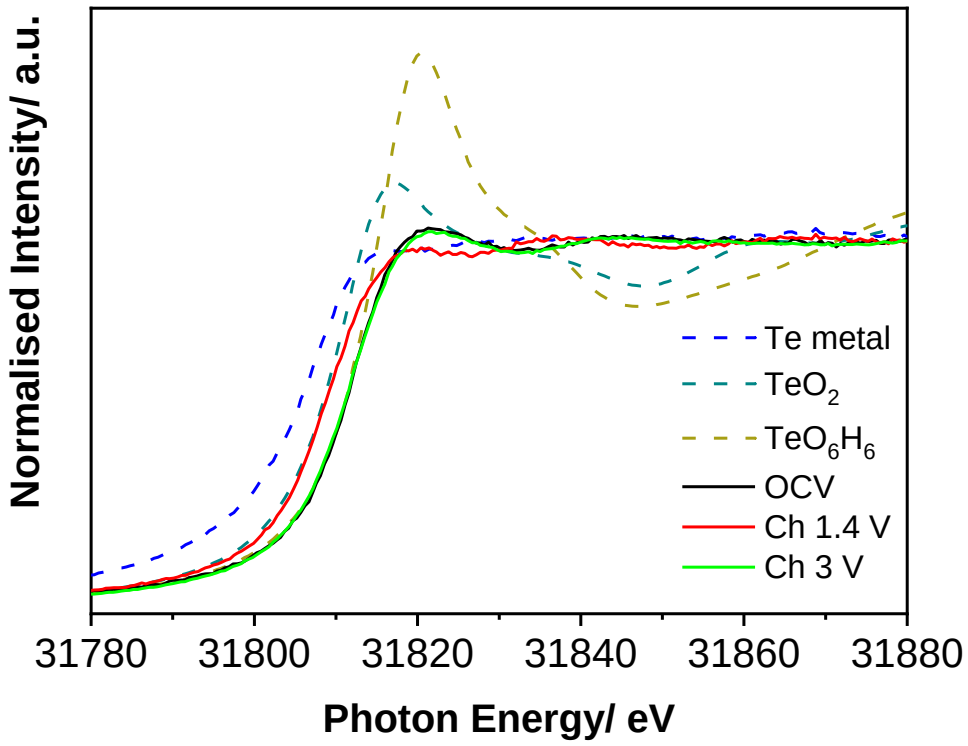

Figure 5.31- Normalized Te K-edge XANES spectra of $TaTe_2$ electrode during the 1st charging process along with standard Te metal, TeO_2 and TeO_6H_6 powders used as reference.

5.3.3.2 Operando XRD studies for the first (de)lithiation cycle

The structural changes and phase evolution of $TaTe_2$ occurring during the first charge/discharge process were probed by operando powder synchrotron X-ray diffraction. Figure 5.32 shows the evolution of the synchrotron X-ray diffraction patterns along with the cycling profile (1st cycle). All diffraction peaks of the electrode before cycling can be indexed to the $TaTe_2$ phase (*C*12/*m*1, [ICSD- 86141]).

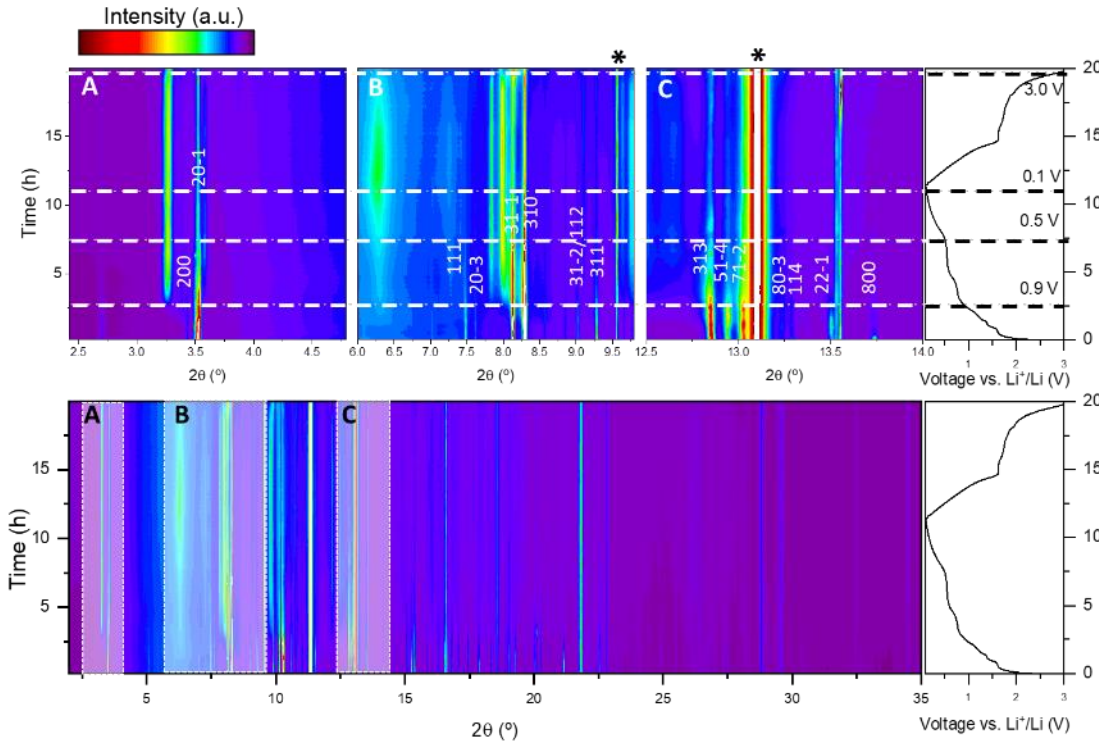

Figure 5.32 - Operando synchrotron X-ray diffraction patterns of the $TaTe_2$ electrode material, recorded during the first charge/discharge cycle with corresponding cycling profile. Cu current collector peaks marked with *.

No significant changes in the diffraction peaks with regard to 2θ degree position/intensity were observed from OCV down to 0.9 V. Upon reaching the first discharge plateau at 0.9 V, the $TaTe_2$ phase peaks start losing intensity. The fact that the main phase peaks remain throughout the whole cycling indicates that a partial irreversible reaction is occurring during the discharge process as suggested by the galvanostatic and cyclic voltammetry results (Sections 5.3.2.1 and 5.3.2.3). A gradual disorder of the interlayer spacing upon Li^+ ions intercalation and consequent fewer van-der-Waals interaction between the crystal layers can be associated with the decrease in intensity observed [45]. The insertion of Li^+ ions into the crystal structure along the c-axis induces the expansion of the lattice parameters in the layered $TaTe_2$ structure consequently increasing the interlayer spacing. Alongside the intensity decay registered, new diffraction peaks appear at 3.25°, 7.29° and 7.85° 2θ values, reflecting

the existence of a biphasic mechanism (Figure 5.33). By comparison with the WTe_2 structure (Chapter 4, Section 4.3.2.2), these peaks can be associated with a lithiated $TaTe_2$ structure (Li_xTaTe_2) and cell parameters can be found in

Table 5.8. To note the slight expansion in the c parameter of the unit cell from 9.365 to 9.723 Å resulting from the insertion of Li^+ ions into the structure.

Table 5.8 - Crystallographic data for $TaTe_2$ compounds at pristine and plateau stage.

h	k	l	2 Theta (°)	d (Å)	c (Å)	b (Å)	a (Å)	from CIF of $TaTe_2$	Step
0	0	3	7.83	3.0286	9.723				Plateau
0	0	3	8.13	2.9171	9.365			9.347	Pristine
2	0	0	3.26	7.2696			15.559		Plateau
2	0	0	3.52	6.7328			14.410	14.8	Pristine
3	1	0	7.98	2.9718		3.762			Plateau
3	1	0	8.29	2.8608		3.713		3.642	Pristine

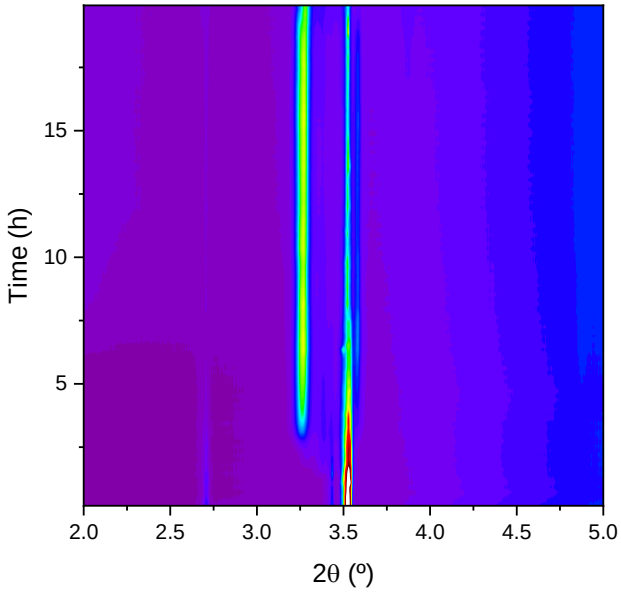

Figure 5.33 - Zoomed region of the operando synchrotron X-ray diffraction patterns of the $TaTe_2$ showing (200) and (20-1) reflections in $TaTe_2$.

An increase of the background signal is also detected around 0.9 V, which can be related to an amorphization of the present phases and/or the appearance of greatly disordered phases. The fact that the appearing peaks are broader than those of the pristine material, can be attributed to cracking and structure delamination. Other possible amorphous candidates present in this reaction are Ta or the oxides, TaO_2 and TeO_2 based on the elements in the electrode. A new diffraction peak at 6.27° was attributed to the Li_2Te phase (Figure 5.34), which starts forming during the discharge process at 0.9 V and reaches maximum intensity at around 0.5 V.

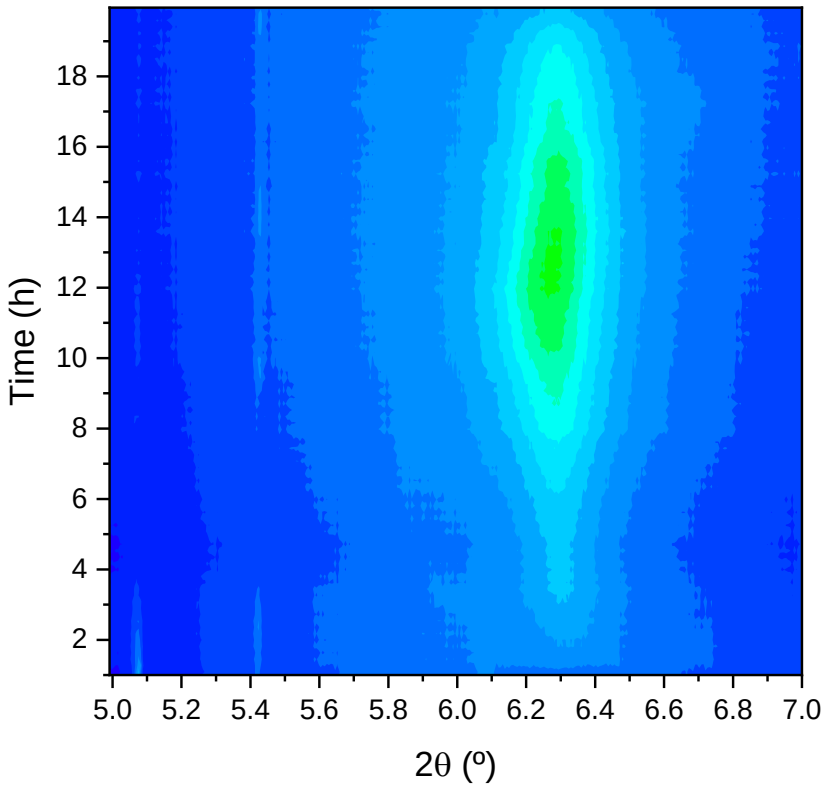

Figure 5.34 – Operando synchrotron X-ray diffraction patterns of the $TaTe_2$ indicating the formation of a Li_2Te phase during cycling.

The maximum intensity of the lithiated $TaTe_2$ phase is reached at t ~ 10h (correspondent to 4.62 mol Li^+ inserted). When discharging from 0.9 V down to 0.1 V, no change in intensity nor shift in the position of the diffraction peaks of the lithiated $TaTe_2$ phase is observed, reflecting a robust structure with no changes in the cell parameters upon lithium insertion. These results corroborate the theory that the initial $TaTe_2$ disintegrates into Ta and Te/Li_2Te upon insertion of Li^+ ion [24], [26]. During the constant voltage period at 0.1 V, no changes in the overall pattern intensity are observed. The full discharge pattern is characterized by the presence of $TaTe_2$, lithiated $LiTaTe_2$ and Li_2Te phases.

During charge, there are no meaningful changes nor in the intensity nor the peaks' position of the main or lithiated phases, a behaviour that has been registered in other layered dichalcogenides materials [46], [47]. This suggests that upon deinsertion of ions, the initial interlayer spacing of the crystal structure is not recovered. That is, the

peaks of the phase formed during the first plateau at 0.9 V are by the end of the charge more intense than those of the initial structure. The fact that the initial $TaTe_2$ phase is not recovered after charging the cell back, evidences the high structural irreversibility of this compound during the first cycle. To note that the peak correspondent to the Li_2Te phase is present throughout the charging process, with a slight decrease in intensity from 1.7 V up to 3.0 V. This suggests that during the first part of the deintercalation process, the Li^+ ions are removed primarily from the lithiated $TaTe_2$ phase and then from the Li alloy.

5.4 Conclusions

$TaTe_2$ was successfully synthesized and further analysed via XRD and electron microscopy analysis. PXRD analysis confirmed the purity of the material obtained, with no extra phases present. Cross-section analysis in SEM and TEM show that the pristine material consists of monodispersed irregular particle blocks consisting of few-layered exfoliated flakes with lateral sizes of ~ 1 μm.

Electrochemical measurements showed that $TaTe_2$ can be used as an anode material for LIBs, with a stepwise insertion of Li^+ ions. Galvanostatic cycling measurements at a low current rate showed an initial discharge capacity of 468.9 mAh g^{-1} and 49.4 % of the initial discharge capacity was still delivered after 30 cycles. The process behind the insertion/deinsertion of Li ions was examined by cycling the electrode at a higher current and a capacity retention of 53.6 % of its initial charge capacity after 30 cycles was achieved. Upon long cycling (100 cycles), a similar capacity retention profile was observed for both high and low current cycled electrodes, (24.5 and 25.4 % for 10 and 100 mA g^{-1}, respectively). The rate capability tests show that the $TaTe_2$ anode does not recover the total of its initial discharge capacity after cycling (88.5 % retention).

The electrochemical results were supported with CV and EIS measurements. The presence of several redox peaks in the cyclic voltammogram corroborates the multiphase reaction occurring in $TaTe_2$ when cycled against Li. The decrease in intensity peaks upon cycling reflects the less stable and reversible electrochemical behaviour of the electrode after the initial conversion reaction and SEI layer formation.

These results were corroborated by the cycled SEM data. The cycled SEM data after 75 cycles also shows the formation of cracks and particle agglomeration as a result of the increased internal strain during the reaction with lithium.

EIS measurements collected at different cycles show a progressive reduction of the total arc radius during cycling, suggesting a less resistive interface between the electrolyte and electrode. An abrupt decrease in charge-transfer resistance was observed upon cycling from the EIS measurement collected at OCV, which can be associated with the increase in the number of nanosized particles obtained after the conversion reaction after the first cycle which facilitates Li^+ transfer. At the same time, an increase in R_{SEI} is observed which can be related to the large-volume changes experienced by Te compounds formed during cycling during lithiation and delithiation.

Structure evolution upon Li^+ ion insertion was studied by XANES and operando XRD measurements. The XAS spectra at OCV state revealed that the formal oxidation state for Ta and Te are +3 and -1.5, respectively. During the discharge process, the Ta L_{III}-edge increases, indicating an increase in the Ta oxidation state. The fact that the spectrum of the discharged sample does not coincide in energy to the Ta metal spectrum, leads us to believe that the $TaTe_2$ structure does not convert totally in Ta metal. At the same time, the movement of the Te K-edge towards lower energies as well as the broadening and flattening of the Te edge suggests changes in the local coordination environment around the Te and the formation of Li_2Te. During ion deinsertion, the decrease in Ta white line intensity suggests the movement of electrons back into the Ta d orbital upon Li^+ extraction. However, at the end of the 1st charging process, not all the Li^+ ions are removed and a $Li_xTa_{1-x}Te_2$ phase is still present. The Te K-edge moves towards higher energies as a result of the reduction of the Te atom. The return of the initial edge feature (wave-like) also corroborates the existence of $Te^{-1.5}$ which implies the reformation of the initial $TaTe_2$.

The XAS data is corroborated by the synchrotron operando X-ray diffraction data. At OCV state, all diffraction peaks can be indexed to the $TaTe_2$ phase. Upon reaching the first discharge plateau at 0.9 V, a decrease in the $TaTe_2$ diffraction intensity is observed indicating an increase in the disorder of the interlayer spacing upon ion intercalation. The insertion of Li^+ ions into the crystal structure along the c-axis induces the expansion

of the lattice parameters in the layered $TaTe_2$ structure consequently increasing the interlayer spacing. To note that, the main phase peaks remain throughout the whole cycling although less intense, reflecting the partial irreversible reaction occurring. Several new peaks are also identified and can be attributed to the formation of a lithiated $TaTe_2$ structure. A new diffraction peak at 6.27° was attributed to the Li_2Te phase, which starts forming at 0.9 V and reaches maximum intensity at around 0.5 V. Upon further discharge (lower than 0.9 V), no change in intensity nor shift in the position of the diffraction peaks of the lithiated $TaTe_2$ phase is observed, reflecting a robust structure with no changes in the cell parameters upon lithium insertion. No meaningful changes nor in the intensity nor the position of the main or lithiated phases are visible during the charging process, suggesting that no structural changes occur upon the first lithium insertion. To note that the peak correspondent to the Li_2Te phase is present throughout the charging process, with a slight decrease in intensity from 1.7 V up to 3.0 V, suggesting that in the first part of the deintercalation process the Li^+ ions are removed primarily from the lithiated $TaTe_2$ phase.

Altogether, the results obtained show that $TaTe_2$ can be successfully used as anode material for LIBs.

5.5 References

[1] M. A. Pell and J. A. Ibers, “New Ternary Group-IV Tellurides with Extensive Te-Te Bonding: The Low-Dimensional Compounds Cs3Ti3Te11 and Cs5Hf5Te26,” *Chem. Mater.*, vol. 8, no. 7, pp. 1386–1390, 1996.

[2] J. A. Cody and J. A. Ibers, “Uranium Tellurides: New One- and Two-Dimensional Compounds CsUTe6, CsTiUTes, Cs8Hf5UTe3o.6, and CsCuUTe3,” *Inorg. Chem.*, vol. 34, no. 12, pp. 3165–3172, 1995, doi: 10.1021/ic00116a006.

[3] J. Beck, “A Polymeric Tellurium Cation by Oxidation of Tellurium with Tungsten Bromides,” *Angew. Chem. Int. Ed. Engl*, vol. 45, no. 1, pp. 25–28, 1993.

[4] J. J. Gao *et al.*., "Origin of the structural phase transition in single-crystal TaT e2," *Phys. Rev. B*, vol. 98, no. 22, pp. 1–7, 2018, doi: 10.1103/PhysRevB.98.224104.

[5] J. Li *et al.*., "Synthesis of Ultrathin Metallic MTe2 (M = V, Nb, Ta) Single-Crystalline Nanoplates," *Adv. Mater.*, vol. 30, no. 36, pp. 1–8, 2018, doi: 10.1002/adma.201801043.

[6] N. V. Podberezskaya, S. A. Magarill, N. V. Pervukhina, and S. V. Borisov, "Crystal chemistry of dichalcogenides MX2," *J. Struct. Chem.*, vol. 42, no. 4, pp. 654–681, 2001, doi: 10.1023/A:1013106329156.

[7] B. E. Brown, "The crystal structures of NbT_2 and $TaTe_2$," *Acta Crystallogr.*, vol. 20, no. 2, pp. 264–267, 1966, doi: 10.1107/S0365110X66000501.

[8] M. Hangyo, S. I. Nakashima, and A. Mitsuishi, "Raman Spectroscopic Studies Of Mx2-Type Layered Compounds," *Ferroelectrics*, vol. 52, no. 1, pp. 151–159, 1983, doi: 10.1080/00150198308208248.

[9] K. Momma and F. Izumi, "VESTA 3 for three-dimensional visualization of crystal, volumetric and morphology data," *J. Appl. Crystallogr.*, vol. 44, no. 6, pp. 1272–1276, 2011, doi: 10.1107/S0021889811038970.

[10] D. Chakravarty, P. Kumar, V. S. Ugale, and D. J. Late, "Microwave-assisted synthesis of few-layered TaTe2 and its application as supercapacitor," *Eur. J. Inorg. Chem.*, vol. 2015, no. 9, pp. 1598–1603, 2015, doi: 10.1002/ejic.201403220.

[11] R. Guzmán, J. Morales, and J. L. Tirado, "Structural, Thermodynamic, and Kinetic Properties of Alkali-Metal Intercalation into Group 5 Metal Ditellurides," *Chem. Mater.*, vol. 7, no. 6, pp. 1171–1177, 1995, doi: 10.1021/cm00054a016.

[12] X. Chia, A. Ambrosi, P. Lazar, Z. Sofer, and M. Pumera, "Electrocatalysis of layered Group 5 metallic transition metal dichalcogenides (MX2, M = V, Nb, and Ta; X = S, Se, and Te)," *J. Mater. Chem. A*, vol. 4, no. 37, pp. 14241–14253,

2016, doi: 10.1039/c6ta05110c.

[13] R. B. Von Dreele and A. C. Larson, “General Structure Analysis Sytem (GSAS),” *Los Alamos Natl. Lab*, vol. LAUR, pp. 86–748, 1994, [Online]. Available: https://permalink.lanl.gov/object/tr?what=info:lanl-repo/lareport/LA-UR-86-0748_REV.

[14] M. Herklotz *et al.*., “A novel high-throughput setup for *in situ* powder diffraction on coin cell batteries,” *J. Appl. Crystallogr.*, vol. 49, pp. 340–345, 2016, doi: 10.1107/S1600576715022165.

[15] “Potentiostats - Biologic.” https://www.biologic.net/product_category/potentiostats-galvanostats/ (accessed Jul. 30, 2021).

[16] M. G. Kim *et al.*., “Unusual Li-ion storage through anionic redox processes of bacteria-driven tellurium nanorods,” *J. Mater. Chem. A*, vol. 3, no. 33, pp. 16978–16987, 2015, doi: 10.1039/c5ta04038h.

[17] K. T. Bennett *et al.*., “Large-Scale Production of 119mTe and 119Sb for Radiopharmaceutical Applications,” *ACS Cent. Sci.*, vol. 5, no. 3, pp. 494–505, 2019, doi: 10.1021/acscentsci.8b00869.

[18] B. Ravel and M. Newville, “ATHENA, ARTEMIS, HEPHAESTUS: Data analysis for X-ray absorption spectroscopy using IFEFFIT,” *J. Synchrotron Radiat.*, vol. 12, no. 4, pp. 537–541, 2005, doi: 10.1107/S0909049505012719.

[19] M. Newville, “IFEFFIT: Interactive XAFS analysis and FEFF fitting,” *J. Synchrotron Radiat.*, vol. 8, no. 2, pp. 322–324, 2001, doi: 10.1107/S0909049500016964.

[20] E. Canadell, S.́phane Jobic, R. Brec, J. Rouxel, and M. H. Whangbo, “Importance of short interlayer Te···Te contacts for the structural distortions and physical properties of CdI2-type layered transition-metal ditellurides,” *J. Solid State Chem.*, vol. 99, no. 1, pp. 189–199, 1992, doi: 10.1016/0022-4596(92)90304-E.

[21] T. Sörgel, J. Nuss, U. Wedig, R. K. Kremer, and M. Jansen, "A new low temperature modification of TaTe2-Comparison to the room temperature and the hypothetical 1T-TaTe2modification," *Mater. Res. Bull.*, vol. 41, no. 5, pp. 987–1000, 2006, doi: 10.1016/j.materresbull.2006.02.020.

[22] A. Vernes, W Bensch, H Ebert, W Heid, and C Nather, "Crystal Structure , Electrical Properties , and Electronic Band Structure of Tantalum ditelluride," *J. Phys. Condens. Matter*, vol. 4310, no. 23, pp. 761–774, 1998.

[23] R. Guzman, J. Morales, and J. L. Tirado, "Chain Cluster Polymerization and Alkali Metal Intercalation into Niobium Ditelluride," *Inorg. Chem.*, vol. 33, no. 16, pp. 3164–3168, 1994.

[24] K. H. Nam, G. K. Sung, J. H. Choi, J. S. Youn, K. J. Jeon, and C. M. Park, "New high-energy-density GeTe-based anodes for Li-ion batteries," *J. Mater. Chem. A*, vol. 7, no. 7, pp. 3278–3288, 2019, doi: 10.1039/C8TA12094C.

[25] K. H. Nam, J. H. Choi, and C. M. Park, "Highly reversible Na-ion reaction in nanostructured Sb 2 Te 3 -C composites as Na-ion battery anodes," *J. Electrochem. Soc.*, vol. 164, no. 9, pp. A2056–A2064, 2017, doi: 10.1149/2.1161709jes.

[26] A. R. Park and C. M. Park, "Cubic Crystal-Structured SnTe for Superior Li- and Na-Ion Battery Anodes," *ACS Nano*, vol. 11, no. 6, pp. 6074–6084, 2017, doi: 10.1021/acsnano.7b02039.

[27] X. Wang, I. Veremchuk, M. Bobnar, U. Burkhardt, J. T. Zhao, and Y. Grin, "Sodium Substitution in Lead Telluride," *Chem. Mater.*, vol. 30, no. 4, pp. 1362–1372, 2018, doi: 10.1021/acs.chemmater.7b05091.

[28] G. K. Sung, K. H. Nam, J. H. Choi, and C. M. Park, "Germanium telluride: Layered high-performance anode for sodium-ion batteries," *Electrochim. Acta*, vol. 331, p. 135393, 2020, doi: 10.1016/j.electacta.2019.135393.

[29] N. Ma, X. Y. Jiang, L. Zhang, X. S. Wang, Y. L. Cao, and X. Z. Zhang, "Novel 2D Layered Molybdenum Ditelluride Encapsulated in Few-Layer Graphene as

High-Performance Anode for Lithium-Ion Batteries," *Small*, vol. 14, no. 14, pp. 1–8, 2018, doi: 10.1002/smll.201703680.

[30] M. B. Pinson and M. Z. Bazant, "Theory of SEI Formation in Rechargeable Batteries: Capacity Fade, Accelerated Aging and Lifetime Prediction," *J. Electrochem. Soc.*, vol. 160, no. 2, pp. A243–A250, 2013, doi: 10.1149/2.044302jes.

[31] M. Srinivaas, C. Y. Wu, J. G. Duh, Y. C. Hu, and J. M. Wu, "Multi-walled carbon-nanotube-decorated tungsten ditelluride nanostars as anode material for lithium-ion batteries," *Nanotechnology*, vol. 31, no. 3, p. 035406, 2020, doi: 10.1088/1361-6528/ab48b2.

[32] C. M. Hayner, X. Zhao, and H. H. Kung, "Materials for Rechargeable Lithium-Ion Batteries," *Annu. Rev. Chem. Biomol. Eng.*, vol. 3, no. 1, pp. 445–471, 2012, doi: 10.1146/annurev-chembioeng-062011-081024.

[33] T. S. Sahu and S. Mitra, "Exfoliated MoS <inf>2</inf> Sheets and Reduced Graphene Oxide-An Excellent and Fast Anode for Sodium-ion Battery," *Sci. Rep.*, vol. 5, no. June, pp. 1–13, 2015, doi: 10.1038/srep12571.

[34] M. Yousaf *et al.*., "Tunable Free-Standing Core-Shell CNT@MoSe2 Anode for Lithium Storage," *ACS Appl. Mater. Interfaces*, vol. 10, no. 17, pp. 14622–14631, 2018, doi: 10.1021/acsami.7b19739.

[35] M. R. Panda *et al.*., "High Performance Lithium-Ion Batteries Using Layered 2H-MoTe2 as Anode," *Small*, vol. 2002669, pp. 1–16, 2020, doi: 10.1002/smll.202002669.

[36] M. R. Panda *et al.*., "Blocks of molybdenum ditelluride: A high rate anode for sodium-ion battery and full cell prototype study," *Nano Energy*, vol. 64, no. July, p. 103951, 2019, doi: 10.1016/j.nanoen.2019.103951.

[37] Z. Chen and J. R. Dahn, "Methods to obtain excellent capacity retention in LiCoO2 cycled to 4.5 V," *Electrochim. Acta*, vol. 49, no. 7, pp. 1079–1090, 2004, doi: 10.1016/j.electacta.2003.10.019.

[38] Y. Liu, J. Wang, Y. Xu, Y. Zhu, D. Bigio, and C. Wang, "Lithium-tellurium batteries based on tellurium/porous carbon composite," *J. Mater. Chem. A*, vol. 2, no. 31, pp. 12201–12207, 2014, doi: 10.1039/c4ta02075h.

[39] C. Luo *et al.*, "Selenium@Mesoporous carbon composite with superior lithium and sodium storage capacity," *ACS Nano*, vol. 7, no. 9, pp. 8003–8010, 2013, doi: 10.1021/nn403108w.

[40] S. W. Donne, "General Principles of Electrochemistry," in *Supercapacitors: Materials, Systems, and Applications*, 2013, pp. 1–68.

[41] R. M. Wightman, P. M. Kovach, W. G. Kuhr, and K. J. Stutts, "Methods To Improve Electrochemical Reversibility At Carbon Electrodes.," *Proc. - Electrochem. Soc.*, vol. 84–5, no. 7, pp. 510–524, 1984, doi: 10.1149/1.2115913.

[42] N. Ding *et al.*, "Determination of the diffusion coefficient of lithium ions in nano-Si," *Solid State Ionics*, vol. 180, no. 2–3, pp. 222–225, 2009, doi: 10.1016/j.ssi.2008.12.015.

[43] T. Tsuchiya, H. Imai, S. Miyoshi, P. A. Glans, J. Guo, and S. Yamaguchi, "X-Ray absorption, photoemission spectroscopy, and Raman scattering analysis of amorphous tantalum oxide with a large extent of oxygen nonstoichiometry," *Phys. Chem. Chem. Phys.*, vol. 13, no. 38, pp. 17013–17018, 2011, doi: 10.1039/c1cp21310e.

[44] P. V. Grundler *et al.*, "Xocolatlite, Ca2Mn24+ Te2O12·H2O, a new tellurate related to kuranakhite: Description and measurement of Te oxidation state by XANES spectroscopy," *Am. Mineral.*, vol. 93, no. 11–12, pp. 1911–1920, 2008, doi: 10.2138/am.2008.2870.

[45] C. Ding *et al.*, "Identifying the origin and contribution of pseudocapacitive sodium ion storage in tungsten disulphide nanosheets for application in sodium-ion capacitors," *J. Mater. Chem. A*, vol. 6, no. 42, pp. 21010–21017, 2018, doi: 10.1039/C8TA07677D.

[46] X. Wang, Z. Guan, Y. Li, Z. Wang, and L. Chen, "Guest-host interactions and

their impacts on structure and performance of nano-MoS2," *Nanoscale*, vol. 7, no. 2, pp. 637–641, 2015, doi: 10.1039/c4nr05773b.

[47] J. R. González, R. Alcántara, J. L. Tirado, A. J. Fielding, and R. A. W. Dryfe, "Electrochemical Interaction of Few-Layer Molybdenum Disulfide Composites vs Sodium: New Insights on the Reaction Mechanism," *Chem. Mater.*, vol. 29, no. 14, pp. 5886–5895, 2017, doi: 10.1021/acs.chemmater.7b01245.

6 Conclusions

6.1 Summary

In this work, the physical characterization of several 2D dichalcogenide anode materials has been described, together with their electrochemical behaviour and possibility of application as electrode anode materials for sodium and lithium-ion batteries. The morphology, crystal size and crystalline phase are key factors that affect the electrochemical performance of electrode materials due to their possible influence on ion absorption sites and diffusion pathways. For that reason, the physical characterization of the materials studied was done employing several diffraction, spectroscopic and electron microscopy techniques such as PXRD, SEM, TEM and Raman spectroscopy. The electrochemical behaviour behind the movement of ions through the van-der-Waals gap of the anode materials was studied using electrochemical methods such as galvanostatic cycling, cyclic voltammetry and electrochemical impedance. Moreover, these processes were further studied by combining electrochemical measurements with XAS and operando PXRD to understand the structural evolution upon ion insertion and extraction. The most significant conclusions resulting from this work are described below.

Chapter 1 and 2 consisted of the study of the tetrahedral WTe_2 (T_d-WTe_2) phase with the orthorhombic space group *Pmn*2_1. Electron microscopy showed that the pristine material consisted of monodispersed irregular particle blocks with a size ranging between 3 and 10 µm. The discharge capacity in SIBs half-cells was measured to be 288 mAh g^{-1} with a 63.5 % capacity retention after 20 cycles at a low current of 10 mA g^{-1} compared with 442 mAh g^{-1} and 40 % capacity retention in LIBs. Further CV and EIS measurements show the stepwise insertion of sodium and lithium into the crystal structure by the presence of several redox peaks. EIS results showed a decrease in electrode stability and contribution of both surface and diffusion-controlled processes during ion movement leading to a less reversible electrochemical behaviour upon the initial conversion of WTe_2 into W and X_2Te (X = Na, Li). The formation of the Na_xWTe_2 phase was revealed to be a kinetically limiting step for Na^+ ion insertion while this step was not identified in the CV data when Li was the intercalated ion. XAS and

operando XRD data showed that not all initial WTe_2 is converted to W metal upon ion insertion and that some initial WTe_2 or some sodiated/lithiated WTe_2 phase is still present throughout the 1st cycle. Data collected showed an increased stacking disorder as a consequence of the Na^+/Li^+ insertion into the structure as a result of the slight expansion of the lattice parameters along the c-axis in the T_d-WTe_2 structure. To note that although in both the sodium and lithium systems, an increase in the interlayer spacing is observed during the plateau phase upon ion insertion, this expansion is bigger in SIBs (14.858 *vs* 15.959 Å for Li^+ and Na^+ ions, respectively) which is related to the smaller size and lighter weight of lithium compared with sodium. This expansion leads to the formation of cracks and particle agglomeration upon continuous ion insertion/extraction as corroborated by cycled SEM data.

Monoclinic $TaTe_2$ with the space group *C*12/*m*1 was synthesized using solid-state methods. The materials exhibit monodispersed irregular particle blocks consisting of few-layered exfoliated flakes with lateral sizes of ~ 1 μm. The electrode was explored as anode material for LIBs displaying an initial discharge capacity at a low current of 10 mA g^{-1} of 468.9 mAh g^{-1} and 49.4 % capacity retention after 30 cycles, contrasting with a 53.6 % capacity retention when cycled at a high current of 100 mA g^{-1}. The presence of several redox peaks in the CV data corroborates the multiphase reaction occurring in $TaTe_2$ when cycled against Li. As observed for WTe_2, the conversion reaction occurring at the end of the 1st discharge process results in a less stable and reversible electrochemical behaviour of the electrode. XAS and operando XRD data showed the formation of a lithiated $TaTe_2$ structure during the discharge process although not all $TaTe_2$ structure is converted to Ta metal and Li_2Te during the conversion reaction. Results suggest that in the first part of the deintercalation process the Li^+ ions are removed primarily from the lithiated $TaTe_2$ phase and only after from the Li_2Te alloy. The formation of cracks and particle agglomeration as a result of the increased internal strain during reaction with lithium was observed as for WTe_2.

6.2 Future Work

Several works have been carried out to characterize the electrochemical activity and performance of 2D transition metal dichalcogenides as anodes for SIBs and LIBs. It should be noted that in this thesis the materials were characterized to focus on the specific capacity, cycle life, coulombic efficiency and rate capability. Other performance parameters such as high-temperature behaviour, thermodynamic properties and theoretical correlations between electrochemical and structural properties have not been investigated. It is therefore suggested that the following efforts should be made to further understand and improve the performances of as-prepared materials:

a) Optimizing or alter the synthesis process to improve the particle size and arrangement of the structure. Smaller particle size could be used to minimize the cracking and instability of the structure, while the use of pillaring atoms could improve the rigidness of the structure.
b) Coating techniques and carbon composites with graphene, for instance, could be adopted to improve the electrical conductivity and rate capability.
c) Using other coating techniques such as atomic layer deposition (ALD) or molecular layer deposition (MLD) could be used to modify the surface function and increase the mechanical strength against volume expansion consequences.
d) Theoretical studies such as DFT could be employed to better understand the ion intercalation sites and how does this affect the stability of the crystal structure during cycling.
e) More detailed studies should also be undertaken regarding the interaction occurring at electrode and electrolyte interphase. This would help to understand the mechanical properties within the SEI layer which can be related to the difficult movement of ions between anode and metal.
f) To understand the optimal uptake of ions to achieve reversible cycling stability, further electrochemical studies should be done.

Although several improvements should be done to tune and improve the materials studied, this work offers contributions to the quickly growing field of electrode development for sodium and lithium-ion batteries and is a timely contribution to the rapidly growing field of electrode development for energy storage technologies.

7 Appendices

7.1 Annexe A - CV Data Calibrations for WTe_2 in SIBs

Table 7.1, Table 7.2 and Table 7.3 shows the value of $I/v^{1/2}$ and $v/v^{1/2}$ for each peak at each scan rate calculated using the maximum intensity of the peak and scan rate.

Table 7.1 – Data correspondent to the linear relationship between the maximum intensity and the different scan rates for peak I for WTe_2 in SIBs.

Peak	Intensity (mA)	Scan rate ($mV\ s^{-1}$)	Scan Rate ($V\ s^{-1}$)	$V^{1/2}$	$I/v^{1/2}$	$v/v^{1/2}$
Peak I	-2.93	1.0	0.0010	0.032	92.65	0.032
	-2.66	0.8	0.0008	0.029	94.05	0.028
	-1.24	0.4	0.0004	0.020	62.00	0.020
	-0.94	0.2	0.0002	0.014	66.47	0.0141
	-0.51	0.1	0.0001	0.010	51.00	0.010

Table 7.2 - Data correspondent to the linear relationship between the maximum intensity and the different scan rates for peak II for WTe_2 in SIBs.

Peak	Intensity (mA)	Scan rate ($mV\ s^{-1}$)	Scan Rate ($V\ s^{-1}$)	$V^{1/2}$	$I/v^{1/2}$	$v/v^{1/2}$
Peak II	-2.34	1.0	0.0010	0.032	73.99	0.032
	-2.10	0.8	0.0008	0.029	74.25	0.028
	-1.43	0.4	0.0004	0.020	71.50	0.020

	-0.75	0.2	0.0002	0.014	52.89	0.014
	-0.32	0.1	0.0001	0.010	32.40	0.010

Table 7.3 - Data correspondent to the linear relationship between the maximum intensity and the different scan rates for peak III for WTe_2 in SIBs.

Peak	Intensity (mA)	Scan rate (mV s^{-1})	Scan Rate (V s^{-1})	$V^{1/2}$	$I/v^{1/2}$	$v/v^{1/2}$
Peak III	3.14	1.0	0.0010	0.032	99.30	0.032
	2.88	0.8	0.0008	0.029	101.82	0.028
	1.68	0.4	0.0004	0.020	84.00	0.020
	1.05	0.2	0.0002	0.014	74.25	0.014
	0.52	0.1	0.0001	0.010	52.00	0.010

The graph of $I/v^{1/2}$ *vs* $v/v^{1/2}$ for each peak can then be represented from the values calculated in the previous tables.

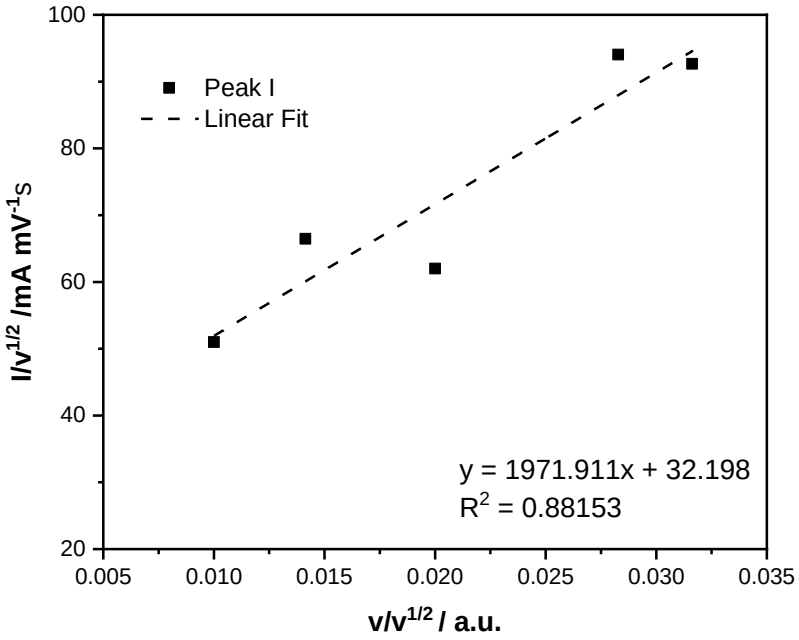

Figure 7.1 - Linear relationship between $I/v^{1/2}$ and $v/v^{1/2}$ for peak I in the scan rate range of 0.1 and 1 mV s^{-1} for WTe_2 in SIBs.

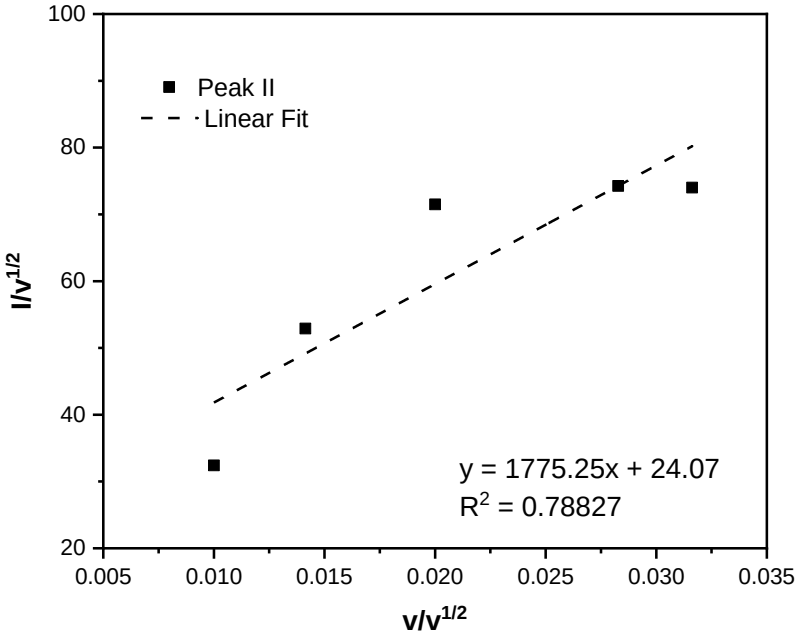

Figure 7.2- Linear relationship between $I/v^{1/2}$ and $v/v^{1/2}$ for peak II in the scan rate range of 0.1 and 1 mV s^{-1} for WTe_2 in SIBs.

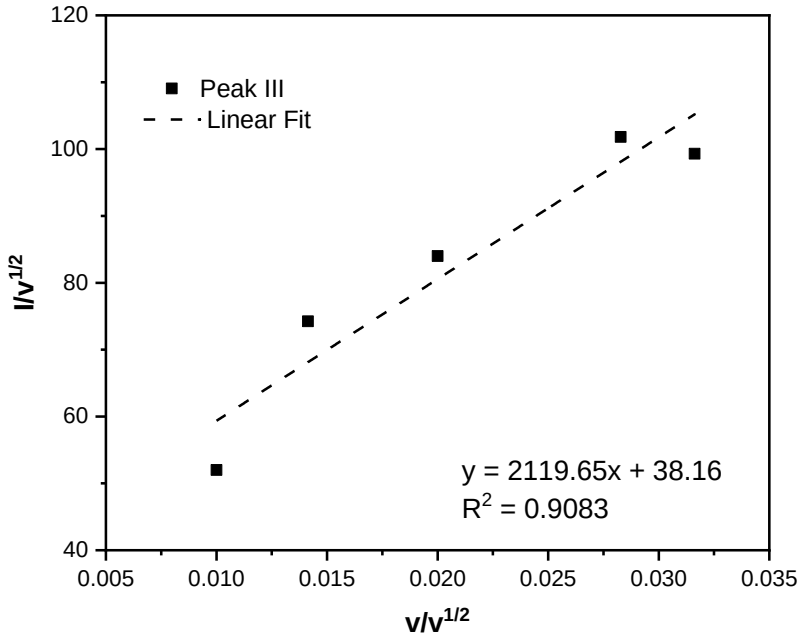

Figure 7.3- Linear relationship between $I/v^{1/2}$ and $v/v^{1/2}$ for peak III in the scan rate range of 0.1 and 1 mV s^{-1} for WTe_2 in SIBs.

Considering the linear regression of the previous graph, the value of k_1v and $k_2v^{1/2}$ can be calculated. For that, we admit that the slope and the intercept of the linear regression represent k_1 and k_2, respectively. The values of k_1v and $k_2v^{1/2}$ for each peak at each scan rate are in Table 7.4, Table 7.5 and Table 7.6.

Table 7.4 – Calculation of the values of k_1v and $k_2v^{1/2}$ at each scan rate for peak I for WTe_2 in SIBs.

	Scan rate ($V\ s^{-1}$)				
	0.001	**0.0008**	**0.0004**	**0.0002**	**0.0001**
k_1v	1.972	1.578	0.789	0.394	0.197
$k_2v^{1/2}$	1.018	0.911	0.644	0.455	0.322

Table 7.5 - Calculation of the values of k_1v and $k_2v^{1/2}$ at each scan rate for peak II for WTe_2 in SIBs.

	Scan rate ($V\ s^{-1}$)				
	0.001	**0.0008**	**0.0004**	**0.0002**	**0.0001**
k_1v	1.775	1.420	0.710	0.355	0.178
$k_2v^{1/2}$	0.761	0.681	0.481	0.340	0.241

Table 7.6 - Calculation of the values of k_1v and $k_2v^{1/2}$ at each scan rate for peak III for WTe_2 in SIBs.

	Scan rate ($V\ s^{-1}$)

	0.001	0.0008	0.0004	0.0002	0.0001
k_1v	2.112	1.696	0.848	0.424	0.212
$k_2v^{1/2}$	1.201	1.079	0.763	0.539	0.382

Using the equation $I(V) = k_1v + k_2v^{1/2}$ and assuming the value of I the max intensity at each scan rate is the intensity recorded in Table 7.7, the value k_1 and k_2 from the straight-line fit between $v^{1/2}$ versus different scanning. An average of the k_1 obtained was done to achieve one single value for each scan rate. The value of k_2 was obtained from the calculation of $k_2 = 100 - k_1$ (Table 7.8).

Table 7.7 – Calculated k_1 values for each peak (I, II and III) at each scan rate analysed for WTe_2 in SIBs.

	k_1 value			
Scan Rate (mV s^{-1})	**Peak I**	**Peak II**	**Peak III**	**Average**
1.0	67.30	75.86	67.50	70.22
0.8	59.30	67.63	58.88	61.94
0.4	49.66	49.66	50.47	49.93
0.2	47.47	7.47	40.37	45.10
0.1	74.27	54.79	40.76	56.61

Table 7.8 – Calculated capacitive and diffusion percentages at each scan rate for WTe_2 in SIBs.

Scan Rate (mV s^{-1})	Capacitive (%)	Diffusion (%)
1.0	70.5	29.5
0.8	62.2	37.8
0.4	49.9	50.1
0.2	45.8	54.2
0.1	53.2	46.8

7.2 Annexe B - CV Data Calibrations for WTe_2 in LIBs

Table 7.9 and Table 7.10 show the value of $I/v^{1/2}$ and $v/v^{1/2}$ for each peak at each scan rate calculated using the maximum intensity of the peak and scan rate.

Table 7.9 - Data correspondent to the linear relationship between the maximum intensity and the different scan rates for peak I for WTe_2 in LIBs.

Peak	Intensity (mA)	Scan rate ($mV\ s^{-1}$)	Scan Rate ($V\ s^{-1}$)	$V^{1/2}$	$I/v^{1/2}$	$v/v^{1/2}$
Peak I	-3.52	1.0	0.0010	0.031	111.34	0.032
	-2.59	0.8	0.0008	0.028	91.61	0.028
	-1.55	0.4	0.0004	0.020	77.35	0.020
	-0.27	0.08	0.00008	0.009	29.63	0.009

Table 7.10 - Data correspondent to the linear relationship between the maximum intensity and the different scan rates for peak II for WTe_2 in LIBs.

Peak	Intensity (mA)	Scan rate ($mV\ s^{-1}$)	Scan Rate ($V\ s^{-1}$)	$V^{1/2}$	$I/v^{1/2}$	$v/v^{1/2}$
Peak I’	2.86	1.0	0.001	0.032	90.57	0.032
	1.99	0.8	0.0008	0.028	70.25	0.024
	1.15	0.4	0.0004	0.020	57.25	0.020
	0.22	0.08	0.00008	0.009	25.04	0.009

The graph of $I/v^{1/2}$ *vs* $v/v^{1/2}$ for each peak can then be represented from the values calculated in the previous tables.

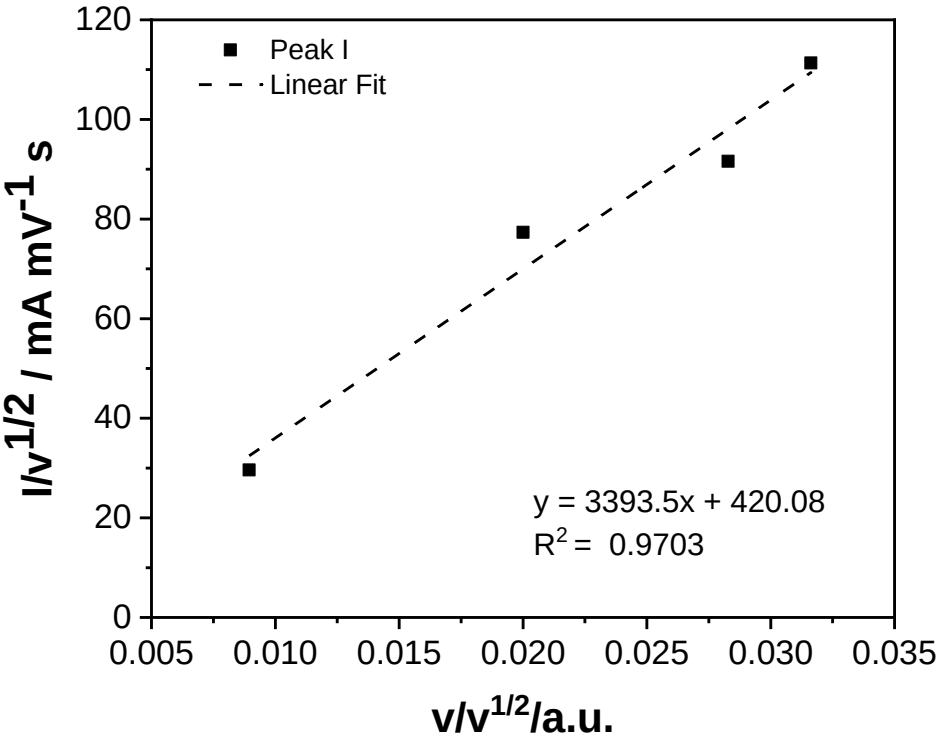

Figure 7.4 - Linear relationship between $I/v^{1/2}$ and $v/v^{1/2}$ for peak I in the scan rate range of 0.08 and 1 mV s^{-1} for WTe_2 in LIBs.

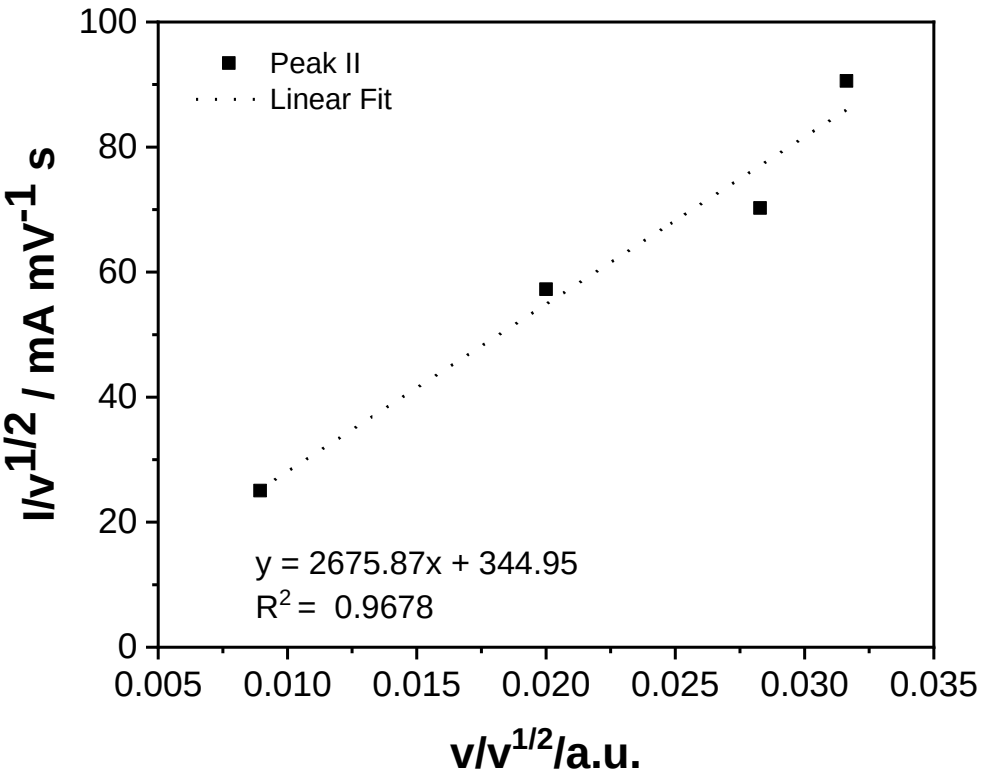

Figure 7.5- Linear relationship between $I/v^{1/2}$ and $v/v^{1/2}$ for peak II in the scan rate range of 0.08 and 1 mV s^{-1} for WTe_2 in LIBs.

Considering the linear regression of the previous graph, the value of k_1v and $k_2v^{1/2}$ can be calculated. For that, we admit that the slope and the intercept of the linear regression represent k_1 and k_2, respectively. The values of k_1v and $k_2v^{1/2}$ for each peak at each scan rate are in Table 7.11 and Table 7.12.

Table 7.11 - Calculation of the values of k_1v and $k_2v^{1/2}$ at each scan rate for peak I for WTe_2 in LIBs.

	Scan rate (V s^{-1})			
	0.001	**0.0006**	**0.0004**	**0.00008**
k_1v	3.394	2.715	1.357	0.271

$k_2v^{1/2}$	0.066	0.059	0.042	0.019

Table 7.12 – Calculation of the values of k_1v and $k_2v^{1/2}$ at each scan rate for peak II for WTe_2 in LIBs.

	Scan rate (V s^{-1})			
	0.001	**0.0006**	**0.0004**	**0.00008**
k_1v	2.248	1.798	0.899	0.179
$k_2v^{1/2}$	0.471	0.421	0.298	0.133

Using the equation $I(V) = k_1v + k_2v^{1/2}$ and assuming the value of I the max intensity at each scan rate is the intensity recorded in Table 7.13, the value k_1 and k_2 from the straight-line fit between $v^{1/2}$ versus different scanning. An average of the k_1 obtained was done to achieve one single value for each scan rate. The value of k_2 was obtained from the calculation of $k_2 = 100 - k_1$ (Table 7.14).

Table 7.13 - Calculated k_1 values for each peak (I and II) at each scan rate analysed for WTe_2 in LIBs.

	k_1 value		
Scan Rate (mV s^{-1})	**Peak I**	**Peak II**	**Average**
1	96.38	78.50	87.44
0.8	90.49	79.61	85.05

0.4	78.54	78.53	78.54
0.08	7.10	80.29	43.69

Table 7.14 - Calculated capacitive and diffusion percentages at each scan rate for WTe_2 in LIBs.

Scan Rate (mV s^{-1})	Capacitive (%)	Diffusion (%)
1	87	13
0.8	85	15
0.4	79	21
0.08	44	56